The Dissertation Committee for William Andrew Hoey Certifies that this is the approved version of the following dissertation:

Rarefied Gas Dynamic Simulations of Planetary Atmospheric Systems

Committee:

David B. Goldstein, Co-Supervisor

Philip L. Varghese, Co-Supervisor

Laurence M. Trafton

Fabrizio Bisetti

Robert E. Johnson

Orenthal J. Tucker

Rarefied Gas Dynamic Simulations of Planetary Atmospheric Systems

by

William Andrew Hoey

Dissertation

Presented to the Faculty of the Graduate School of

The University of Texas at Austin

in Partial Fulfillment

of the Requirements

for the Degree of

Doctor of Philosophy

The University of Texas at Austin

December 2017

Dedication

To my beloved friends and family; to strive, to seek, to find, and not to yield.

"I leave Sisyphus at the foot of the mountain! One always finds one's burden again. But Sisyphus teaches the higher fidelity that negates the gods and raises rocks. He too concludes that all is well. This universe henceforth without a master seems to him neither sterile nor futile. Each atom of that stone, each mineral flake of that night filled mountain, in itself forms a world. The struggle itself toward the heights is enough to fill a man's heart. One must imagine Sisyphus happy."

– Albert Camus, “The Myth of Sisyphus,” 1942.

Acknowledgements

"I cannot rest from travel; I will drink
Life to the lees. All times I have enjoy'd
Greatly, have suffer'd greatly, both with those
That loved me, and alone"

I'd first like to thank my advisors Prof. David Goldstein, Prof. Philip Varghese, and Dr. Laurence Trafton for their guidance and supervision, their many thoughtful comments and suggestions, and their remarkable talent for finding new and interesting projects for me to pursue over these five years. Truly –

"How dull it is to pause, to make an end,
To rust unburnish'd, not to shine in use!
As tho' to breathe were life!"

I owe a great deal to the graduate students of our research group, present and former, who have built a truly amazing tool in the planetary DSMC code and with whom I had many worthwhile and enlightening conversations. My work began in following the research of Andrew Walker and Chris Moore toward simulating the Ionian atmosphere and, though they had left Texas before I arrived, both were quite responsive to my early questions. Andrew later became my mentor during the Los Alamos Space Weather summer program in 2014 and helped direct me in putting together the Earth code.

My colleagues here at UT proved invaluable resources, particularly William McDoniel and Parvathy Prem – key portions of my Earth and Tvashtar projects are built on their work, and I benefited a great deal from their expertise and their persistent efforts in improving our code. Seng Yeoh, as co-author on my first significant paper, was a thoughtful and warm presence who helped to guide me through that daunting exercise.

"I am a part of all that I have met;
Yet all experience is an arch wherethro'
Gleams that untravell'd world whose margin fades
For ever and for ever when I move."

I'd like to thank the students with whom I worked closely during the past few years on the various extensions of my projects. Peter Ackley and I went on quite an adventure in building the Tvashtar hybrid code, and we had many fruitful conversations between the frequent classes he had to teach. I'd like to thank Yasvanth Poondla for his work in developing a Mie scattering analysis of Tvashtar's suspended particles and for his consistent contributions to my cherished pub trivia team. And I'm fortunate to have had the pleasure of working with Natalie Atkinson and Sergio Tovar, who've picked up the Bondi-Hoyle and Earth projects respectively, as well as Jared Berg, Arnaud Mahieux, Saikishan Suryanarayanan, and Peter Clarke, among others.

"To follow knowledge like a sinking star,
Beyond the utmost bound of human thought."

I would have left aerospace many years ago had it not been for Prof. Joseph Powers, an exceptional professor, advisor, and friend who showed me that there might be interesting and worthwhile pursuits in the field after all. I thank Prof. Fabrizio Bisetti, Prof. Robert Johnson, and Dr. Orenthal Tucker profusely for their insightful commentary and direction as my dissertation committee members. Prof. Paul Shapiro taught a delightful course in astrophysical gas dynamics and made possible the analyses of Appendices G and H with his suggestion that I consider the Bondi-Hoyle problem as an analog for the Pluto-Charon system. And I was lucky to have met Prof. Jack Holt, with whom I took several remarkable courses and from whom I learned a great deal, and not only about planetary geology and field-work.

"There lies the port; the vessel puffs her sail;
There gloom the dark, broad seas. My mariners,
Souls that have toil'd, and wrought, and thought with me,—
That ever with a frolic welcome took
The thunder and the sunshine,"

I deeply appreciate all those who have supported me through these years, particularly my incredible circle of friends from Notre Dame. Here in Austin, I thank my infinitely charming roommates, colleagues in aerospace engineering, and fellow mariners – Heath Reising, Leon Vanstone, Timothy Haller, Stephen Voelkel – who, yes, toil'd, wrought, and even occasionally thought with me. And of course Jennifer King, who often helped remind me to take care of myself, and that after thunder comes sunshine.

Finally, of course, none of what I've done or who I am would have been possible without the unconditional love, unflagging support, and all-too-often unappreciated sacrifices of my mother and father, my extended family, and my brother, John Alex, who is indescribably important to me.

"Come, my friends,

'T is not too late to seek a newer world."

– Alfred, Lord Tennyson, “Ulysses,” 1842.

Rarefied Gas Dynamic Simulations of Planetary Atmospheric Systems

William Andrew Hoey, Ph.D.

The University of Texas at Austin, 2017

Co-supervisors: David B. Goldstein and Philip L. Varghese

My doctoral research involves the advanced numerical simulation of rarefied (low-pressure) planetary atmospheres and volcanism with advanced physical modeling, in application of the Direct Simulation Monte Carlo (DSMC) method. This method is the approach of choice for modeling a wide range of continuum-to-rarefied systems - in which the average spacing between molecules in the flow becomes comparable to the flow length scales, and in which traditional means of computing fluid dynamics with the partial differential equations of continuum theory break down. DSMC is a probabilistic technique by which the motions and collisions of representative molecules are computed. Multiple gas species are modelled, along with non-equilibrium radiation, high speed collisions, photochemistry, and a wide range of other relevant physics. Comprehensive atmospheric simulations are computed in parallel on one- and three-dimensional domains that, depending on the scope of a particular project, can span entire atmospheric systems from planetary surface through vacuum. These projects are ongoing efforts in modeling and understanding global-scale atmospheric flows and the processes by which such flows are populated and propagated, and they represent advancements of the state-of-the-art in planetary atmospheric simulation.

I have produced and presented research on four distinct topics: 1) simulations of the complete atmosphere of Jupiter's volcanic moon Io including sublimation and plasma-sputtering processes; 2) the creation of a novel neutral density model for Earth's upper-atmosphere in partnership with Los Alamos' ISR division; 3) multi-species simulations of the rarefied gas dynamic, transfer, and escape processes of the Pluto-Charon system; and 4) investigations of the canopy unsteadiness and development of transient filamentary structure as observed by the New Horizons probe at the Ionian Tvashtar plume site.

In the course of these projects, and using my research group's existing planetary-science DSMC code as a foundation, I have developed a novel, generalized framework for rarefied atmospheric simulation that enables efficient and thorough construction of entire upper-atmospheric models. My dissertation offers an analysis of the methodology of rarefied gas dynamic planetary atmospheric simulation, in addition to discussion of each project's scientific context, the results of my simulations, and their relevance toward the explanation of various observed phenomena in planetary atmospheric science.

Table of Contents

List of Tables

List of Figures

Chapter 1: Introduction

1.1 Rarefied Flows in Planetary Systems

Our solar system features an incredible diversity of gas dynamic processes at planetary scale: a rocky-planet atmosphere at eighty times Earth's surface pressure and others so ephemeral that they exist only in daylight; geysers exhausting water vapor to space from vast hidden lakes; active volcanoes with explosive, persistent eruptions that form looming and collisional canopies. With few exceptions these processes are so diffuse as to be non-equilibrium – space is, after all, a near vacuum – but they are not necessarily free-molecular; intermolecular collisions often play an essential role in their driving physics. My research has involved the advanced numerical simulation of such *rarefied* planetary atmospheres and volcanic processes with state-of-the-art physical modeling in an application of the Direct Simulation Monte Carlo (DSMC) method. This method is the approach of choice for modeling a wide range of continuum-to-rarefied systems – in which the average spacing between molecules in the flow becomes comparable to the flow length scales, and in which traditional means of computing fluid dynamics with the partial differential equations of continuum theory (e.g. the Navier-Stokes equations) break down. Throughout this work I describe comprehensive atmospheric and volcanic calculations performed in parallel on one- and three-dimensional domains that, depending on the scope of a particular project, can span entire atmospheric systems from planetary surface through vacuum. These projects reflect ongoing efforts in modeling and understanding global-scale atmospheric flows and the processes by which such flows are populated and propagated, and represent advancements of the state-of-the-art in planetary atmospheric simulation. I present

original research on topics related to four distinct planetary systems including my own simulations of, and model development for,

1. Earth's rarefied, neutral-density upper atmosphere;
2. transfer and escape processes in the Pluto–Charon system;
3. the transient plume structure and evolution of Io's Tvashtar plume; and
4. the complete sublimation-driven atmosphere of Io itself.

This dissertation combines these topics in a broad analysis of the methodology of rarefied gas dynamic planetary atmospheric and volcanic simulations, and features discussions of each topic's scientific context and the results and conclusions of my simulations.

1.2 A Brief Review of the DSMC Method and Planetary Codebase

1.2.1 An Overview of Rarefied Flows

If a gas is dense and energetic enough to reliably transfer information from molecule to molecule via collision, its molecules will exhibit a Maxwellian velocity distribution and its behavior can be well-modeled as a continuous fluid with, for instance, the Navier-Stokes equations. A primary limitation to such models occurs when a fluid becomes very diffuse ('rarefied') and intermolecular collisions become infrequent; this is a common condition in planetary science: e.g. as the upper edges of atmospheres bleed off into the near-vacuum of space. Continuum models of fluid dynamics break down for gases of sufficient rarefaction, in which "gradients of the macroscopic variables become so steep that their scale length is of the same order as […] their *mean free path*" (Bird, 1994). More generally, continuum conservation equations are only valid to the extent that

viscous stress and heat flux may be expressed in terms of gradients of velocity and temperature, respectively. A useful ratio in expressing the level of rarefaction in a gas is the Knudsen number, which relates mean free path[1] λ to a flow characteristic length L as

$$\lambda = \left(\sqrt{2}\, n\, \sigma\right)^{-1}, \tag{1.1}$$

$$Kn = \lambda / L, \tag{1.2}$$

for number density n and molecular cross-section σ. This is most clearly expressed for a local characteristic length L relating a macroscopic property (i.e. n) to its spatial gradient,

$$L = n/(\nabla n)\,, \tag{1.3}$$

although other relevant length scales may also be used (e.g. the geometric parameters of a system). A Knudsen number Kn_H may be calculated for a characteristic atmospheric flow in which L is taken to be the atmospheric 'scale height', a macroscopic length scale reflecting the exponential decay of pressure with altitude in an isothermal atmosphere,

$$L_H = kT/mg. \tag{1.4}$$

Continuum assumptions begin to substantially falter for flows with Knudsen number above ~0.1 while the Boltzmann equation, which the DSMC approximates, remains valid throughout this range. Figure 1.1 shows the local mean free path, scale height, and Kn_H in a representative column of Earth's atmosphere between 300 km to 1000 km altitude.

[1] The distance between intermolecular collisions, defined in equation (1.1) for a homogeneous set of molecules modeled as hard spheres with Maxwellian-distributed velocities.

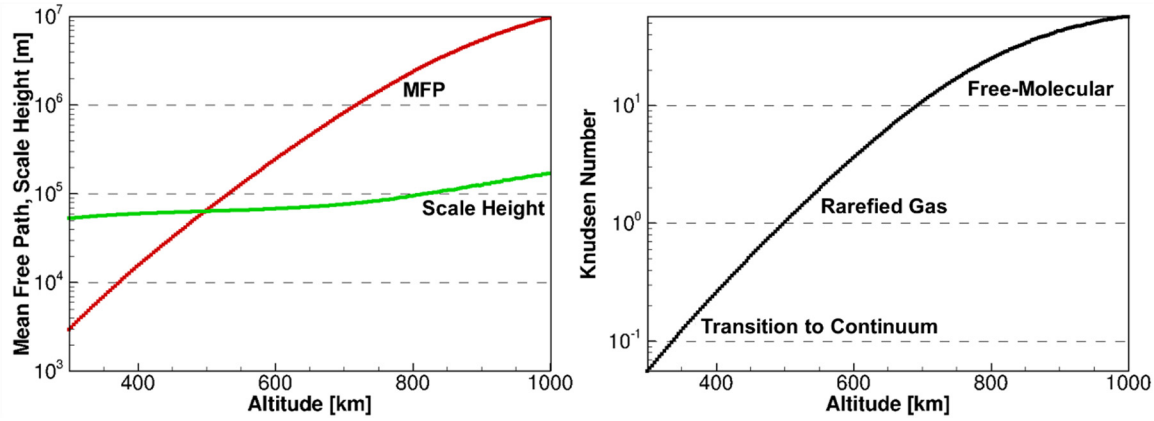

Figure 1.1: The local mean free path and scale height (at left) and resultant Knudsen number Kn_H (at right) through a column of the Earth's upper atmosphere.

1.2.2 The DSMC Method and Implementation[2]

The Direct Simulation Monte Carlo method, hereinafter referred to as 'DSMC', is a probabilistic technique by which the motion and collision of a set of *computational* molecules is simulated, representing the motion and collision of *real* molecules in a gas flow (Bird, 1994). The ratio of real to representative molecules is denoted F_{NUM}, which is typically selected to be O[10^{22}–10^{26}] in this work. A DSMC domain is decomposed into cells in which particles move and collide: only particles within the same cell can collide, and they do so in a binary and probabilistic manner. Between collisions particles translate under the influence of any force field present. A key assumption in DSMC is that particle movement and collision phases can be decoupled over a time interval much shorter than the mean time between collisions, τ_{coll}. Thus, the particle collision and movement phases

[2] Portions of this review first appeared in "Rarefied Gas Dynamic Simulation of Transfer and Escape in the Pluto-Charon System," and were co-authored by S. Yeoh.

are executed in sequence in DSMC over a time-step, Δt, chosen to be much smaller than τ_{coll}. Macroscopic flow properties of interest are obtained by averaging over molecular properties in each cell. A resolved DSMC calculation satisfies the collision integral in the Boltzmann equation (Nanbu, 1986) and indeed solves the Boltzmann equation itself (Wagner, 1992) – therefore it is valid for flow regimes from the continuum through free-molecular. However, it has broadest application in modeling moderately rarefied gas flows, as computational expense becomes prohibitive if one attempts to model continuum flow at molecular scale and it is unnecessary to append a collisional model in simulating free-molecular flow.

Throughout this work I adapt and apply a planetary DSMC codebase developed from the original procedure introduced by Bird (1994). This code has been applied elsewhere in simulations of the volcanic plumes and atmosphere of Io (Zhang *et al.*, 2003; Zhang 2004; Moore *et al.*, 2009; Walker *et al.*, 2010; Moore 2011; Walker 2012; McDoniel *et al.*, 2015; McDoniel 2015), of Enceladus' south polar two-phase plumes (Yeoh *et al.*, 2015; Yeoh 2015), of comet impacts on the moon and subsequent water ice deposition (Stewart, 2010; Stewart *et al.*, 2011; Prem *et al.*, 2015; Prem 2017), of the Europan water plume observed by HST in 2012 (Berg *et al*., 2016), and of the plume impingement of rockets landing on the lunar surface and resultant dust dispersal (Morris *et al.*, 2015). While the planetary DSMC code contains many features and physical models developed both for general and project-specific applications, most of these have been described in detail elsewhere, i.e. in the dissertations and papers of the code's many contributors. In each chapter's methodological review I highlight and explain those functions relevant to my own work as they arise, alongside those which I have developed.

In most applications described herein multiple gas species are modeled, along with non-equilibrium radiation, high speed collisions, photochemistry, and a range of

other relevant physics. The molecular model applied throughout is that of the variable hard sphere (VHS). Our code tracks the internal energy states of the gas molecules, notably their rotational and vibrational states, though in certain problems vibrational modes are hardly excited (e.g. at the low temperatures of Pluto, ≤ 100 K). Energy exchanges occur between the translational and the internal modes as well as among the internal modes through collisions via the statistical Larsen-Borgnakke exchange model (Borgnakke and Larsen, 1975; Bird, 1994). Calculations are performed in a noninertial reference frame that is fixed to the center of each body (i.e. Earth, Pluto, and Io) and that rotates with it. Therefore, computational particles travel along ballistic trajectories between collisions, under the influence of not only the gravitational fields of their primary body, but also secondary bodies (i.e. the Moon, Charon, and Jupiter) and the Coriolis and centrifugal forces arising from rotation in this noninertial frame. In our simulations, the equation of motion of a particle between collisions is given by

$$\ddot{\boldsymbol{r}}_{\boldsymbol{part}} = \boldsymbol{g}_{\boldsymbol{P}} + \boldsymbol{g}_{\boldsymbol{S}} - 2\left(\boldsymbol{\omega}_{\boldsymbol{P}} \times \dot{\boldsymbol{r}}_{\boldsymbol{part}}\right) - \boldsymbol{\omega}_{\boldsymbol{P}} \times \left(\boldsymbol{\omega}_{\boldsymbol{P}} \times \boldsymbol{r}_{\boldsymbol{part}}\right), \tag{1.5}$$

where $\boldsymbol{r}_{\boldsymbol{part}}$ is the position vector of the particle. The superscript dot notation indicates differentiation with respect to time. The first two terms on the right hand side, $\boldsymbol{g}_{\boldsymbol{P}}$ and $\boldsymbol{g}_{\boldsymbol{s}}$, are the variable gravitational accelerations due to the primary and secondary bodies respectively, proportional to the inverse of the square of the distance of the particle from the centers of the respective parent bodies. The third and fourth terms are the Coriolis and centrifugal accelerations respectively, where $\boldsymbol{\omega}_{\boldsymbol{P}}$ is the rotational velocity of the primary. The positions and velocities of the particles are obtained by integrating Equation 1.5: either by using a second-order predictor corrector scheme, as in our prior work, or by

using an 8th-order adaptively-stepped and error-controlled Runge-Kutta Prince-Dormand scheme incorporated for the Pluto-Charon problem (described in Appendix E).

DSMC requires that the cell size and Δt be smaller than the scale length, L, of the microscopic flow gradients and τ_{coll} respectively; in this work, L is chosen based on the gradients of the gas density, as in Equation 1.3. Since macroscopic flow gradients are not expected over length scales shorter than the local mean free path of the gas, λ, i.e. $\lambda < L$, the cell size requirement is satisfied if the cell size is smaller than λ. Our DSMC code uses a *spherical* coordinate grid that allows for non-uniform cell size distribution in each of the radial (r), zenith (θ) and azimuthal (φ) directions, as shown in Figure 1.2, an example of a simulation domain for the Pluto-Charon system. Generally, I have chosen a cell size distribution in each direction such that the cell sizes are smaller than λ everywhere in the simulation domain, and have also chosen Δt to be smaller than τ_{coll} everywhere. A notable exception occurs in the innermost stages of the Tvashtar problem, where real mean free paths reduce to millimeter scale – instead, I demonstrate in Chapter 5 that these inner stages resolve gradient length scales.

All simulations are computed in parallel on multiple processors distributed along the azimuthal and zenith coordinates. Throughout this work any single run was performed on between 16 and 1152 processors and ranged from O[10^1–10^4] CPU-hours (SU) in expense. Processors may be distributed in a number of ways, the simplest naïve scheme being on a uniform, equirectangular grid in φ and θ (azimuthal and zenith, or longitude and latitude) coordinates. For full-planet atmospheric problems in which global column densities vary globally only by small factors (i.e. the Earth and Pluto), static non-uniform grids may be applied in zenith which concentrate about the equatorial plane such that the total number of computational particles per processor, a useful proxy for expense and which ought to scale with surface area, does not vary significantly. For problems in

which densities vary by orders of magnitude in φ and θ – i.e. for plume simulations – McDoniel (2015) and Prem (2017) have recently developed an adaptive load-balancing scheme for processor redistribution in those coordinates on the basis of molecule count.

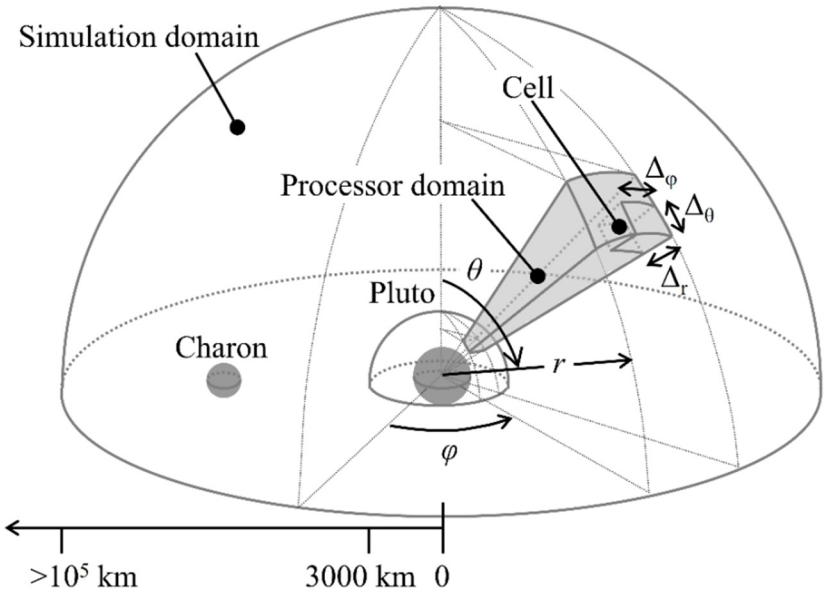

Figure 1.2: The shape and extent of the Pluto-Charon simulation domain. The processor and cell distributions shown (i.e. a spherical coordinate system parallelized in θ and φ) are consistent with those used throughout this work. Note that this drawing is not to scale. (Figure by S. Yeoh.)

In a typical simulation, the total number of computational particles per processor is of order O[10^5 to 10^6], with as many as O[10^8] occupying the complete domain at any one time. For the longest-term simulations of the Pluto-Charon system, or for multiple stages of the massive Tvashtar plume, as many as O[10^{11}] distinct particles may be generated over the course of a run to steady-state. Pseudo-random number generation

with the Mersenne Twister SFMT19937 algorithm (Saito and Matsumoto, 2006) is employed to ensure valid statistics, and is vectorized for speed.[3]

1.3 DISSERTATION OUTLINE

In Chapter 2, I introduce a novel model for Earth's rarefied neutral density upper atmosphere built within the familiar planetary DSMC framework. Chapter 3 describes the adaptation and extension of this model toward the simulation of rarefied gas dynamic atmospheric transfer and escape processes in the Pluto–Charon system, including both a range of simulations with boundary conditions drawn from pre-encounter predictions, and a new analysis informed by observations made during the July 2015 New Horizons encounter. My work toward simulations of the Ionian Tvashtar plume is split between two chapters – Chapter 4, on the development of a hybrid DSMC/entrained-particle model for parametric simulation of spatiotemporal variance in particle flux at the vent; and Chapter 5, on constraining New Horizons observations of the 2007 Tvashtar eruption via parametric DSMC simulations of the steady gas-field. Concluding thoughts are provided in Chapter 6. My simulations of Io's atmosphere – which build on the results of, and models developed by, Moore (2011) and Walker (2012) – are addressed in Appendix A. Supplementary material informing, extending, and adding context to this dissertation is available in Appendices B through I and referenced throughout the text, while a list of relevant publications and presentations of my work can be found in Appendix J.

[3] The SIMD-friendly Fast Mersenne Twister pseudorandom number generation algorithm, as implemented in Intel MKL (the Math Kernel Library).

1.3.1 A Novel Model for Earth's Rarefied Upper Atmosphere[4]

Developing a robust predictive capability for Earth's rarefied and neutral-density upper atmosphere is an essential goal of both the satellite operations and space weather communities. To that end, I extended the DSMC planetary-science code base established in modeling of the Ionian environs to reflect terrestrial physics, as described in Chapter 2. Model development includes the incorporation of lower boundary conditions consistent with the commonly-used semi-empirical atmospheric model NRLMSISE-00 (MSIS); ultraviolet radiation and photo-chemistry rates modeled with reference to space weather indices; and a model for radiative absorption into molecular rotational states with rates attenuated by integrated column density, initially developed for the lunar case by Prem (2017). To test this new implementation, a range of one- and three-dimensional simulations was computed on domains extending from the mid-thermosphere, near the continuum-rarefied transition, into the free-molecular regime above Earth's exobase. Comparisons with results drawn from MSIS and from indirect satellite mass density measurements are employed in benchmarking model accuracy.

1.3.2 Simulating Transfer and Escape in the Pluto-Charon System[5]

The Earth project required substantial modifications to our planetary codebase enabling atmospheric generation by Maxwellian flux across an arbitrary mid-atmospheric surface. These adaptations allowed me to quickly turn the Earth code toward the Pluto-Charon system, motivated by the needs for ongoing New Horizons data analysis and

[4] I presented this research at the concluding session of the Los Alamos Space Weather Summer School, in a summary report to the Laboratory's Intelligence and Space Research Division, and at the December 2014 meeting of the American Geophysical Union.

[5] Our work on the Pluto-Charon system was the subject of a poster at the 2016 Lunar and Planetary Science conference and a paper published in *Icarus* in early 2017.

interpretation following the July 2015 encounter, and for new kinetic models toward predicting and evaluating escape from Pluto's rarefied upper atmosphere. Our novel, three-dimensional DSMC model of the plutonian upper atmosphere spans from below the exobase – where continuum flow transitions to the rarefied regime – to fully free-molecular flow hundreds of thousands of kilometers from Pluto's center. It accounts for the gravitational fields of both Pluto and Charon, the centripetal and Coriolis forces due to our Pluto-fixed reference frame, and the presence of Charon as a sink for impacting particles. Using this model, I analyze the escape processes of N_2 and CH_4 across a range of solar heating conditions, and evaluate the three-dimensional structure of the upper plutonian atmosphere, including gas transfer to and deposition on Charon.

1.3.3 An Investigation of the Unsteady Ionian Tvashtar Plume

Jupiter's moon Io supports its rarefied atmosphere with tidally-driven episodic volcanism: its many plumes emit volatile gases that contribute directly to the local atmospheric column, and that condense to the surface in frost deposits which sublimate under diurnal insolation and are sputtered by incident plasma. The largest volcanic plumes of Pele-class exhibit violent and intricate structure, with their canopies rising hundreds of kilometers above Io's surface. In early 2007, New Horizons (NH) captured an active Tvashtar plume in a time sequence of panchromatic images at high spatial resolution, and observed both discrete "filamentary" patterns in descending particulate structure and a large traveling canopy wave. These are transient and asymmetric features, indicative of Tvashtar's unresolved and complex vent processes.

1.3.3.1 Developing a Hybrid Model for Simulating Transient Canopy Structures[6]

In Chapter 4, I introduce a methodology developed with collaborator Peter Ackley for identifying vent spatiotemporal scales in rarefied plumes, in which we move entrained dust / condensate particles through steady DSMC flowfields. We simulate variable source configurations parametrically, tracing canopy structures forward and backward in time.

1.3.3.2 Constraining Tvashtar's Source and Canopy with Parametric Simulations[7]

Available observational data for the 2007 Tvashtar plume offers only limited constraints on the state of its source region. In Chapter 5, I describe parametric DSMC simulations of the Tvashtar plume in which I vary source parameters (i.e. aspect ratio, temperature) and compare resultant canopies to NH observations. This work offers new constraints on the 2007 Tvashtar source and provides insight into the influence of source configuration on the overall gas field and canopy structure of Pele-class plumes.

1.3.4 Modeling Global Flow in Io's Rarefied Atmosphere[8]

As outlined above, Io has a complex rarefied atmosphere sourced by volcanism. Its primary constituent is sulfur dioxide (SO_2) which freezes onto Io's cold surface in patches of frost. That frost sublimates when exposed to sunlight during the diurnal cycle, remains temporarily suspended as an ephemeral atmosphere, and freezes during night as it falls back onto the surface. The resultant flow forms a tenuous 'bubble' of sublimation

---

[6] The hybrid model has been presented at the 30th International Symposium on Rarefied Gas Dynamics and published in the conference proceedings in a paper co-authored by Peter Ackley.

[7] Recent Tvashtar work is the subject of two pending *Icarus* manuscripts.

[8] This work was presented at the fall 2013 meeting of the AAS Division for Planetary Sciences, and at the Io Workshop 2013 at SwRI in Boulder, CO.

atmosphere that tracks the subsolar point around Io and remains constrained to the equatorial band; this atmosphere may be penetrated by the largest active plumes. Meanwhile, as Io continually transits the Jovian plasma torus, a continuous stream of S and O ions strike the surface frosts at ~57 km/s and energize SO_2 gas in resultant sputtering events. My introduction to DSMC planetary atmospheric simulations involved the continued development of our group's comprehensive model – developed by Moore (2011) and Walker (2012) – of this tenuous, sulfur-rich Ionian atmosphere. Results and notes on future work are detailed in Appendix A.

Chapter 2: A Novel Model for Earth's Rarefied Upper Atmosphere

2.1 Chapter Overview

Improving both the accuracy and robustness of simulations of Earth's upper atmosphere is a priority for the satellite operations and space weather communities. Here, I apply DSMC in three-dimensional and transient neutral-density simulations of Earth's rarefied upper atmosphere: I extend the planetary-science code base established in the modeling of the lunar and Ionian environs to reflect the physics and boundary conditions of Earth's upper atmosphere[9]. Comprehensive atmospheric simulations are computed in parallel on a domain extending from the mid-thermosphere, near the continuum-rarefied transition, through 1000 km altitude. Relevant physics of the simulation code include multi-species photo-chemistry, tracking of particle rotational and vibrational states, and non-equilibrium radiation. Substantial model development is demonstrated in application to the Earth's atmosphere, including the incorporation of lower-boundary conditions consistent with the NRLMSISE-00[10] (MSIS) semi-empirical model, ultraviolet radiation and photo-chemical rates determined by space weather indices, and radiative absorption of sunlight attenuated by integrated column density. Comparisons with results drawn from the MSIS semi-empirical model and from indirect satellite mass density measurements are employed in benchmarking model accuracy. Avenues for further development include hybridization with continuum global circulation models in the mid-

[9] This research was supported by the Los Alamos Space Weather Summer School, by LANL Institutional Computing, and by the Institute of Geophysics, Planetary Physics, and Signatures (IGPPS) at LANL.

[10] The Naval Research Laboratory Mass Spectrometer and Incoherent Scatter Radar model, named for the observational methods that built the bulk of its initial datasets. Here I refer to the most recent version, published in 2000; the 'E' denotes that this version of the model extends to the exobase.

thermosphere and the extension of the planetary code's magnetic field and charged-particle models to the Earth case. Notes on the necessary next steps to extend the Earth model and adapt the updated physics models of Prem (2017) are available in Appendix B.

2.2 Detailed Introduction and Motivation

The space weather and satellite operations communities employ a range of models in simulating thermospheric composition, density, and temperature; these models are imperfect in their application to that rarefied and non-equilibrium regime, in which improving the accuracy and robustness of predictive simulations is a priority. To that end, and in an extension of Los Alamos' IMPACT[11] project, I developed a novel model for Earth's upper atmosphere by modifying our existing planetary-science code base to reflect the essential terrestrial physics. The result, presented in this chapter, enables transient neutral-density simulations for regions of Earth's atmosphere above the transition to rarefied flow.

As discussed throughout this work, the DSMC method is the approach of choice for modeling a wide range of continuum-to-rarefied flows with mean free path comparable to characteristic flow length scale (Bird, 1994). In the Earth application, multiple gas species are modeled, each having different numbers of rotational and vibrational degrees of freedom, along with the processes of non-equilibrium radiation (for either transparent or partially opaque gases), high-speed collision, and photochemistry. The emphasis of the Earth DSMC is on the incorporation of all relevant physics and the development of a framework for predictive capability, given boundary conditions: at its

[11] Integrated Modeling of Perturbations in Atmospheres for Conjunction Tracking, a project intended to help avert orbital collisions by developing improved models to predict trajectories of satellites and space debris.

lower surface such a model requires macroscopic atmospheric properties (i.e. species number densities and temperature) to be drawn from an established atmospheric model.

MSIS is a semi-empirical model of atmospheric composition, temperature, and mass density that extends in applicability from the Earth's surface to its exobase; it is a widely used and familiar tool in the space weather and satellite operations communities (Picone *et al.,* 2002). As the most recent in a series of Mass Spectrometer Incoherent Scatter Radar models that yield atmospheric properties from spherical harmonic expansions, MSIS interpolates and extrapolates on an extensive and diverse dataset that incorporates decades of ground-, balloon-, rocket-, and satellite-based observations of Earth's atmosphere. MSIS is publicly available and, as an empirical model, it is simple to evaluate – therefore it can be directly linked to the planetary DSMC and called to generate mid-atmospheric boundary conditions tens of millions of times during a full-scale planetary simulation without undue computational expense. It should be noted that a primary drawback of MSIS and similar 'semi-empirical' models is their inherent inability to provide physically-motivated forecasting. While operationally invaluable, these statistical and empirical models extend only as far as their datasets: they cannot account for gradual atmospheric change over time, and they provide no causal understanding or insight into the atmosphere's driving physics. An alternate method of terrestrial atmospheric prediction is a generalized circulation model (GCM); GCMs are complex hydrocodes that solve the partial differential equations of fluid dynamics, and can incorporate wide ranges of relevant atmospheric physics (Belehaki *et al*., 2009). These are truly predictive models, but are far more expensive to evaluate on-the-fly than any semi-empiric 'fit' to observations. Furthermore, in their formulation about the Navier-Stokes equations GCMs are only valid insofar as the atmosphere behaves as a

continuous fluid; they generally neglect nonequilibrium effects that become increasingly dominant with altitude.

The purpose of this work is the development of a prototype rarefied gas dynamic model for Earth's neutral-density atmosphere that offers a unique, physics-based *predictive* capability in the high-altitude regimes for which continuum techniques are invalidated. Unlike the Ionian atmospheric problem, it is infeasible to begin this model at the planetary surface; instead, a mid-atmospheric boundary must be selected from an existing model. For the general case of transient simulations, it is most efficient to link with an inexpensive semi-empirical model – i.e. MSIS – for on-the-fly evaluations at that boundary at arbitrary altitude. For steady-state simulations, however, it could be feasible to use the result of a GCM calculation to generate a one-way linked boundary condition.

2.2.1 Project Benchmarks

A set of objectives was established at the project outset to direct Earth DSMC model development. The first such objective was to link the MSIS code to the planetary DSMC, and to modify the DSMC such that simulation particles could be generated on the lower boundary of a domain positioned above Earth's surface via a Maxwellian flux. This generation is informed by species number density and bulk temperature output from the MSIS model, which required conversion of the global simulation time in the DSMC to UTC, the conversion of code coordinates into geocentric latitude and longitude, tracking of local solar time, and the general overhaul of code parameters and species information to match the physics of the Earth system. To link with MSIS, the Earth DSMC model takes input of $F_{10.7}$ and AP parameters – solar flux and geomagnetic activity indices,

respectively[12] – as well as a date and time in UTC and a domain in latitude, longitude, and altitude. It advances a simulation through time, at each step interfacing with MSIS on every cell on the lower boundary of the initially-empty domain, generating an atmosphere which rises, expands, and ultimately achieves a quasi-steady state that exhibits transient variation on a diurnal scale.

With atmospheric generation complete, the next objective was the introduction of a solar heating model, achieved largely through radiative absorption into the rotational states of trace species. Molecules able to accept such radiation are those with permanent electric dipoles, none of which are included in the MSIS atmosphere. However, trace species present in Earth's mid-thermosphere and above with the necessary dipolar structure and composed of atoms in the MSIS system include NO, OH, and H_2O. In practice, solar heating was passed to the rotational states of representative molecules of these species at a rate attenuated by their atmospheric depth – the molecules then experienced rotational relaxation and potentially spontaneous photon emission while transferring their internal energy to the remainder of the atmosphere via collision. That process necessitated incorporation of models for solar shadow, for the attenuation of solar heating with atmospheric shielding, and for Monte Carlo photon transfer between molecules as developed in Prem *et al.* (2015) and Prem (2017).

Additional objectives included the incorporation of dissociative photochemistry for the Earth species and the ability to toggle between rates for quiet and active sun cycle cases to match a specific simulation date. The photodissociation process alters

[12] $F_{10.7}$ reflects daily measurements of radio flux at 10.7 cm and is a widely-used solar index that correlates well with EUV irradiance. AP is a daily geomagnetic disturbance index that reflects the global variance in ionospheric and magnetospheric activity. The combination of these indices is the input not only for MSIS, but also for the Horizontal Wind Model (HWM) and the ionospheric / emission line model TRANSSOLO. Belehaki *et al*. (2009) offers an extensive overview of these and other space weather models.

atmospheric chemistry, introducing energy into the translational modes of daughter species and serving as a secondary mechanism for atmospheric heating. Finally, satellite-tracking functions were developed to facilitate code comparison with mass-density observations from the CHAMP and GRACE[13] satellite datasets.

2.3 METHODOLOGY

2.3.1 Development and Application of the Earth DSMC Model

In application of the Direct Simulation Monte Carlo method, the motions and collisions of a number – here, O[10^6 to 10^9] – of representative molecules in a rarefied flow are computed, offering a probabilistic solution to the Boltzmann equation. In the context of the Earth simulation, these representative molecules are introduced as Maxwellian flux through the lower boundary, with species number densities and bulk temperatures along that boundary drawn from the semi-empirical MSIS model. This process of surface flux creation occurs at the start of each time-step, and within each boundary cell. MSIS is queried at the boundary altitude, with cell-centered geocentric latitude and longitude at the local solar time. Geomagnetic and solar flux indices are set manually in these simulations and are not coupled to the simulation time; however, the DSMC is linked with code enabling the interpolation of such values from historic space weather datasets. The number of simulation particles generated for one species in a time step of length Δt may be calculated

$$\sqrt{\frac{k\,T}{2\,\pi\,m_s}}\left[\frac{n_s\,A\,\Delta t}{F_{NUM}}\right], \tag{2.1}$$

[13] Challenging Minisatellite Payload; Gravity Recovery and Climate Experiment.

with k the Boltzmann constant, temperature T, species mass m_s, species number density n_s, surface cell area A, and weight ratio (that is, real-particles-per-simulation-particle) F_{NUM}. The result is necessarily a real number, so generation of an integer count of particles requires sampling from a Poisson distribution. MKL and GSL library functions were tested for this purpose, but Garcia and Wagner (2006) present an algorithm for DSMC applications that outperforms them in this DSMC regime, and it is employed here. Positions of newly-generated particles fluxing into the domain are distributed uniform-random on the boundary surface with Maxwellian velocities drawn by accept-reject sampling about the most probable molecular speed. The geometry of a representative full-planet calculation may be seen in Fig. 2.1 to scale, including the boundary surface position, processor distribution, and slices through the top of the collisional domain.

Photodissociation of sunlit molecules alters chemistry and introduces heat to the atmospheric column. Particles in sunlight are selected to photodissociate with probability

$$P_i = 1 - \exp[-\Sigma_j^{N_i}(k_{i,j}\Delta t)], \tag{2.2}$$

in which N_i is the number of photoreactions available for species i, and $k_{i,j}$ is the rate of the j-th photoreaction of that species. When a molecule is photodissociated in the DSMC, it is broken apart into its daughter species, increasing the number of particles present in the simulation; its internal energy is directed into the relative translational motion of the products, as is the reaction's mean excess energy as given by Huebner *et al*. (1992).[14] Product velocities are isotropically oriented. Rates change markedly over the 11-year

[14] This database of photodissociation and photoionization rates was updated in a subsequent publication, Huebner *et al*. (2015), although the rates relevant to this terrestrial case have not changed substantially.

solar cycle; both active and quiet sun cycle photochemistry data are included in the DSMC code, as shown in Table 2.1, and I added functionality for toggling between them.

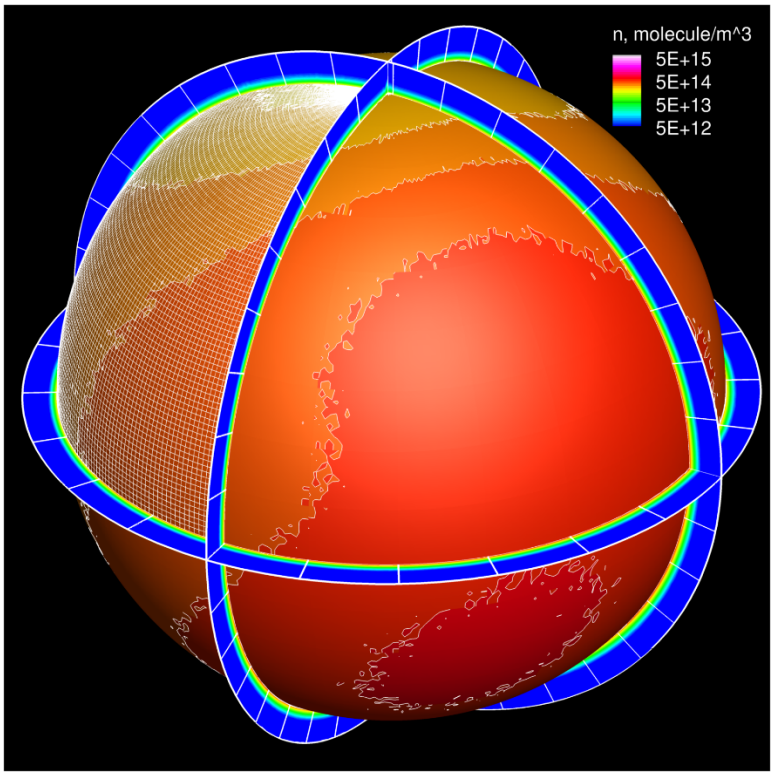

Figure 2.1: Number densities are shown along the lower boundary surface at 300 km altitude. Slices show the extent of the collisional 3-D DSMC calculation, which extends to 1000 km, with appended vacuum buffer cell (not shown).

A primary mechanism for heat introduction into the simulation is through the absorption of solar infrared radiation into the rotational states of molecules with permanent electric dipole moments. Emission band strengths are calculated for such diatomics – NO and OH, for these simulations – from kinetic theory, and are fit to observations in the literature for more complex molecules (i.e. H_2O). The rate of infrared

emission is modeled with a power law in temperature, with exponent 2.0 for diatomics and linear triatomics. Absorption may occur as solar radiation penetrates the atmosphere or as radiation emitted spontaneously from cooling molecules is re-absorbed. The latter process is implemented via a photon Monte Carlo method developed in Prem *et al.* (2015) and extended in Prem (2017). Column density is integrated in an independent and comparatively coarse grid oriented parallel to incident sunlight, allowing the attenuation of photo-dissociation and radiative absorption rates with atmospheric shielding.

Reactant	Products	Reaction Rate (Active / Quiet) [s^{-1}]		Excess Energy (Active / Quiet) [eV]	
O_2	O + O	6.78×10^{-6}	4.23×10^{-6}	1.675	1.431
N_2	N + N	1.56×10^{-6}	6.61×10^{-7}	3.380	3.380
NO	N + O	3.21×10^{-6}	2.20×10^{-6}	2.720	1.840
OH	O + H	3.35×10^{-5}	1.98×10^{-5}	5.576	4.370
H_2O	OH + H	1.76×10^{-5}	1.03×10^{-5}	4.040	3.420

Table 2.1: Unattenuated photodissociation rates and excess energies of terrestrial species.

The remainder of the DSMC method is straightforward to apply in this case – simulation particles are moved within the time step, passing between processors and interacting with domain boundaries if necessary – they are indexed within the cell structure and may collide with one another within a cell. Particles are moved via the integration of their gravitational equation in a second-order predictor-corrector scheme; in this neutral-density simulation, forcing includes gravity but neglects E and B fields. Non-inertial forcing models are available in the planetary DSMC code, but were not adapted to the Earth—Moon system for this work: Earth is not tidally-coupled to the

Moon, posing a more difficult problem than either the Io or Pluto-Charon applications. The moon's gravity is neglected in this work.

In the DSMC method collisions are probabilistic, not deterministic, and may occur between sampled representative molecules within the domain's cells. A gas of sufficient rarefaction allows the treatment of solely binary collisions, in which the timescale for collision dynamics between two representative molecules is dwarfed by the mean time between collisions: these assumptions allow for particle collision and motion to be decoupled. In these Earth simulations collisions drive bulk motion and transfer energy between molecules, but do not induce chemistry – an Arrhenius mechanism for dissociative and recombinative reactions was considered, but its treatment ultimately deemed beyond the scope of this work. Lastly, representative molecules are sampled within cells (not necessarily of the same configuration as the collision cells) in calculating bulk atmospheric properties: these are the output densities, temperatures, and pressures ultimately compared against MSIS and the satellite datasets.

2.3.2 Treatment of the Simulation Domain

Our domain selection is motivated by the finding that, in a set of 1-D trial cases representative of a range of Earth atmospheric configurations, atmospheric transition to behavior as a continuum fluid occurs near 300 km while the transition to collisionless, ballistic flow (at $Kn_H \approx 100$) occurs at 1,000 km (see Fig. 1.1). As continuum GCMs are established below 300 km and the particle-based DSMC method increases rapidly in computational expense with atmospheric density at lower altitudes, 300 km is employed as the lower boundary for the simulations discussed herein – this choice is examined in more depth in Appendix C. A 1,000 km upper boundary is selected for direct comparison

against the MSIS model, which also terminates at that altitude. However a vacuum buffer cell of O[10^5-10^6] km is appended to the domain top, in which particles move in purely ballistic trajectories and without collision sampling, to prevent non-physical escape. Particles that exit the domain top or bottom are deleted from the simulation[15].

One-dimensional simulations are first considered – this bears the necessary caveat that DSMC simulations are not strictly one-dimensional in particle motion, as it is critical that representative molecules retain their three translational degrees of freedom. Instead, such simulations are performed in thin columns with periodic edge boundaries. As the only interface between the Earth DSMC model and the MSIS comes on the lower boundary surface, it is useful to compare temperature, number density, and molar fraction profiles against the MSIS output to determine how the complex physics of the DSMC simulation can replicate that empirical fit. Full-planet, three-dimensional simulations are next considered. A property of interest is the integrated column density, that is, the particle count per unit area taken from the lower boundary into the exosphere. It is in these three-dimensional simulations that satellite paths may be tracked through cells, and comparisons of mass density made.

2.4 A One-Dimensional Equatorial Simulation

A one-dimensional simulation is performed in which the domain encompasses an equatorially-centered grid 3° on edge: latitudes from -1.5° to 1.5° and longitudes from 0.0° to 3.0° are considered. The simulation lower boundary is set to 300 km altitude, while the upper limit of the collisional domain is chosen at 1,000 km. After a period of equilibration (of duration 9,300 s) at the outset of the calculation, during which the

[15] This is enforced as a vacuum condition at both ends of the domain, although this is balanced at the domain's lower boundary by the constant inward Maxwellian flux through the generation surface.

initially-empty domain is populated by flux across its lower boundary, time-averaged flow field properties are calculated between 17:15 and 17:25 LST on 01 January 2000. To ensure sufficient representative molecule populations at high altitudes, on the order of 3×10^5 particles are employed per cell column. This balance is enforced by adjusting the weighting of simulation particles between columns[16]. The MSIS species (N, O, N_2, O_2, He, and H, with Ar neglected at these altitudes) are generated from that model's density output, while trace species NO, OH, and H_2O are generated to the order of their estimated concentrations: one part-per-thousand NO (Rusch *et al.,* 1991), and one part-per-million[17] OH and H_2O. Species properties are sourced from Bird (1994) and Ozawa (2007).

The DSMC number density profile, shown in the top portion of Figure 2.2 as pink scatter points of cell-sampled values versus the MSIS in white, demonstrates a close match: at 1,000 km, the models agree to within 3 %. It is important to note that these results are a natural outgrowth of the simulation physics – the DSMC only interfaces with MSIS during particle generation on the lower boundary. The DSMC temperature is noisy, even in the time-average, but a spatial average across the domain (shown in green) demonstrates the MSIS trend of near-constant temperature, including heating at the lower boundary that corresponds with radiative absorption of NO.

The selection of the lower boundary altitude has substantial influence on the expense and accuracy of the calculation; I examine this effect in depth in Appendix C.[18]

---

[16] 1-D simulations are parallelized by subdividing the total column in θ and φ among processors (generally in either 4x4 or 8x8 configurations), and bulk properties at each altitude level are ensemble averaged.

[17] As per Huang and Hickey (2007), OH concentrations should be O[10^{-7}-10^{-6}] at 100-110 km; Schlatter (2010) has H_2O at 10^{-7} at 120 km. Andrew Walker and I were unable to find estimates for either OH or H_2O concentrations in the literature above that altitude (i.e. past 120 km). Therefore, even generating these species at an optimistic one part-per-million at 300 km in a calculation with O[10^5-10^6] molecules per processor effectively limits their heating contribution to nil.

[18] Appendix C includes a series of 1-D test cases with boundaries at 200, 250, and 300 km for 9 Jan 2005 in domains otherwise equivalent to that of the Figures 2.2 and 2.3 result.

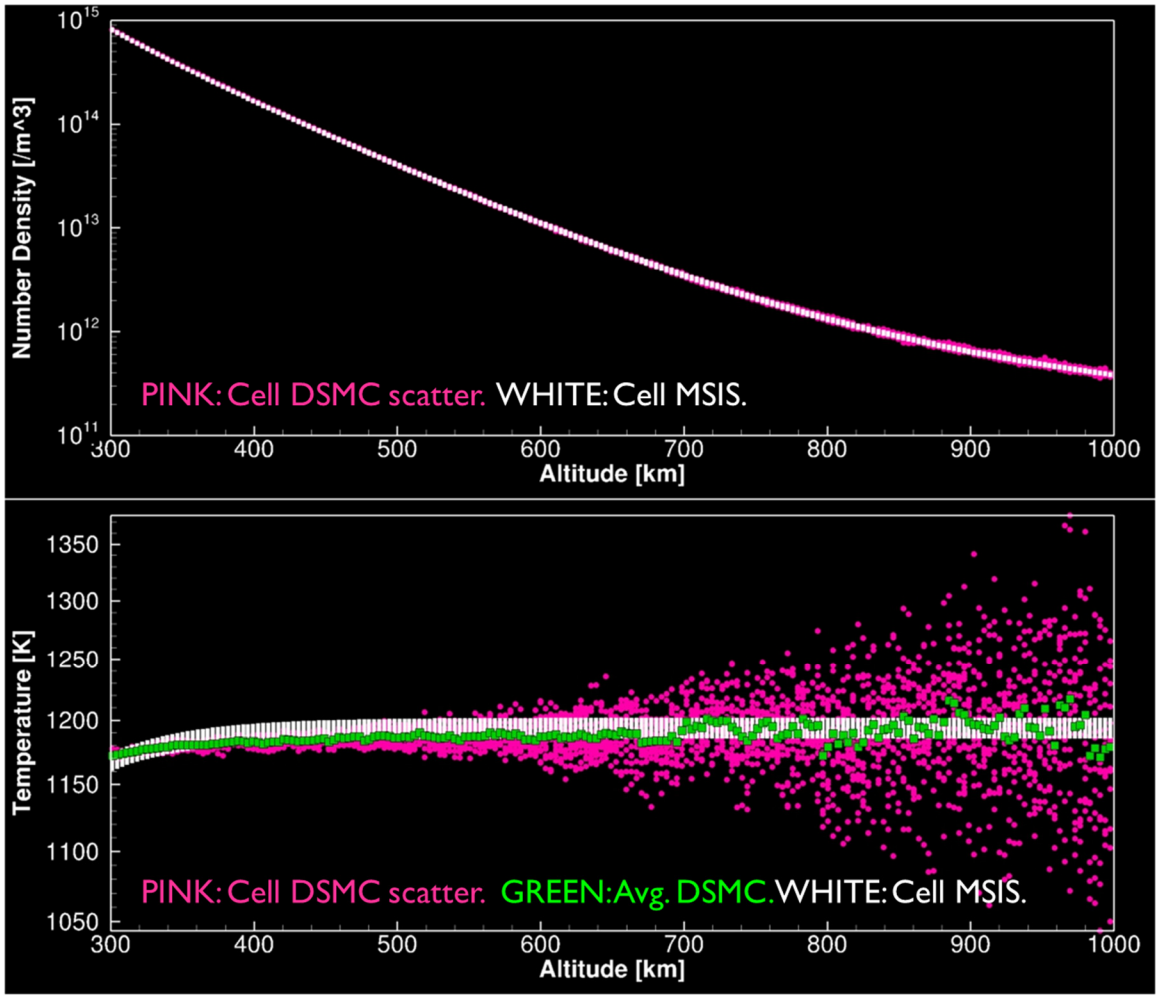

Figure 2.2: Cell-sampled total number density and temperature vs. MSIS expectation. Within the column, 64 processors subdivide the domain in latitude and longitude, each forming an individual column with a uniform distribution of cells in altitude. In both the top and bottom figures, the white points represent each cell's bulk property value as drawn from MSIS at a given altitude, while the pink points represent the cell values within the DSMC calculation. In the bottom figure, the green line represents the average total temperature value taken across all processors at each altitude.

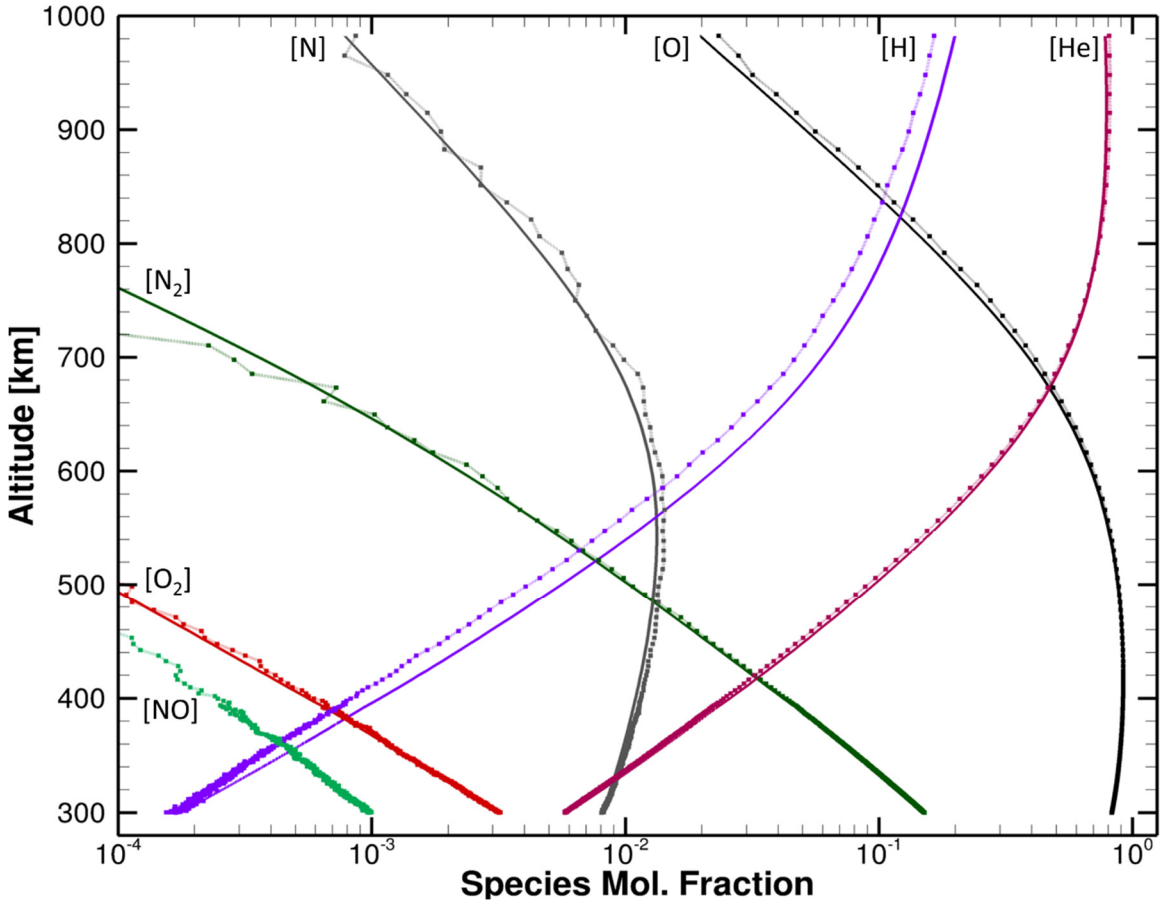

Figure 2.3: Local species molar fractions (dotted lines) versus MSIS expectation (solid lines), over a 600 s time-average. NO is not represented in MSIS, but is introduced at the lower boundary at one-part-per-thousand of the total flux, as it plays a significant role in upper atmospheric heating.

Molar fractions trend closely in altitude with their corresponding MSIS profile and exhibit separate species scale heights, shown in Figure 2.3. A notable disagreement is monatomic hydrogen, comparatively underrepresented by the DSMC in this calculation: a consequence of non-physical escape. A vacuum boundary condition is enforced at the edge of the buffer cell (here, effectively 11,000 km above the Earth's surface), which eliminates any particles that pass above the boundary – even if they have insufficient energy to escape Earth's gravity, and would ultimately fall back along their ballistic

trajectories. This effect is only noticeable here for hydrogen, due to its low mass and consequently large species scale height, and is reparable by either extending the vacuum buffer cell or by checking particle kinetic energy against gravitational potential at the boundary. I eventually added such functionality in the course of the Pluto-Charon work.

2.5 TRANSIENT FULL-PLANET SIMULATIONS

Three-dimensional, transient, and full-planet simulations were necessary for comparison against the CHAMP satellite dataset. For the case demonstrated in Figure 2.4, 9 Jan. 2005 was selected as a simulation date with anomalously low geomagnetic activity. Solar flux and geomagnetic indices were set per their observed values on that date, with reference to the simulation time in UTC. In the top panel of Figure 2.4, total column density (integrated along the r coordinate) is shown on an equirectangular projection. Peak density lags the subsolar point, presently at 180°, by about three hours. Note the seasonal bias: the summer (southern) hemisphere exhibits a substantially more active atmosphere than its counterpart. The bottom left panels show species column densities of N_2 and He, concentrated at the S and N poles, respectively – separate species evolve to quite different density profiles across the planet. At bottom right, species column densities are mapped onto the Earth's globe and viewed downward onto the subsolar point at 180°. White lines on the globe's surface mark the MSIS species number densities at the surface itself. As expected, the structures of DSMC integrated column density by species adhere closely to the MSIS species density values on the generation surface; as the molecule in any atmospheric column falls off rapidly above that surface with altitude. An additional 3-D, transient, full-planet simulation, performed as a test of the recent 2017 distribution of the Earth DSMC, is shown in Appendix B.

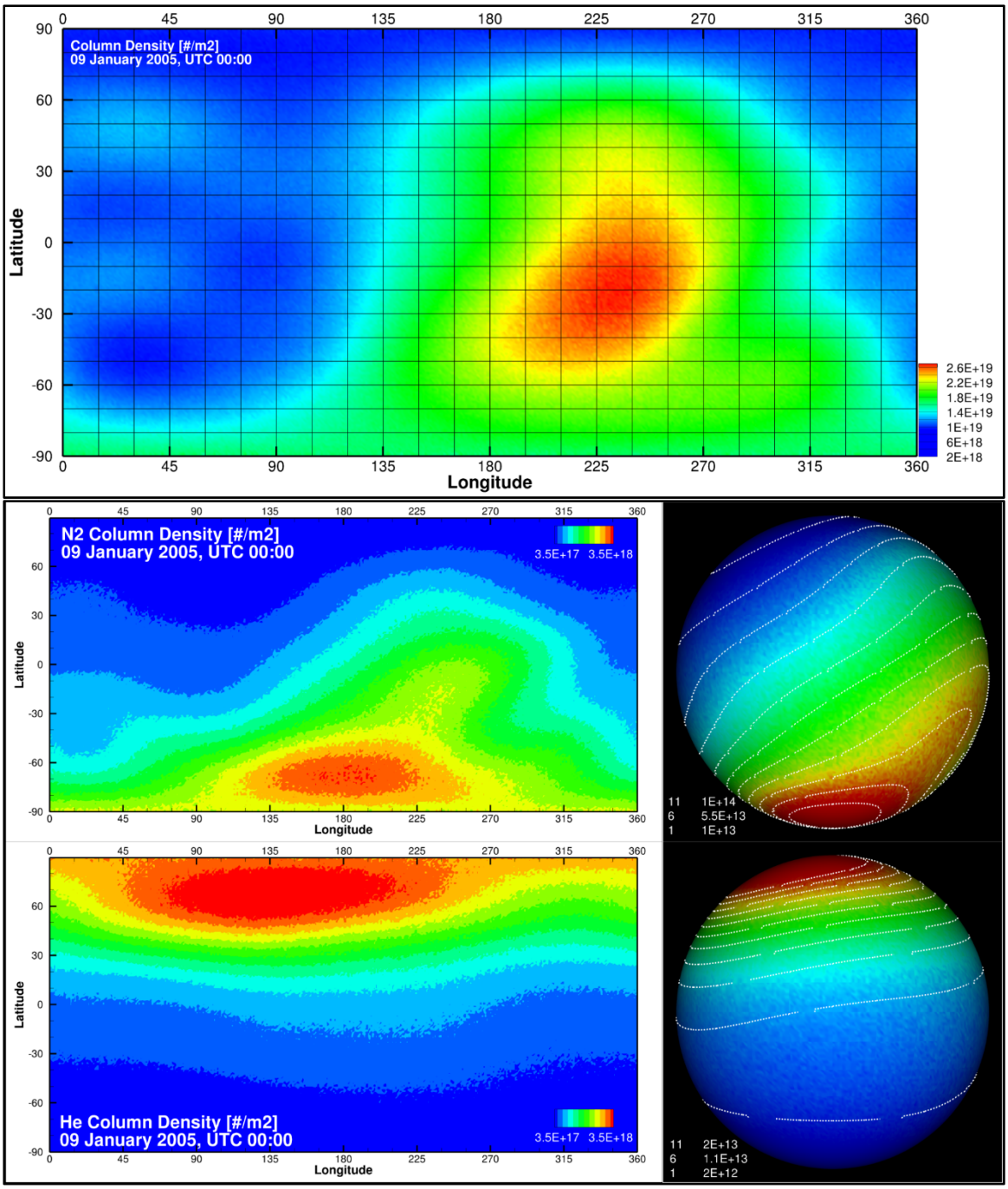

Figure 2.4: Full-planet atmospheric simulations demonstrating total (at top) and select species column densities. Figures projected onto the globe (at right) are looking down on the subsolar point, presently at 180° longitude. Note the seasonal polar variance in He and N_2 densities. [144-processor simulation]

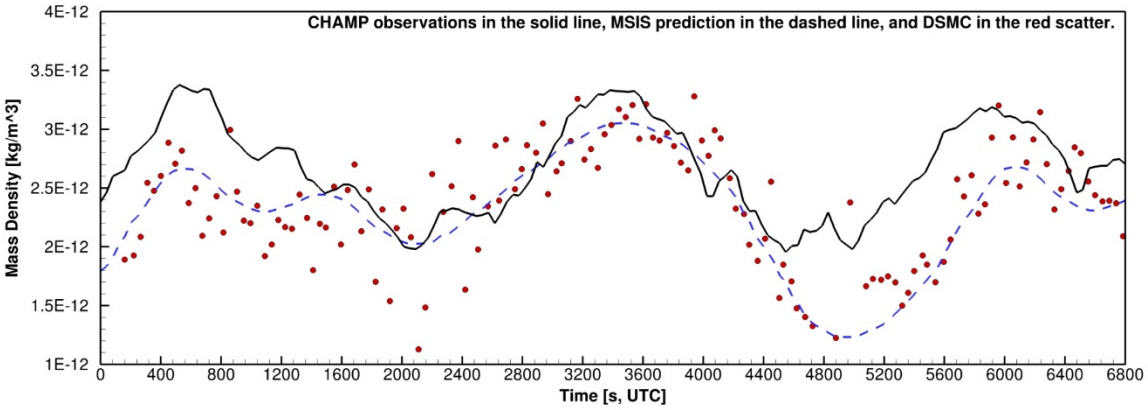

Figure 2.5: Comparison of mass-density observations from the CHAMP satellite mission[19] with an MSIS (semi-empiric) result, and with the result of a 3-D DSMC calculation.

The DSMC mass-density values are shown in Figure 2.5 to trend closely with the MSIS and CHAMP data-sets, although there is an evident bias toward the former when they disagree. This is unsurprising as CHAMP operates here below 400 km, near the lower boundary informed in the DSMC by MSIS. In this calculation, DSMC output was time-averaged in bins between CHAMP data-points at roughly 50 s intervals. Satellite mass-density was compared against the value of the DSMC mass-density in the cell occupied by the satellite at a given time: this could be refined by averaging density among cell nearest-neighbors and weighting against the actual satellite position within its cell. Periods of high noise in the DSMC calculation (e.g. 1,600 to 2,400 s) correspond to the satellite passing over a polar region, an artifact of small cells in such regions.

[19] This comparison was sourced from a LANL-internal database of mass densities along the trajectory of CHAMP (given in latitude, longitude, and altitude coordinates vs. times UTC); these densities were presumably obtained by analysis of the drag CHAMP experienced. While this data is no longer available, personal communication with S. Bettadpur at the University of Texas CSR suggests that a comparable database exists or could easily be generated from an improved analysis of drag on the GRACE satellites.

2.6 CONCLUSIONS

A fully three-dimensional and transient model of the rarefied component of Earth's neutral atmosphere is presented. The DSMC method has many advantages in this domain: most notably, its comparatively low expense and high stability in the rarefied regime by comparison with continuum solutions, and the ease with which the method may be modified to include new physics. DSMC results demonstrate close agreement with the trends of MSIS throughout the atmosphere, in a natural consequence of the code physics and MSIS-informed creation on the lower boundary surface. Future work may include the comparison of wind patterns against observation and the linking with semi-empirical neutral atmospheric wind models on the lower boundary (i.e. HWM-07), the addition of more sophisticated physics and chemistry models, and large-scale, direct comparison against other GCM datasets. Appendix B addresses the extension of updated radiative functions and their adaptation for the terrestrial case, and outlines essential steps toward general continued improvement of the Earth DSMC.

Chapter 3: Rarefied Gas Dynamic Simulation of Gas Transfer and Escape in the Pluto-Charon System[20]

3.1 Chapter Overview

In this chapter, I describe the development of a novel application of the planetary DSMC code toward three-dimensional simulations of Pluto's rarefied upper atmosphere; this work was motivated by the need to better understand New Horizons (NH) data captured during the July 2015 encounter. The model domain spans from several hundred km below Pluto's exobase – where continuum flow transitions to the rarefied regime – to fully free-molecular flow hundreds of thousands of km from Pluto's center, and its equations of motion account for the gravitational fields of both Pluto and Charon, the centripetal and Coriolis forces due to the rotation of Pluto in our reference frame, and the presence of Charon as a temporary sink for impacting particles. Using this model, I analyze the escape processes of N_2 and CH_4 from Pluto across different solar heating conditions, and evaluate the three-dimensional structure of the upper plutonian atmosphere, including gas transfer to and deposition on Charon.

3.2 Introduction and Literature Review[21]

The atmosphere of Pluto is supported by the vapor pressure of volatile ices, primarily N_2, with minor contributions from CH_4 and CO (Gladstone *et al.*, 2016). Of these, N_2 dominates both in the ice phase (Owen *et al.*, 1993) and in the lower

[20] Portions of this chapter first appeared as our *Icarus* manuscript "Rarified Gas Dynamic Simulation of Transfer and Escape in the Pluto-Charon System." The research was supported by the NASA Outer Planets Research (OPR) grant NNX11AD88G.

[21] Section 3.2 was co-authored by S. Yeoh and first appeared in our *Icarus* manuscript.

atmosphere to 1800 km, although toward the exobase the abundance of minor species increases and CH_4 composes the majority of escaping flow (Gladstone *et al.*, 2016). The volatile ices have a non-uniform distribution over Pluto, and the ice mixture percentages, composition and grain size also vary over the globe (Olkin *et al.*, 2007; Protopapa *et al.*, 2008; Grundy *et al.*, 2014). Owing to a lower vapor pressure than for N_2, the atmospheric mixing ratio of CH_4 was projected to be on the order of 10^{-3} (O[10^{-3}]) prior to the New Horizons encounter (Young *et al.*, 1997; Lellouch *et al.*, 2015). The New Horizons methane atmospheric mixing ratio of ~0.25 % was somewhat lower than the anticipated value of ~0.44 % (Stern *et al.*, 2015; Lellouch *et al.*, 2015). However, NH found the concentration of methane at Pluto's exobase to be as high as ~42 %, which suggests that methane, not nitrogen, composes the bulk of material transferred from the plutonian atmosphere to Charon and escaping the system. The hydrocarbons C_2H_2 and C_2H_4 have also been detected with atmospheric mixing ratios of ~3×10^{-6} and ~1×10^{-6} respectively (Stern *et al.*, 2015).

The atmosphere of Pluto is complex and time-variable, as the plutonian surface experiences large changes in insolation during its orbit. Dramatic seasonal atmospheric changes were predicted beginning in the early 1980s (Stern, 1981; Trafton and Stern, 1983), driven by the sensitivity of vapor pressure to temperature, the large variation in Pluto's heliocentric distance (29.5 to 49.6 AU), and the high axial obliquity (120°) of the orbit of Pluto. Such changes are supported by several stellar occultation observations. Between observations in 1988 and 2002, the atmospheric pressure of Pluto was found to increase by a factor of two (Elliot *et al.*, 1989, 2003; Hubbard *et al.*, 1988; Millis *et al.*, 1993; Pasachoff *et al.*, 2005; Sicardy *et al.*, 2003; Yelle and Elliot, 1997). Subsequent observations indicated that pressure continued to increase until leveling off after 2007, and has not since collapsed (Elliot *et al.*, 2007; Zalucha *et al.*, 2011; Olkin *et al.*, 2014,

2015). However, the upper atmospheric thermal structure remained largely the same throughout (Elliot *et al.*, 2007; Person *et al.*, 2008; Young *et al.*, 2008). The New Horizons (NH) occultation experiment found a somewhat lower surface pressure (~10-11 microbars) than anticipated by extrapolating the ground-based stellar occultation results to the surface (Gladstone *et al*., 2016).

Pluto's atmosphere undergoes escape in a process that was once thought to be hydrodynamic (McNutt, 1989; Yelle, 1997; Trafton *et al.,* 1997; Krasnopolsky, 1999; Tian and Toon, 2005; Strobel, 2008), but that has since been demonstrated to occur on a molecule-by-molecule basis (Tucker *et al.,* 2012, Erwin *et al.,* 2013). A key finding of NH was that Pluto's upper atmospheric temperature of ~70 K was significantly colder than expected (Gladstone *et al*., 2016). Upper atmosphere occultation opacity indicated a dearth of nitrogen that could be reasonably fit by such a cold temperature. These results suggest there is an as-yet-unidentified radiative cooling mechanism, perhaps associated with C_2H_2 or HCN. This low upper atmospheric temperature reinforces the understanding of plutonian atmospheric escape as a process by which individual molecules at the tail end of the thermal velocity distribution at the exobase obtain sufficient upwardly-directed energy to escape in a Jeans process (Volkov *et al.,* 2011), rather than via the hydrodynamic process that had informed models of the Pluto-Charon system prior to Tucker *et al.* (2012).

Moreover, the expected N_2 escape rate is reduced from pre-encounter predictions by four orders of magnitude, to 10^{23} s^{-1}: such a low rate would be consistent with a much-reduced altitude of atmospheric interaction with the solar wind and an undetectably thin atmosphere at Charon. The exobase parameters referenced in this work as NH observations are the results of a model constrained by the LOS density measurements of Gladstone *et al*. (2016), which extend up to 1500 km above Pluto.

3.2.1 Review of Plutonian Upper Atmospheric Models

Different regions on the surface of Pluto receive different amounts of insolation; this leads to a net sublimation-driven flow of volatile ices towards regions of lower insolation, forming 'sublimation winds'. This transfer of volatiles through the atmosphere is accompanied by a transfer of latent heat that effectively redistributes the absorbed solar heat to the entire exposed volatile surface, causing the volatile ice to be nearly isothermal (Trafton and Stern, 1983) though the composition of the volatile ice varies across the globe (Spencer *et al.*, 1997; Protopapa *et al.*, 2008; Grundy *et al.*, 2014). To achieve a near-isothermal ice surface, the mass of the atmosphere must be large enough for it to be globally near hydrostatic equilibrium. In this case, the sublimation winds must everywhere be subsonic (Trafton and Stern, 1983; Ingersoll, 1990; Trafton, 1990; Trafton *et al.*, 1997).

A significant fraction of the surface of Pluto is not volatile, so its temperature is regulated only by a balance between insolation and advection. However, the vapor pressure at the ice temperature governs the atmospheric pressure around the globe, including in regions lacking volatile ice. While the atmosphere breaks spherical symmetry by rotation, sublimation winds, and surface topography, all but recent upper-atmospheric models of Pluto are essentially one-dimensional, providing the same vertical structure over the entire globe.

These 1-D models have been used to estimate the hydrodynamic escape rate of the atmosphere of Pluto at perihelion. Hunten and Watson (1982) pointed out that the escape of the atmosphere of Pluto, which was long thought to be hydrodynamic, is energy-throttled by adiabatic cooling of the expanding atmosphere, which is regulated by the downward conduction of solar EUV+UV heat absorbed in the thermosphere. Previous

model-dependent hydrodynamic escape rates ranged from 10^{27} to 10^{28} s^{-1} (Hubbard *et al.*, 1990; Krasnopolsky, 1999; McNutt, 1989; Trafton *et al.*, 1997; Yelle, 1997).

McNutt (1989) used a self-consistent analytic approach to study the escape of CH_4 and CO and found the escape rate sensitive to solar EUV heating. Yelle (1997) accounted for solar EUV heating, thermal conduction and viscous mechanical dissipation and numerically solved the Navier-Stokes equations for the hydrodynamically escaping atmosphere of Pluto for N_2 and CO. Trafton *et al.* (1997) solved the hydrostatic escape equations for a CH_4 atmosphere and estimated an escape rate of ~3.3×10^{27} s^{-1}. Krasnopolsky (1999) extended the analytic approach of McNutt (1989) to include several previously neglected terms, including the solar UV heating of the upper atmosphere of Pluto, which he argued was six times stronger than the solar EUV heating. Then, he applied his approach to the hydrodynamic escape of N_2 from Pluto, with CH_4 diffusing upward through it, and found substantial variations in the structure of the extended atmosphere of Pluto and the escape rate with solar cycle. He estimated the N_2 escape rate of $(2.0–2.6) \times 10^{27}$ s^{-1} at mean solar activity and varies by a factor of 3–4 over a cycle.

Tian and Toon (2005) solved the time-dependent hydrodynamic escape equations for a planetary atmosphere and applied them to the hydrodynamic escape of N_2 from Pluto, deriving a perihelion escape rate an order of magnitude higher than Krasnopolsky (1999). They argued that this discrepancy arose from the single-altitude heating approximation made by Krasnopolsky. Strobel (2008) solved the steady-state equations for hydrodynamic escape and accounted for the solar EUV heat absorbed by N_2, the near-IR and UV heat absorbed by CH_4 and the rotational cooling by CO as a function of solar activity. At the time of the NH flyby in July 2015, they predicted an N_2 escape rate of ~2.2×10^{27} s^{-1} and a peak thermospheric T of ~103 K at a radial distance of 1890 km.

3.2.2 Kinetic, Rarefied Gas Dynamic Simulation of the Pluto-Charon System

The calculations above were made based on the continuum assumption, which is valid only in the lower atmosphere; this assumption fails approaching the exobase, necessitating the use of a kinetic model of the upper atmosphere. Tucker *et al.* (2012) modeled the continuum region of the atmosphere with one-dimensional fluid equations and coupled this model to a direct simulation Monte Carlo (DSMC) kinetic model of the upper atmosphere to constrain the thermally-driven escape of N_2 from Pluto. They adopted the temperature and density profiles of Strobel (2008) at the lower boundary (R=1450 km) and considered two solar heating conditions, obtaining escape rates of ~4.8 $\times$ 10^{25} s^{-1} and ~1.2 $\times$ 10^{27} s^{-1}, respectively. These rates are comparable to the Jeans escape rates for the same conditions. They concluded that the thermally-driven escape from Pluto is therefore similar in nature to Jeans exospheric escape, and must be treated molecule-by-molecule to account for its non-Maxwellian molecular speed distribution.

Charon is located ~19,600 km from Pluto (~17 Pluto radii) and its Hill sphere extends as close to Pluto as ~12,700 km. Its presence contributes to the three-dimensionality of Pluto's atmosphere, as Charon gravitationally perturbs flow from Pluto's exobase. The three-dimensional, free-molecular simulations of Tucker *et al.* (2015) demonstrated several significant binary atmospheric phenomena, including the influence of Charon on the morphology of the system's density field and the potential for Roche-like atmospheric transfer to, and the persistence of a thin atmosphere about, Charon itself. These simulations predicted that the atmosphere of Pluto would, at nominal solar heating conditions, deposit molecules onto Charon at a rate of O[10^{25}] s^{-1}.

In this work, I present our DSMC model of the plutonian atmosphere from its exobase out to hundreds of thousands of km. While the lower, continuum atmosphere of Pluto is complex and three-dimensional in nature, we only consider the effects of Pluto's

rotation and input particles into the simulation domain with the appropriate conditions at the lower boundary – an opportunity for future work may be to source input conditions from a fully three-dimensional simulation using an established global circulation model (GCM) for the lower plutonian atmosphere. Our DSMC model accounts for both the gravitational fields of Pluto and Charon, the centrifugal and Coriolis forces due to the rotation of Pluto, and the presence of Charon as a sink for impacting particles.

Our DSMC model improves upon the simulations of Tucker *et al.* (2012, 2015) by representing collisions in our simulation over a three-dimensional domain including Charon that extends from the sub-exobase region of Pluto out to 32,000 km in radial distance, well past the transition to free-molecular flow. To prevent aphysical escape, a free-molecular region is appended to our domain that extends to 150,000 km, and that specularly reflects particles that have insufficient mechanical energies to escape the system at that distance. This reflection is energy-preserving, and accurate in the steady-state solution over the time-span of these simulations to the extent that the flow is nearly axisymmetric at the upper boundary surface. The one-dimensional simulations of Tucker *et al.* (2012) only consider collisions to 10,000 km and neglect Charon's influence on the flow entirely, while the three-dimensional simulations of Tucker *et al.* (2015) that include Charon neglect collisions above the exobase, employing instead an entirely free-molecular model that corrects for the effect of collisions in enhancing transfer and escape fluxes by increases in lower boundary temperature. I find that the consideration of collisions alters the flowfield, most notably by promoting flux to Charon by O[10 %] and increasing the proportion of that flux generated on the anti-Charon hemisphere of Pluto's exobase between the Case A simulation presented in Section 3.4 and a trial, free-molecular solution – these results are presented in Appendix C. Furthermore, we markedly increase the resolution in computational particles compared to previous work,

with values of F_{NUM} ranging from 3×10^{24} to 5×10^{25} in the cases presented in Sections 3.4 and 3.5, allowing us to obtain better statistics, reduce noise and improve spatial resolution in our results. We also employ a two-species model that includes methane; Tucker *et al.* (2015) considered only escaping nitrogen.

Using this model, we analyze the transfer and escape processes of N_2 and CH_4 from the plutonian exobase, with boundary conditions at the exobase interface as functions of solar heating. I consider several heating conditions, focusing on a comprehensive, high-resolution simulation with an exobase equivalent to the unheated atmosphere computed in Tucker *et al.* (2012) and a case computed in response to the observed conditions at the New Horizons encounter. The minimum, medium, and maximum solar heating cases considered in Tucker *et al.* (2015) are addressed in Appendix F. In particular, I examine the processes of gas falling back through the lower boundary and of gas escaping the Pluto-Charon system, including calculated escape rates. I also investigate the deposition of gas over the surface of Charon, including the spatial distributions of the impacting particles. This helps us ascertain whether Charon has an atmosphere, and how dense such an atmosphere might be. This is constrained by the New Horizons observation of no detectable atmosphere at Charon, bracketing the maximum extent of Charon's atmosphere to be roughly O[1 picobar] in pressure or O[10^{20} m^{-2}] in column density (Stern *et al.*, 2015; Stern *et al.*, 2016; Gladstone *et al.*, 2016). In addition, I use our model to investigate the three-dimensional fields of several gas properties, including density and temperature, around Pluto and Charon. This enables us to gain a better understanding of the mechanisms underlying the atmospheric escape process and the transfer of material between Pluto and Charon. As new NH data become further available, the current modeling work will provide a framework for future improvements,

including coupling to a GCM model of the lower atmosphere for more accurate input conditions at the lower boundary and the inclusion of other gas species, such as CO.

In Section 3.3, I describe the unique aspects of the Pluto-Charon DSMC model, including the assumptions made and physics used. In Section 3.4, I present our results for and discuss the flowfield evolving from a pre-encounter unheated exobase while, in Section 3.5, I present and discuss a simulation of the Pluto–Charon system at the New Horizons encounter. In Section 3.6 I summarize our findings, give conclusions, and propose future work.

3.3 METHODOLOGY

3.3.1 Implementation of the DSMC Method in the Pluto-Charon Case

DSMC is suitable for modeling the atmosphere of Pluto from well below the exobase region out to hundreds of thousands of km as the flow passes through multiple regimes, from moderately collisional in the exobase region to free-molecular far away. Moreover, the non-equilibrium nature of such flows can be captured by DSMC, which accounts for the different internal molecular energy modes (e.g. rotational and vibrational) and the energy exchange between them. As demonstrated by Beth *et al.* (2014), this sort of collisional kinetic model is necessary to generate particles that populate satellite orbits, which, in some cases, can compose a majority of those at sufficient distance above a planetary exobase. However, in the Pluto-Charon system and in these simulations, perturbations due to Charon prevent satellite particles from forming long-term stable orbits. Perturbations not represented in this work – for instance, those due to other Pluto-system moons, radiation pressure, and solar wind interaction – may also act to eliminate satellite particles.

In our current simulations, we consider a mixture of CH_4 and N_2. The molecular model used is the variable hard sphere (VHS) model with the appropriate parameters for both species (Bird, 1994).

The barycenter of the Pluto-Charon system is located *outside* either body at ~2042 km from the center of Pluto along the line connecting the centers of the two bodies. Pluto and Charon are mutually tidally locked to one another, thus the rotational and orbital periods of Charon and the rotational period of Pluto are all equal. The Pluto-Charon system used in our simulations is shown in Fig. D.1., where we have made the following simplifying approximations:

(i) The orbital plane of Charon coincides with the equatorial plane of Pluto.
(ii) Charon executes a perfectly circular orbit around Pluto.
(iii) The axes of rotation of both Pluto and Charon are perpendicular to the orbital plane of Charon (and thus also the equatorial plane of Pluto).

These approximations are corroborated in the initial New Horizons report, which finds Charon's orbital inclination with respect to the equatorial plane of Pluto to be 0.0° while its orbital eccentricity is ~0.00005 (Stern *et al.* 2015). The important geometric parameters of the Pluto-Charon system used in our simulations are summarized in Table D.1 and compared to the values recorded by NH and those employed in simulations in the literature. Pluto exhibits an axial tilt of ~120° relative to the ecliptic, but this work does not incorporate solar dependence in heating models or exobase boundary conditions.

The positions and velocities of particles are obtained using an 8th-order adaptively-stepped error-controlled Runge-Kutta Prince-Dormand scheme. The Lagrange point between Pluto and Charon (typically labeled L1) plays an important role in material

transfer and the structure of the number density field. This Lagrange point is unstable, thus a particle placed there will ultimately depart from equilibrium due to any slight perturbation, including the round-off errors introduced by numerical integration. I performed a study to compare this integration scheme with a second-order predictor-corrector scheme employed in our prior DSMC applications and in Tucker *et al.* (2015), more details on which can be found in Appendix E.

3.3.2 Simulation Parameters

The planetary DSMC code applies a spherical coordinate system that allows for non-uniform cell size distribution in each coordinate, as shown in Fig. 1.2. For this problem, I have chosen a cell size distribution in each direction such that cells are smaller than λ everywhere in the simulation domain. I have also chosen Δt to be smaller than τ_{coll} everywhere; at the exobase, the most restrictive times between collisions are O[10^2] s. More details on the various simulation parameters used can be found in Table D.2.

Based on the simplifying approximations made to the system, we can expect symmetry across the equatorial plane of Pluto and thus only simulate the region north of the equatorial plane. The simulation domain is hemispherical in shape and centered on Pluto, extending in the radial direction from the exobase to >1.5 × 10^5 km (~2.5 R_P to >126.5 R_P) from the center of Pluto, as shown in Fig. 1.2. Within Pluto's gravitational predominance, a Knudsen number can be defined based on the atmospheric scale height, as outlined in Section 1.2.1. Each species has a separate characteristic scale height, dependent on its mass; at equivalent density and altitude, methane's lower mass relative to nitrogen will facilitate its preferential escape. While the exobase by definition occurs at the Kn_H = 1 interface, the simulations described herein draw their lower boundary

conditions from work which employs slightly different values for the system geometry, as detailed in Table D.1. (Tucker *et al.*, 2015, Stern *et al.*, 2015). I opt to preserve reported number densities, temperatures, and exobase locations as ratios of R_P such that, at the lower boundary, simulation Kn_H are between 0.1 and 1.0. As upper-atmospheric flow becomes more rarefied and transitions to free-molecular with radial distance from the plutonian exobase, Kn_H approaches infinity.

With a time-invariant flux of particles into the domain across the lower boundary (exospheric) surface, a steady state is expected to develop for atmospheric and escaping flow in our rotating reference frame. Simulations are run until this steady state is achieved within the domain, which typically takes on the order of $\sim 8 \times 10^6$ s, or about fifteen system orbits. A simulation has evolved to equilibrium when the following quantities reach their respective steady values:

(i) Total number of particles in the simulation domain
(ii) Particle flux across the *lower* boundary (out of domain)
(iii) Particle flux across the *upper* boundary
(iv) Particle flux onto the surface of Charon

Each of these quantities reaches their steady values at a different rate, and I begin to sample the flow field after steady-state is achieved. To reduce the statistical noise present in the samples, I simply perform time-averaging over a longer period.

3.3.3 Computational Methodology

Particles are introduced into the simulation domain through the lower boundary as a Maxwellian flux, with the number density and temperature along that boundary specified according to the solar heating conditions considered. For a particular cell along the lower boundary, the average number of computational particles generated per time-step, Δt, is given by

$$N_{create} = \sqrt{\frac{k_b T_{cell}}{2\pi m_{N2}}} \left[\frac{n_{cell} A_{cell} \Delta t}{f_{num}}\right], \tag{3.1}$$

where T_{cell}, n_{cell} and A_{cell} are the temperature, number density and surface area of the cell at the lower boundary, respectively. The particles are placed across the cell surface according to a uniform random distribution while their velocities are randomly drawn from a half-range Maxwellian distribution corresponding to T_{cell}. In the current work, I assume uniform conditions across the entire lower boundary. The values of number density and temperature used can be found in Appendix D. Global uniformity is a reasonable approximation, as corroborated by the New Horizons observation of a nearly isotropic exobase (Stern *et al.*, 2015, Gladstone *et al.*, 2016).

Unless noted otherwise, any particle impacting Charon in this work is removed from the simulation domain: thus, Charon acts as a sink for particles. For each such particle, the time and spatial coordinates of exobase generation and impact on Charon are stored, in addition to particle species. This information is used to analyze the nature of deposition onto Charon for the limiting case in which all particles that impact, stick. It is also used to generate supplementary simulations in which these same particles instead equilibrate with the surface and diffusely reflect from Charon on impact, with their resultant velocities drawn from a half-range Maxwellian distribution at the imposed

surface temperature, and continue to diffusely reflect until they achieve escape velocity. In the highly-rarefied (nearly free-molecular) flow regime about Charon, it is permissible to superpose the resultant number density fields to compare the opposing extremes of total sticking and total diffuse-reflection at Charon. As more data become available, e.g. detailed maps of Charon's surface temperature, frost coverage, and composition, it will be possible to implement more complex and realistic boundary conditions.

While the Charon surface temperature employed in the present work is taken to be an isotropic 53 K, with a global map of surface temperature, one could implement a sticking boundary condition where only a fraction of impacting particles stick to the isotropic surface (Tucker *et al.* employ a simple linear distribution of temperature with latitude as nitrogen interacts with Charon in their 2015 work). If frost coverage and properties are also known, one could enforce a residence time for the sticking particles, introducing transient variability as particles stay stuck to the surface for a finite period of time and are then released back into the flow. These mechanisms are comparable to those developed in our codebase for simulation of adsorbing and desorbing sulfur dioxide in the comprehensive Ionian atmospheric simulations of Walker *et al.* (2012). The precise nature of particle interaction with the Charon surface is a critical boundary condition for study of local atmospheric dynamics and the propagation of transferred material to regions of the Charon surface, as to the cold-traps in polar regions that are eventually photolytically processed into tholins (Grundy *et al.* 2016). However, we do not anticipate the boundary conditions implemented on Charon to have a significant effect on vacuum escape rates or overall flowfield structure because only a small proportion of the escaping flow ends up impacting Charon (approximately 3.3–3.6 %, see Tables 3.2 and F.2.).

Simulations are computed in parallel on multiple processors distributed along the azimuthal and zenith coordinates. In this work, a single run is typically performed on 240

processors over several dozen hours, or O[10^3–10^4] CPU-hours. I have distributed the processors in a non-uniform grid in zenith concentrated about the equatorial plane such that the total number of computational particles per processor does not vary significantly. In a typical simulation, the total number of computational particles per processor is O[10^6], with O[10^8] occupying the complete domain at any one time, and as many as O[10^{11}] distinct particles generated over the course of a run to steady-state.

In these simulations, I have maintained O[10^2] particles per cell near the lower boundary with values of F_{NUM} varying across simulations from 10^{24} to 10^{26}. Adequate resolution in particle count is especially important near the lower boundary where the flow is densest and most collisional, as two or more computational particles are required in a cell for collisions to actually occur. While cells expand in volume with radial distance from the exobase, it is not necessary to maintain correspondingly high particle counts per cell as the flow becomes increasingly less collisional. Multiple cubic mean-free-paths are resolved everywhere throughout the flow.

3.3.4 Pre- and Post-Encounter Cases

In the following sections, we examine two cases, distinct in exobase boundary conditions, to illustrate the effect of upper atmospheric temperature and methane fraction on the overall atmospheric structure. Case A represents a cool, not cold, atmosphere case in which lower boundary conditions are drawn from one-dimensional hybrid fluid-kinetic simulations of the atmosphere below the exobase by Tucker *et al.* (2012) without solar heating, for which converged values of temperature and number density are reported at R = 2836 km. This condition was employed isotropically in preliminary three-dimensional simulations of the near-exobase region, not addressed herein, from which the converged

Case A boundary condition at R = 3000 km and Kn_H ~0.4 is drawn. In contrast, Case B matches its exobase directly to the lower boundary conditions determined by the ALICE and REX instruments on NH at two locations (during ingress and egress) as reported by Gladstone *et al.* (2016). Therefore, this result represents the nature of the three-dimensional atmospheric structure at the time of the NH encounter. In Appendix F, I pursue three other cases for direct comparison to and in extension of the previous work of Tucker *et al*. (2015), corresponding to various levels of applied solar heating in the lower continuum atmosphere. Those simulated atmospheres are more expansive than that observed by NH, with warmer exobases and higher nitrogen fractions, but could correspond to hypothesized instances of high rates of nitrogen escape in the past (Gladstone *et al.*, 2016).

3.4 AN UNHEATED EXOBASE

We first consider Case A, an hemispherically-symmetric atmosphere generated just below the exobase at 1,815 km above Pluto (R = 3,000 km) with total number density 1.34×10^{13} m^{-3}, temperature 85.5 K, F_{NUM} 3×10^{24}, and composition 99.56 % N_2 and 0.44 % CH_4 by mole as consistent with an evenly-mixed methane fraction through the upper atmosphere (Young *et al.*, 1997; Lellouch *et al.*, 2015). Results are presented for a steady-state simulation equilibrated over 16 million seconds (29 diurnal cycles) performed on the TACC Stampede supercomputer cluster on 240 processors at approximately 50,000 CPU hour expense. The number density field presented in Fig. 3.1 captures the evolved flowfield in a reference frame fixed to Pluto and in which Charon, due to the system's mutual tidal lock, remains stationary. The limit of the domain shown

in this figure is 32,000 km from Pluto's center, but an appended free-molecular domain (not pictured) extends to 150,000 km.

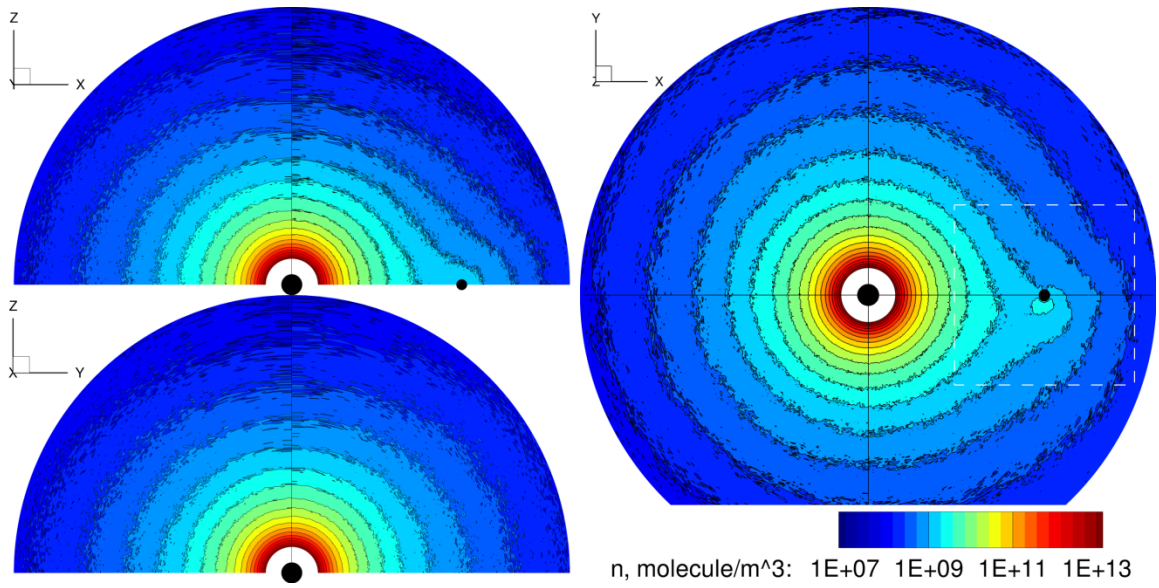

Figure 3.1: A three panel view shows orthogonal cut-planes in contours of total number density. Pluto and Charon are marked in black, and Pluto's collisional atmosphere in white. Both bodies are rotating counterclockwise when viewed down the polar Z axis (at right), and are likewise revolving CCW about the barycenter. Note the distortion of the density field due to Charon's gravity, and the evident transfer of escaping atmosphere to a high-density region at Charon's trailing hemisphere. The dashed white square is the region about Charon 20,000 km on edge considered in Figs. 3.4 and 3.5.

With radial distance from the isotropic exobase, the density field distorts toward Charon along the Pluto–Charon axis, ultimately creating a bridging structure that arcs through the L1 Lagrange point and toward Charon's trailing (wakeward) hemisphere, while a corresponding and diffuse return flux passes material from Charon back to the

wakeward side of Pluto. The density increase about Charon occurs primarily near the equatorial plane, in this case for which all particles that strike Charon stick to its surface.

Fig. 3.1 demonstrates these novel structures in the number density field on a set of three mutually orthogonal cut-planes intersecting at Pluto's center. The Case A exobase is detailed in Table 3.1, and related to the New Horizons observation and the minimum solar heating exobase calculated pre-encounter by Tucker *et al.* (2015). The variance in exobase position between Case A and the unheated, one-dimensional fluid-kinetic result reported by Tucker *et al.* (2012) stems from use of a different collision cross section in the VHS molecular model of our DSMC approach and minor updates to Pluto system values. Number densities and temperatures in the isotropic near-exobase region of the Case A flowfield otherwise match closely with the 2012 result.

Exobase	Radius [R_P km]	T	n [#/m^{-3}]	N_2 [#/m^{-3}]	CH_4 [#/m^{-3}]	λ_J N_2	λ_J CH_4
Case A Result	2.59 R_P / 3070	85.5	9.10×10^{12}	9.04×10^{12}	5.46×10^{10}	11.2	6.4
New Horizons	2.36 R_P / 2800	70.0	$7–12 \times 10^{12}$	$4–7 \times 10^{12}$	$3–5 \times 10^{12}$	14.1	8.1
Tucker (2015)	6.84 R_P / 8105	79.0	5.0×10^{11}	5.0×10^{11}		4.8	
Tucker (2012)	3.29 R_P / 3900	85.0	1.7×10^{12}	1.7×10^{12}		8.8	

Table 3.1: The Case A exobase parameters compared against the conditions observed by New Horizons (Gladstone *et al*. 2016), the nominal solar-heating case applied in the Tucker *et al.* (2015) pre-encounter prediction, and the one-dimensional unheated case considered in Tucker *et al.* (2012).

The key differences between Case A and the NH encounter are in temperature and methane fraction: New Horizons encountered a surprisingly cold exobase, with fully ~42 % methane by molar fraction. Total exobase number density for the unheated Case A

lower boundary falls within the observed bounds, and the exobase position within 0.1 R_P. While a cold exobase slows escape to vacuum, as relatively few particles cross the exobase with energies sufficient to depart Pluto, this effect is counteracted by methane's low mass and correspondingly high scale height: relative to nitrogen, methane preferentially escapes. The non-dimensional Jeans parameter captures this behavior, and is used to calculate unperturbed Jeans escape rates: Jeans theory predicts that the New Horizons exobase will have escape rates 2–3 times higher than Case A, with methane composing over 99 % of escaping material.

At steady-state, the DSMC simulation yields rates of molecule flux into and out of the domain, including rates of vacuum escape and flux to Charon by species. Table 3.2 reports these rates in comparison with relevant values from the NH observation and prior simulations. The Tucker *et al.* (2015) pre-encounter prediction represents the result of a three-dimensional free-molecular simulation in a comparable domain to the DSMC, but with a lower-atmospheric solar heating model inconsistent with Case A. The Tucker *et al.* (2012) result noted is consistent with the Case A no-heating condition, but calculated in a one-dimensional domain. The steady-state vacuum escape rate is shown to be in good agreement with the NH observation, underpredicting the encounter value by just ~30 %.

Particles incident on Charon are recorded, and maps of deposition by species are shown in Fig. 3.2. Total deposition onto Charon is slightly in excess of 10 % methane by mole for the Case A lower boundary conditions, a significant increase over the generation fraction of 0.44 %. Both methane and nitrogen are observed to deposit preferentially onto Charon's leading hemisphere with peak flux at about 315° E (45° W) longitude, although the difference between the global minimum (at 135° E) and maximum depositional rates is only a factor of two. This depositional pattern represents only the *initial* impact of particles onto Charon. The result that Charon's leading face experiences peak deposition

while a high density structure forms in Charon's wake can be explained in part by the moon's gravitational focusing of its incident flow, a phenomenon considered in depth in Appendices G and H. These results are broadly consistent in morphology with the results for the density field and depositional pattern on Charon reported by Tucker *et al*. (2015).

Fluxes, all [s^{-1}].	Inward	Outward	Escape Rate	Charon: N_2	Charon: CH_4
Case A Result	9.64×10^{28}	9.63×10^{28}	$3.6–4.2\times10^{25}$	$1.4–1.5\times10^{24}$	$1.5–1.6\times10^{23}$
New Horizons			$5–6\times10^{25}$		
Tucker (2015)	2.5×10^{28}	2.3×10^{28}	2.2×10^{27}	5.7×10^{25}	
Tucker (2012)			4.8×10^{25}		

Table 3.2: Rates of flux into and out of the domain at the exobase boundary, to vacuum (the system escape rate), and to Charon for each species in the DSMC Case A calculation are compared to the NH encounter (Gladstone *et al.*, 2016) and the nominal and unheated cases in the literature.

The boundary condition at Charon's surface shapes flow in the near-Charon region. If particles are permitted to diffusely reflect from Charon, as opposed to permanently sticking on its frost regions, they may continue to 'hop' along its surface. Such particles may be considered as adsorbing to the surface, equilibrating to the local temperature, and being diffusely re-emitted in a process that will ultimately result either in their escape or their travel to, and deposition in, a sufficiently cold region. While particles hop, they may have the effect of creating a persistent atmosphere about Charon. To escape, an emitted particle must have kinetic energy in excess of its gravitational potential at the surface, and will have been drawn from the tail of a Maxwellian distribution. In these steady-state calculations, the residence times of adsorbed particles are not relevant.

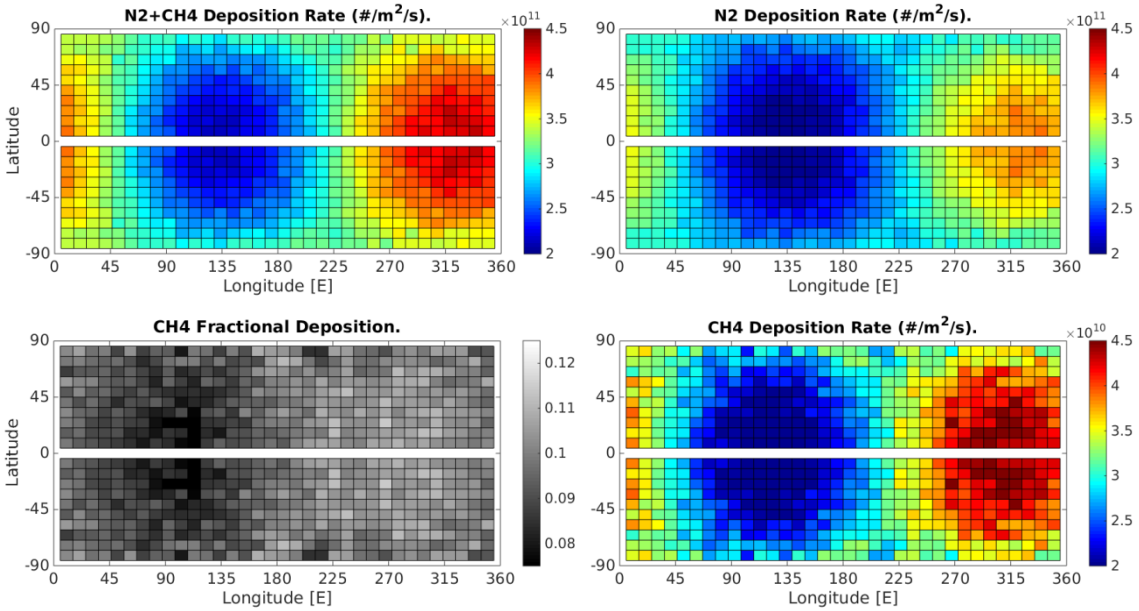

Figure 3.2: In the DSMC simulations shown here and in Fig. 2, particles that strike Charon stick and are stored. Depositional rates onto Charon's surface for Case A (a no-heat exobase) are shown alongside the fraction of methane in incident material, of order ~10 %. Data mirrored over the equator for clarity.

The simulation shown in Fig. 3.1 applies a uniform sticking condition at Charon. The Case A study is continued in a separate simulation, however, by re-emitting the particles stored at Charon as though they had diffusely reflected from its 53 K uniform surface. All further collisions with Charon are then treated in the same fashion so that particles tend to hop over Charon's surface. The resultant flow is sufficiently rarefied as to be non-collisional, and may be superposed with the result in which all particles stick to Charon, which is also non-collisional in the near-Charon region. The effect is that of two distinct flows and simulations, one of which contains all particles that *have* interacted with the surface (via diffuse reflection), and the other containing only particles that *have not* interacted with Charon's surface (i.e. that shown in Fig. 3.1, and equivalent to a

uniform sticking condition: all particles in this field that have interacted with Charon have stuck). Summing these yields a result for a total flowfield that permits diffuse reflection at Charon. These flows are shown from left to right in Fig. 3.3, each panel of which occupies a square region 20,000 km on edge centered at Charon in the equatorial plane, as demonstrated by the dashed white region of Fig. 3.1. The left panels (a-c) show number densities, while the right (d-f) show column densities integrated along the polar axis. At top (a, d) are particles which have struck and reflected off Charon alone; at center (b, e) the result for the flowfield in which all particles stick to Charon; and at bottom (c, f) is the super-imposition: the total flowfield, permitting diffuse reflection. A diffuse transfer structure from Charon back toward Pluto is evident in the reflected particles, while the near-Charon region highlights the shape of the gas transfer structure arcing through L1. These two cases, in which either all particles stick at Charon or all particles reflect, bracket the range of possibilities for Charon's boundary conditions. If particles are permitted to bounce off of Charon, the Fig. 3.3 result suggests that a thin atmosphere could persist on the moon, an atmosphere effectively shared between bodies in a binary system. The maximum pressures of such an atmosphere in this Case A simulation are O[10^{-15}] bar, significantly lower than would have been detectable by the NH instrumentation at O[10^{-12}] bar.

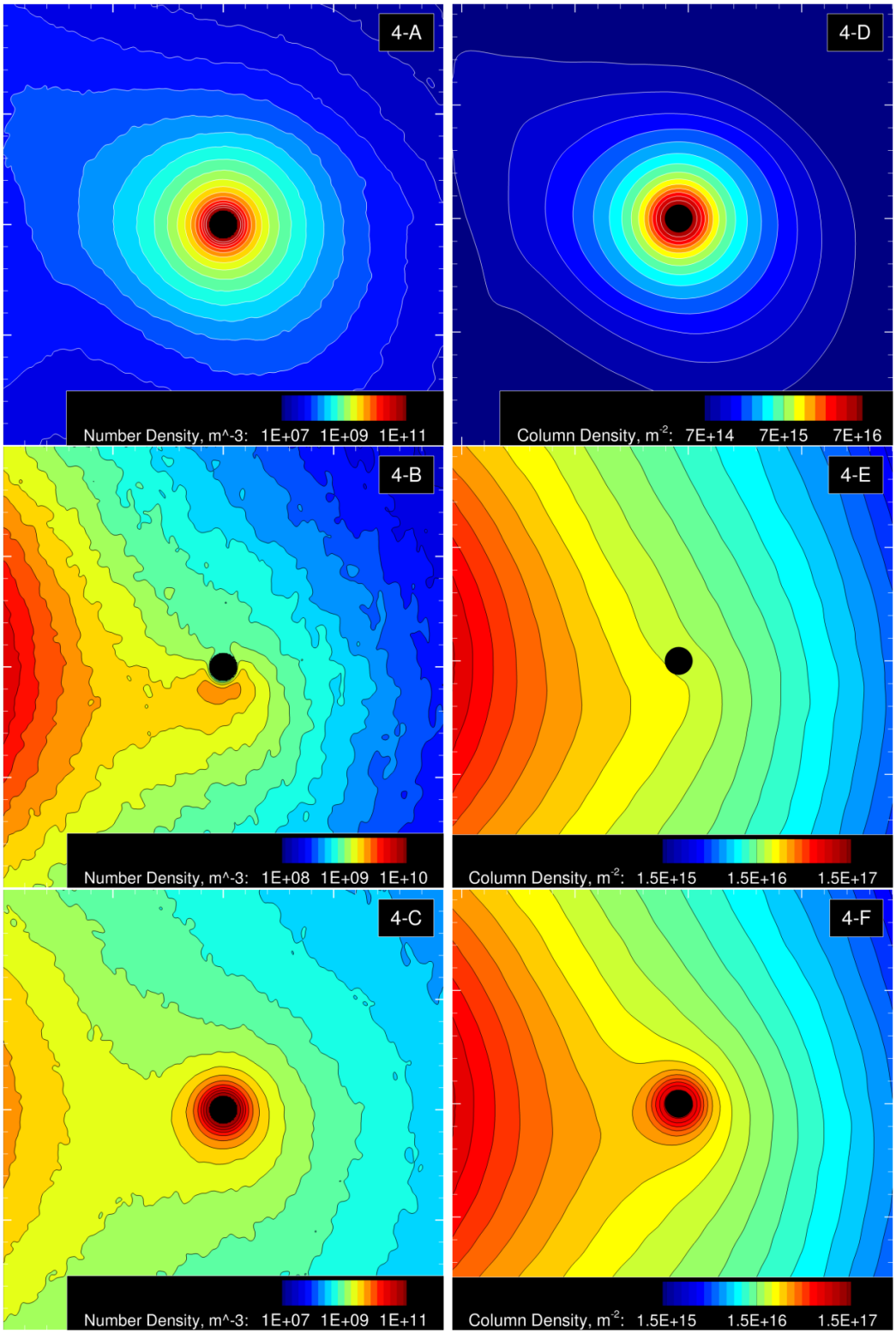

Figure 3.3: Number, column densities about Charon for sticking and reflecting cases.

Two radii above the Charon surface, roughly half of the local number density is composed of reflected particles, as shown in Fig. 3.4. Fig. 3.4 shows the same inset domain about Charon, 20,000 km on edge, as Fig. 3.3. This atmospheric feature shows an asymmetric effect about Charon along the axis perpendicular to the polar and Pluto–Charon axes: Charon's leading face sees, proportionally, more atmosphere perpetuated by surface interaction, corresponding to the inflated wakeward density and an isotropic distribution of particles leaving Charon's surface (after many diffuse reflections).

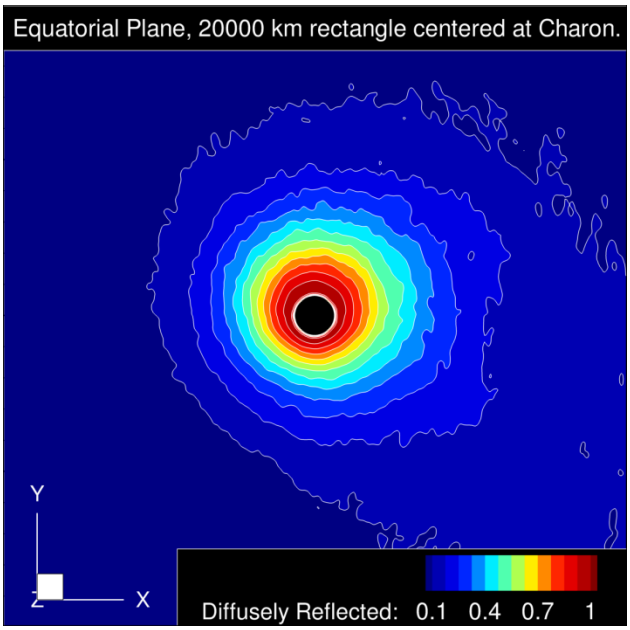

Figure 3.4: The fraction of particles in the region about Charon that have reflected from its surface. The reflected particles perpetuate a thin atmosphere, with pressure less than 10 femtobar. This superposed flowfield represents a result in which all particles that initially arrive at Charon reflect diffusely with temperatures equilibrated to the surface temperature (uniform at 53 K), accurate in the steady-state.

In examining flowfield structure, it is important to note that the flow above Pluto's exobase trends toward a free-molecular state in which individual particles only rarely experience collisional interactions. The DSMC results exhibit comparable structure to the Roche transfer phenomenon that occurs between semi-detached binary stars, as in the Algol system (Blondin *et al.* 1995) when one partner overfills its equipotential surface, as demonstrated in Figure 3.5. However, Roche theory is fundamentally hydrodynamic, its equations continuum in origin. The DSMC result is an ensemble and time average across a collection of particles primarily engaged in non-collisional and independent ballistic trajectories and not a representation of a 'bulk' flow; therefore, the structure of the Pluto–Charon density field, and specifically the nature of transfer to Charon, are distinct phenomena unique to a rarefied escaping atmosphere shared among bodies in a binary configuration.

3.5 PLUTO–CHARON AT THE NEW HORIZONS ENCOUNTER

A second simulation, labeled Case B, is performed with boundary conditions from the New Horizons encounter for the atmosphere generated at the exobase conditions. As a result, the situation should directly match other NH observables, like vacuum escape rate. Case B is performed at an F_{NUM} of 5×10^{25} on 240 processors, and results shown were run to ~10.5×10^6 s (19 diurnal cycles). The significant changes between Case B and the unheated pre-encounter exobase (Case A) are the exobase temperature and methane fraction: New Horizons observed a cold ~70 K exobase at ~42 % methane, as detailed in Table 3.1. Vacuum escape rates and rates of deposition onto Charon are calculated for the equilibrated DSMC calculation and compared to those reported by Gladstone *et al.* and

Bagenal *et al.* (2016), and the Case B simulation is shown to match the NH observed vacuum escape rate closely. Results and boundary parameters are reported in Table 3.3.

Likewise, the structure of the Case B density field, its total rates of deposition and escape, and the depositional pattern observed on Charon do not change markedly from the Case A result. Fig. 3.6 shows the Case B flowfield both in a hemispheric region of 32,000 km radius and in a 20,000 km square about Charon for direct comparison against Figs. 3.1 and 3.3. The escape rate and total rate of flux to Charon for Case B are each about double the corresponding rates for Case A, which agrees with the ratio of total unperturbed Jeans escape rates at the two exobase conditions. The flowfields of Case B show the same transfer structures and Charon-wakeward asymmetries of Case A, as evidenced in Figs. 3.6 – 3.8.

Exobase Conditions	Case B Boundary	NH Observation
Temperature T [K]	69	~ 70
Nitrogen n_{N2} [10^{12} m^{-3}]	5.5	4–7
Methane n_{CH4} [10^{12} m^{-3}]	4.0	3–5
Total number density n [10^{12} m^{-3}]	9.5	7–12
Exobase (boundary) altitude [km]	2800	2750–2850
System escape rate [s^{-1}]	7×10^{25} (>99 % CH_4)	$5 – 6 \times 10^{25}$ (>99 % CH_4)
Flux to Charon [s^{-1}]	2×10^{24} (~98 % CH_4)	

Table 3.3: The selected Case B lower boundary parameters, drawn from NH observation, and rates of vacuum escape and flux to Charon's surface.

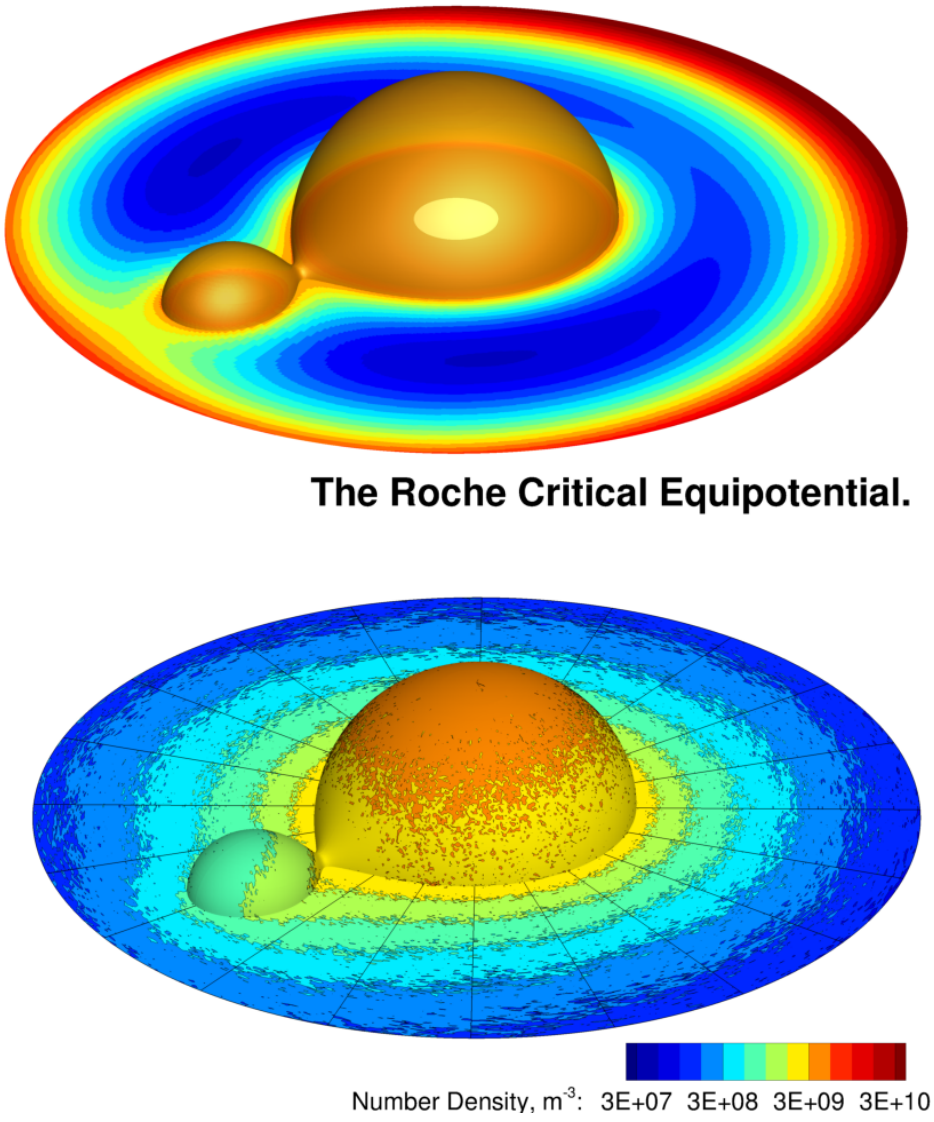

Figure 3.5: (Top) The Roche equipotential surface connects the potential lobes about Pluto and Charon through the L1 Lagrange point and is the defining surface parameterizing gas transfer between semi-detached binary stars. While the potential is critical in considerations of particle mechanical energy (e.g. for propagating particles in satellite orbits, as in Beth *et al.* 2014), the theory governing Roche transfer is developed in fundamentally continuum terms. (Bottom) The number density field for Case A is projected onto the Roche equipotential surface.

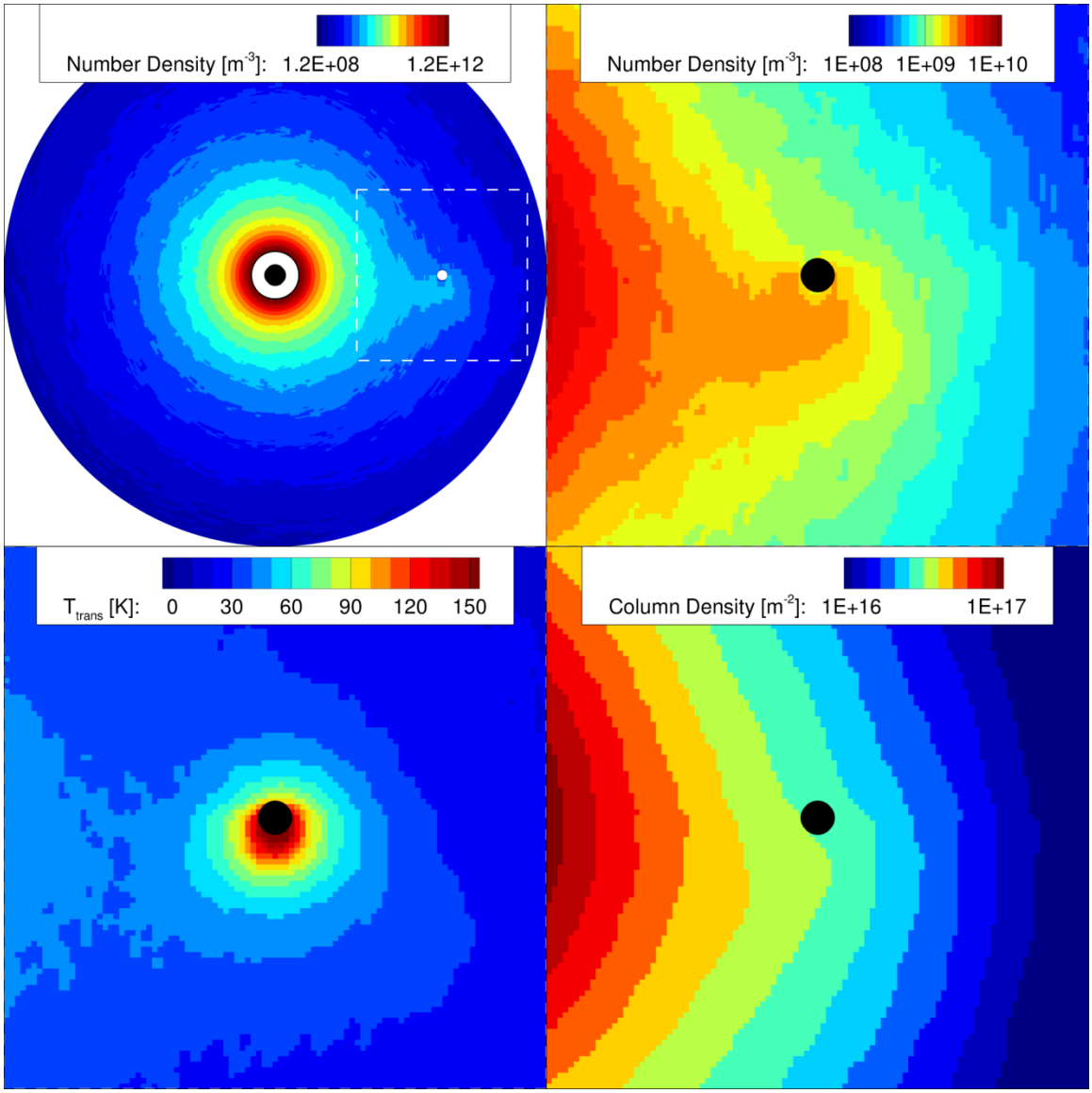

Figure 3.6: (Top left) Number density about Charon in the NH simulation, Case B. The dashed square marks an inset region 20,000 km on edge about Charon, shown in the remaining panels. (Top right) The bridging gas transfer structure which arcs toward Charon's trailing hemisphere is preserved in Case B. (Bottom left) The translational temperature, a frame-independent result, peaks towards Charon's trailing hemisphere. (Bottom right) Column density LOS integrations down the polar axis demonstrate a slight wakeward asymmetry, but emphasize that the bridging structure is confined to a narrow, equatorial band when the boundary condition at Charon is uniform sticking.

The translational temperature of the highly non-equilibrium flow about Charon is shown in the bottom left panel of Fig. 3.6. The velocity distribution of this flow is non-Maxwellian, and its tail is enhanced with high-speed particles. Note the enhancement in translational temperature as flow about Charon is gravitationally focused into the high-density region in the moon's wake. Additional discussion of this gravitational focusing effect is included in Appendices G and H.

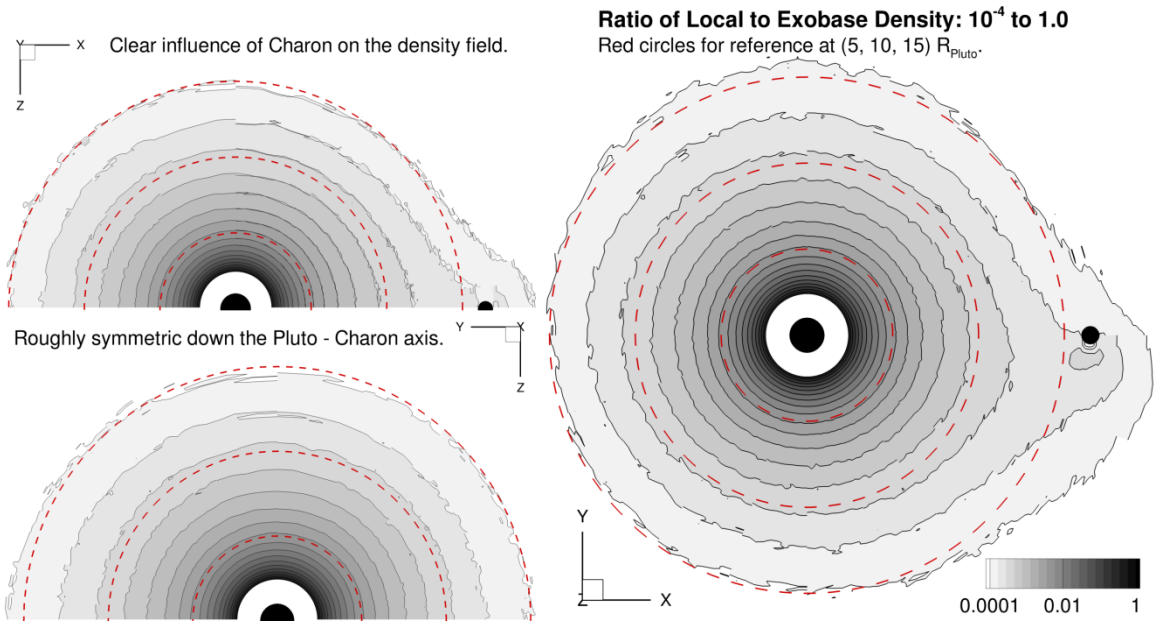

Figure 3.7: In the Case B New Horizons result, number density decreases rapidly with radial distance from Pluto: for most of the flow the ratio of local to exobase density reaches 10^{-4} by 15 R_P. The region around Charon is an exception, as the density field is shown to distort toward the moon both along the Pluto-Charon axis and in its wake. This structure has comparable shape to that seen in the Case A field (Fig. 3.1).

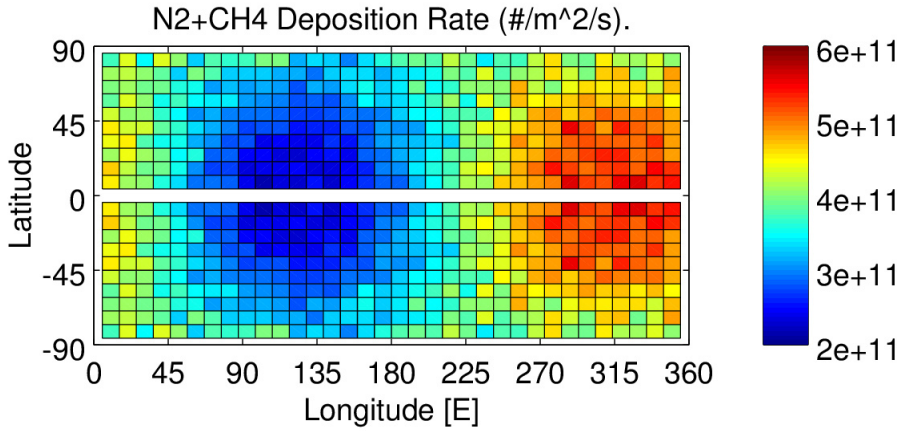

Figure 3.8: In the New Horizons simulation (Case B), depositional rates onto Charon are comparable in magnitude and structure to those in the no-heat simulation (Case A), but methane now composes about 98 % of the flux relative to nitrogen. This corresponds to the increase in exobase molar fraction from 0.44 %, as hypothesized pre-encounter, to fully 42 %: as a lighter species, methane preferentially escapes.

Individual particles can be characterized by their mechanical (total) energy: the sum of their kinetic and (negatively-signed) gravitational potential energies in an inertial, barycentric reference frame. Particles with positive potential energies may escape, while particles with negative energies are, in a sense, gravitationally bound. The vast bulk of molecules fall into the latter category, having insufficient energies to escape the system, unsurprising as the mean thermal speed at the exobase is about one-third the escape velocity from Pluto. The Maxwellian draw of a high-energy particle is correspondingly rare, and the alternative routes for escape are either an imbuement of energy via collision, or an accelerating interaction with Charon (which itself requires substantial energy to reach). In Fig. 3.9, narrow bands of mechanical energies about zero are considered: these represent particles with potential and kinetic energies nearly equivalent. Such particles will approach the edge of the system and either narrowly escape to vacuum, or fall back into the domain over a long time-span. For this specific class of particles, a coherent

spiral structure is visible with consistently-spaced bands trailing the wakeward hemispheres of Pluto and Charon; Pluto's band is more diffuse. This result suggests that the Pluto–Charon system may leave a detectable cork-screw tail, if only certain energy molecules were taken up by the solar wind.

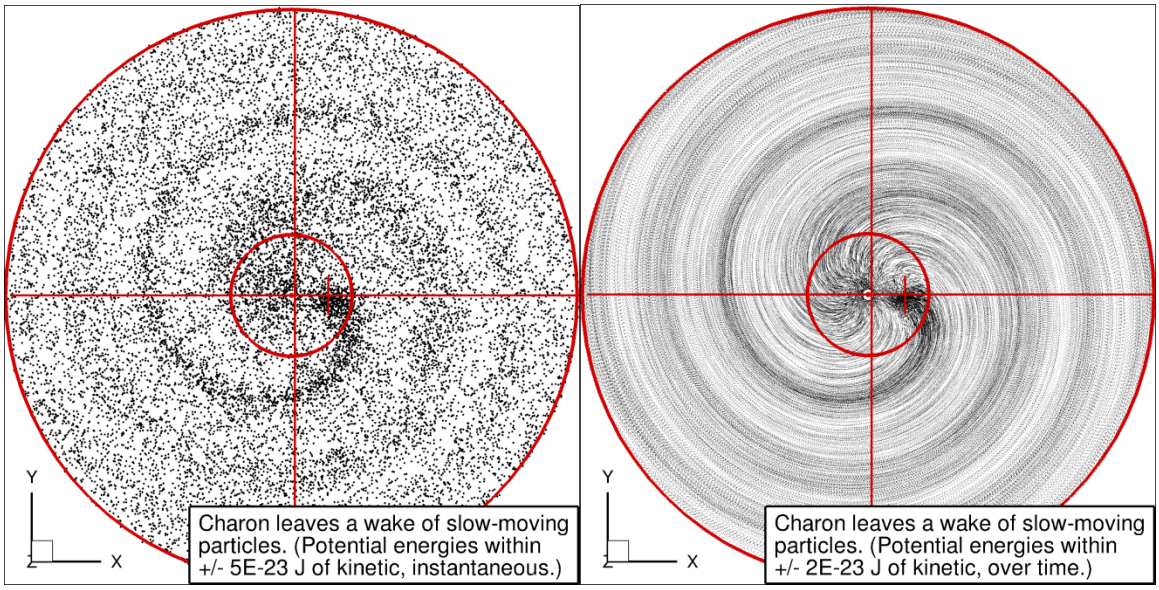

Figure 3.9: (Left) An instantaneous depiction of a subset of computational particles with mechanical energies in the range $\pm 5 \times 10^{-23}$ J. The domain shown extends to 150,000 km from Pluto's center, while the interior circle shows a portion of the computational domain extending to 30,000 km consistent with that depicted in Figs. 3.1, 3.6, and 3.8. The axes cross on the barycenter, and Charon's position is marked with a cross. (Right) The trajectories of a narrower subset of these particles, $\pm 2 \times 10^{-23}$ J, are shown over a 20 hr period to emphasize this spiral pattern.

3.6 CONCLUSIONS

A fully three-dimensional model of the steady-state, rarefied component of Pluto's upper atmosphere is presented, demonstrated for the pre-encounter prediction

most similar to that observed by New Horizons, and applied in a simulation of the NH encounter exobase and resultant flowfield. While the majority of the domain by volume can be well approximated by free-molecular flow, I do find molecular collisions in the upper atmosphere (near the plutonian exobase) to be significant in shaping the flowfield, as addressed in Appendix C. Results for exobase parameters and rates of escape to vacuum and transfer to Charon are compared against the pre-encounter literature and against the observations of New Horizons, matching well with the latter.

Gas-transfer structures are noted in a binary atmospheric configuration, including preferential deposition of material from Pluto's escaping atmosphere onto Charon's leading hemisphere, peaking at 315° E (45° W) along the equator. As the moon gravitationally focuses incident flow a high density structure forms in its wake, discussed in Appendices G and H. In the event of total diffuse reflection from Charon, a returning flux forms that is preferentially directed toward Pluto's trailing hemisphere. Charon is shown to be capable of supporting a thin atmosphere at column densities as high as 1.5×10^{17} m^{-2} in simulations with a plutonian exobase condition similar to that observed by New Horizons and a diffusely reflective boundary at Charon's surface. Case B, computed from the observed NH exobase, yields a vacuum escape rate of 7×10^{25} CH_4 s^{-1} in good agreement with that encountered (Bagenal *et al.*, 2016; Gladstone *et al.*, 2016) and a rate of deposition onto Charon of 2×10^{24} s^{-1} of which ~98 % is methane.

Improved boundary conditions for Charon anticipated in forthcoming New Horizons results include frost properties, fractional maps, and surface temperature distributions which will allow for refined simulations of the transport of 'hopping' particles along Charon's surface that inform the study of geologic features, like the dark red region at Mordor Macula formed when methane cold-trapped at Charon's poles is photolytically processed into tholins (Grundy *et al.* 2016). We have not considered the

effects of UV radiation or solar wind charge exchange in these simulations; given Pluto's extreme distance from the sun, we might anticipate low loss rates to photoprocesses. The NH results presented by Bagenal *et al.* (2016) suggest that upper atmospheric interactions with the solar wind do occur within our domain, but also that such interactions are unlikely to influence our solutions given the low reported densities of pick-up CH_4 ($O[10^2\ m^{-3}]$) close to Pluto. Such phenomena may be addressed in future work. Improvements to existing plutonian GCMs would allow for the hybridization of the planetary DSMC code with fluid models at the continuum-rarefied boundary.

Chapter 4: Developing Hybrid Simulations of Io's Tvashtar Plume[22]

4.1 Chapter Overview

Jupiter's moon Io supports its rarefied atmosphere with prolific tidally-driven episodic volcanism. Its largest volcanic plumes erupt violently and exhibit intricate structure, their canopies rising to hundreds of km above the Ionian surface. In early 2007, the NASA New Horizons (NH) spacecraft captured the active Tvashtar plume in a time sequence of panchromatic images at high spatial resolution and observed both discrete "filamentary" patterns in the descending particulate structure, and a prominent traveling canopy wave. These are transient and asymmetric features, indicative of Tvashtar's unresolved and complex vent processes.

In this chapter, I introduce a methodology for identifying vent spatial and temporal scales in the rarefied plume. Three-dimensional DSMC simulations of the collisional gas flowfield are combined with a flow-tracking dust particulate model, developed with Peter Ackley, a graduate student collaborator. Application of this hybrid scheme enables a broad exploration of parameter space in pursuit of the critical frequencies (in inputs at the vent) that qualitatively reproduce dynamical phenomena observed in Tvashtar's collisional canopy, and provides insight into the dynamics of transient extra-terrestrial plumes.

---

[22] Portions of this chapter first appeared as our *Rarefied Gas Dynamics AIP Conf. Proc.* manuscript "DSMC Simulation of Io's Unsteady Tvashtar Plume." The research was supported by NASA's Outer Planets Research program, under grant NNX14AO39G. The hybrid particle-tracking method outlined in this chapter is the subject of a pending *Icarus* manuscript by P. Ackley, and extensions of the DSMC models described herein are discussed in Chapter 5 and in my own pending *Icarus* manuscript.

4.2 INTRODUCTION: THE 2007 TVASHTAR PLUME

Io is the innermost of Jupiter's four Galilean moons. Locked in a tidal resonance with Jupiter and its Galilean satellites Ganymede and Europa, Io experiences sufficient internal friction and deformation under gravitational forces to create magma and drive the moon's intense volcanism: Io's hundreds of active volcanoes are the most of any body in the Solar System. In 2007, the New Horizons probe, as it passed through the Jovian system, captured images of a volcanic plume erupting from the Tvashtar region on the volcanic satellite Io. Five of these images, which were taken at equal intervals over an eight-minute period, reveal an asymmetric plume with two notable features: a traveling canopy wave on one side of the plume and discrete filamentary structure within the plume (see Fig. 4.1). The origin of these features is not yet completely understood, but the plume's unsteadiness and asymmetry suggest that they were created by asymmetric, unsteady vent processes.

A first step in understanding what type of vent process could be responsible for generating the unsteady motion in Tvashtar's plume is to try to determine rough constraints on the length and time scales of vent processes that are implied by length and time scales observed in the plume. Prior applications of our planetary DSMC code have included the simulation of unsteady and axisymmetric Ionian plumes (Zhang *et al.* 2003, 2004; Zhang 2004) and steady asymmetric plumes (McDoniel *et al.* 2010, 2015; McDoniel 2015) of Pele class. In this chapter I present novel DSMC results for the 2007 Tvashtar case informed by that prior work, and I demonstrate a new hybrid technique for constraining scales of vent heterogeneity and transience in gas and particulate mass flux by mapping structure at the vent to observed structure in the Tvashtar canopy.

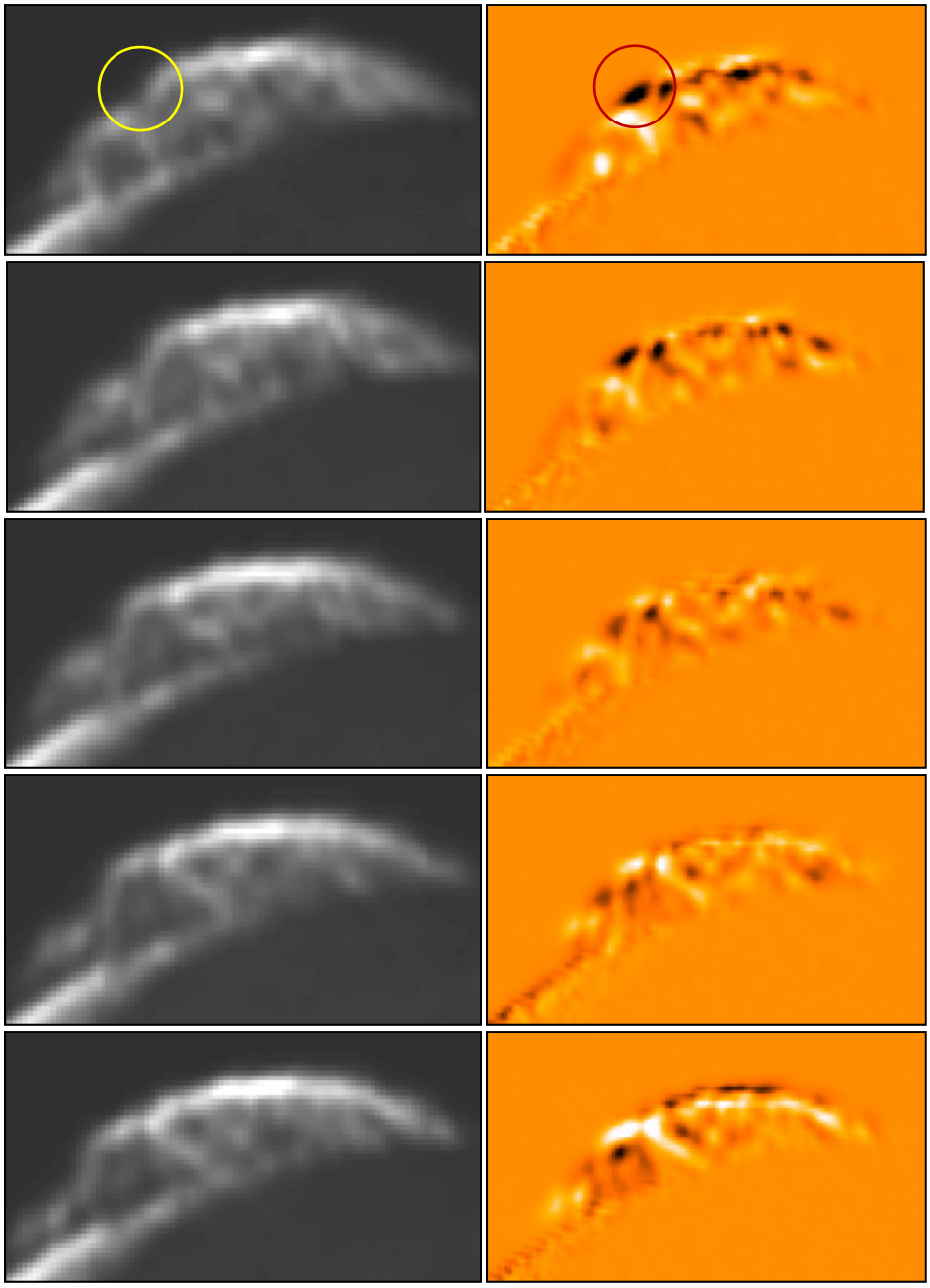

Figure 4.1: (Left) Five NH LORRI observations of the active Tvashtar plume, deconvolved. (Right) Corresponding differential brightness, the discrepancy between pixel brightness in each frame relative to the mean.
Periodic structure is seen to cascade down the canopy over the 8-minute observation period. Circled regions correspond to a visible notch in the canopy of relatively low integrated brightness, which can be tracked moving tangentially at about 400 m/s.

During the 2007 eruption observed by NH, Tvashtar exhibited a canopy height of 320 to 360 km: Spencer *et al.* (2007) estimate a canopy within this range by an analysis of NH LORRI images (i.e. those of Fig. 4.1) which primarily capture scattering from suspended particles, while Jessup and Spencer (2012) estimate a gas canopy height at or above 360 km in contemporaneous HST observations. Tangential velocities in the canopy range from 350 to 700 m/s (Spencer *et al.,* 2007). Tvashtar has apparently erupted intermittently from a number of sources, with at least two observations of bright, hot vent regions of horizontal orientation and roughly rectangular shape with high aspect ratio (i.e. extended cracks) made by the Galileo probe between 1999 and 2000 (Fig. 4.2).

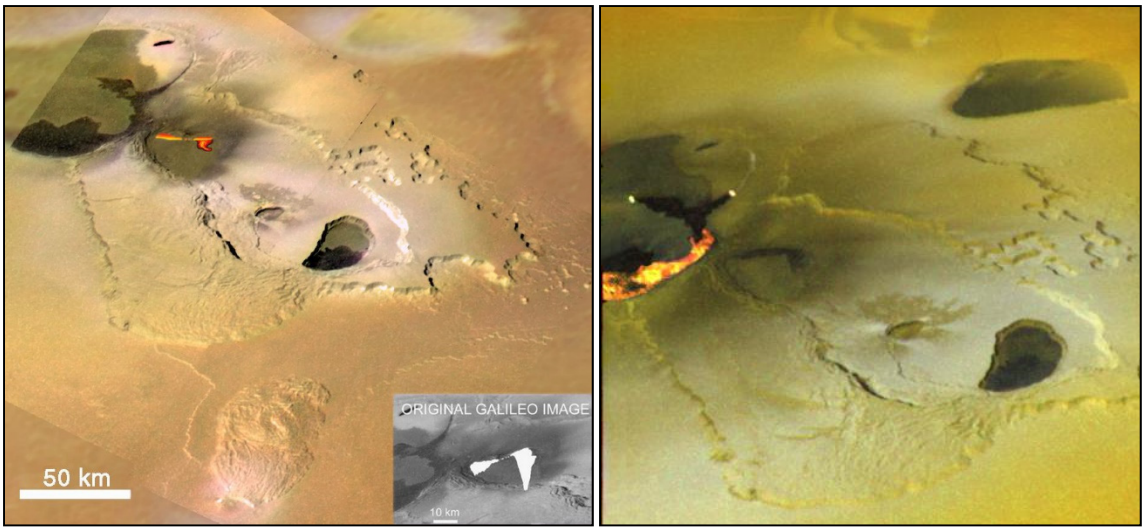

Figure 4.2: The Galileo mission captured images of an active Tvashtar Catena in Nov. 1999 (left) and Feb. 2000 (right); note that two separate sources are seen in these images, and each appears to be of high aspect ratio. The 2007 eruption emanated from a third source in the same vicinity (Rathbun *et al*. 2014) but the NH mission did not capture surface images comparable in resolution to these. (NASA/JPL-Caltech/University of Arizona).

4.3 METHODOLOGY

The most comprehensive model of the Tvashtar plume might involve simulating upward from the surface of a lava lake with a complex geometry of intermittent source regions that demonstrate spatial and temporal variability in the emission of both gas (primarily SO_2) and particulates. Single calculations at this resolution are tractable with our current methods, but the limitations of our knowledge of, and constraints on, Tvashtar's spatiotemporal scales require too broad an exploration of parameter space to be assaulted in full detail. Therefore, we introduce and justify a series of simplifications to our simulations of particulate emission at arbitrary mass flux from the Tvashtar vent, reducing our computational expense from the order of tens of thousands of processor-hours to minutes of work on a single core. First, work by McDoniel *et al.* (2011, 2015) demonstrates that the simulation of a distribution of thousands of small, adjacent source regions directly at the surface of the vent produces a result indistinguishable with altitude from simulations upward from a virtual and uniform vent surface at which the shock geometries emanating from the individual sources may be assumed to have converged. This *virtual vent* itself may demonstrate spatially and temporally variable gas and particulate emission. However, an additional simplification reduces the spatiotemporal variability of the virtual vent to a uniform and steady gas outflow, and explores only the spatial and temporal variability in the particulate emission itself, with grains that tend to move along with the gas in the DSMC but experience realistic drag and 'slip'. This is the approach applied, for instance, by McDoniel (2015) for Pele.

Finally, from the same virtual vent with uniform and steady gas outflow, we can explore spatial and temporal variability in the particulates as if those particulates moved wholly along with the gas (as in the limit of small particles). This assumption will be valid provided the mass flow rate of the particles is much smaller than that of the gas;

that the particles are individually small enough to track the gas flow, i.e. < 1-micron diameter, consistent with the results of Jessup and Spencer (2012); and that the gas flow from the vent is steady (or that the timescales of variance in this gas flow are far longer than for the corresponding timescales of particle flow). Beginning with this model, and informed by LORRI image analysis, we will identify Tvashtar's scales and reproduce its physics in increasingly realistic, comprehensive DSMC calculations.

In our implementation of this model, motions of gas and particles are simulated separately. First, DSMC is used to simulate the eruption of the gas until it reaches a quasi-steady state. Then, the local average velocity and number density are calculated at discrete points throughout the flow field and exported. A second simulation is performed in which particles are introduced at the virtual vent according to a specified mass flux function and propagated throughout space according to the velocity fields derived from the DSMC simulation. With this method, the expensive DSMC simulation only needs to be run once, while the relatively inexpensive particulate simulation can be run many times with many different mass flux functions. In this way, hypotheses for how vent parameters affect the imaged plume structure can be posed and tested with relative efficiency for steady plumes.

The simulations of this chapter employ a rectangular vent of 8×24 km (i.e. aspect ratio 3) selected as a first approximation to this complex, asymmetric source region, and motivated by the analysis of Tvashtar's 2007 source by Rathbun *et al.* (2014). The DSMC simulations apply a virtual vent of spatially-uniform outflow at 100 % SO_2 with initial temperature 500 K, upward normal velocity 850 m/s, and vapor mass density of 6.4×10^{-7} kg m^{-3} consistent with a flow that has expanded to Mach ~3.0. These conditions are drawn from McDoniel (2015) and produce a plume of Pele class roughly comparable to the 2007 Tvashtar observation. In the work of Chapter 5, I discuss the development of

novel constraints on Tvashtar's vent velocity and thermodynamic conditions derived through a range of parametric DSMC calculations that aim to match a plume in which the visibly-scattering particles entrained with the gas travel at Tvashtar's 360+ km altitude.

4.4 DSMC SIMULATIONS OF THE TVASHTAR GAS FIELD

To resolve the characteristic scales of the dense and collisional vent region, a multiply-staged calculation is performed: inner stages are calculated within a small domain above the vent source, while an outer stage encompasses the remainder of the domain, including the collisional plume canopy. To exploit the two symmetry axes of flow from a rectangular vent, a first stage is run in a quadrant centered at the origin with a radius and height of 30 km. As particles transit domain boundaries, information may be stored and sampled to generate influx for each subsequent, nested outer stage. Once the gas reaches a quasi-steady state, the local average velocity of the gas is calculated for a set P_1 of discrete points within the cylindrical domain. Similarly, local average velocity is calculated for a set P_2 of discrete points within the larger domain. In addition, local number density is calculated for points in P_2 so that the validity of the velocity calculations in this domain can be determined during subsequent particulate simulations. A description of each stage presented in this work is contained in Table 4.1. Figure 4.3 corresponds to the inner domain, and Fig. 4.4 to the combined inner and outer domain.

DSMC Domains	Inner (Near-field)	Outer (Full Domain)
Radial Extent	30 km	650 km
Maximum Height	30 km	450 km
Processor Count	32	240
Collision Cells	1×10^6	7×10^6
Simulated Molecules	2×10^7	2×10^8
CPU Hours	O[10]	O[1000]

Table 4.1: Description of the DSMC domains applied in Chapter 4.

4.5 PARTICULATE SIMULATION[23]

In the particulate simulations, a particle launched from the virtual vent is moved through space over discrete time steps with a first order Euler step (later work applies a third-order Adams-Bashforth scheme). In general, a particle's velocity is updated by using Delaunay triangulation to linearly interpolate the appropriate velocity field derived from the DSMC simulation. However, if the particle is in the outer domain, the number density at its position is first calculated to determine whether the DSMC velocity data are valid. If the number density does not exceed some minimum level, the velocity field data are assumed to be invalid, and ballistic motion is assumed. The method for introducing new particles at the virtual vent is specified as follows. In the simplest simulations, point sources are manually specified and particles are emitted from these sources at regular

[23] Section 4.5 was co-authored by P. Ackley and first appeared in our *Rarefied Gas Dynamics* manuscript. The model described herein was developed primarily by P.A. with modest collaborative input from myself.

time intervals. More generally, an acceptance-rejection method is used that depends on some specified mass flux function, $M(x, y, t)$. The general form of the mass flux function chosen[24] is:

$$M(x,y,t) = \sum_{n=1}^{p} A_n \sin\left[\frac{2\pi}{B_n}(x - \omega_n t)\right] \cdot \sum_{j=1}^{p} A_j \sin\left[\frac{2\pi}{B_j}(y - \omega_j t)\right] \quad (4.1)$$

where A, B, ω, p are constants chosen to yield traveling sinusoidal waves of mass input. The results of varying the length and time scales of vent processes can then be explored by specifying different combinations of values for these constants. At the beginning of the simulation, the maximum value of M is determined to create a normalized version of this function for use in the acceptance-rejection method.

4.6 RESULTS

Results are first presented for DSMC domains encompassing a full plume with a uniform and steady mass flux at the virtual vent. Then, the DSMC velocity fields are used to generate trajectories of flow-tracking dust particles from sources of arbitrary mass flux, representing spatiotemporal variance in grain emission.

[24] Requiring the same spatial and temporal frequencies for the X and Y dimensions may be unphysical for elongated vents. Standing waves in these two dimensions would have different spatial eigen-frequencies in this case. The simulations of Chapter 4 are highly simplified and not yet satisfyingly constrained by observation. They do, however, probe dust trajectories from various vent locations in the simulated gas plume, to aid interpretation of the observed images. (L. Trafton, personal communication, Sept. 2017).

4.6.1 Producing a DSMC Velocity Field

Figure 4.3 shows contours of number density through the quarter-cylindrical inner stage on planes aligned with the vent's narrow (X-Z) and broad (Y-Z) axes. Superimposed streamlines, in black, also illustrate the trajectories along which the particulates will travel as their velocities are drawn from the DSMC velocity field (i.e. their motion is identical to the bulk gas flow). The simulated plume exhibits axis switching, expanding much more along the vent narrow axis with increasing altitude: axis switching is a collisional phenomenon observed in asymmetric rectangular vents. Prior work has shown that entrained dust may switch axes differently than the bulk gas flow (McDoniel *et al.* 2015), underscoring the importance of simulating drag on the dust particles via their collisions with gas in the DSMC calculations, once constraints are set on their generation via the flow-tracking particulate calculations[25]. Directly adjacent to the vent in the inner stage of this calculation, mean free paths[26] are of order 0.1 m, and in this calculation cell characteristic lengths at the surface interface determined by cube root of volume are of order 10 m, such that the lower portion of this stage will be under-resolved. Likewise, implementation of a collision limiting scheme accelerates the calculation by artificially prescribing a limit to collisions per particle per cell per time step (typically < 10). Solving the inner stage calculation comprehensively – with cell sizes that resolve several mean free paths, time steps that capture the mean time between collisions (O[10^{-3} s at the vent]), and unlimited collisions – would not be prohibitively expensive, with an estimated cost on the order of 1,000–10,000 processor hours. However, the result reported in Figs. 4.3 was sufficiently accurate for this demonstration

[25] This is beyond the scope of the Tvashtar grant (i.e. offering hypotheses toward the formative physics of transient canopy structures), but it could be explored in future work along the lines of McDoniel (2015).
[26] This topic is examined in more depth in Chapter 5.

and, costing only ~10 processor hours, allowed for wide examination of SO_2 vent conditions. Contours of number density through the full domain are shown Fig. 4.4, and material ejected from the plume, falling back to Io's surface, is observed to form a stable and collisional canopy shock with maximum altitude ~320 km, matching the lower bound of canopy height observed in NH Tvashtar observations. Note the hollow region in the plume's interior and the lack of atmosphere or escaping material above the canopy shock. Little of Io's persistent sublimation atmosphere is observed or predicted at Tvashtar's high latitude of ~62° N as demonstrated in Appendix A (see also Walker *et al.* [2012]) and this general confinement of the bulk flow to a spout and sharply-bounded, collisional canopy (i.e. in speed, Fig. 4.8), matches the behavior of the NH images in Fig. 4.1. Though interaction with incident Jovian torus plasma has been shown to alter the shape and structure of Pele's plume (McDoniel *et al.* 2015), this effect is not considered in our present work for Tvashtar.

Chapter 5 builds on these results, in a comparable framework of a steady-gas-flow SO_2 DSMC model without particles, and its calculations are performed in four stages with substantially improved spatial and temporal resolution relative to this work. With a steady SO_2 condition now shown to closely match Tvashtar's behavior, future work in the DSMC code could have dust particle spatiotemporal scales informed by results from the flow-tracking code, in an iterative process.

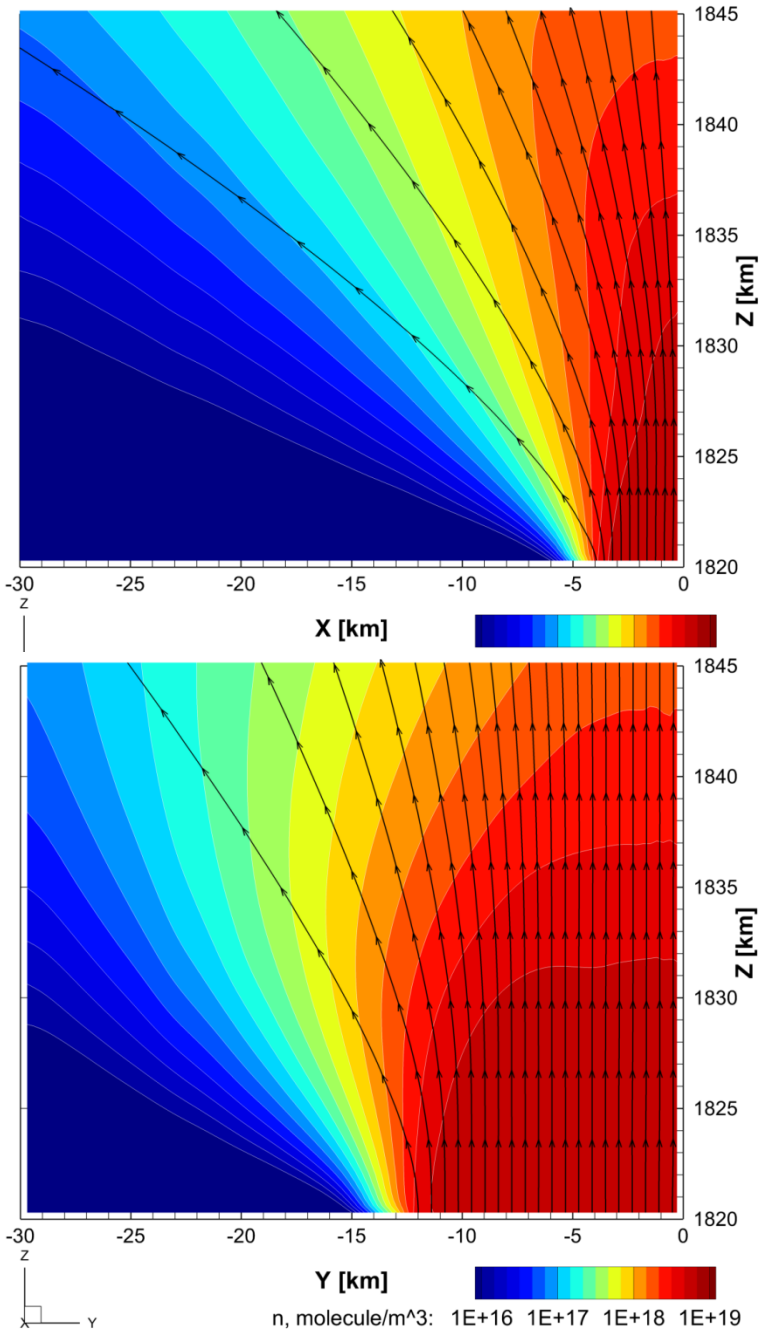

Figure 4.3: Contours of SO_2 number density in the inner domain in polar X-Z and Y-Z frames, overlain with streamlines for particles released from the vent in particulate simulations. The innermost stage, which holds the vent, is used to stage further nested domains in DSMC simulations. Note axis-switching, as the broadest expansion occurs along the vent's narrow axis with altitude.

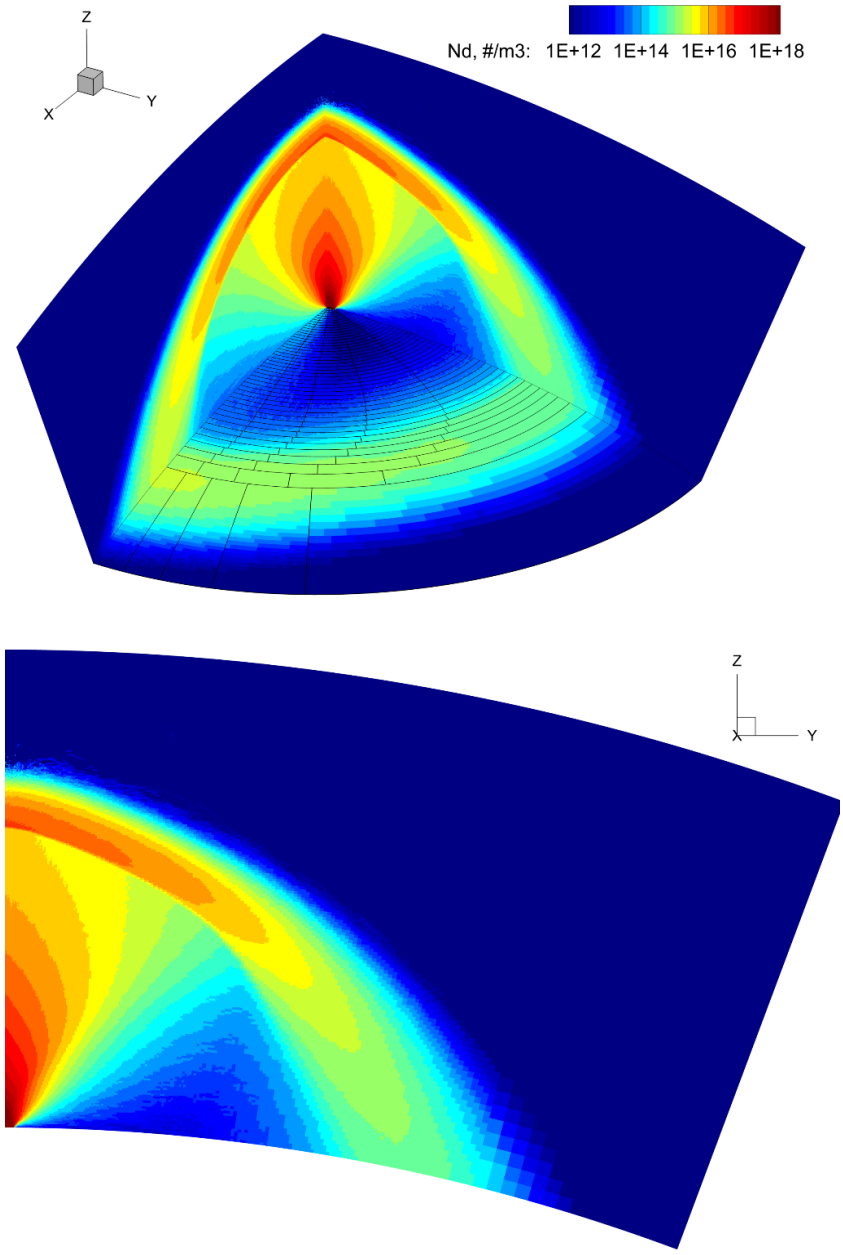

Figure 4.4: At top, SO_2 number density in a full quarter-cylindrical domain with orthogonal slices in the X-Z and Y-Z planes through the polar axis, and also on Io's surface adjacent to Tvashtar. The adaptive processor grid is marked along the surface. The clear shock structure forms a gas canopy with peak 320 km above the vent. Below, a direct view of number density in the Y-Z plane, corresponding to the vent's broad axis. The depositional ring begins to form at about 400 km from the vent.

4.6.2 Flow-Tracking Dust Particle Results[27]

Given the steady-state DSMC velocity field, roughly representative of Tvashtar in shape and scale, a range of flow-tracking particulate simulations are performed to exhibit methods of tracking structure and motion through the plume. Figure 4.5 summarizes the concept of the virtual vent in its schematic by which a complex source region, perhaps composed of bubbling or sloshing lava, is modeled as convergent to homogeneous outflow with altitude. It also shows a graphical representation of an arbitrary mass flux function at an instant in time. The difference in particle densities above select peaks in the mass flux graph demonstrates that high amplitudes in the mass flux function correspond to regions of greater particle output. Regions where the mass flux function is negative are simply shown as white because a negative value will never result in the generation of particles in our acceptance-rejection scheme.

The mass flux function used to generate the particulate plume in Figs. 4.5, 4.6, and 4.8 is of the general form specified earlier with constants $p = 2$, $A_1 = A_2 = 5$, $B_1 = B_2 = 4$ km, $\omega_1 = 0.2$ km s^{-1}, $\omega_2 = -0.2$ km s^{-1}. This function is of the same general character represented by the graph in Fig. 4.5, but each of its peaks is identical, and each rises and falls uniformly in time. This results in a uniform pulsing outflow of particles over time across different regions of the vent. In a movie of the mass flux function, the vent appears to have a checkerboard-like pattern in which some squares emit particles at a fluctuating rate while other squares never emit particles. The consequence of this scheme can be seen in the structure of the plume and the depositional pattern of particles around the perimeter. The tendrils and streamers seen in the structure of the plume, as well as the depositional pattern around the perimeter, correspond to fluctuating peaks in mass flux.

[27] Section 4.6.2 was co-authored by P. Ackley and first appeared in our *Rarefied Gas Dynamics* manuscript. The simulations and figures of this Section were a collaborative effort unless otherwise noted.

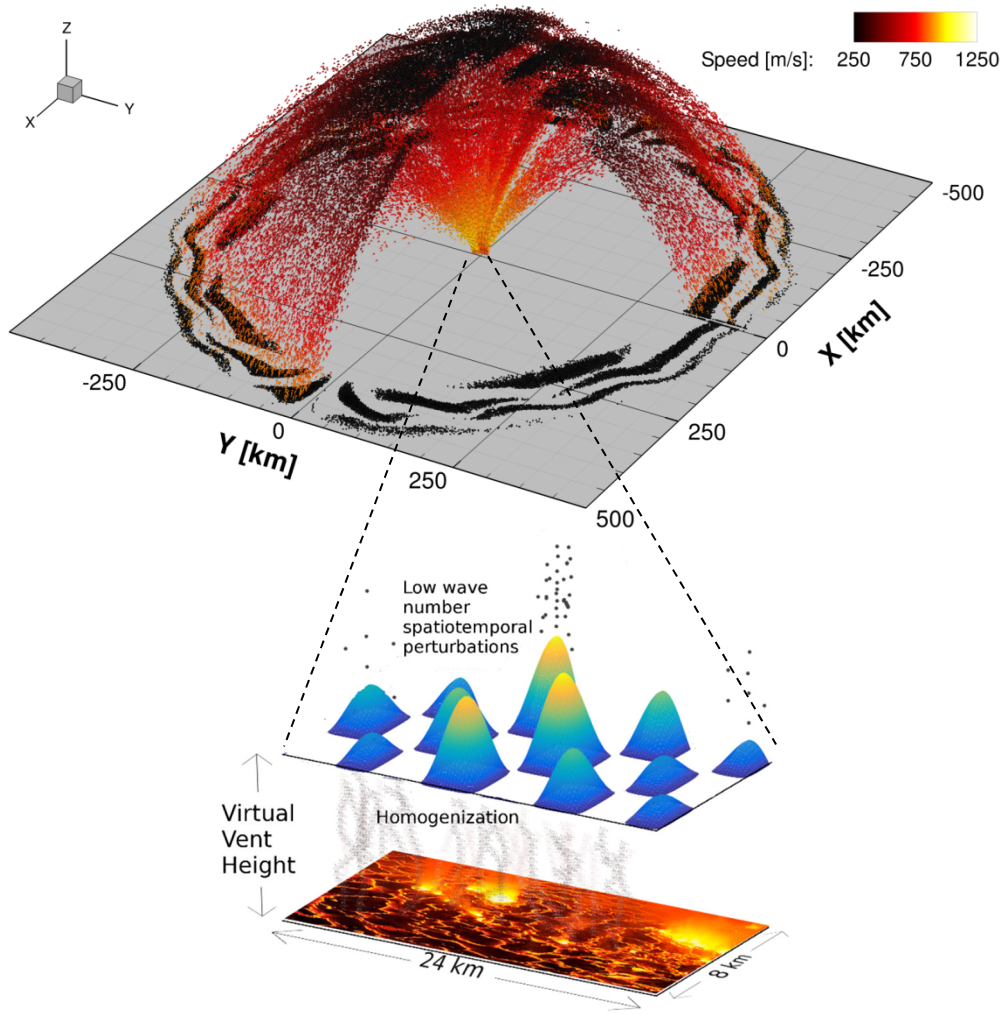

Figure 4.5: Particles emanating from the vent surface converge and are approximated as low wave number spatiotemporal perturbations at the virtual vent with a mass flux function consisting of traveling sinusoidal waves. This schematic illustrates the particle generation process employed throughout these simulations. At top, a simulated particulate plume with those in the first octant blanked to reveal the plume's interior structure. The discrete groups of particles in the depositional pattern, and visible as descending tendrils in the canopy, correspond to maxima in the graph of the mass flux function. (Figure by P. Ackley).

Figure 4.6 reveals the different particle trajectories that are generated by injecting dust at two different source locations within the first quadrant of the rectangular vent, with the particles superimposed upon a complete plume for context. The red particles are initially distributed evenly along the perimeter of an equilateral triangle with side length 0.6 km that is coplanar with the vent and centered at (2 km, 4 km). The blue particles are initially distributed evenly along a congruent triangle centered at (3 km, 10 km). The red particles, which have initial positions closer to the center of the vent, follow a relatively steep initial trajectory and encounter the canopy at a higher altitude than do the blue particles, which are launched from positions closer to the edge of the vent. These differences in trajectories demonstrate how features and structures found in the plume could be mapped back to specific source locations of dust injected at the vent. Figure 4.6 also offers insight into how features that originate at the vent transform into features in the plume. Both sets of particles are originally arranged in the shape of equilateral triangles at the vent. As the particles move through the plume, this shape is enlarged and distorted, but a general triangular shape remains recognizable throughout each trajectory. When the red particles reach the canopy ~450 s after their generation, those that correspond to the vertices of the original equilateral triangle form a triangle with side lengths of 24 km, 49 km, and 27 km and an area of approximately 190 km^2. When the blue particles reach the canopy at 380 s, their corresponding vertices form a triangle with side lengths of 23 km, 45 km, and 34 km and an area of approximately 375 km^2. Comparing these results to the original patterns, which have side lengths of 0.6 km and areas of approximately 0.16 km^2, we can determine rough correlations between length scales at the vent and length scales in the canopy. By repeating these simulations with particles that are arranged in different shapes and introduced at different locations in the vent, we can develop more robust connections between length scales at the vent and those

in the plume and broaden our understanding of how particular structures deform as they move through the plume. These connections can then be used to help determine the broad constraints on the actual vent processes implied by the images of the plume in the NH Tvashtar observations.

The time step used in the particle simulations must be sufficiently small to accurately resolve paths through the canopy's sharp velocity gradient but should be sufficiently large to facilitate rapid computation. One way to constrain the time step duration is to first move a set of particles *forward* in time from the vent over a fixed period, and then move these particles *backward* through the plume with the same period, time-step, and algorithm for determining particle velocities. After the backward integration in time, the proximity of the final particle locations to their initial positions in the vent serves as a metric for determining whether the time step is sufficiently small to accommodate the canopy structure. Figure 4.7 shows the results of this process for two different time steps for two sets of particles launched from the same location in the vent, and with point sources arranged in the same equilateral triangular geometry as the Fig. 4.6 test. The red particles, moved with a 0.01 s time step, return to a configuration proximal to the initial position and with the shape of the equilateral triangle still largely intact. The blue particles, moved with a 0.1 s time step, return to a comparably distant position, with their triangular structure severely compromised. The oblique view of Fig. 4.7 illustrates errors in reconstructing the initial vertical positions.

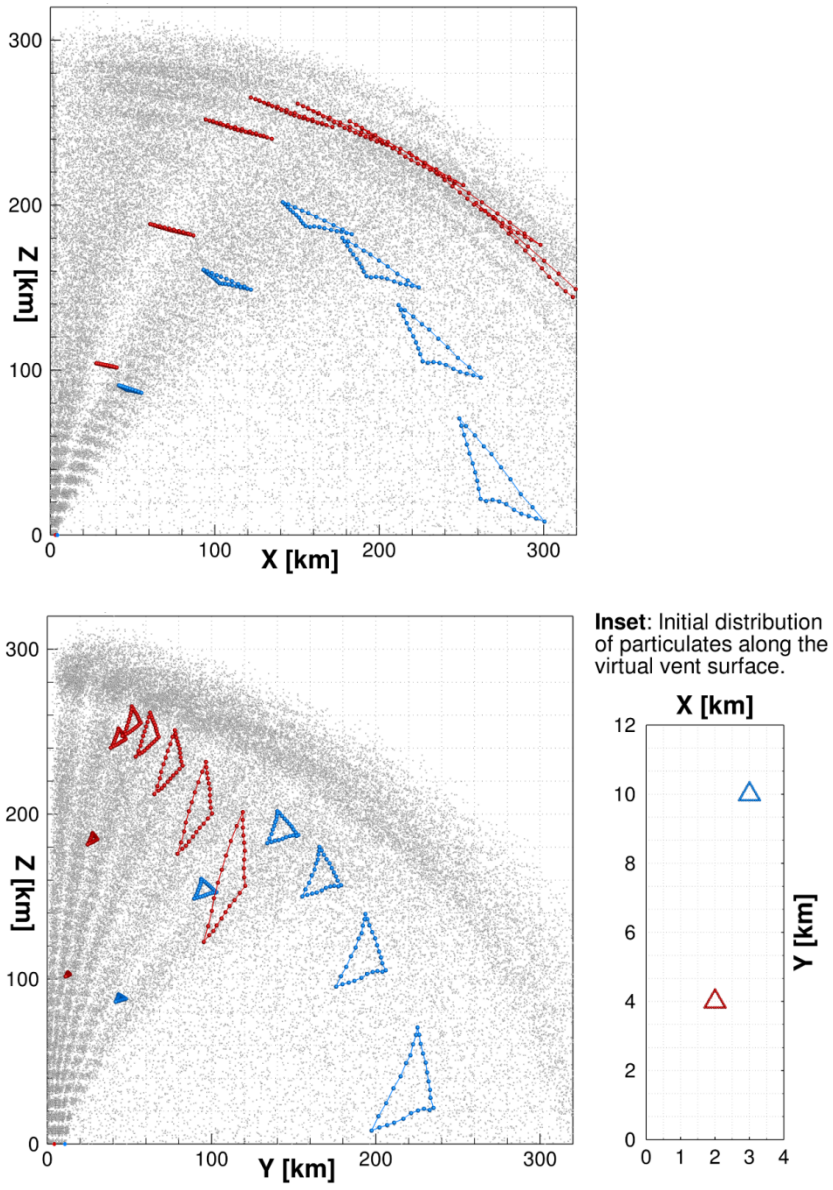

Figure 4.6: Flow-tracking dust particles in a Tvashtar plume of uniform gas flux, viewed in the X-Z and Y-Z orientations. The particles in gray are the same flowfield represented in the isometric view of Fig. 4.5. Superimposed on this background plume are the particle trajectories that result from injecting dust in equilateral triangles of edge length 600 m at two distinct regions within the first quadrant of the rectangular vent. Triangles are shown at 125 s intervals from launch to 1000 s (those in blue have fallen to the surface by 875 s). The original position of these test particles in the vent is shown in the inset, right. (Figure by P. Ackley).

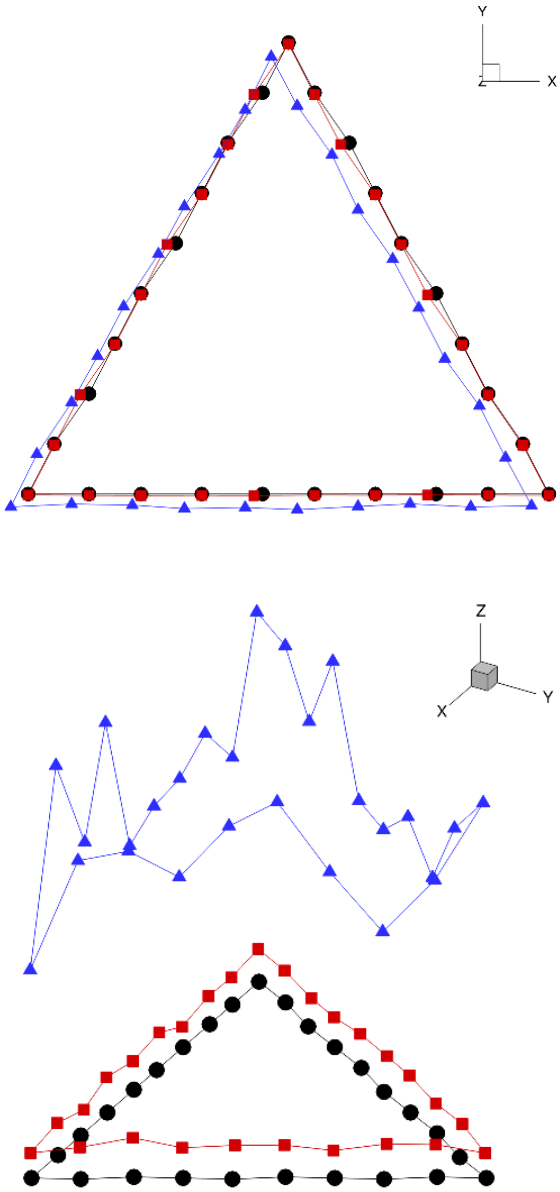

Figure 4.7: (Top), top view; (Bottom), oblique view. Positions of particles integrated forward in time through the DSMC velocity field over a 1000 s period, and then integrated backward in time over the same period. Particles shown as red squares move with a time step of 0.01 s, while blue triangles move at 0.1 s. Black circles are a reference, representing initial position of particles in the vent, for both colors, and their true final position in the limit of an infinitely small time step. The side length of the triangle formed by the black circles is 600 m. (Figure by P. Ackley).

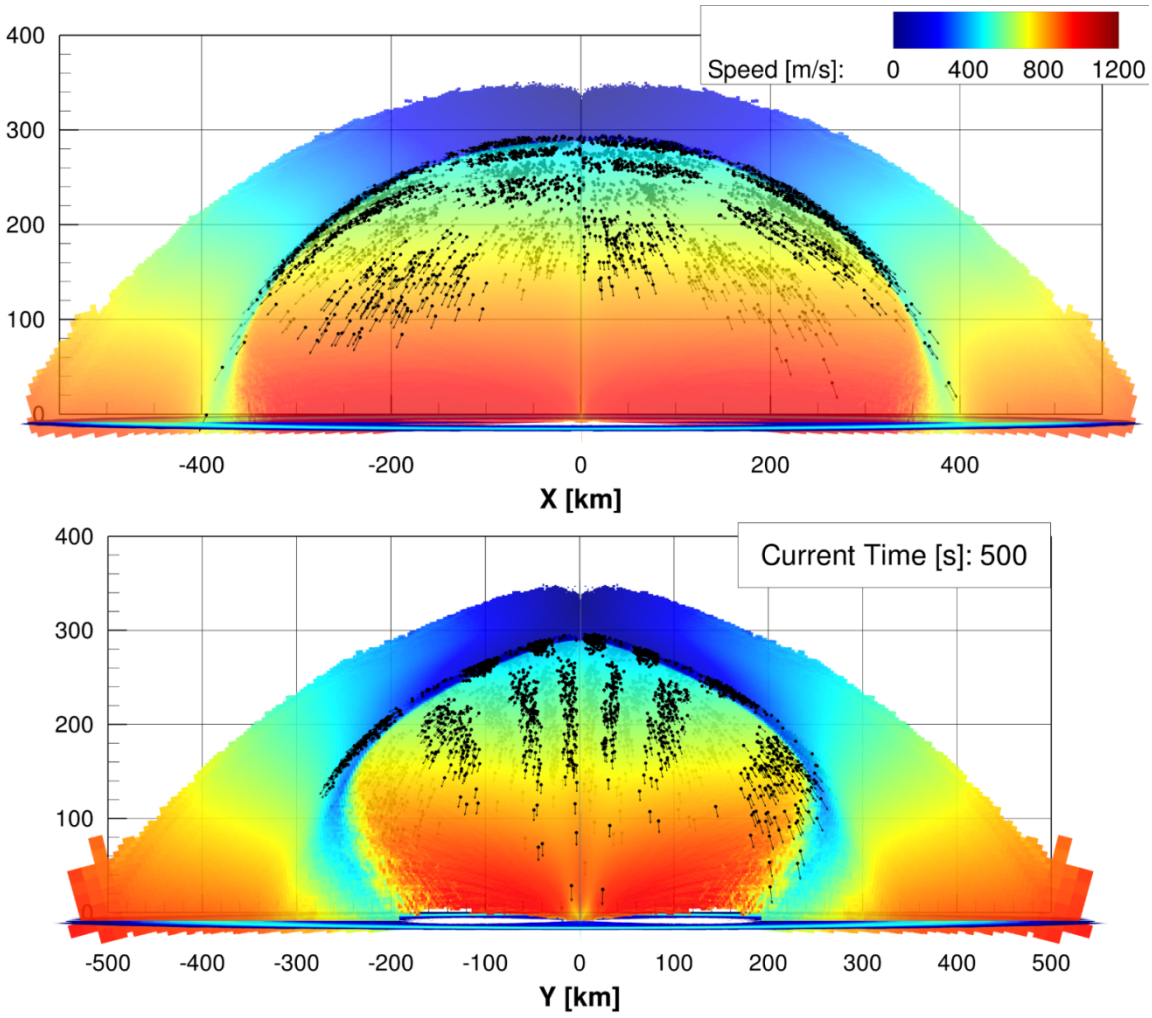

Figure 4.8: Contours of speed in the DSMC calculation are shown in the translucent X-Z and Y-Z planes. A single pulse of particulates is released from the vent in a spatially-variant checkerboard-sinusoidal mass flux function in a 60 s period. This pulse propagates through the plume, interacts with the canopy shock, and begins to disperse over 500 s. Visible striations and tendrils are observed to have formed in the canopy, particularly evident with line-of-sight oriented along the vent's narrow axis, i.e. looking at the Y-Z plane.

Figure 4.8 exhibits a case of interpretable structure while looking through the plume. A single pulse of test particles is emitted in a mass flux identical to that reflected

in Figs. 4.5 and 4.6, over one 60 s period. As those particles emanate from the vent and are carried into and swept along the canopy shock, they begin to disperse from their initially discrete packets, forming tendrils that are most visible along a line of sight parallel to the vent's broad axis. After ~500 s, all particles have reached the canopy, and are either on its near side (shown in solid black) or visible in faded black, as seen through the translucent planes. These planes are colored in bulk speeds as calculated in the DSMC, and shown in the X-Z (narrow) and Y-Z (broad) vent axes: note the sharp gradient in speed at the canopy shock interface. Only cells with sufficient resolution in representative DSMC molecules for confidence in the gas field result are illustrated; that threshold is taken here to be 10 / cell / time-step.

In addition to serving as a method for validating the size of the time step, the ability to integrate particles backward in time can be used to directly connect length scales observed in the plume with length scales at the vent. To do this, a structure in the Tvashtar images (Fig. 4.1) could be identified and the spatial coordinates of its constituent particles relative to the vent could be deduced geometrically. Then, these particles could be integrated backward in time to determine their initial positions in the vent. The primary difficulty in executing this strategy is the ambiguity in depth-of-field that arises when viewing a three-dimensional plume as a projection on a flat plane. In reality, the Tvashtar plume is three-dimensional, but the images in Fig. 4.1 are two-dimensional, consisting of pixels that are the result of line-of-sight integrations of particles in the plume. Thus, when we identify a structure in these images, we cannot be sure of the true depth of its constituent particles. However, this is mitigated by the fact that the majority of particles in this type of plume are found in the thin outer 'shell' of the collisional canopy shock. The tilt of the plume away from the observer in the LORRI images and the movement of NH between frames could in principle resolve this problem.

4.7 CONCLUSIONS

A process is described by which the spatial and temporal scales of structure in Tvashtar's transient canopy may be simulated and traced back to their origins at the vent. DSMC is applied in steady and asymmetric simulations of the Tvashtar plume; these results are applied to generate test particle trajectories through a sampled velocity field. The results presented in this work reflect a flow-tracking particle model in which dust is entrained in the bulk gas motion. In even this simplified model, complex filamentary structures and tendrils that echo those observed at Tvashtar are reproduced with simple variance in the parameters of dust emission at the vent. However, the influence of dust-gas velocity slip and drag may be significant, as demonstrated in McDoniel *et al.* (2015).

The next chapter will explore the results of high-resolution DSMC simulations with steady gas flowfields and unsteady dust influx at their sources. These spatial and temporal scales are informed both by analysis of the Tvashtar images and by the results of the test particle code.

Chapter 5: Parametric DSMC Simulation of the 2007 Tvashtar Plume

5.1 Chapter Overview

Chapter 4 outlined a two-part hybrid method by which the Tvashtar gas field is modeled first in steady-state DSMC calculations, then passed to a particle-tracking code that simulates spatial and temporal variance in particle release from the vent. We demonstrated in the preliminary results of that chapter our model's ability to trace structure forward and backward through the gas field, and its utility in representing a range of canopy structures similar to those observed by the New Horizons (NH) probe in 2007 (i.e. filamentary structures and traveling notches). However, the results of the particle-tracking code are entirely dependent on the input DSMC gas field, which is itself shaped by the boundary condition at Tvashtar's source. Unfortunately, this boundary is under-constrained: NH only briefly transited the Jovian system on a gravity assist, and so it did not capture detailed Ionian surface imagery (e.g. like that of Galileo, Fig. 4.2).

In order to produce DSMC flowfields representative of the observed properties of the 2007 Tvashtar eruption, I varied the thermodynamic and geometric parameters of our simulated Tvashtar vent through a range of parametric simulations, and derived novel constraints on conditions at the virtual vent. This process included the implementation of a condensation / sublimation model for particle growth through the Tvashtar plume in the particle-tracking and DSMC codes, the revision and updating of a model for opacity in SO_2 flows initially developed by Zhang (2004), and the analysis of DSMC simulations across a range of aspect ratios and vent configurations. These calculations are performed through four stages each and at much higher resolution than my previous work, which was necessary to resolve high aspect ratio vents at the surface level. Throughout this

chapter, I will primarily discuss parametric variation of aspect ratio: rectangular vents with ratios of 1, 3, 10, and 15 are considered as potential Tvashtar sources while all other parameters (temperature, density, mass flow, Mach number, and source area) are held constant at values motivated by observational constraints.[28] The boundary conditions of the DSMC Tvashtar simulations discussed in Chapters 4 and 5 are compared in Table 5.1.

An analysis of the gas-field and particle-tracking results has allowed us to select one of the parametric cases as a most likely fit to the 2007 NH observation: the aspect ratio 3 (AS-03) case in a lava-lake configuration with vent temperature ~1287 K, which is consistent with the range of direct vent constraints in the literature, i.e. Spencer *et al.* (2007) and Rathbun *et al.* (2014). This result also matches the indirect constraints of gas canopy height and condensate particle size distribution reported by Jessup and Spencer (2012) via HST observation. The AS-03 result is likewise consistent with NH imagery – I have processed the available Ionian surface imagery captured by New Horizons and use it to develop new depositional ring constraints on the 2007 eruption, including elliptical fits to the dark/light ring interface consistent with a source region of aspect ratio less than or equal to 3. I also suggest a method by which the slope of canopy descent along the canopy minor axis can be related to vent aspect ratio, and show preliminary results linking candidate NH images to the shape of the simulated AS-03 gas canopy. In confirming the selected thermodynamic conditions, I have simulated an additional, four-stage plume at vent aspect ratio 3 from an alternate, cooler source condition of ~1240 K suggested in Rathbun *et al.* (2014) and I demonstrate that this configuration produces a

[28] These four cases are in addition to the case described in Chapter 4, with thermodynamic conditions like those for Pele in the work of Zhang (2004), and the alternate AS-03 case discussed in this chapter for which I explore source temperature variance within the range of Rathbun *et al.* (2014). There are a number of additional cases I tested, across thermodynamic conditions that proved less convincing matches to the NH / HST observations of 2007 Tvashtar, that are not discussed in this dissertation.

canopy inconsistent with the height and depositional ring radius of the 2007 NH observation – unlike the higher-temperature AS-03 case. Finally, I have developed an alternate hypothesis for the NH observations of canopy unsteadiness in the Tvashtar plume – transient perturbations in the structure of the gas canopy shock itself, borne along with the bulk gas flow, produce apparent travelling notch-like structure and may even grow unstable, inducing temporary canopy collapse.

5.2 SELECTING VENT CONDITIONS FOR REALISTIC TVASHTAR SIMULATIONS

5.2.1 Observational Constraints on Vent Conditions

Constraints on the selection of Tvashtar's 2007 vent parameters are few. From Spencer *et al.* (2007), a single-temperature blackbody fit to LEISA observations of the source at ~1287 K provides a lower bound for magma temperature within the range of basaltic volcanism characteristic of the region's recent prior eruptions (e.g. as viewed by Galileo; Milazzo *et al.,* 2005). Spencer *et al.* suggest a hotspot of 49 km^2 and 1200 K as a likely match to the Tvashtar source, centered at 62.5° N, 122.5° W. Rathbun *et al.* (2014) report point-brightnesses from three distinct LORRI observations of three points each, scattered along circa 20 km and nearly parallel linear tracks (Figs. 5.1 and 5.2), and offer two potential fits to the Tvashtar source: either ~1280 K from 30 km^2, or ~1240 K from 50 km^2. Rathbun *et al.* posit that the vent was in a 'lava lake' configuration at the time of the 2007 observation (i.e. extended along Io's surface, and not erupting as an explosive fire fountain) due to the cosine dependence of power output on emission angle. The various eruptions observed by Galileo and Cassini between 1999 and 2001 were likewise characterized by eruptions along a series of long, high aspect ratio fissures throughout the Tvashtar region (i.e. Galileo images: Fig. 4.2), although several were fire-fountains.

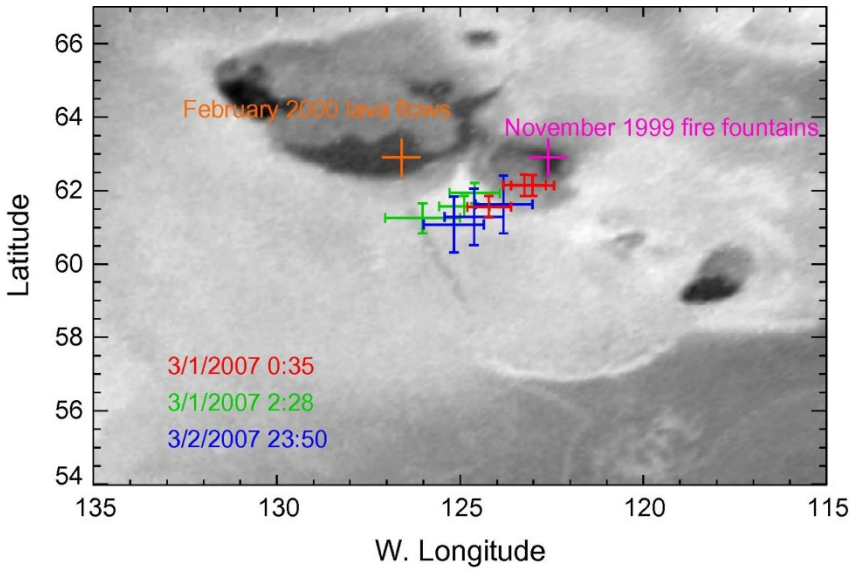

Figure 5.1: "Location of Tvashtar eruption locations overlaid on the SSI basemap." Orange and pink points mark Galileo-era eruptions, the source regions of which are shown in Fig. 4.2. The NH LORRI point-brightness observations are shown – with their associated uncertainties in latitude and longitude – in red, green, and blue. Figure from Rathbun *et al*. (2014).

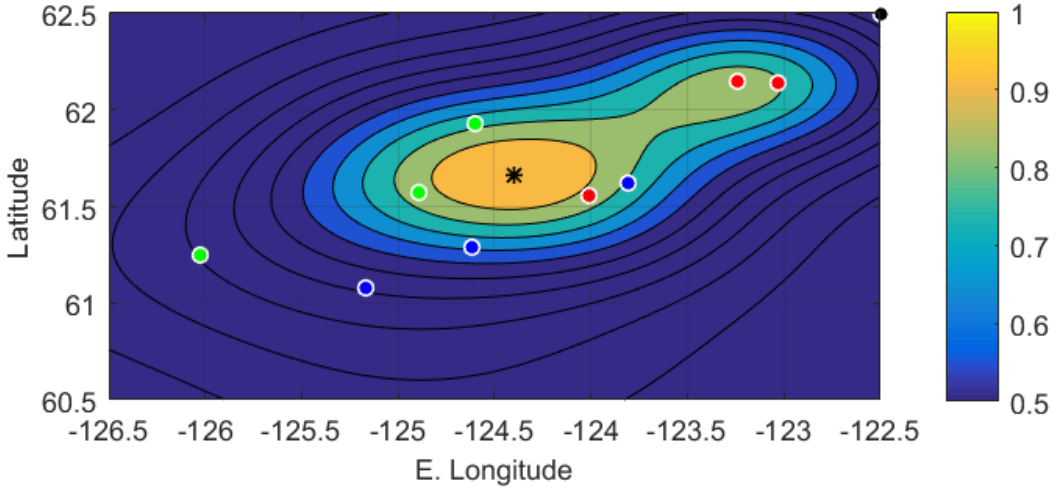

Figure 5.2: Red, green, and blue mark the NH LORRI observations; contours show the normalized sum of unit-volume Gaussians centered at each, applying reported uncertainties as standard deviations in latitude and longitude. The 'most probable' hotspot location by this metric is 61.7° N, 124.4° W, and marked with a black star. For comparison, the black point at top right is the hotspot location predicted by Spencer *et al.* (2007) for the same observation.

Jessup and Spencer (2012) report an inferred column density of O[10^{21} m^{-2}] disk-averaged using a peak gas canopy height of 460 km, and estimate a total of O[10^8 kg] SO_2 aloft during the HST observations of the 2007 Tvashtar plume if its ratio of S_2/SO_2 is taken to be lower than 0.05. These cases correspond to mass flow rates between 50,000 and 160,000 kg/s SO_2, which are consistent with the flow rates of the various Pele configurations of comparable class to Tvashtar simulated by Zhang (2004) and McDoniel (2015). Taken together, we have linked constraints on source area and temperature, a loose expectation of high (or at least non-unity) aspect ratio in a distributed horizontal 'lava lake' configuration, and an indirectly-derived constraint on mass flow rate. We will need to motivate additional selections to close this system in source boundary conditions – i.e. exhaust velocity and density.

As reviewed in Chapter 4, McDoniel's model for the DSMC Pele source is of a 'virtual vent' surface O[1 km] above the lava lake at which emissions from a broad field of small fissures or holes have converged to form a homogeneous Mach 3+ front. This is consistent with observations characterizing Pele's source as relatively low in active area, i.e. with a ratio of gas-emitting surface area to total surface area of ~0.1 (Davies, 2007). In this work, we likewise assume that gas at the lake surface is in thermal equilibrium with the lava and that it will expand rapidly to a Mach 1.0+ condition given the near-vacuum ambient atmospheric pressures. However, without constraints on the ratio of active to inactive lake surface at Tvashtar, we cannot simulate the expansion from small-scale structures exhausting at the sonic condition to a homogenous, supersonic virtual vent surface. Instead, we simulate directly from a virtual vent at the sonic condition itself, assuming that the Tvashtar source has a *high* active area (i.e. of nearly 1). This could reflect complex transient structure in the lava lake surface, like the roiling bubbling of a terrestrial analog lava basin – e.g. Nyarigongo (Lopes *et al.,* 2004) – or the 'waves'

through resurfacing lava at the Ionian Loki site suggested by de Kleer *et al.* (2017). Given a source temperature and area, I therefore model flow from the virtual vent as having expanded to Mach 1.0+ (in practice, to a condition slightly above the sonic, generally M≈1.02) with its stagnation temperature that of the lava observation, and its velocity oriented normal to the vent surface. In prior work, Zhang (2004) and McDoniel (2015) have shown that the structure of a plume's collisional canopy shock is generally insensitive to density if the plume can be modeled as optically-thin, provided that the vent ejects sufficient material to form a collisional canopy in the first place. McDoniel (2015) presents a simple analytic argument for plume height as a function of vent stagnation temperature, spreading angle, and gravity; however this model is less useful for non-axisymmetric plumes which have no unique spreading angle, and it neglects the effects of radiation from the rotational and vibrational states of individual molecules to the black-body of space. In selecting a source density, I varied source mass flow rate and temperature to match indirect constraints of gas canopy height in a range of simulations not otherwise described in this dissertation. Jessup and Spencer (2012) suggest gas canopy heights for Tvashtar between 360 and 460 km, while the New Horizons images reflect dust canopy heights of a somewhat lower altitude (320-360 km). This discrepancy is to be expected; drag on dust particles will result in their formation of a distinct and interior canopy (Zhang, 2004; McDoniel, 2015). The gas canopy heights for the range of aspect ratios examined in this parametric study fall between 380 and 430 km.[29]

Table 5.1 lists the boundary conditions selected for the simulations discussed throughout this Chapter, as well as the other Tvashtar-like cases seen in this work.

[29] The definition of 'canopy height' might be the gas flow canopy shock surface (as a lower boundary), or an upper boundary at which the gas suspended atop the canopy shock layer falls below some arbitrary level in density (i.e. <5 % of the value after the jump). Results for each DSMC calculation are listed in Table 5.3.

	AS-01	AS-03	AS-10	AS-15	AS-03 Alt.	RGD
Vent Aspect Ratio:	1	3	10	15	3	3
Major Axis [km]	2.739	4.743	8.660	10.607	6.123	12.5
Minor Axis [km]	2.739	1.581	0.866	0.707	2.041	4.0
Vent Area [km^2]:				30	50	200
Mass Flow Rate [kg/s]:				2.00×10^5	1.00×10^5	1.09×10^5
[30]**Stagnation T_0 [K]:**				1287	1240	1500
Mach Number:				1.0+	1.0+	~ 3.0
Translational T [K]:				1120	1080	500
Normal Velocity [m/s]:				440	430	850

Table 5.1: The boundary conditions of the various Tvashtar-like simulations discussed throughout this work (Chapters 4 and 5). Conditions in **bold** are those for which I have an observational constraint or physical assumption, and those in *italics* are the actual inputs into the DSMC generation routines. Lengths reported are for the vent geometry in the symmetric quadrant.

5.2.2 Configuration of Parametric Domains

Calculations are performed in nested stages, each of which is computed to a steady state condition. As simulation particles cross the stage boundaries, they are deleted as though they had crossed a vacuum boundary, but their information is stored and later sampled to provide the boundary flux into the next stage. The result for each parametric case reflects a four-stage calculation for which the generation and staging processes are very similar to those described in the previous chapter. Excepting the source dimensions,

[30] The virtual vent condition applied in the RGD case is consistent with the expansion of flow from small, adjacent fissures in a low-active-area lava lake at T_0 1500 K to a homogeneous virtual vent surface. The details of these simulations are found in Section 4.2 of McDoniel (2015).

all inputs are identical for Stages 1, 2, and 3 at each aspect ratio. In Stage 4, however, there are minor changes between cases made in an effort to produce the best possible resolution in the canopy of each. These include manual tweaks to processor counts and locations, e.g. uses of a dedicated polar cap, and modifications to F_{NUM}, gridding in the altitude coordinate with linear segments, application of a radial weighting scheme to preserve resolution along the symmetry axis, and small differences in the lengths and manners of time-averaging. Table 5.2 provides domain configurations characteristic of these simulations. While any individual four-stage calculation is of O[10^4] CPU-hour expense, the entire range of simulations necessary to settle on thermodynamic conditions for the source and to select domain parameters that adequately resolved flow length and time scales was an O[3×10^5] CPU-hour exercise. As in Chapter 4, all calculations are performed in a single quadrant, exploiting the symmetry axes of the rectangular vents.

	Stage 1	**Stage 2**	**Stage 3**	**Stage 4**
Time-step [s]:	0.025	0.1	0.25	0.25 to 0.5
Total time [s]:	45	180	450	3,600+
F_{NUM}:	1×10^{22}	2×10^{22}	6×10^{22}	6×10^{23}
Domain radius [km]:	12	20	200	750
Domain height [km]:	6	30	80	400
Processors:	408	528	768	769
Mols. / processor:	1×10^6	8×10^5	8×10^5	1×10^6
Cells / processor:	5×10^4	5×10^4	5×10^4	3×10^4
CPU-hours:	**1,600**	**1,600**	**2,400**	**6,000+**

Table 5.2: The simulation and domain parameters for each stage of a full calculation.

5.3 THE 3-D DSMC DOMAIN FOR TVASHTAR SIMULATIONS

5.3.1 Simulation of the Vent Near-Field: The Inner Stages

The three inner stages of the DSMC calculation contain the initial expansion of the gas and capture its early axis switching; therefore, it is critical to resolve them well in space and time. The small size of each inner domain relative to the length scales of the canopy structure is necessary to resolve flow gradients, and to capture the complex shapes of both the *opacity surfaces* and the innermost *sublimation surface*.[31] The opacity surfaces bound regions in which the plume is sufficiently thin for its molecules to experience radiative loss from their vibrational states. Within the innermost sublimation surface, condensate particle sublimate more rapidly than they grow; Tvashtar's brightness and visibility in the LORRI observations of light scattered from suspended particles are dependent on the size of these particles and thus sensitive to this limiting surface.

5.3.1.1 Stage 1: The Virtual Vent

The first stage contains the source region itself. In the high aspect ratio limit the vent's elongation can prove difficult to resolve adequately in space, given our spherical coordinate system and polar-axis centered domain with two planes of symmetry. Adaptive gridding is necessary to capture these vent shapes and preserve their sharp edge and corner boundaries; in this work, 408 processors with 50,000 cells each are applied in each inner stage. Defining the cell characteristic length scale L_{cell} as the cube root of volume, stage 1 L_{cell} values are of order 10 m with the smallest values concentrated in the regions directly above the source. At steady state, the grid is distributed such that each processor contains O[10^6] simulation particles, for an average of 20 per cell per time-

[31] These processes are discussed in more depth in the following sections, i.e. 5.3.2 and 5.3.3.

step; a time-step of 0.025 s is selected such that particles will transit no more than one cell per step and can resolve their most restrictive radiative timescales. For a Pele-class plume, the SO_2 mean free path at the vent can approach millimeter scale – the resolution of which would prove computationally intractable in a DSMC calculation that ultimately extends to thousands of km. However, flow density gradient length scales even within this first stage are generally of order 100 m or greater, and minimally O[10 m] along the vent's edges. These scales are spatially resolved in each stage 1 grid and calculated as Equation 1.3. Figure 5.3 shows the processor decomposition over the source region for the aspect ratio 10 case (AS-10), viewed on the surface plane and colored by number density. Each region demarcated in white represents a single processor, which will contain O[10^6] simulation particles among 50,000 cells, with some 100 cells distributed in θ and φ. At the pole, a processor 'cap' prevents cells from shrinking to infinitesmal size (McDoniel, 2015; Prem, 2017). Note the sharp boundaries at the edges and corner, as adaptive load-balancing has preserved the rectangular source geometry to O[10 m] scale.

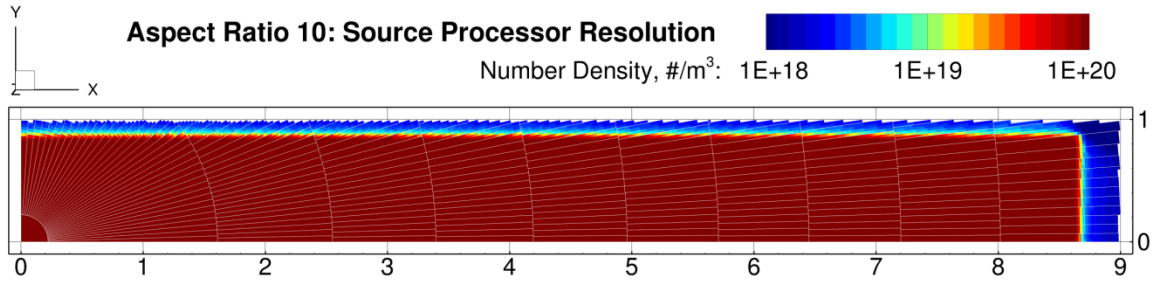

Figure 5.3: The processor decomposition over the source region for AS-10; lengths in [km]. Though processors are adaptively load balanced in θ and φ coordinates, they are shown to resolve the source's sharp edges.

The gradient length scale (Eqn. 1.3) throughout the first stage is shown in Figure 5.4 for the AS-10 case. Density gradients are steepest near the surface and at the edges of the vent, where their length scale approaches O[10 m]; by the stage 1–2 interface at 6 km altitude this value has stretched to >O[1 km] throughout the flow.[32] Mach number and density in stage 1 are shown in Fig. 5.5 for the same case. Flow expands from M=1.0+ at the vent to M>3.0 at 6 km and likewise begins to 'axis-switch' – such that the vent's major axis aligns with the minor axis of gas extent, and vice-versa – within this distance.

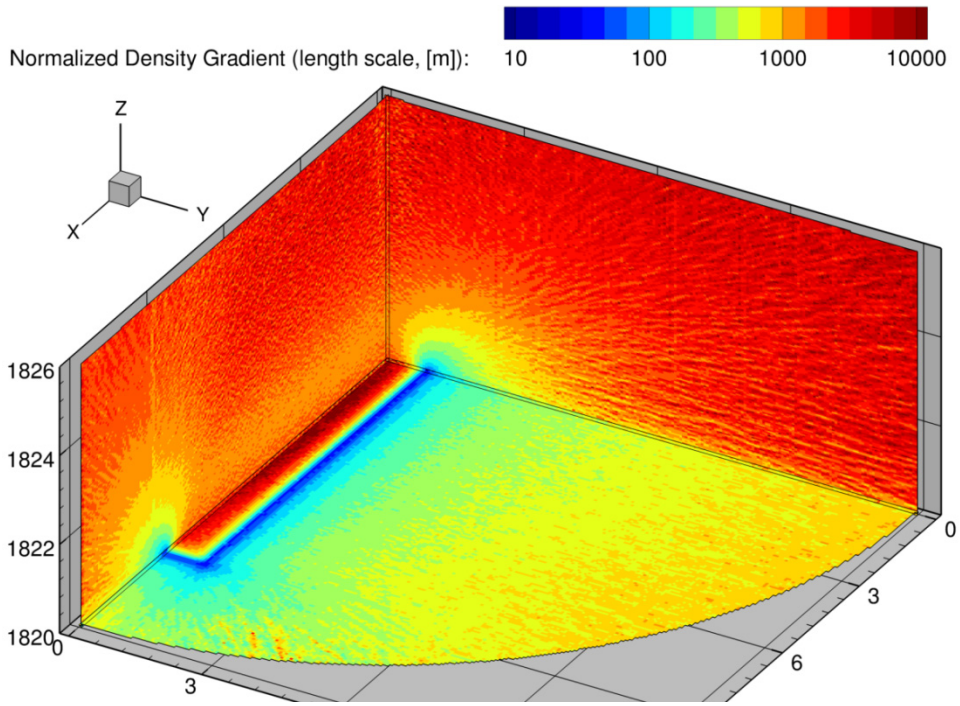

Figure 5.4: Contours of the density gradient length scale in an AS-10 inner stage. Along the edges of the vent $L_{gradient}$ reduces to O[10 m] but is never smaller than the calculation's cellular resolution length scale L_{cell}. Above the source, rapid expansion into vacuum promotes gradient length scales of O[1 km].[33]

[32] While gradient length scales at vent edges are on the order of local cell size, this may be because cells are too large to resolve finer gradients – at sharp edges and corners, we expect gradients to approach the MFP. However scales *everywhere else* in stage 1 are much larger than local cell sizes, which is reassuring.

[33] In future work, it may be prudent to link a continuum solver for stage 1 calculations – or at least the adiabatic region inside opacity surfaces. Knudsen numbers relative to either density gradient or vent scales are quite low in stage 1, ranging from 10^{-8} to 10^{-6} at the vent to 10^{-4} at the upper boundary.

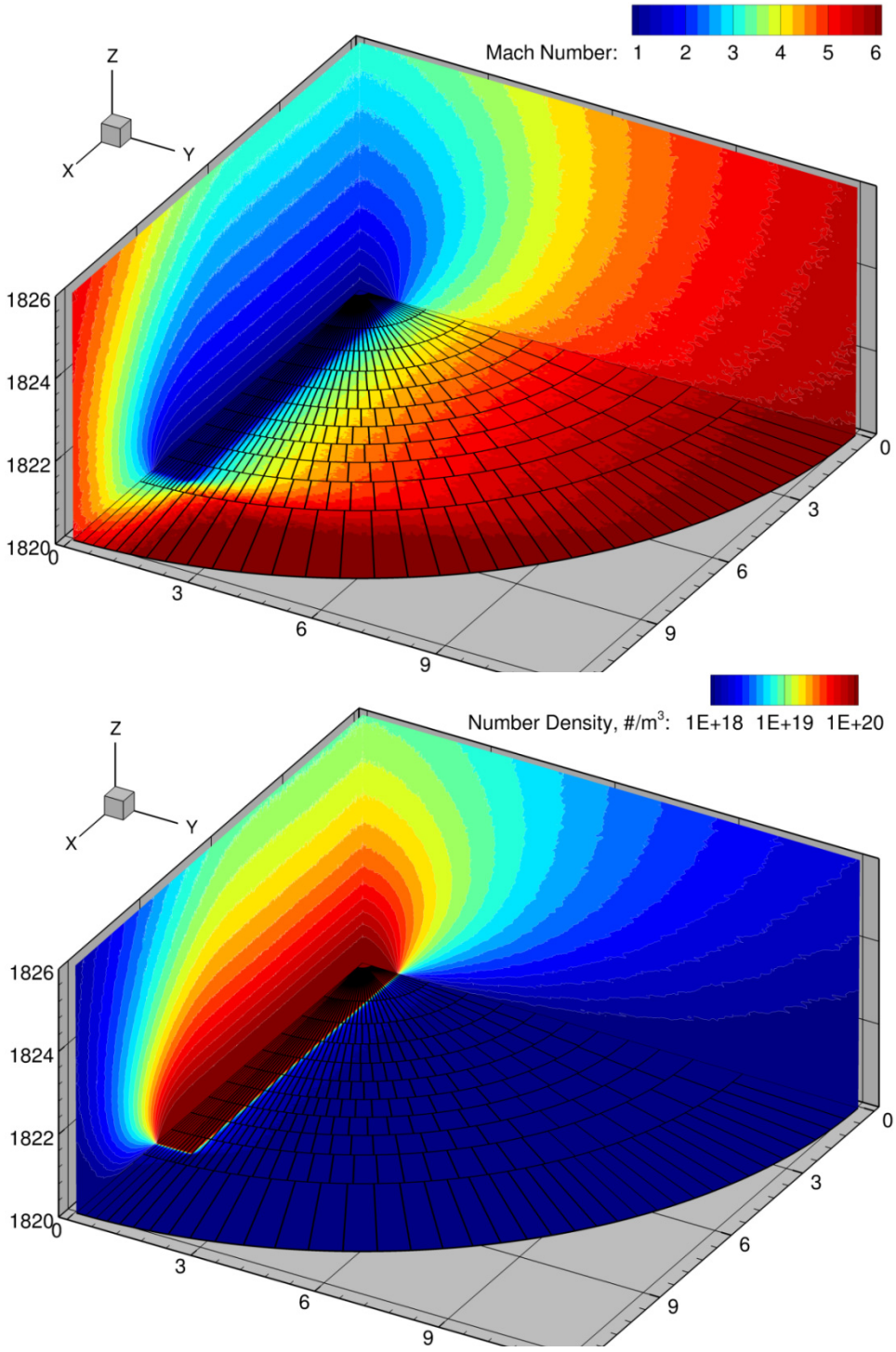

Figure 5.5: (Top) Contours in Mach number: in the first stage of the aspect ratio 10 (AS-10) case, flow expands rapidly from M=1.0+ at the vent to supersonic conditions. (Bottom) Corresponding contours in number density.

5.3.1.2 Stage 2: Modeling Gas Opacity

The second stage of the calculation, seen in Figs. 5.6 and 5.7, extends 20 km in radius and to 30 km altitude. It encompasses the majority of the 'opacity surfaces,' within which the flow is not optically-thin, and molecules are not permitted to radiate from their vibrational modes. The stage-to-stage patching condition is only valid if no information can physically propagate from the outer stage back into the inner stage; the flow must not only be supersonic, but it must be supersonic in the velocity coordinate normal to the boundary. This is a particularly important distinction in stage 1: for high aspect ratio source configurations, flow expands rapidly along the vent's initially narrow axis and thus at low altitudes will travel almost parallel to Io's surface.[34]

Recent work has included the implementation of a physical model for limiting radiation from SO_2 vibrational modes to appropriately optically-thin regions of the flow, adapted from Zhang (2004) and rewritten for the current version of the planetary DSMC code. Each cell structure now carries instantaneous translational temperature and information necessary to efficiently compute a local photon mean free path that can be compared to a flow characteristic length scale. A reasonable length scale to select might be the radius of curvature of the flow's opaque region, but it is variable and difficult to calculate on-the-fly in these inherently stochastic simulations. I instead select a constant scale of 1 km (on the order of the vent edges). Three opacity surfaces exist, each corresponding to a specific SO_2 vibrational band: inside each surface, the corresponding band will not radiate because spontaneously emitted photons are reabsorbed before they can escape. The opacity model acts as a switch, only permitting radiation from the

[34] Given too low a selected altitude for the stage 1 – stage 2 interface, the resultant Mach number normal to the upper boundary's surface might well be subsonic toward the domain edges. In any case if the flow into a new stage is *not* supersonic normal to the wall, material from the outer stage will be pushed unphysically into the inner stage, the geometry of which is empty. Exotic sprays and jets will form and may eventually interfere with canopy structure.

vibrational modes of particles that occupy optically thin regions of the flow, above the dense and bright source region. It is an improvement to prior work on Tvashtar, as it allows for the retention of energy that would otherwise be unphysically lost, substantially changing both the canopy height and structure of the spout.

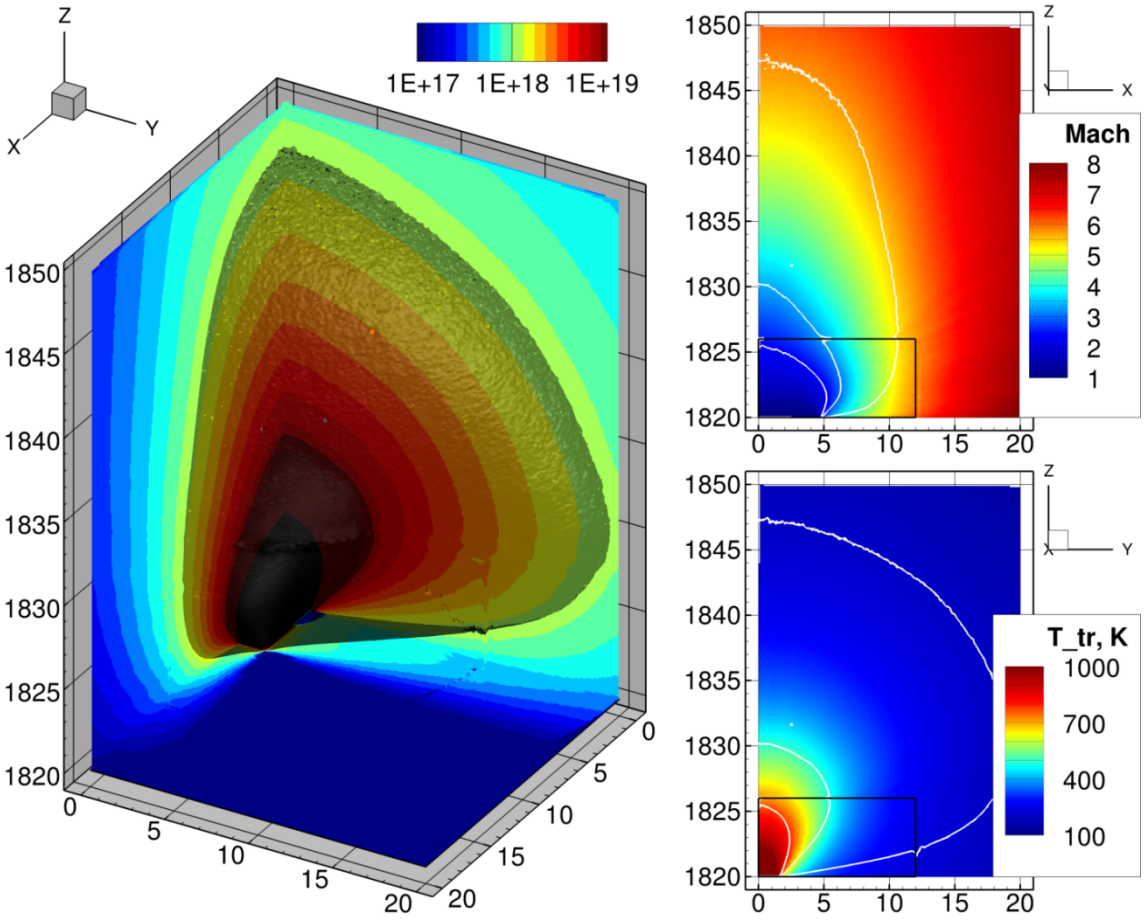

Figure 5.6: Stages 1 and 2 are shown for the aspect ratio 3 vent condition (AS-03). Opacity surfaces are colored in dark isocontours at left, and drawn in white on the symmetry planes at right. All lengths shown are in kilometers.

The effects of gas opacity on canopy height and extent are pronounced: the model's effect is to account for the physical effect of energy remaining trapped in the flow in the vent region, and so it results in higher canopies and more distant depositional rings. It should be noted that the opacity model can also make a canopy's height and extent dependent on its source mass flux: the absorption rate calculation shows a linear dependence in number density. In a calculation that either neglects opacity effects and thus radiates everywhere or, alternately, models a flow too cold to significantly populate vibration (e.g. cryovolcanism), prior work within our group has demonstrated that canopy and shock configurations are generally insensitive to changes in density, so long as the vent emits sufficient material to form a collisional shock in the first place. Figure 5.6 demonstrates the influence of this opacity model within the first two stages of the AS-03 calculation. At left, the opacity surfaces for each vibrational band are shown as dark, translucent isosurfaces. In the background, the symmetry and surface planes show color contours of number density. Note the axis switching effect: the gas field expansion, and the most extensive opacity isosurface, align with the vent's minor axis. To the upper right, color contours of Mach number in the X-Z symmetry plane are viewed normal to the vent's major axis. The white lines denote the intersections of the opacity isosurfaces with the symmetry plane, and the black box represents the boundary between the calculation's first and second stage. The flow expands rapidly from its Mach 1.02 condition at the vent, and is everywhere supersonic normal to the stage 1 boundary. Below this, the translational temperature in the Y-Z symmmetry plane is viewed normal to the vent's minor axis. The gas field expansion is broadest in this plane. Note the rapid decrease in translational temperature outside the first and second opacity isosurfaces: as the gas begins to radiate from its vibrational modes, it cools quickly in translation and rotation as well, given that flow mean free paths at these altitudes are of centimeter scale

and thus the gas is quite collisional. Figure 5.7 shows the variation in gas structure with increasing aspect ratio, including a pronounced shift in the steepness of opacity surfaces.

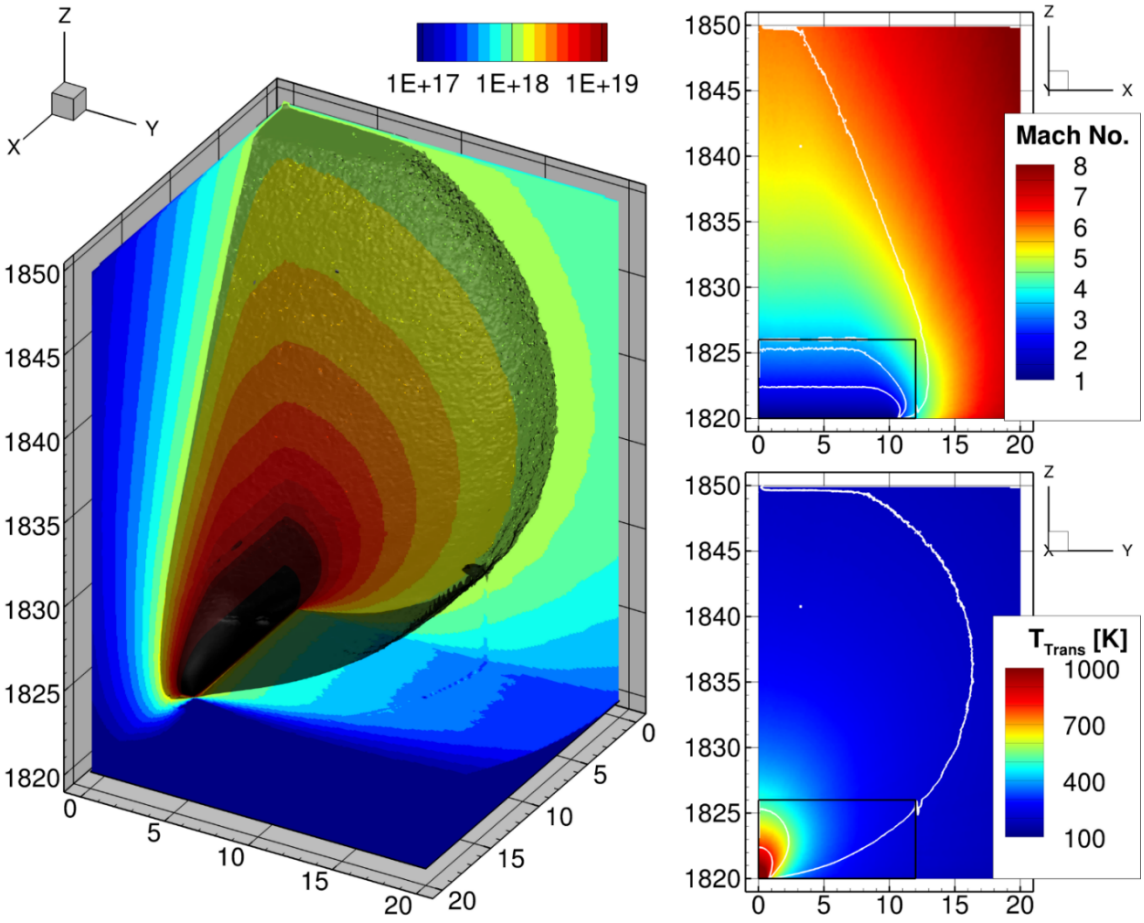

Figure 5.7: In the AS-15 limit, the inner opacity surfaces close just above the vent, as the gas axis-switches and rapidly expands along the vent's initially narrow direction. Translational temperature, viewed in the Y-Z plane and down the vent's narrow axis, is much lower with altitude than in the AS-03 case as much of the flow is optically thin in at least two vibrational bands within 4 km of the source.

5.3.1.3 Stage 3: Modeling Condensate Particle Growth

Within the canopy, a 'spout' structure rises up from Tvashtar's source; above that source the spout quickly rarefies, expanding to fill the canopy interior and decreasing in temperature and density with distance from the vent. At its edges, rising and falling material collide and form into the collisional canopy shock surface. Much of the lower spout is resolved in the third stage of these parametric DSMC calculations; the extensive width of this domain (which stretches 200 km along the surface) is critical in capturing the gas field's expansion, such that the final patch of boundary molecules into the outer stage is spread over the largest possible surface. This allows the processor distribution in the final domain – which is load-balanced on the basis of particles – to resolve the outer edges of the canopy and avoid clustering too tightly around the axis. The panels of Figs. 5.8(a-c) show several properties of the AS-10 case through the inner three stages on the familiar system symmetry planes. Fig. 5.8a shows the rising SO_2 spout structure in contours of number density: the flow has clearly 'switched axes' such that the gas field expands most broadly along the vent's minor axis. In Fig. 5.8b, contours of Mach number demonstrate that the initially M=1.0+ flow has expanded to a hypersonic condition by the stage 2 boundary at 30 km altitude, at which point the spout's gas core moves upward at ~1 km/s. High-velocity particles travelling nearly tangential to the surface make up most of the M>16 flow outside the spout, and will cause a two-spike velocity distribution when they eventually interact with and drive through the canopy, as discussed in Zhang (2004). Fig. 5.8c shows the growth rate for the radii of condensate particles; in the hot, dense region directly above the vent sublimation dominates condensation, and particles are unable to grow. The vertical extent of this sublimative region (i.e. to 60 km) is representative of each parametric-in-aspect-ratio case, and could help to explain the non-observation of clear lower spouts in most NH LORRI imagery of the 2007 eruption.

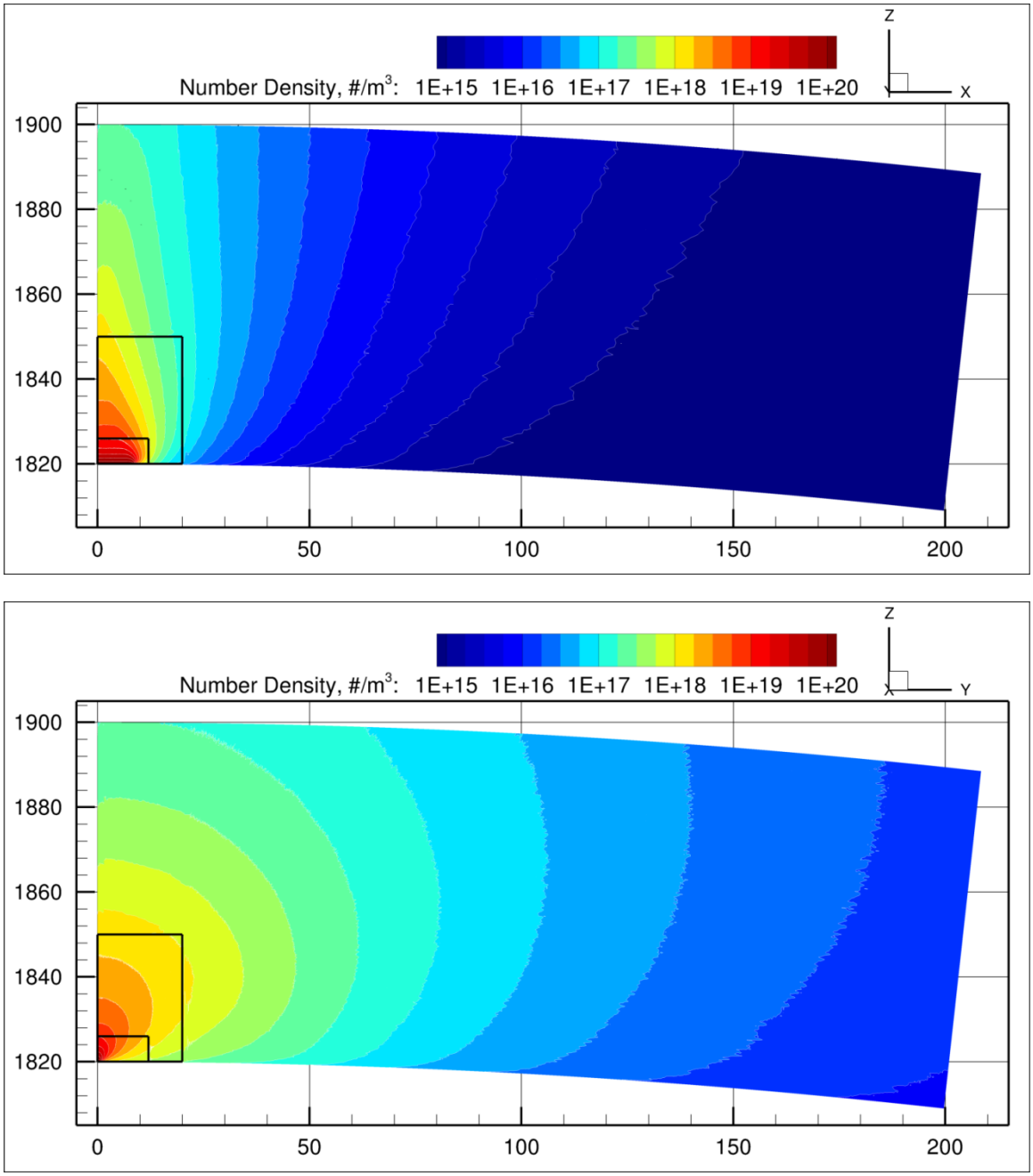

Figure 5.8a: Contours of number density in the three inner stages of the AS-10 case; the vent major ('broad') direction is aligned with the X-axis, while the canopy extends farthest along the Y-axis. The black lines mark the stage 1 and 2 boundaries.

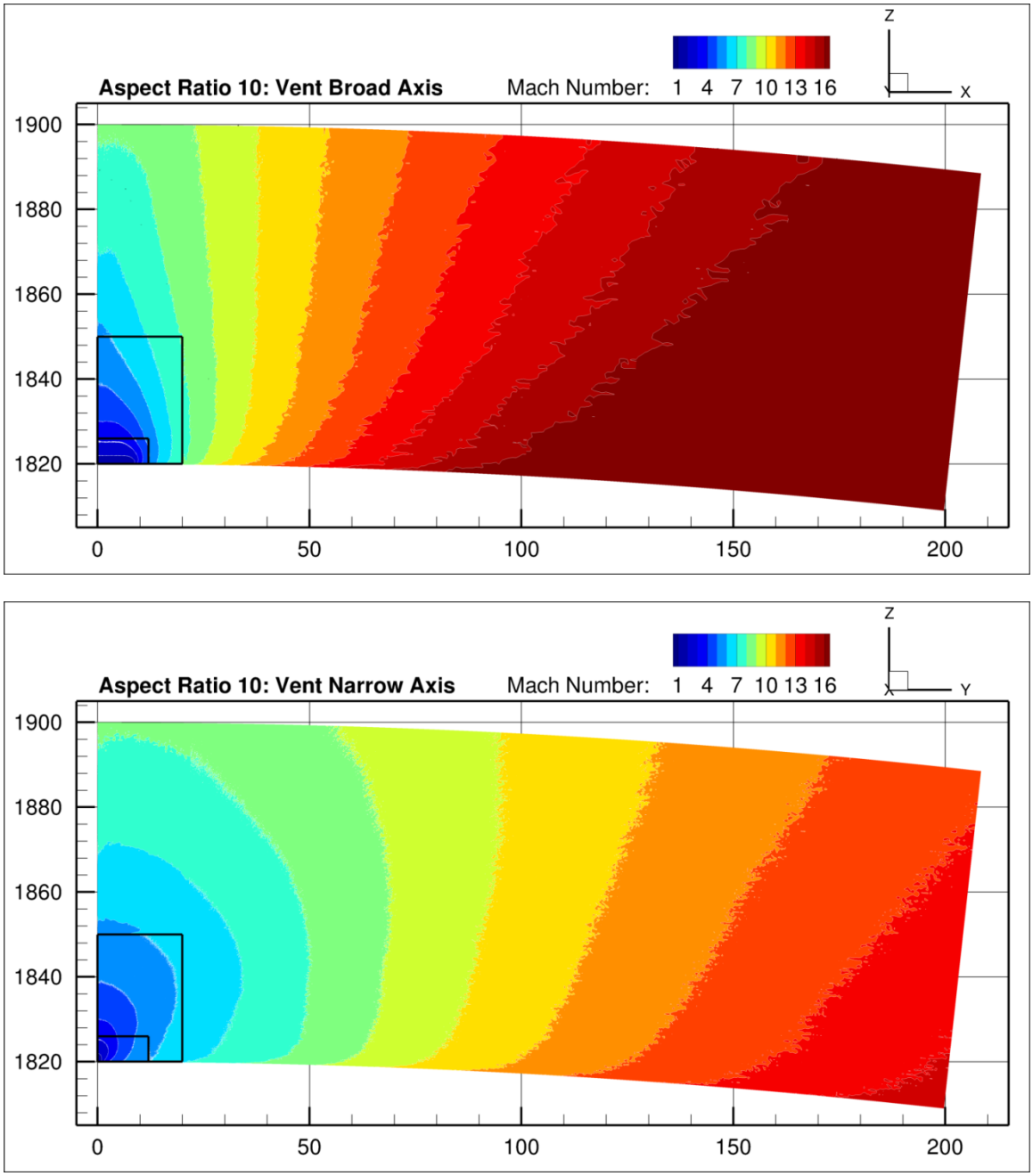

Figure 5.8b: Contours of Mach number in both symmetry planes of the AS-10 case for the inner three stages. As aspect ratio increases, this axis switching effect grows more pronounced.

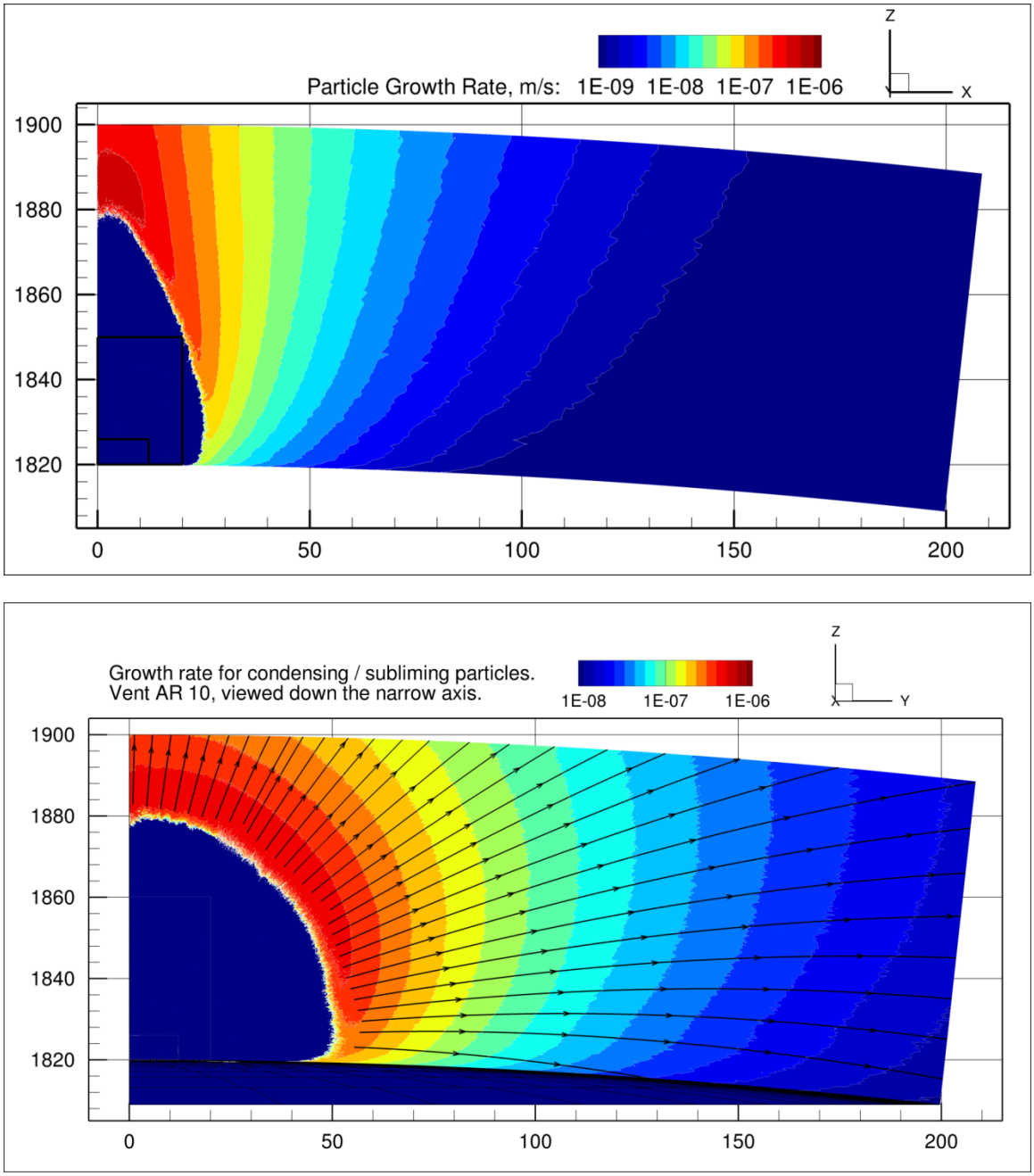

Figure 5.8c: Contours of condensate growth rate in the inner three stages of the AS-10 case. The inner 'sublimation surface' marks the boundary outside which the flow has cooled sufficiently to begin condensing into droplets; pathlines in the bottom figure show trajectories of such particles, which are modeled as though they are perfectly entrained with this gas flow.

We expect that some fraction of the visible suspended particles in the Tvashtar plume and canopy are droplets of condensed SO_2 that scatter incident light. Given some distribution of seed value sizes for grains at the vent, we can derive an analytic model[35] for the mass growth rate dm/dt of a condensate droplet dependent on the grain radius r_D, the gas density n, and the gas translational temperature T_{TR}, using kinetic theory equations for equilibrium flux through a surface to describe the number of expected incident molecules on a surface of the test-particle's droplet radius. This model assumes condensate particles that are perfectly entrained with the gas flow, and present in sufficiently low loading that their condensation does not deplete the background gas field. Furthermore, our model assumes that the gas through which the droplet travels is nearly Maxwellian. This is a reasonable assumption for these Tvashtar simulations, which exhibit Kn (based on scale height) that range from $< 10^{-3}$ at the sublimation boundary to no higher than 10^{-1} in the rising spout, and 10^{-2} or lower in the gas canopy. The growth rate could be modified by a 'sticking-coefficient' fraction that we take to be 1 in our model to bracket maximum droplet sizes. Mass growth can be related directly to volumetric growth assuming an even distribution of incident particles on the droplet, allowing the development of a differential equation for droplet radius growth (dr/dt) that can be solved with explicit numeric methods in the test-particle code:

$$\frac{dr_D}{dt} = n\sqrt{\frac{k_B m_{SO_2} T_{TR}}{2\pi {\rho_{SO_2}}^2}}, \tag{5.1}$$

[35] The same model applied in Yeoh (2015) for the growth of water ice droplets in the Enceladus plumes; here it has been adapted by P. Ackley and myself. The results of the condensation-sublimation model in the context of the hybrid particle-tracking code will be examined in more depth in our upcoming *Icarus* manuscript, "Hybrid Dust-Tracking Method for Modeling Ionian Volcanic Plume Observations," on which P. Ackley is first-author. Throughout this chapter I will primarily focus on my work in the DSMC simulations and gas-field constraints on its source, which will be the subject of its own *Icarus* manuscript.

in which ρ_{SO_2} is the density of liquid SO_2. As test particles move from the vent through the spout and into the plume canopy, they are given values of density and temperature as interpolated from a DSMC gas field solution, and their radius is tracked over time.

Why can't we see particles moving 'upwards' in the NH LORRI images? Perhaps they haven't grown sufficiently in Tvashtar's spout region, and only have time to grow while suspended in the canopy. We can expect two peaks in growth rate for a given test-particle released in the virtual vent: first in the high-density region directly above the vent, and secondly in the canopy suspension. Growth in the first region will be relatively rapid (highest overall number densities occur prior to the vent's expansion into vacuum), but may be limited by the very short time that particles spend in this region. Growth in the canopy may be limited by relatively low number densities vs. the lower spout – but particles in the canopy move quite slowly once they have interacted with the canopy shock and are thus suspended for a considerable time, especially those released from the vent center. Another process that may limit the visibility of spout particles is *sublimation* of condensed material in hot regions of the flow. If we model sublimation as a process of vapor pressure equilibrium with the Clausius-Clapeyron equation,

$$P_{vap} = Ae^{-\Delta H_{vap}/RT_{TR}}, \tag{5.2}$$

for ideal gas constant R, constant A, and enthalpy of vaporization ΔH_{vap}, the condensate growth rate can also model the sublimation of condensed material about particles as:

$$\frac{dr_D}{dt} = \left(n - n_{vap}\right)\sqrt{\frac{k_B m_{SO_2} T_{TR}}{2\pi {\rho_{SO_2}}^2}} = \left(n - \frac{Ae^{-\frac{\Delta H_{vap}}{RT_{TR}}}}{k_B T_{TR}}\right)\sqrt{\frac{k_B m_{SO_2} T_{TR}}{2\pi {\rho_{SO_2}}^2}}. \tag{5.3}$$

The values applied for SO_2 in the Clausius-Clapeyron model are $A = 1.52\times10^{13}$ Pa and ΔH_{vap} = 37.5 kJ mol^{-1}, consistent with Walker (2012). Note the exponential dependence of the growth-limiting n_{vap} term on translational temperature. One effect of sublimation on the condensate model is to limit (or perhaps entirely prohibit) growth in the spout; in the hottest regions of flow directly above the vent, particles cannot grow, as they effectively sublimate away any growth instantly in maintaining vapor pressure equilibrium. This is the effect visible in Fig. 5.8c. It is also a significant factor in the growth of particles in the canopy – as condensate particles reach the canopy shock, the steep jump in translational temperature across the shock creates a region of sufficiently rapid sublimative ablation to eliminate *any* condensate growth whatsoever that had occurred below the canopy. However, particles in this condensation-sublimation model will begin to grow again if they reach about 20 km above the shock surface, well within the extent of the suspended gas canopy. This effect is visible in Figs. 5.9, and also in 5.11(a,b). I find the limiting sublimation surfaces to be useful in characterizing the shape and extent of the spout and canopy regions, and refer to them throughout this work.

5.3.2. Canopy Formation in the Outer Stage

A canopy shock forms above the Tvashtar source as gas moving upward through the spout slows under the influence of Io's gravity, and begins to fall back into itself. This shock structure is stable and collisional, supported by the momentum balance between rising and falling material. Table 5.3 lists the canopy heights – defined directly above the vent at 1) the shock surface, at 2) the upper limiting surface at which condensation above the shock can begin to occur, and at 3) the maximum extent of the gas canopy at which density drops to <5% of the value just above the shock – for each of the four parametric-

in-aspect-ratio cases, as well as an alternate AS-03 case discussed in Section 5.4.3 and the case of Chapter 4; these canopy height values are accurate to within ±2 km. The table also includes the integrated SO_2 mass aloft for each full plume. Recall that each of the parametric-in-aspect-ratio cases has the same thermodynamic conditions at the vent. As a result, we see that they rise to the same gas canopy heights in each metric, and support the same mass aloft. This mass is a near match to the SO_2 mass aloft of 2.3×10^8 kg inferred by Jessup and Spencer (2012) for the 2007 HST observation of a wholly-SO_2 plume with source mass flux 1.6×10^5kg/s (the condition which most closely corresponds to our boundary condition). Likewise, the disk-averaged column density reported for that plume, $2.1\pm1.0\times10^{21}$ m^{-2}, matches well with the DSMC results of Figures 5.10(a,b), which show column density integrations of SO_2 gas through each interpolated canopy along lines-of-sight normal to the symmetry axes. While canopy height, major axis extent, and Y-Z plane structure are comparable for each aspect ratio, increasing vent aspect ratio has several major effects on the flow. First, it reduces canopy length along the minor axis, promoting steeper descent. Higher aspect ratios thus yield canopies of decreasing volume, which, for constant mass flow, correspond to higher density. In the X-Z plane high aspect ratio vents exhibit narrow, dense curtains rising straight above them with little expansion, which could provide a useful observational constraint.

As source aspect ratio increases with all other properties constant, the canopy minor axis falls to Io more rapidly, the overall volume of the canopy is *reduced*, and canopy density *increases*. Figures 5.11(a,b) show the canopy structure of an AR-03 case viewed down the symmetry axes and with the source on the limb, while Fig. 5.11c shows a view of that canopy from above. Two translucent isosurfaces colored in number density mark the canopy: the inner ‘bubble’ aligns with the shock, and the outer one captures the sublimation boundary for the condensate particle model, which occurs toward the middle

of the gas canopy. One half of each bubble is cut away for clarity, and Io's surface is also colored by number density. Note that the slope of the canopy's descent is much more gradual in the major axis than in the minor, particularly toward the canopy edges. Indeed, as source aspect ratio increases and the extent of the canopy minor axis recedes, the slope of the canopy minor axis descent *increases*, which offers a novel observational constraint.

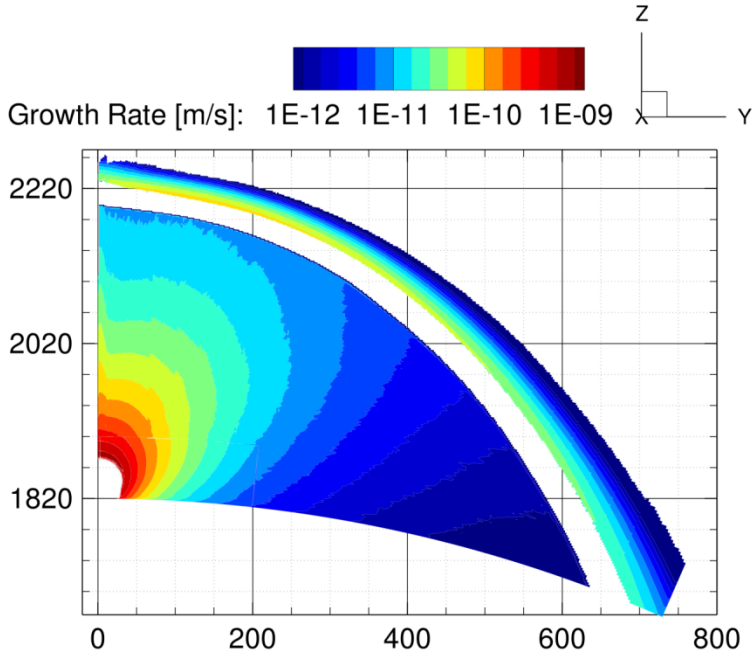

Figure 5.9: Growth rates throughout the AS-01 flowfield. Note the formation of growth-limiting surfaces both within the spout and above the canopy shock.

Canopy Height [km]	**AS-01**	**AS-03**	**AS-10**	**AS-15**	**Alt AS-03**	**Chap. 4**
Shock Surface	381	378	380	382	291	280
Sublimation Boundary	402	402	405	400	312	300
Upper Surface (<5%)	434	431	431	432	335	320
SO_2 Mass Aloft [kg]	2.28×10^{8}	2.27×10^{8}	2.28×10^{8}	2.28×10^{8}	1.0×10^{8}	4.0×10^{7}

Table 5.3: Canopy heights and total mass aloft for each Tvashtar-like plume result.

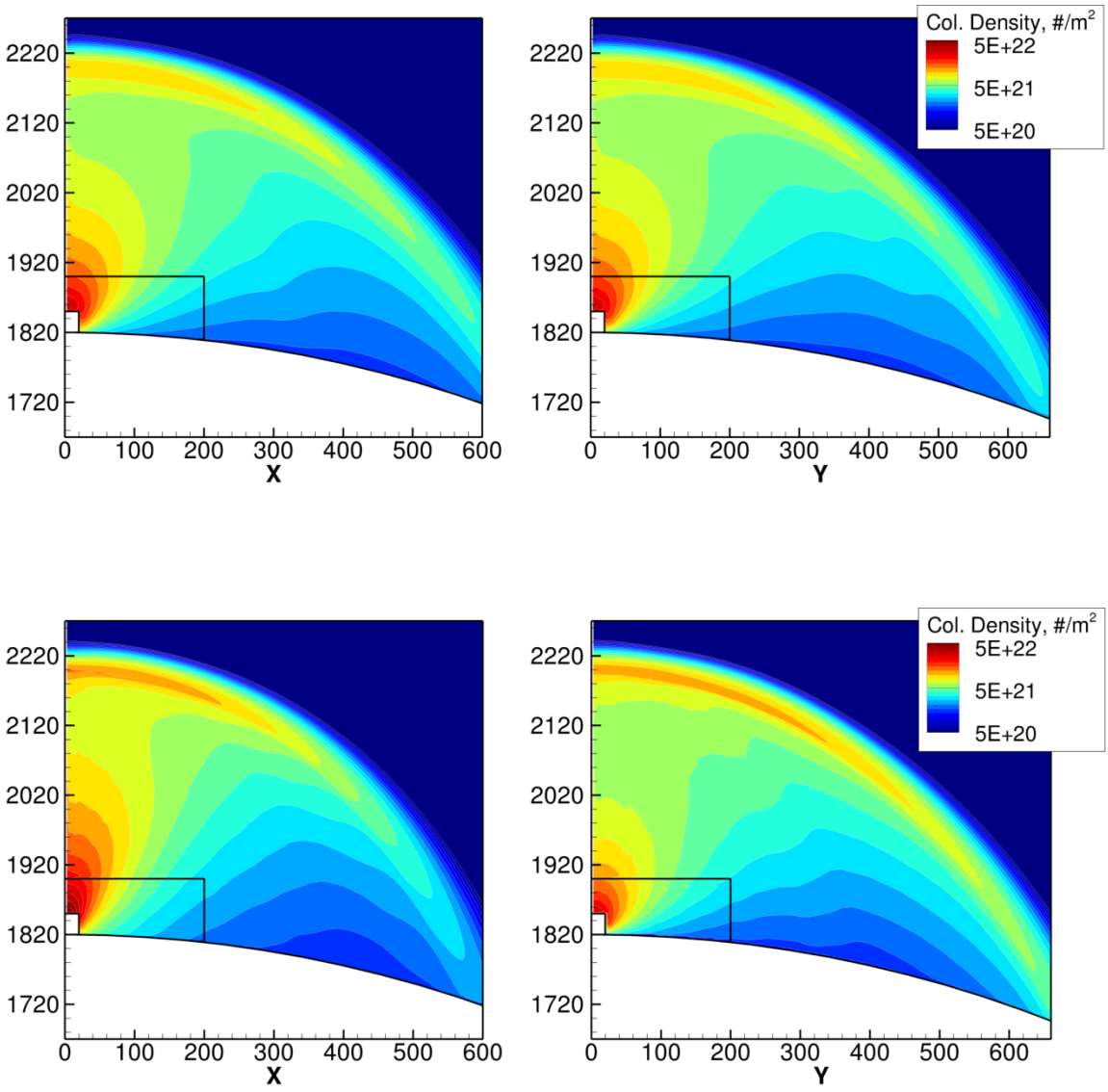

Fig. 5.10a: Column density integrations of SO_2 through the canopy showing the effect of varying source aspect ratio. (Top) AS-01 case. (Bottom) AS-03 case. The rectangle in black marks the stage 3 outer boundary, and the rectangle filled in white covers stages 1 and 2. Vents extend along the X-axis and so are aligned horizontally in left panels, and into-the-page in right panels.

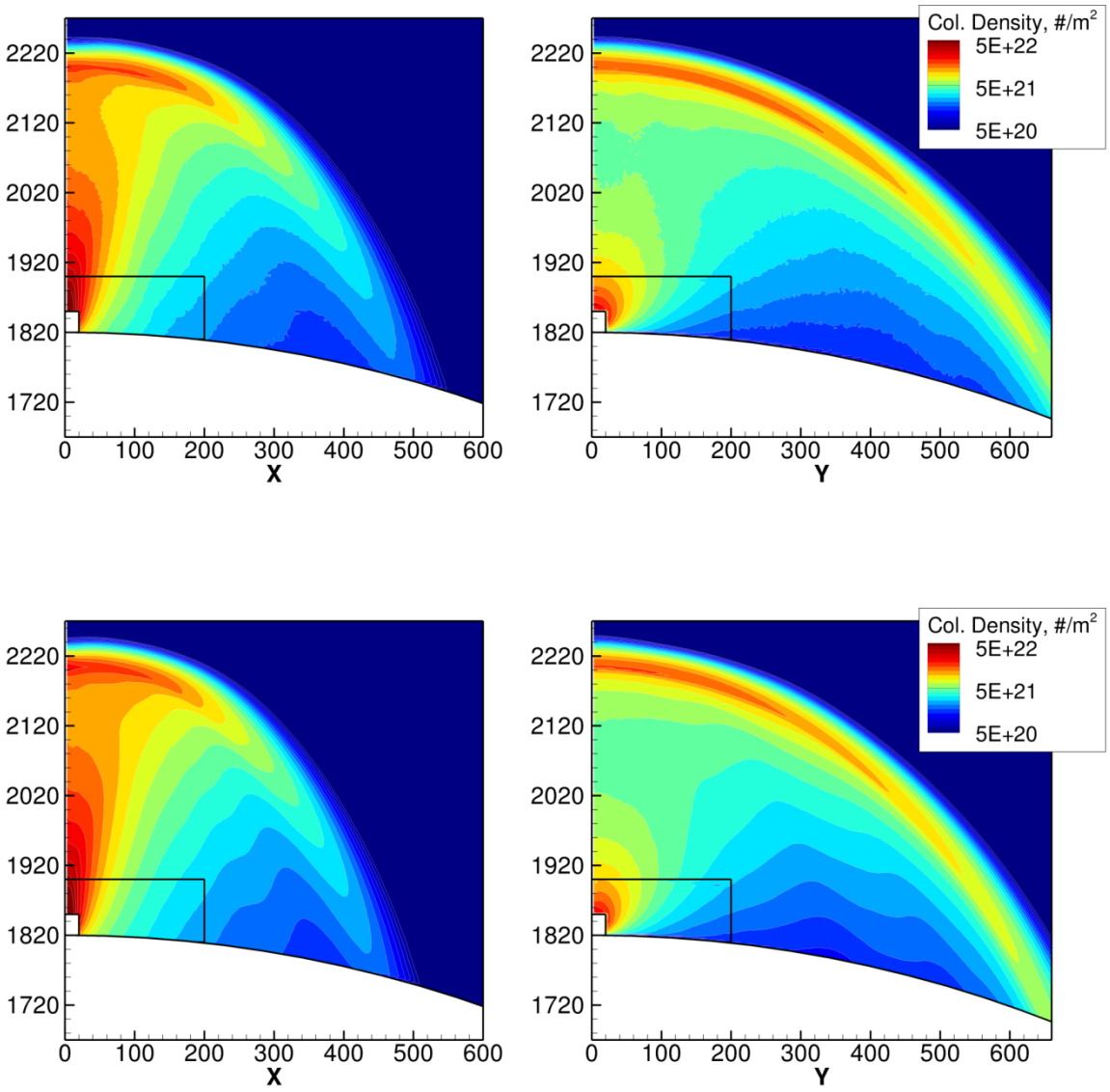

Fig. 5.10b: Column density integrations of SO_2 through the canopy showing the effect of varying source aspect ratio. (Top) AS-10 case. (Bottom) AS-15 case.

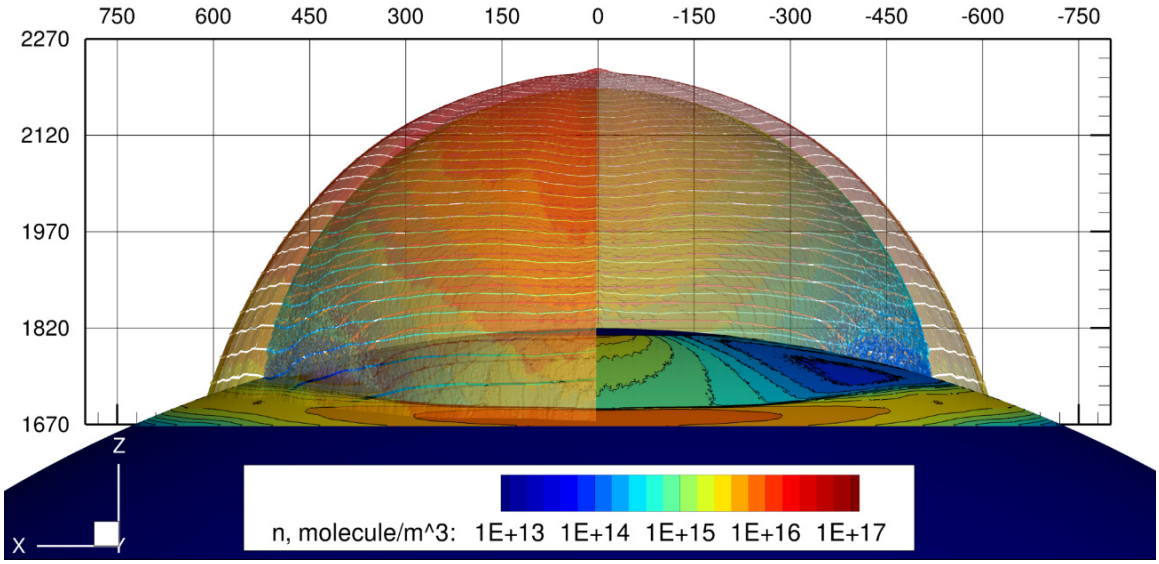

Fig. 5.11a: (X-Z Axis): The AS-03 canopy's *minor axis* extent, viewed normal to the vent's broad orientation (the vent aligns with the X-axis). Two translucent isosurfaces reflect the upper and lower limits of the SO_2 gas canopy. Note that peak gas deposition onto Io's surface aligns with the canopy *major* axis.

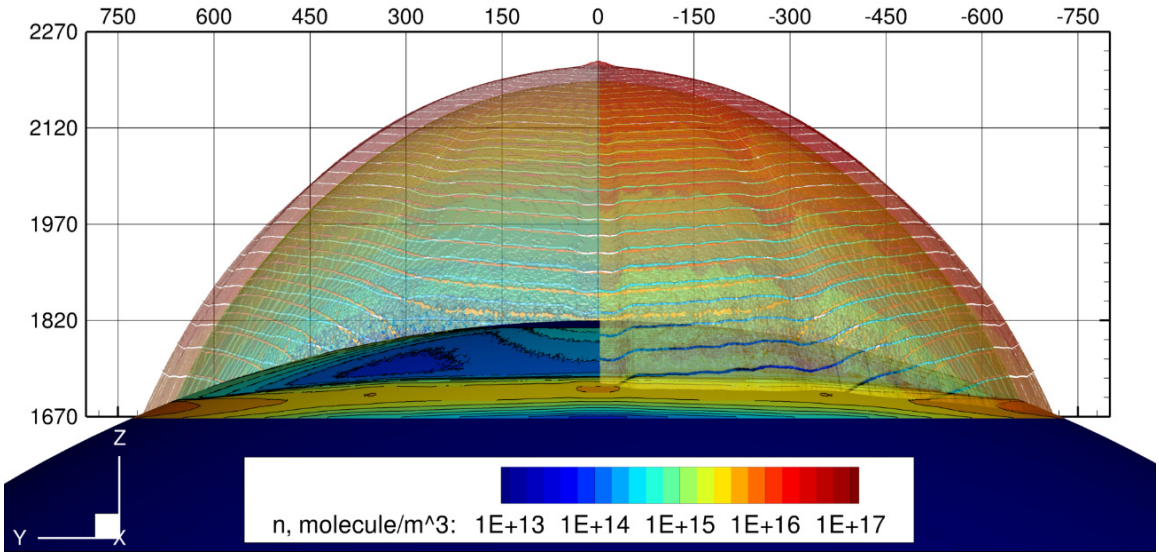

Fig. 5.11b: (Y-Z): The AS-03 canopy's *major axis* extent, viewed along the vent's broad orientation. Note that the slope of the canopy's descent is much more gradual in the major axis than in the minor, particularly toward the canopy edges. Isosurfaces reflect upper and lower limits of the gas canopy.

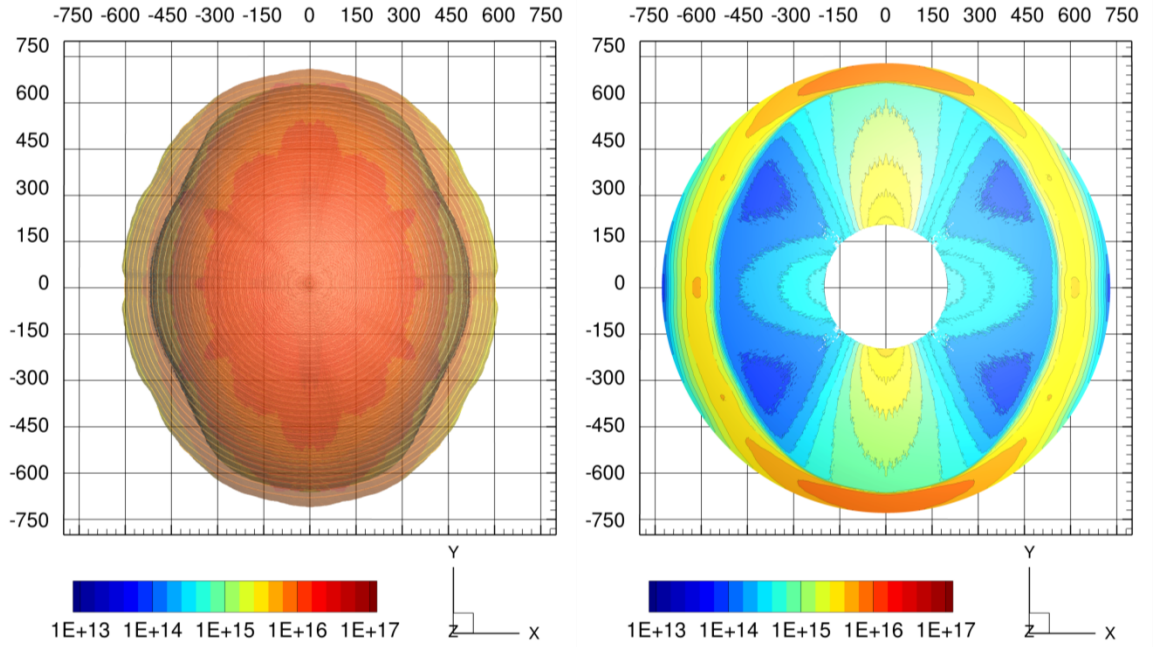

Fig. 5.11c: (X-Y): The AS-03 canopy viewed from above (i.e. down the polar axis in perspective from 4.184×10^6 km distant). At left, the shock surface (interior) and the bounding sublimation surface (exterior) maintain similar shapes but 'grow apart' along the canopy minor axis. At right, contours of number density along the surface show the formation of a gas depositional ring. (The stage 4 domain truncates 750 km in arc length from the origin.)

5.4 Toward Novel Observational Constraints on the Tvashtar Source

5.4.1. Gas Field Shape and Structure

While we initially expected that high-aspect-ratio source regions would prove the best match to the 2007 Tvashtar observation – given the nearly parallel linear orientations of the point-brightnesses reported by Rathbun *et al.* (2014) along ~20 km tracks and the Galileo observations of long, narrow source regions in 1999 and 2000 (e.g. Fig. 4.2) – the AS-10 and AS-15 plumes demonstrate striking spout and canopy structures unlike anything we see in the NH imagery. Fig. 5.8a, for instance, shows that high-aspect-ratio sources provoke significant axis switching inside the canopy and produce a dense spout

core with density contours almost surface-normal when viewed normal to the vent major axis (i.e. down the Y-axis in this work, or down the canopy minor axis). Column density integrations through the gas field, like those of Figs. 5.10(a,b), will demonstrate a pronounced 'curtain' rising up from a high-aspect-ratio vent when viewed from this orientation, but no such structure when viewed normal to it. The NH LORRI images effectively capture the column-integrated brightness (i.e. per pixel) scattered from the particles suspended in the canopy; however, Fig. 5.8c shows that the growth of particles in the condensation/sublimation model will be rapid within this 'curtain' above the limiting sublimation surface – vents of increasing aspect ratio will tend to produce more visible spouts, particularly when viewed down the canopy minor axis. However, the NH LORRI imagery tends not to show discernable spout structure from any orientation, consistent with a low-aspect-ratio source (i.e. $<<10$). As noted in Section 5.3.2, the canopy height and total mass aloft for each parametric plume remain constant with increasing aspect ratio. Furthermore, the *extent* of each plume along the canopy major axis remains constant – the right panels of Fig. 5.10(a,b) are nearly indistinguishable in shape and structure. A primary change occurs in the rate of descent of each canopy along its *minor* axis, which steepens with increasing aspect ratio – high-aspect-ratio sources produce canopies which fall back to the surface rapidly along their minor axes. Such canopies are increasingly eccentric; they cover less volume than their counterparts produced by low-aspect-ratio sources, but support the same mass aloft and are therefore denser overall. If the 2007 Tvashtar source region were of high aspect ratio (i.e. AS-10 or AS-15), NH imagery captured over the fly-by should reflect a canopy that changes markedly in shape – specifically in its steepness – with changing viewing angle relative to the vent axes. This is not the case: none of the LORRI images shows a canopy shaped anything like those which form above high-aspect-ratio sources (Fig. 5.10b, Fig. 5.12).

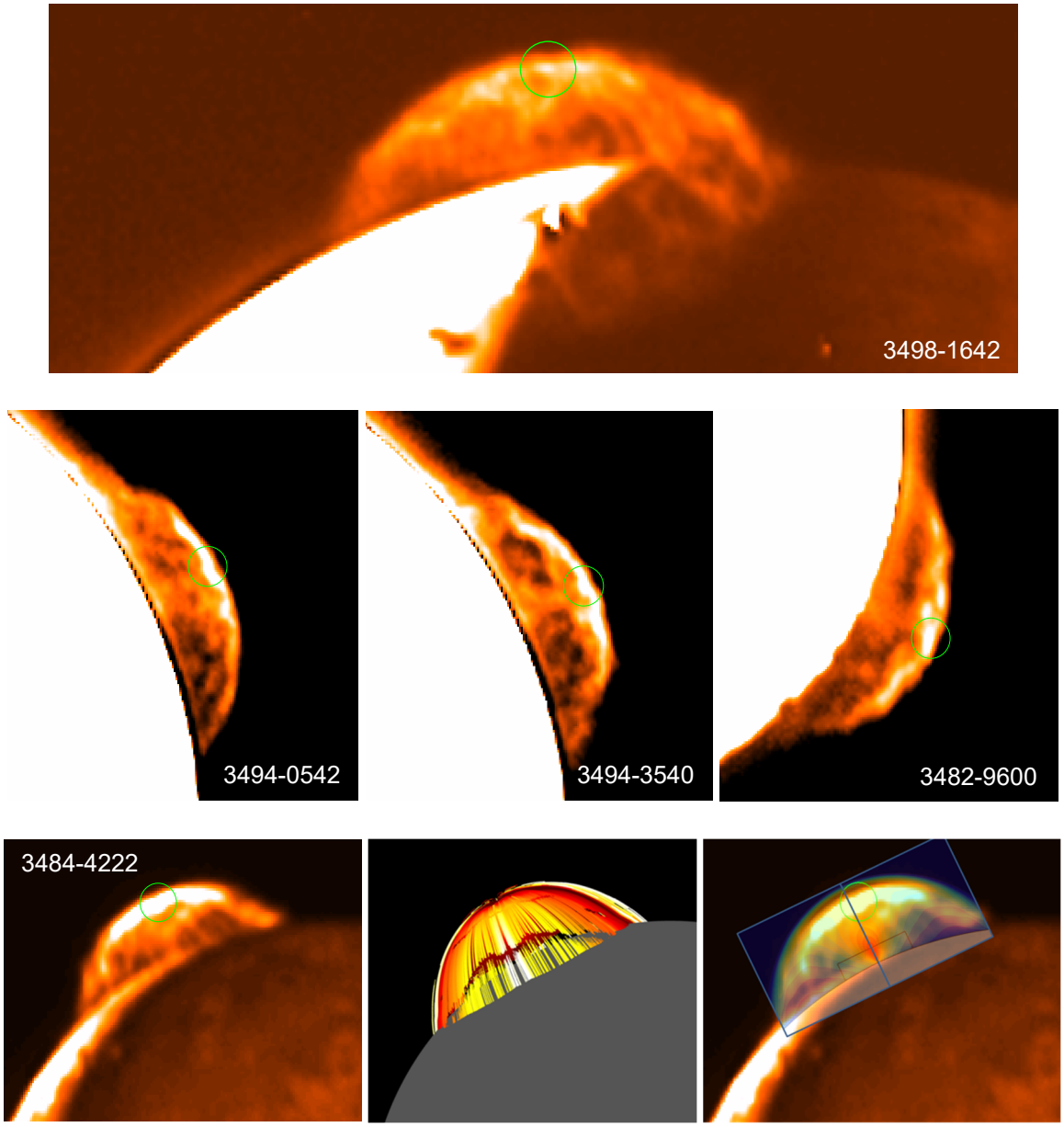

Figure 5.12: Deconvolved LORRI images; times marked in MET [seconds] (Trafton *et al.*, 2016). (Top) A rare view in which 3-D canopy shape can be discerned; the canopy does not appear oblong, as in AS-10+ cases. (Center) Three images in which Tvashtar is positioned on the limb such that nearly the full extent of the canopy can be seen. Canopy slopes are gradual, consistent with low-aspect-ratio sources – or views down the canopy minor axis. (Bottom) A fourth LORRI image with Tvashtar on the limb matches well in shape with the AS-03 result for the entrained particle field, viewed from the same distance and orientation as NH, and with the DSMC gas field.

5.4.2 Depositional Ring Configuration

The New Horizons probe could not resolve Tvashtar's vent dynamics in detail, as Galileo could Pele's (i.e. Fig. 4.2). However, depositional rings observed by the probes in 2000-2001 and again in 2007 may be compared – Fig. 5.13 shows the state of Tvashtar's ring during the Galileo era. A series of coarse NH images of Io's surface were stitched together into a map published in Spencer *et al.* (2007); this map likewise shows a clear depositional ring about Tvashtar, and an analysis of its shape, thickness, and radius can provide valuable constraints on the observed eruption. Mapping that equirectangular projection onto Io's globe and rotating it to center the Tvashtar vent, the dark and light rings are seen to match a coherent ellipse of low eccentricity (Figures 5.14, 5.15).

For the AS-03 plume, the *gas* depositional ring extends approximately 700 km in the major axis direction at its peak density and to perhaps 630 km in its minor axis, as seen in Fig. 5.11c.[36] Note that the gas deposition along the major axis greatly exceeds that along the minor axis, and the consistent depositional ring width of O[100 km]. Within the canopy, Io's surface in the major axis direction (Y, aligned with the vent's initially narrow direction) will be continuously resurfaced by SO_2 that has not interacted with the canopy; the minor axis direction (X, along the vent's long axis) will experience much less resurfacing. Especially notable are the regions along the diagonals, which experience several orders of magnitude less deposition than inside either the adjacent ring or the sprays along the vent symmetry axes. These are reminiscent of the 'butterfly wings' observed at Pele, which form as heavy dust grains launched from the vent fall short of the gas canopy and form interior depositional patterns (McDoniel, 2015). The inability of gas to resurface these regions in high aspect ratio plumes suggests that such patterns might

[36] I will report distances *along the curved surface*, while the Cartesian scales visible in figures with views oriented down the polar axis (e.g. Figs. 5.11c, 5.16, 5.17) reflect distances as projected onto a plane. The difference is a factor of $\frac{\theta}{\sin(\theta)}$, which is ~2.5 % when measuring Tvashtar's ring radii of ~700 km.

have been present in 2007. Figure 5.11c shows an AS-03 depositional ring viewed down the plume axis, with Io's surface colored in number density.[37] Only stage 4 is visible here; the inner stages are within the 200 km radius blank region at center. The DSMC domain boundary, at 750 km in arc length from the origin, is sufficient to contain the AS-03 canopy minor axis, but does not contain all expansion along the major axis. Figures 5.16(a,b) and 5.17(a,b) show surface gas and particle rings, respectively. Fig. 5.16 reports condensation onto the surface; note the focusing of this deposition along the canopy major axis with increasing vent aspect ratio. Fig. 5.17 demonstrates that larger droplets concentrate on the outside of the ring; they travel along the outside of the canopy and thus have more opportunity to grow.

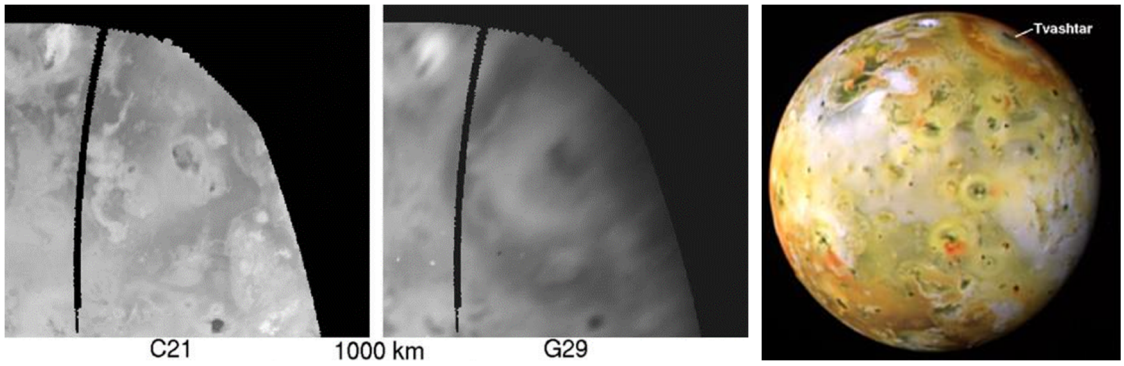

Figure 5.13: (Left) Between Galileo orbits 25 and 29, Tvashtar erupted along a 25 km fissure in a fire-fountain configuration and left a vivid ring of about 720 km radius on the surface, stretched along its N-S axis to a maximum of 780 km southward (Geissler *et al.*, 2004). These distances match well with those produced in the lower aspect ratio DSMC simulations discussed here. (Right) In 2001, Galileo captured this image of a mature ring during I29.

[37] This quantity reflects the gas density in the first DSMC cell above the surface plane and is not a direct measure of depositional flux. However, it is a reasonable proxy for deposition, as the first cell is within 1 km of the surface and the flow tends to be surface-normal rather than surface-tangential, particularly in the ring as the canopy drives into the surface. Depositional fluxes are reported in Figures 5.16(a,b).

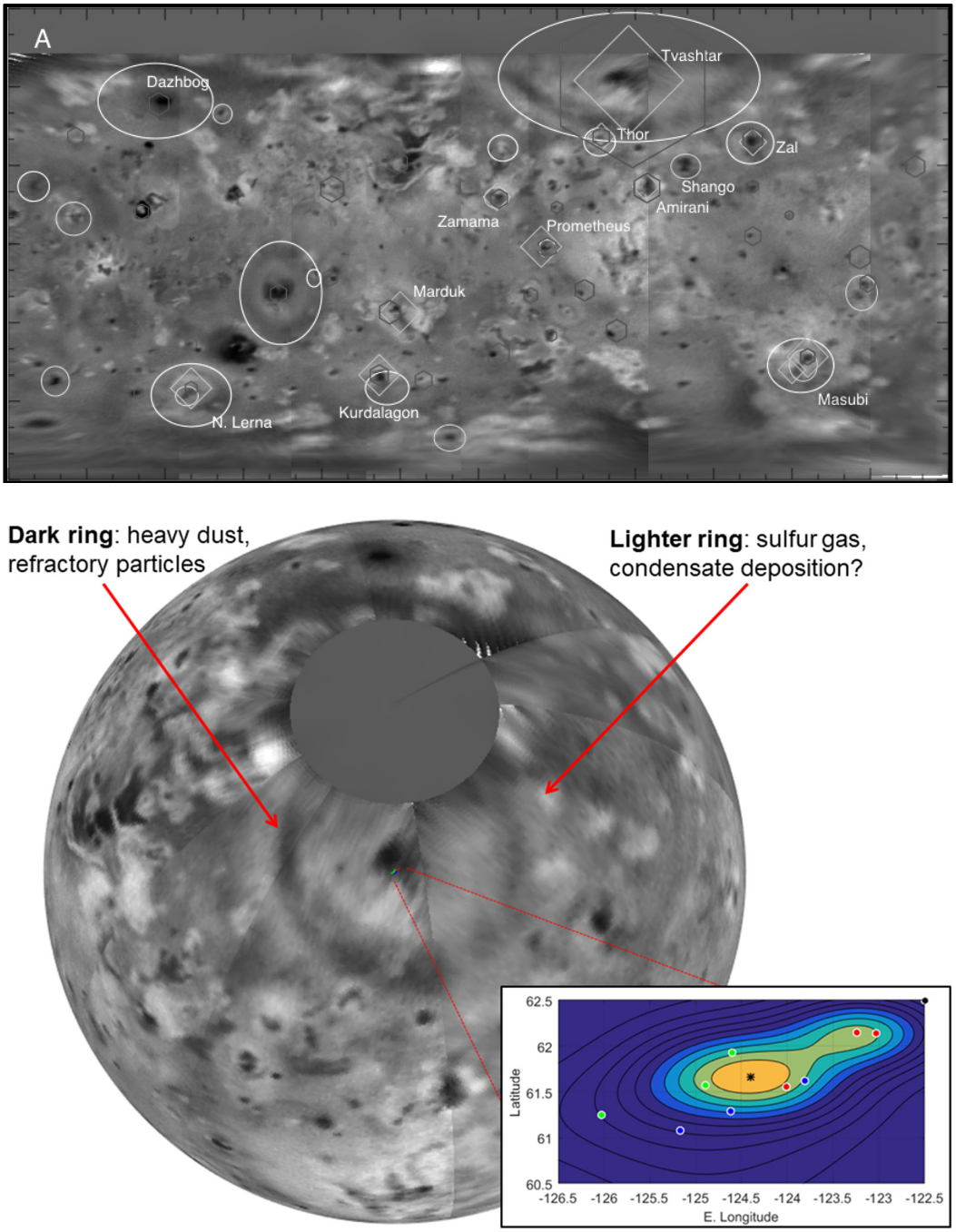

Figure 5.14: (Top) An equirectangular surface map of Io via NH surface imagery and contemporaneous with the 2007 activity, from Spencer *et al*. (2007). (Bottom) Image mapped onto a globe and viewed downward onto the source region, with an inset of the Rathbun *et al*. (2014) data from Figs. 5.1 and 5.2; elliptical dark and light rings are evident about Tvashtar.

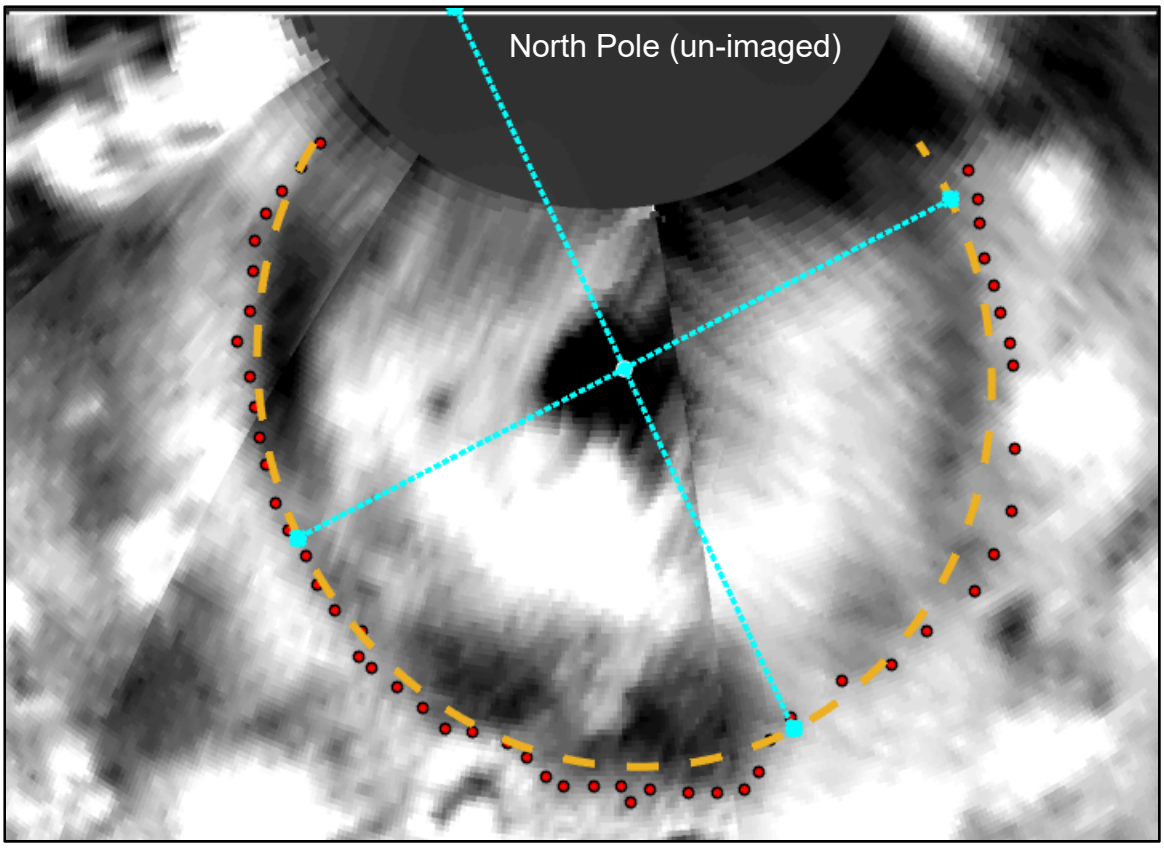

Figure 5.15: The equirectangular NH LORRI surface map of Spencer *et al*. (2007) is mapped onto a globe and rotated such that the view is directly downward onto the site of the 2007 Tvashtar eruption reported by Rathbun *et al*. (2014). The perspective and viewing angle are characteristic of the NH observations (~4×10^6 km distant) and consistent with the perspectives of the simulated ring figures. 53 red points are hand-selected at the highest contrast surface (i.e. the outer edge of the dark ring) and are least-squares-fit by the ellipse outlined in gold, following the method of Halir and Flusser (1998). This fit reflects a dark ring major axis ~ 5% longer than its minor axis.

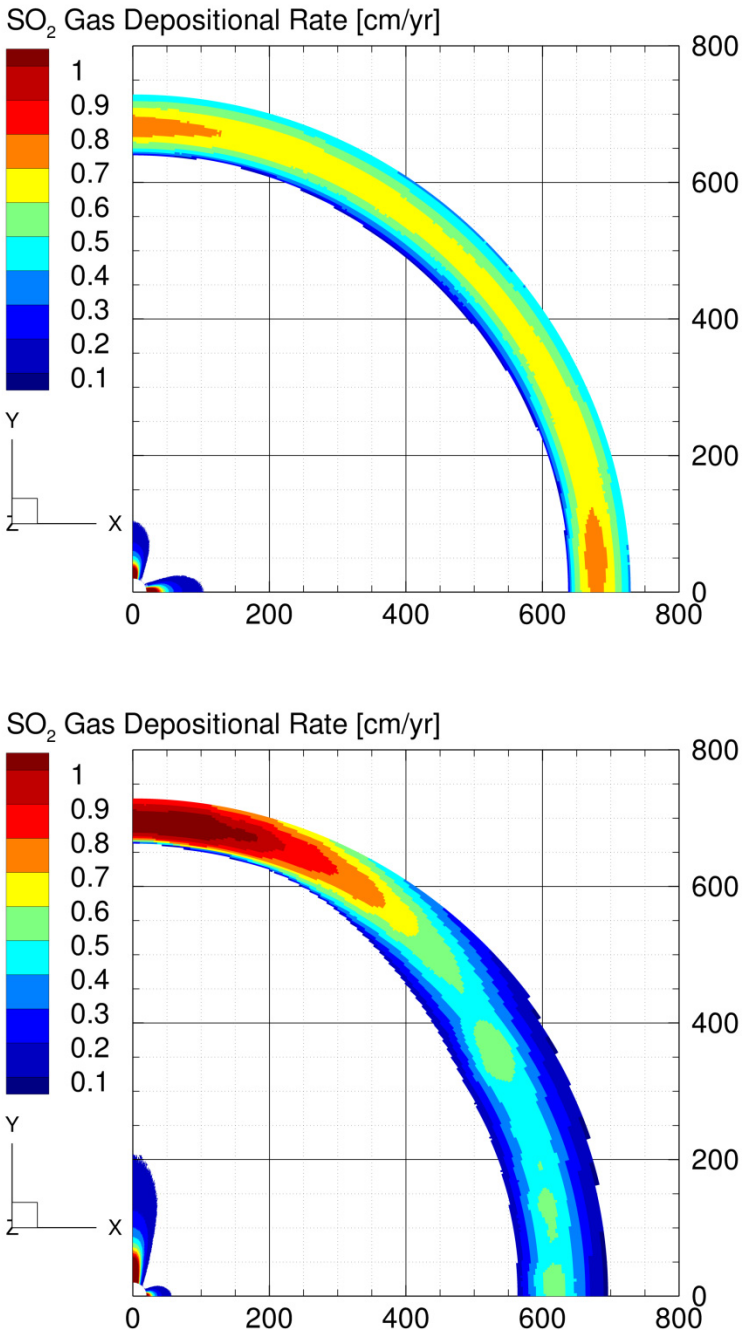

Fig. 5.16a: The depositional rings of SO_2 gas for AS-01 (top) and AS-03 (bottom) cases; low aspect ratio plumes tend to deposit gas uniformly in their rings.

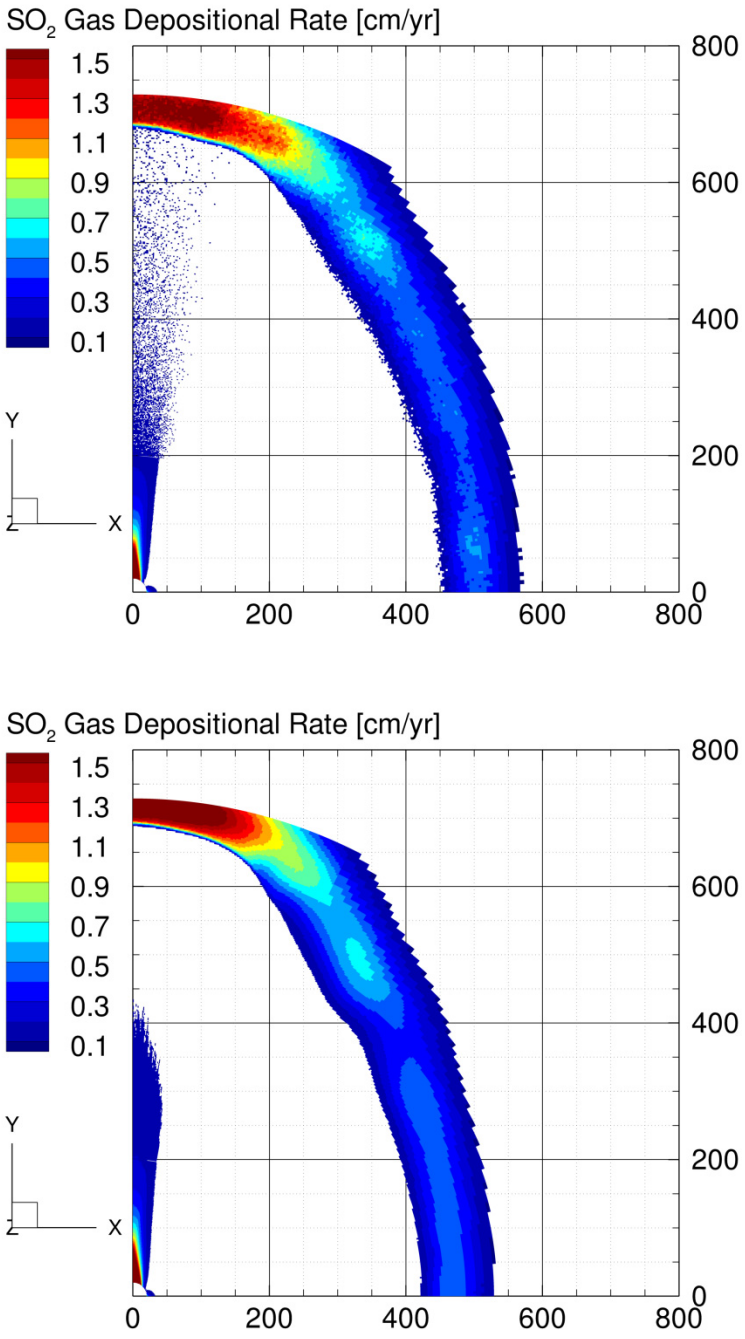

Fig. 5.16b: The depositional rings of SO_2 gas for the AS-10 (top) and AS-15 (bottom) cases; high aspect ratio plumes tend to concentrate gas deposition along their canopy major axes. Note that the DSMC domain terminates at 750 km along the curved surface from the vent center.

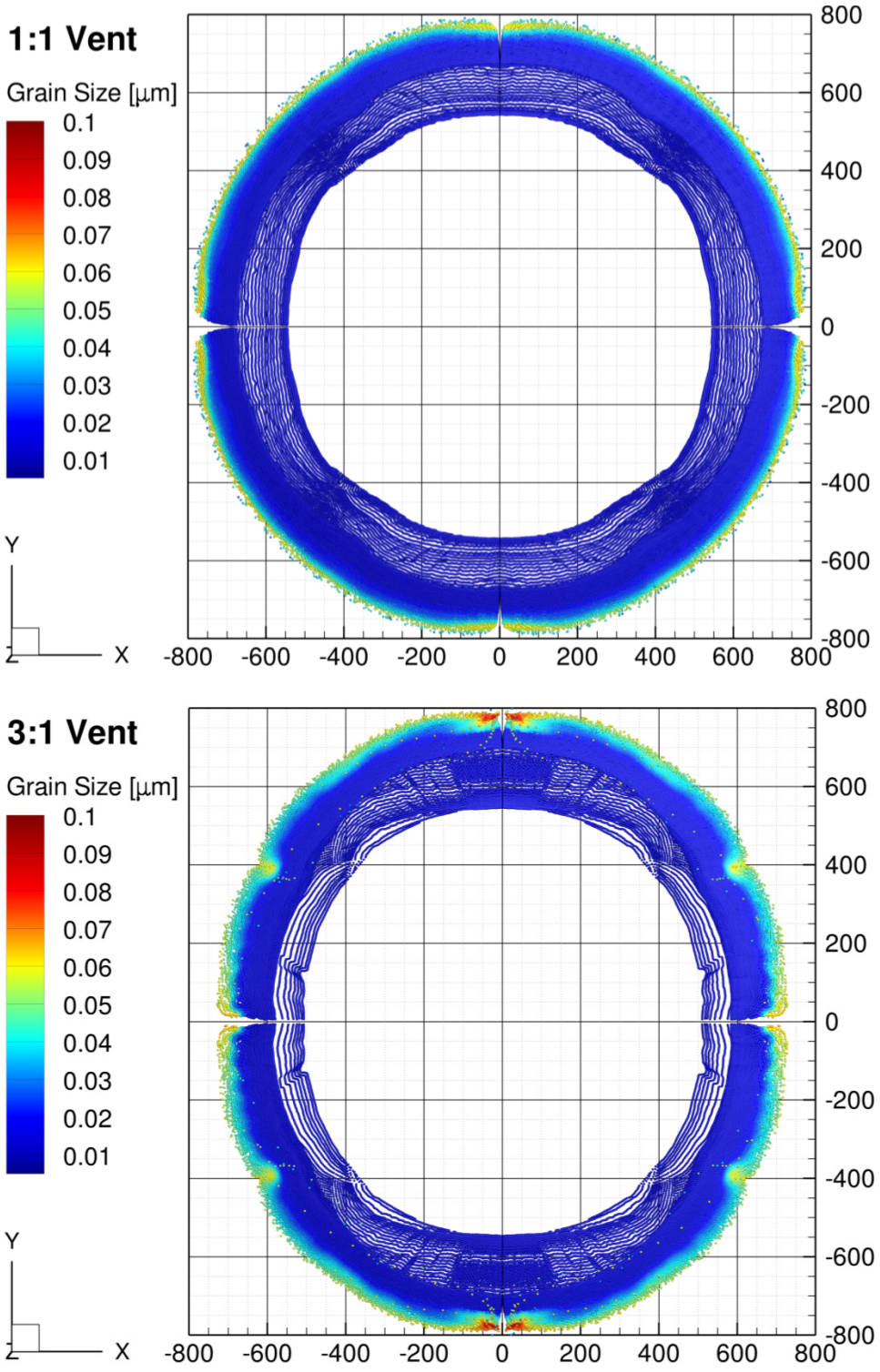

Fig. 5.17a: Depositional rings of condensates entrained in AS-01 and AS-03 plumes.

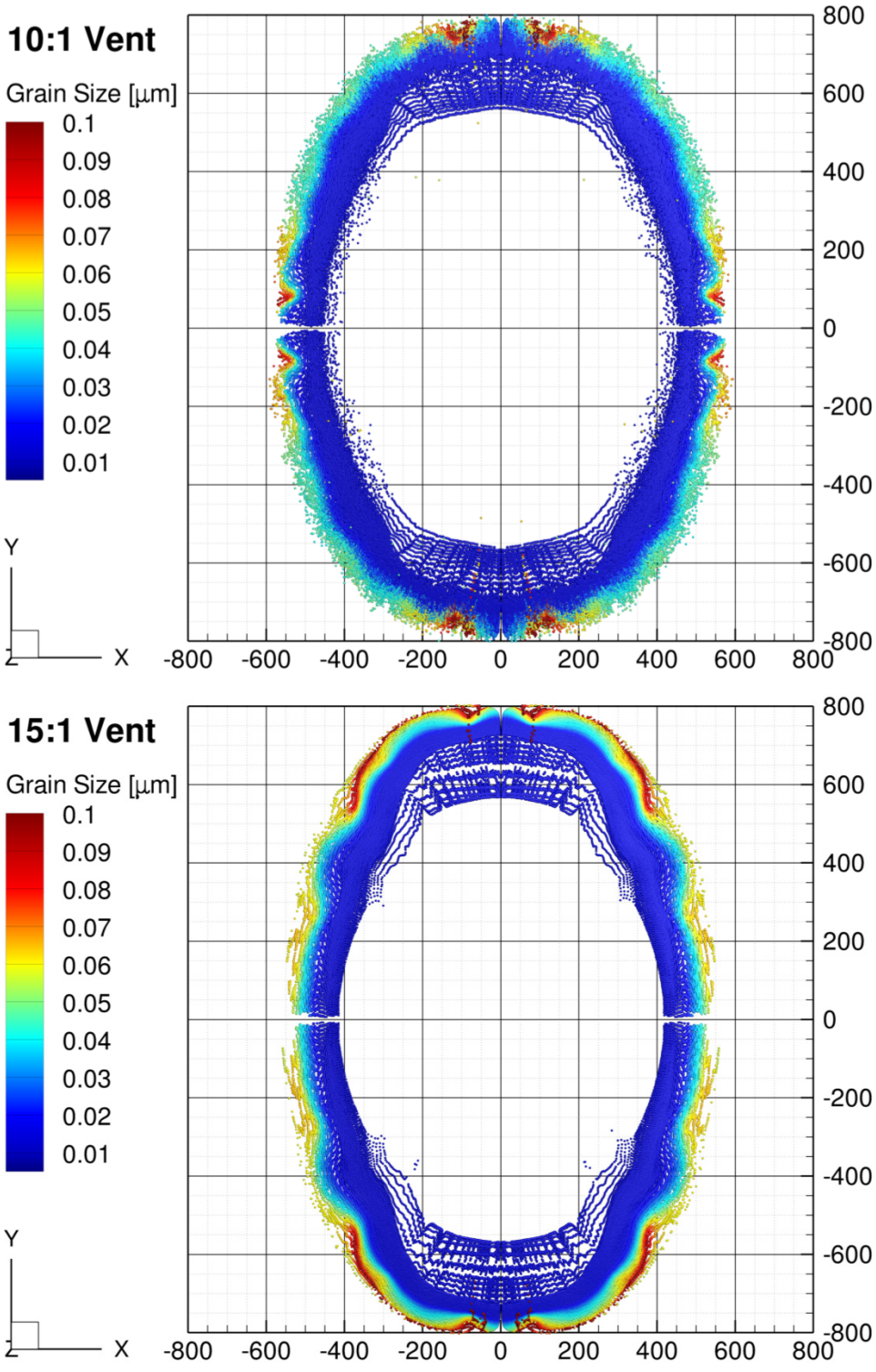

Fig. 5.17b: Depositional rings of condensates entrained in AS-10 and AS-15 plumes.

5.4.3 Alternate Thermodynamic Conditions for the Aspect Ratio 3 Vent

In the prior sections, results of the AS-03 DSMC calculation are shown to be morphologically consistent with the NH observations of Tvashtar's canopy shape and depositional structure. Recall that the vent boundary conditions for the parametric AR cases are selected from the first[38] of the two options presented by Rathbun *et al.* (2014): T_0 = 1280 K and source area = 30 km^2. In this section, I consider the alternate boundary condition: T_0 = 1240 K and source area = 50 km^2. How well could such a vent, in an aspect ratio 3, lava-lake configuration with Mach 1.0+ flow, match NH observations of depositional ring shape, radius, and thickness; or canopy shape and height?

I performed a full four-stage calculation for these conditions that was otherwise equivalent to the other parametric cases; the results are shown in Figs. 5.18(a,b) through 5.21. This alternate set of source parameters produces a canopy too low and a depositional ring too small to match the 2007 NH Tvashtar plume. As expected, the reductions of source T_0 and mass flow rate and corresponding increase in area had no significant effect on the shapes of the canopy or the depositional ring, only changing their sizes. Reducing the stagnation temperature at the vent from 1287 K to 1240 K reduced canopy height by nearly 20 %, far beyond the 4 % linear expectation of the analytic model of McDoniel (2015). This effect is coupled to the reduction in mass flux at the vent by a factor of two: the reduction in density changes the extent of the opaque regions. Since the source region and inner spout can begin radiating sooner in this flow, energy is lost more rapidly and the canopy cannot grow sufficiently. This helps justify the use of 200,000 kg/s SO_2 flow in the other parametric cases.

---

[38] Instead of the 1280 K value suggested by Rathbun's point brightness fits, I actually apply the more tightly-constrained value of 1287 K obtained via LEISA and reported by Spencer *et al.* (2007). I also vary the mass flux at the vent from 200,000 kg/s to 100,000 kg/s in this alternate case to bracket the range about the largest values for SO_2 gas mass flow rate for plumes of <5 % S_2 reported by Jessup and Spencer (2012).

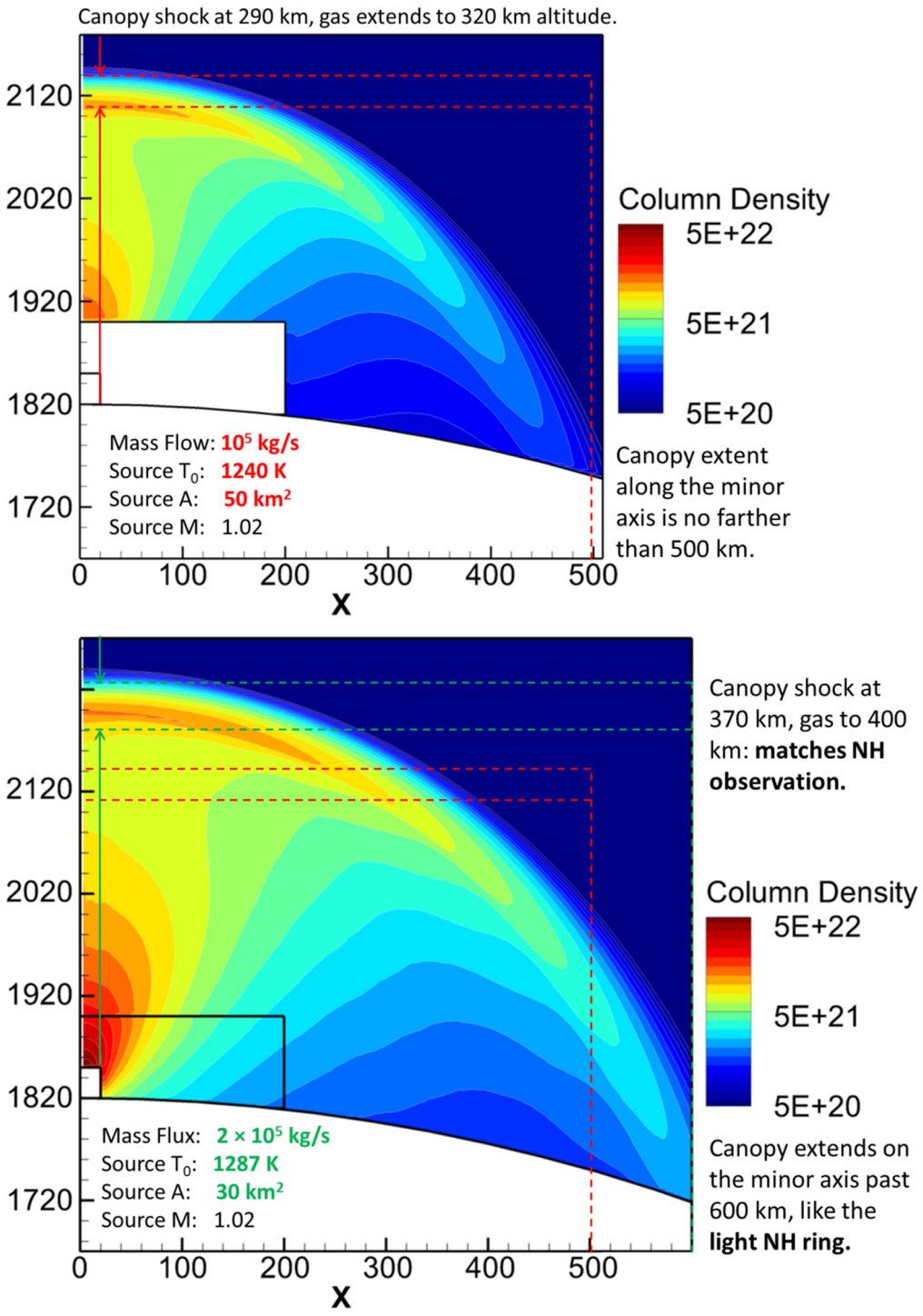

Fig. 5.18a: Canopy *minor axis* view: integrated column density for a case with alternate vent parameters (i.e. 1240 K, 50 km^2) in an AR=3 configuration at top, and the AS-03 case – which provides the best overall fit to Tvashtar – at bottom.

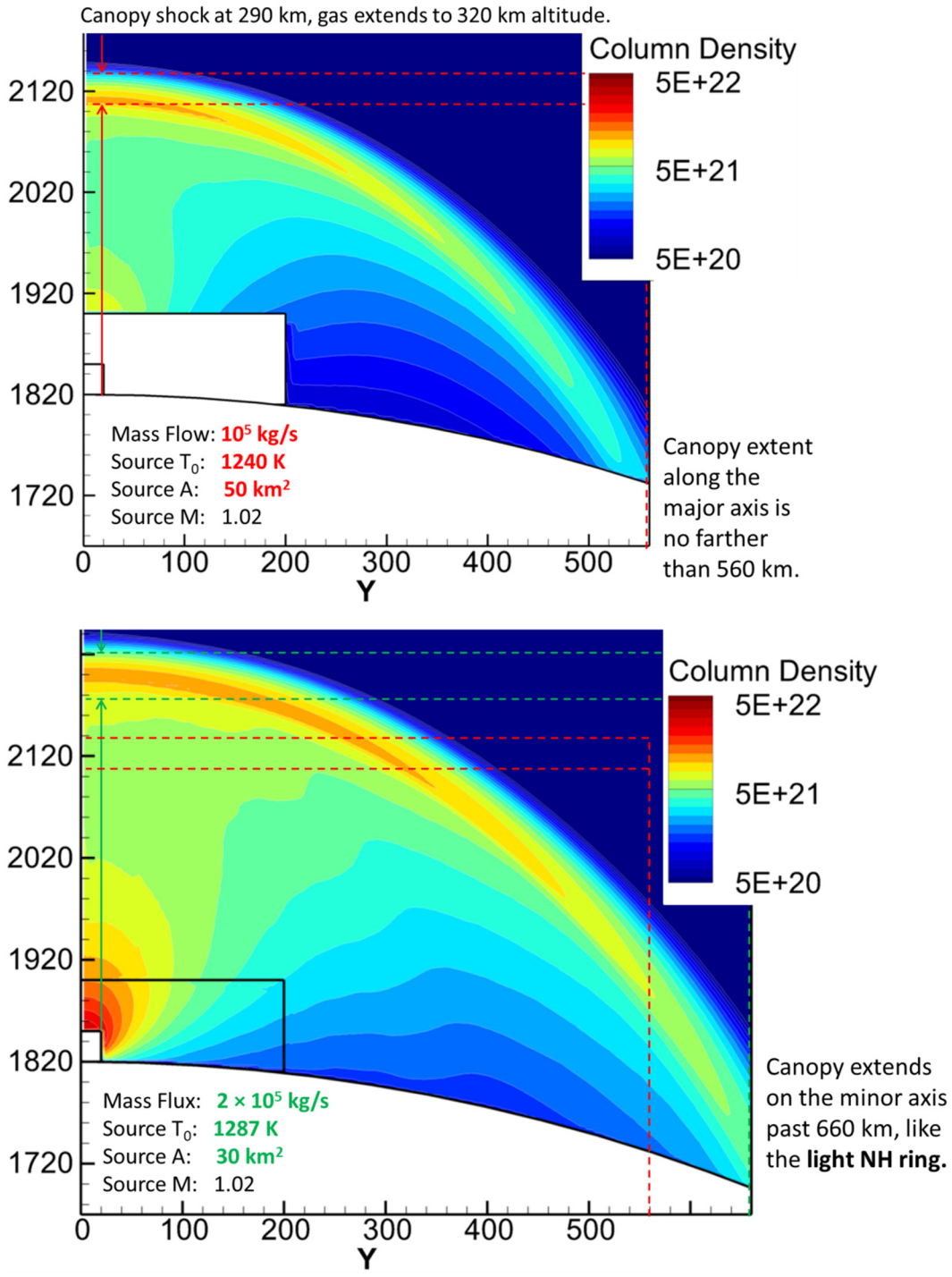

Fig. 5.18b: Canopy *major axis* view: integrated column density for a case with alternate vent parameters (i.e. 1240 K, 50 km^2) in an AR=3 configuration at top, and the AS-03 case – which provides the best overall fit to Tvashtar – at bottom.

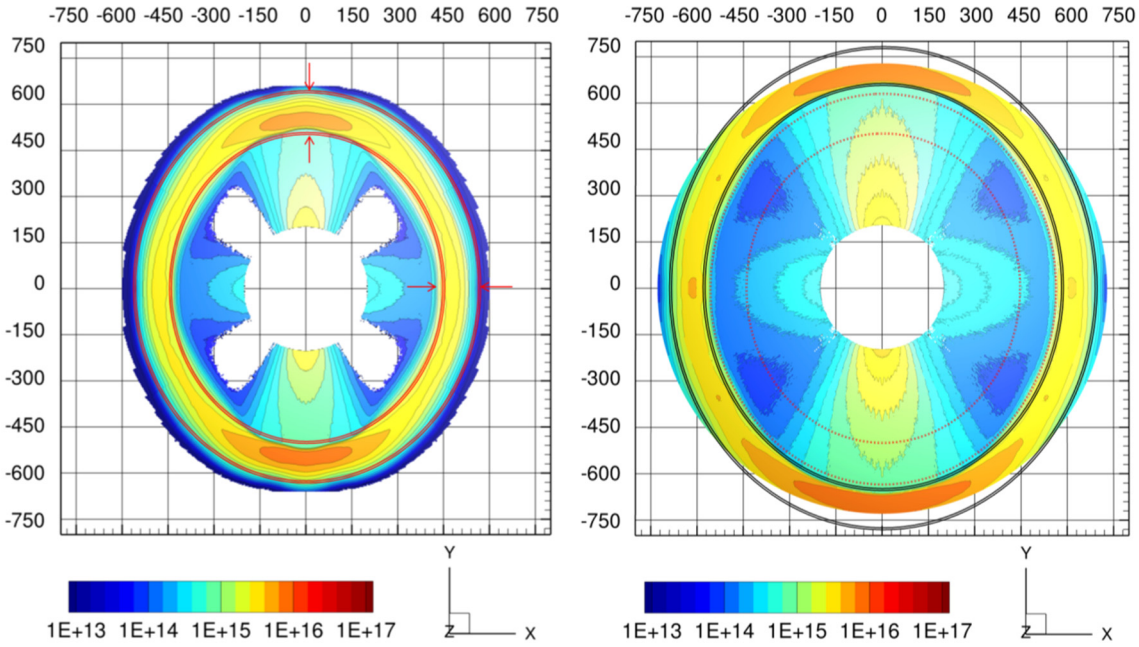

Figure 5.19: (Left) Contours of number density along the surface, approximating a gas depositional ring for a case with vent parameters (1240 K, 50 km^2) in an AR=3 configuration. The ring is 100-150 km wide, as in the AS-03 case. However, this ring doesn't extend sufficiently far along the surface to form either NH ring. (Right) The AS-03 gas ring extends out to ~780 km in the major axis and ~720 km in the minor, consistent with NH (and Galileo) observations. Interior red rings match the alternate case of the left figure.

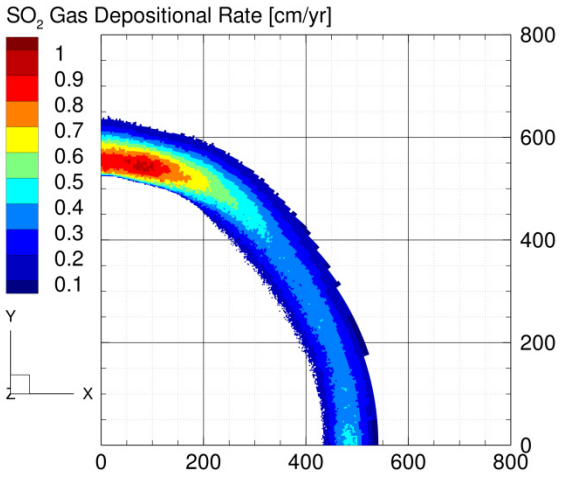

Figure 5.20: Gas depositional rates for the alternate aspect ratio 3 configuration.

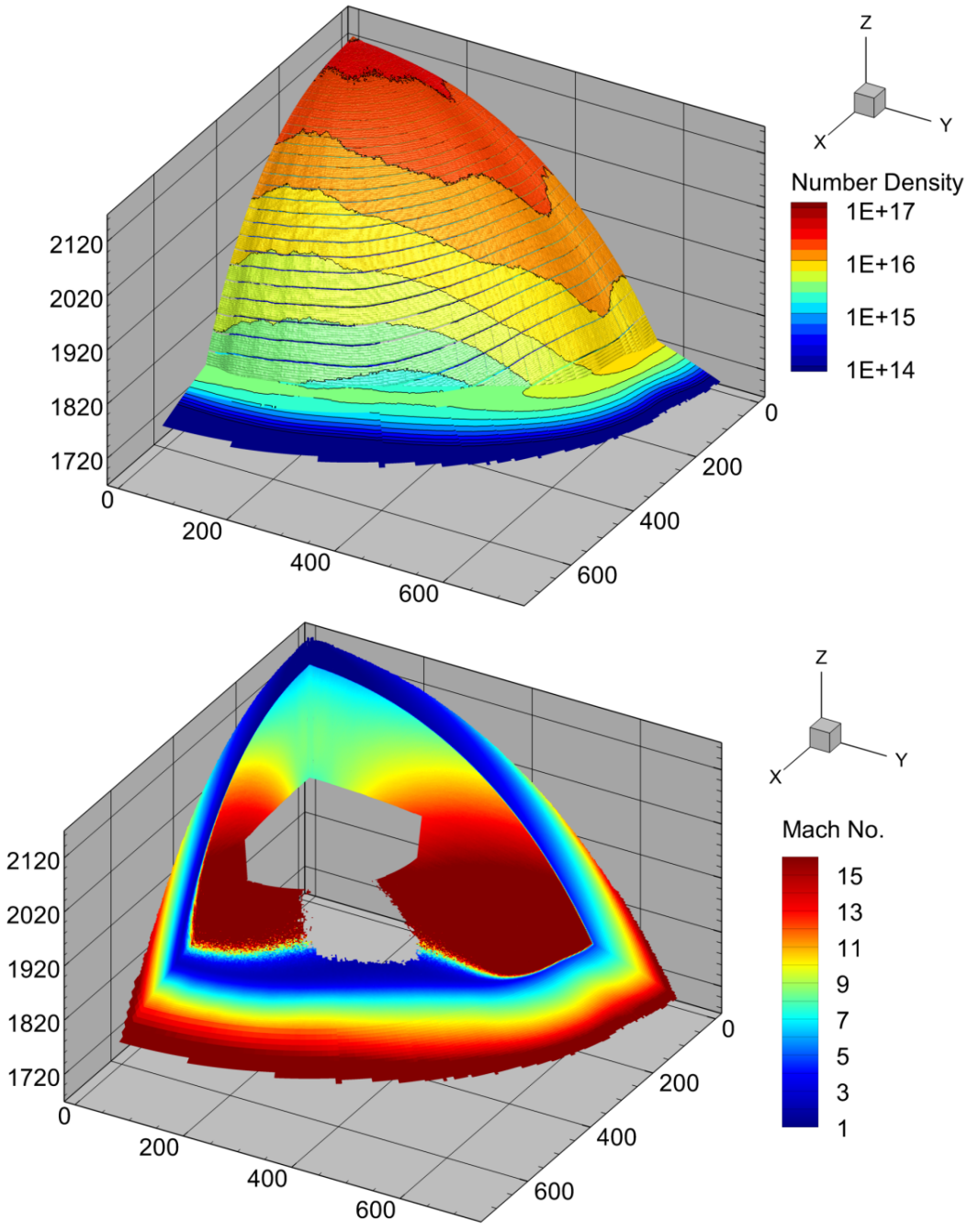

Figure 5.21: Overall, the shape and structure of the alternate aspect ratio 3 plume are very similar to the AS-03 case, despite the changes in vent thermodynamic condition. At top, an isocontour of the outer sublimation surface, colored in number density, shows a familiar canopy shape with minor rippling. At bottom, Mach number contours on the major and minor axis symmetry planes show a canopy shock at just 290 km, much lower than NH observed.

5.4.4 Final Virtual Vent Conditions

We have arrived at a set of vent conditions (i.e. the AS-03 case) that incorporate or represent all available observational constraints. The stagnation temperature of 1287 K and source area of 30 km^2 are consistent with both the Spencer *et al.* (2007) LEISA-reported temperature and the higher-temperature Stefan-Boltzmann fit Rathbun *et al.* (2014) provide to match the source brightness. The Mach number of 1.0+ is selected to match the high-active-area lava-lake condition. The mass flux of 200,000 kg/s is slightly higher than the 110,000-160,000 kg/s range of Jessup and Spencer (2012) for a >95 % SO_2 plume, but our higher flux produces the correct range of canopy condensate sizes (~ 0.05 to 0.08 microns).[39] The gas canopy height of 380-430 km falls within the range of the Jessup and Spencer (2012) projections from HST data. The gas depositional ring's width, shape, and radius are all consistent with the NH surface map, and the canopy shape and orientation are consistent with a vent oriented parallel to the tracks of point-brightnesses reported by Rathbun *et al*. (2014) and primarily viewed parallel to the vent major axis. Synthetic brightness images produced in the particle-tracking code closely approximate the structures of the 2007 NH observations, as seen in Fig. 5.22.

[39] Discussed in depth in an upcoming manuscript with P. Ackley.

5.5 PRODUCING SYNTHETIC DATA WITH THE HYBRID APPROACH

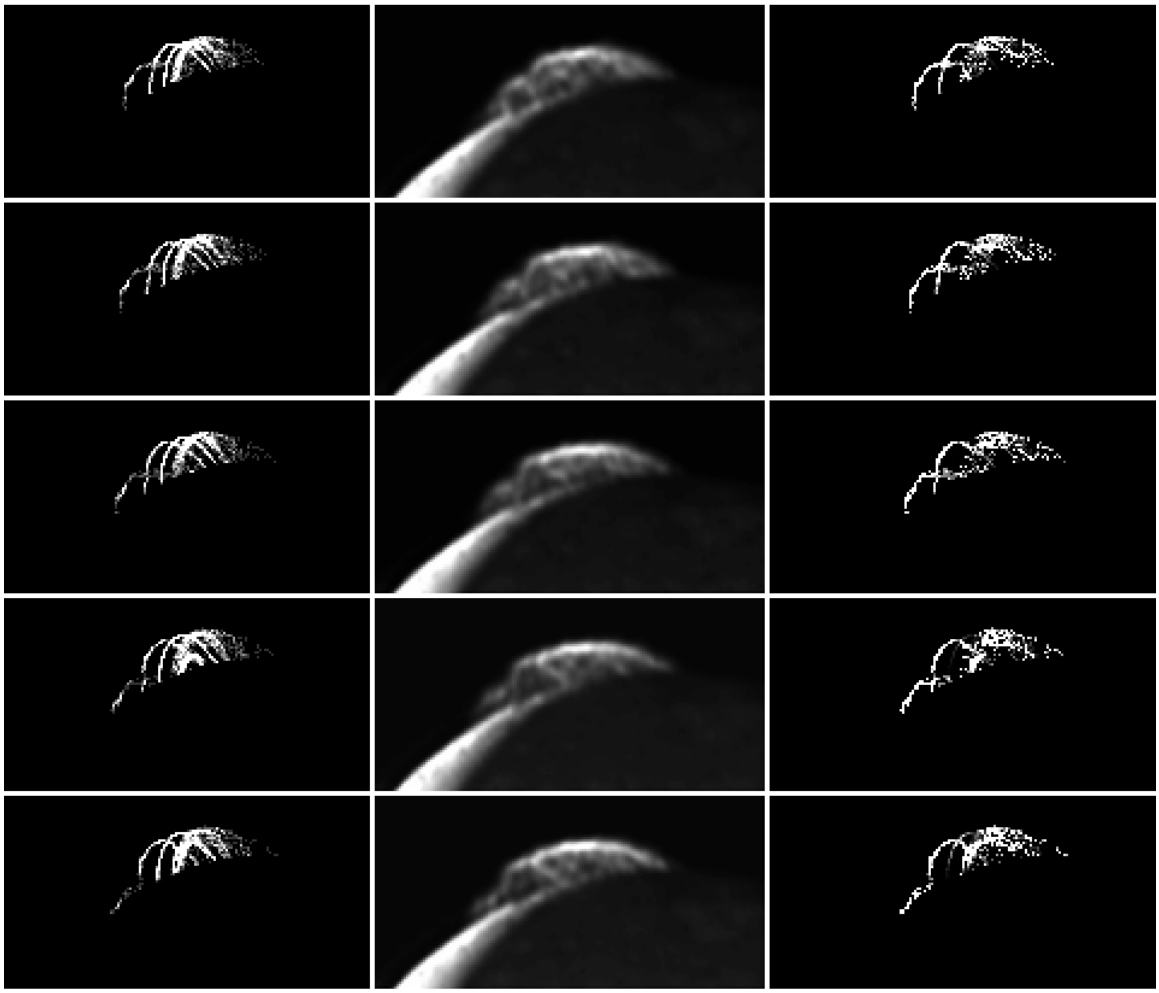

Figure 5.22: Synthetic data showing the integrated brightness of light scattered from condensate particles in a simulated Tvashtar plume of AS-03 configuration which releases particles from two cracks aligned with the source long axis and in sinusoidal pulses of 15 minute period. Integrations are performed along lines-of-sight; from top to bottom, images are spaced two minutes apart to match the NH observation; brightness units are arbitrary.

(*Left*) Rayleigh scattering from the condensate particles, which are of average size ~0.05 microns.

(*Center*) The deconvolved NH LORRI observations.

(*Right*) Column integrations of molecule count, or brightness from uniformly sized particles.

5.6 AN ALTERNATIVE HYPOTHESIS FOR OBSERVED CANOPY INSTABILITY

A key objective of this work is to suggest and support potential explanations for the formation and propagation of the transient canopy structure visible in sequential NH LORRI imagery of Tvashtar, including the visible notch moving tangentially along the left canopy edge (Fig. 5.23). We have developed plausible matches for such structure in an entrained dust and condensate model coupled to *steady* gas-field solutions, i.e. in the preliminary results of Chapter 4, but could this notch instead reflect a *transient* gas-field result generated by a high-amplitude density pulse at the source?

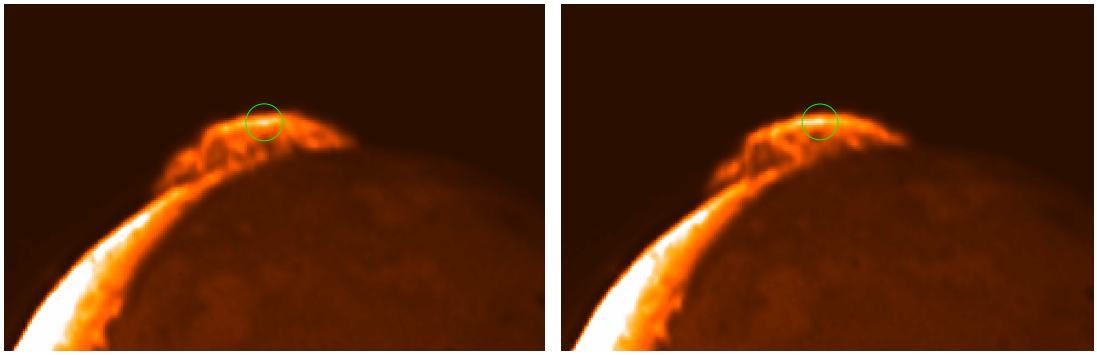

Figure 5.23: Two selected frames from the NH LORRI movie of transient canopy structure, after deconvolution by L. Trafton (2016); note the wave propagating along the left side of the canopy. (See also Fig. 4.1.)

During the start-up process of each plume, material rising up through the spout and falling back ballistically to Io must balance to form a canopy shock (provided the vent ejects sufficient gas to support a collisional flow). This can be a dramatic process, spawning transient instabilities that propagate tangentially along the nascent canopy structure. In fact, the AS-03 case undergoes a dramatic but temporary *collapse* along the canopy major axis that ultimately corrects and stabilizes to form a steady canopy. This behavior provides insight into an alternative hypothesis for the visible wave and notch structures present in the 2007 Tvashtar observation.

The collapse event occurs between 4500 and 5000 s into the stage 4 calculation and along the canopy major axis, as a high-density perturbation travels along the upper edge of the canopy shock, growing in size, until the resulting distortion exceeds the density of the underlying gas by more than an order of magnitude. At this point, the canopy collapses in a localized bubble onto the surface; the gap quickly refills with new material sloughing along the uncollapsed canopy behind it. Figures 5.24(a,b) through 5.26(a,b) examine this transient collapse event for the AS-03 canopy. Figures 5.24(a,b) show contours of Mach number on the canopy major axis plane, which exhibit the formation and propagation of a 'notch' in the canopy shock, which eventually completely collapses a pocket of the canopy onto the surface. However, the steady gas flow quickly reforms this pocket, and within 10,000 s of the simulation start a stable canopy has formed. Figures 5.25(a,b) follow the collapse in contours of pressure on the same major axis plane, while Figures 5.26(a,b) exhibit the structure of the perturbation itself to be wave-like, as a high-density ring emanates outward from the pole and moves radially throughout the entire canopy, which only collapses the major axis.

The start-up process described in this work reflects the most extreme limit of a density fluctuation at the source: a step-function in density, an expansion into initial vacuum. While prior work (Zhang, 2004; McDoniel, 2015) has shown that *small* changes in density at a plume's source do not, in general, affect canopy structure or behavior, in this limit of an instantaneous start-up complex structures form, propagate along the AS-03 canopy, and induce a collapse. This phenomena appears to be physical in origin: the time and position of its formation is insensitive to processor distribution, grid resolution, and grid adaptation in altitude, and there are sufficient simulation particles (10+) in all cells in the vicinity of the collapse. It ought to be studied in more depth in future work.

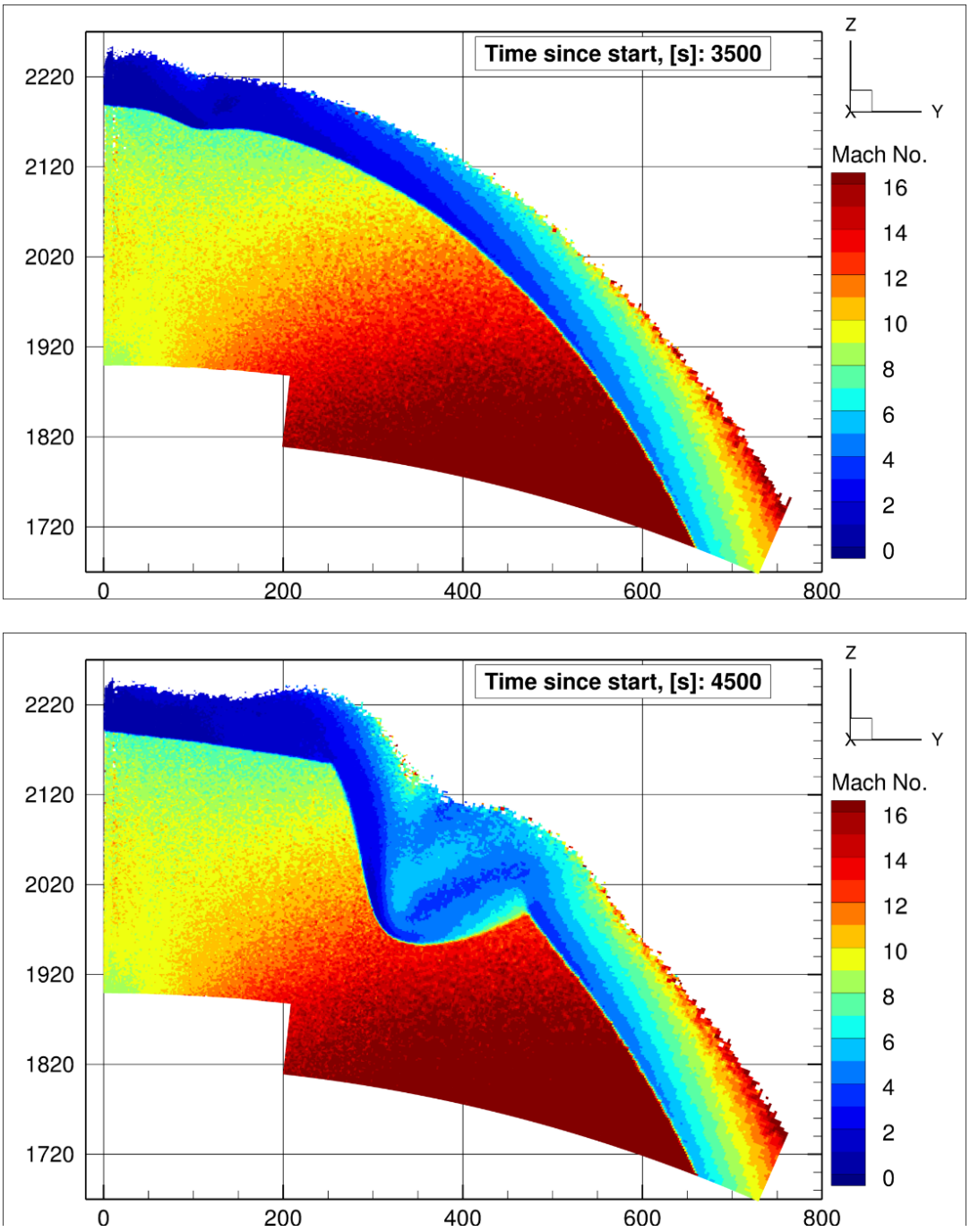

Fig. 5.24a**:** An instantaneous snapshot of a slice through the canopy major axis at 3,500 s and 4,500 s after the stage 4 start-up in contours of Mach number. A ripple begins to travel along the collisional canopy as it forms. This ripple grows as it progresses, and eventually its high density can no longer be supported by the gas rising to meet it at the canopy shock.

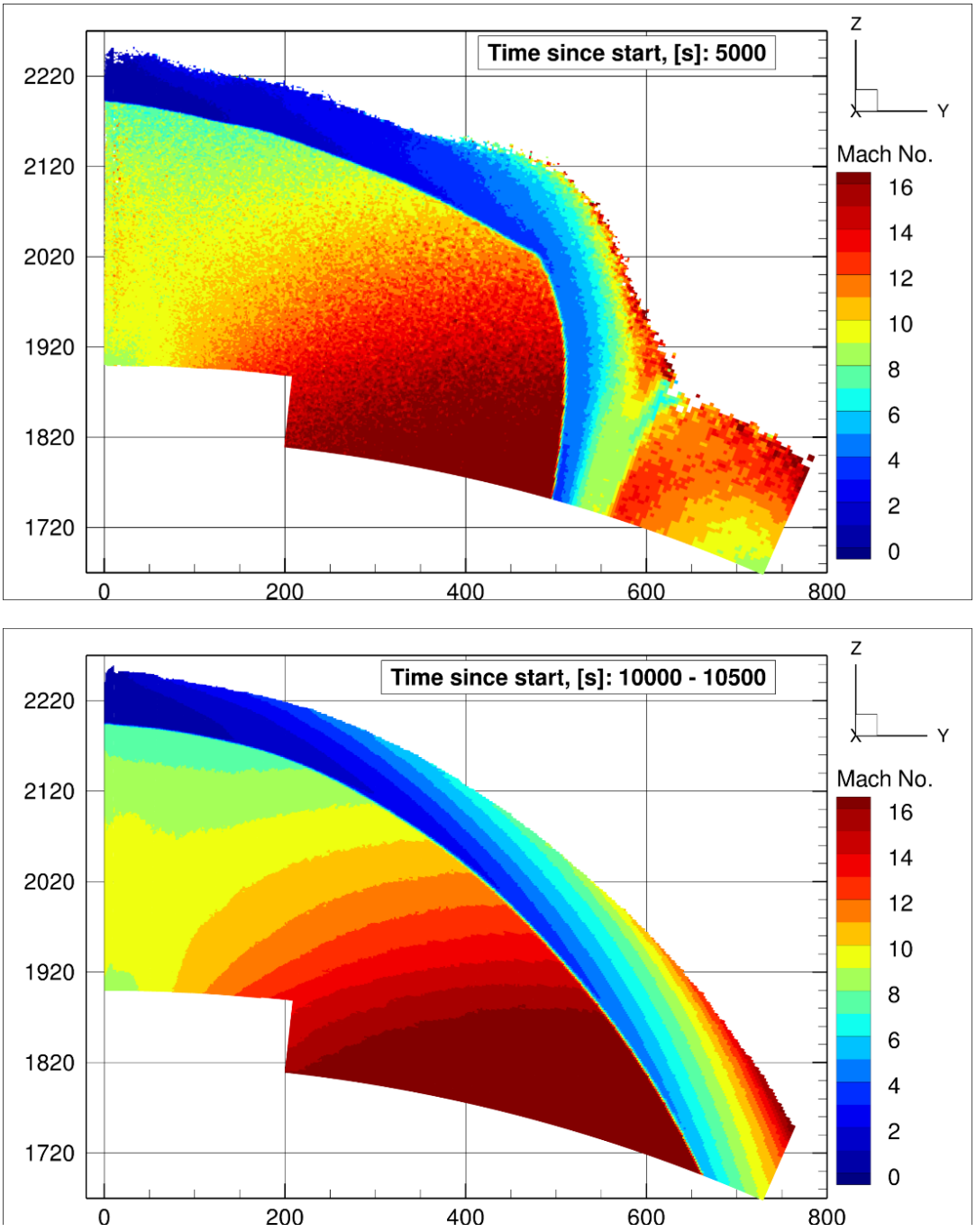

Fig. 5.24b: Slices through the canopy major axis at 5,000 s after stage 4 start-up. The perturbation has grown unstable, and ultimately collapses a portion of the canopy. After another 5,000 s, the AS-03 canopy has recovered and almost completely stabilized. This stabilizaation process features an oscillatory rising and falling of the canopy, which quickly damps.

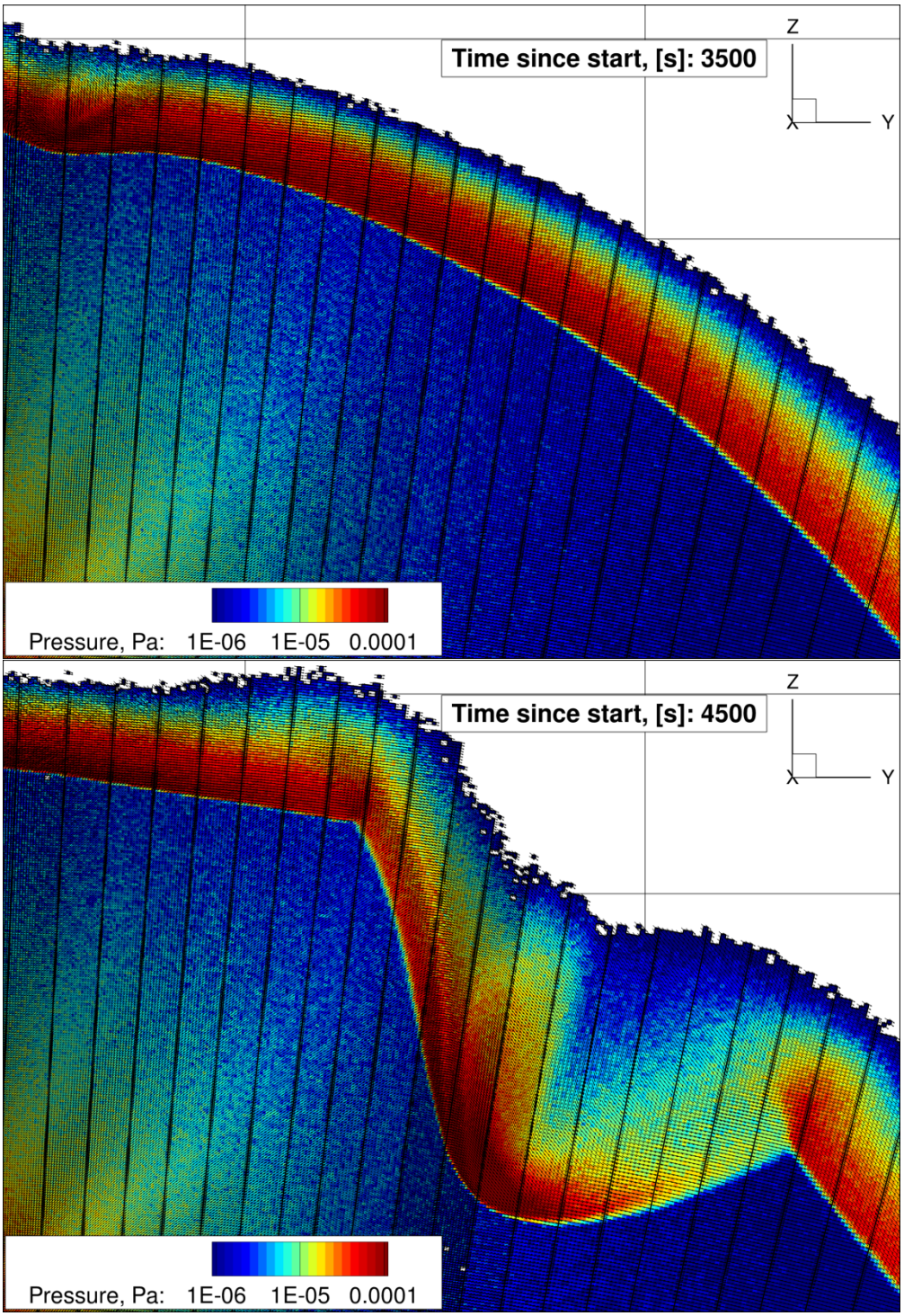

Fig. 5.25a: The start-up collapse of the AS-03 canopy is characterized by the formation of a high-density ring that propagates outward from the pole and eventually forms an unstable, high-pressure pocket along the canopy major axis.

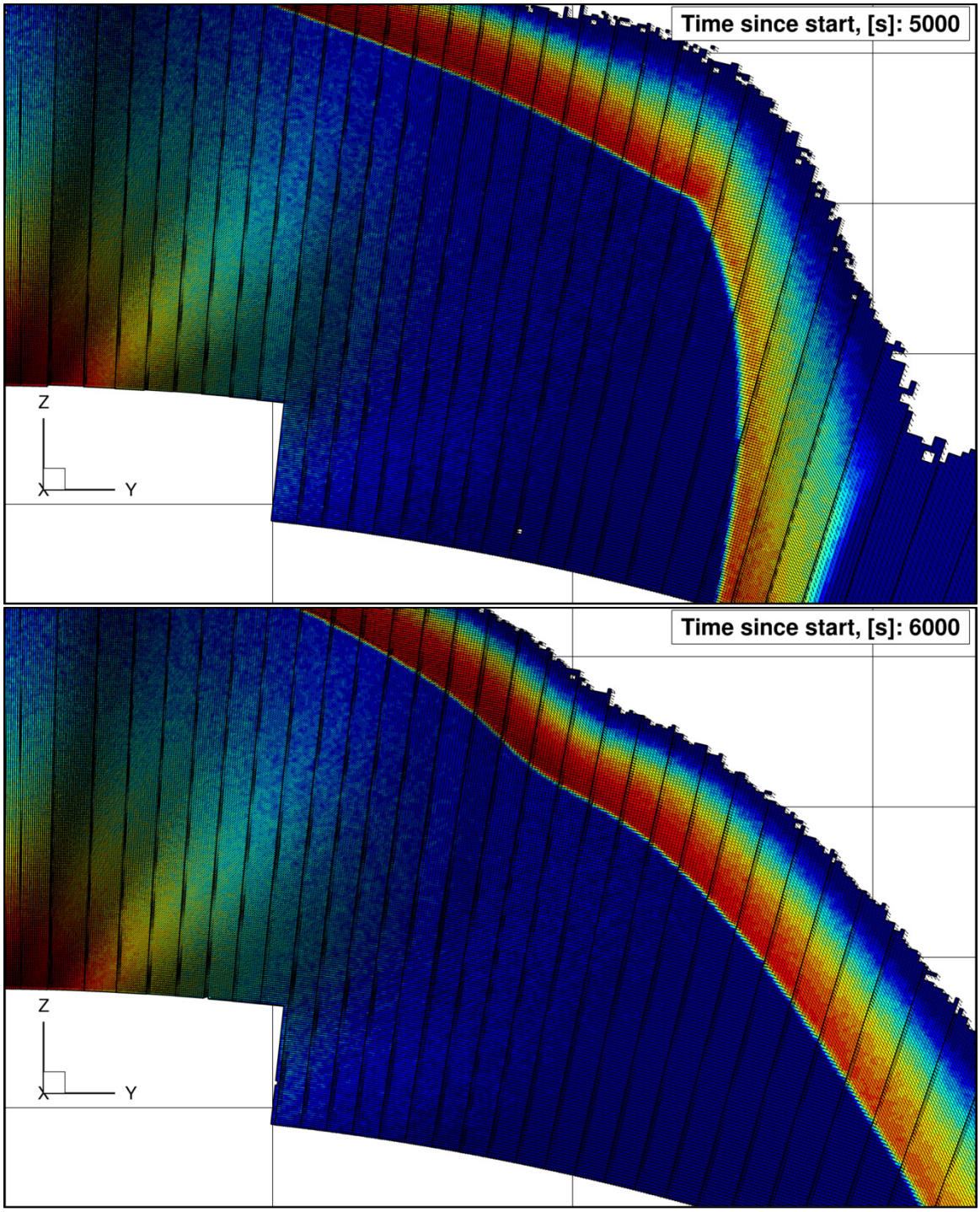

Fig. 5.25b: As the pocket collapses onto the surface, the canopy begins to reform and stabilize in its wake. (As in the previous figure, slices are shown along the canopy major axis, and colored in contours of pressure on the same scale.)

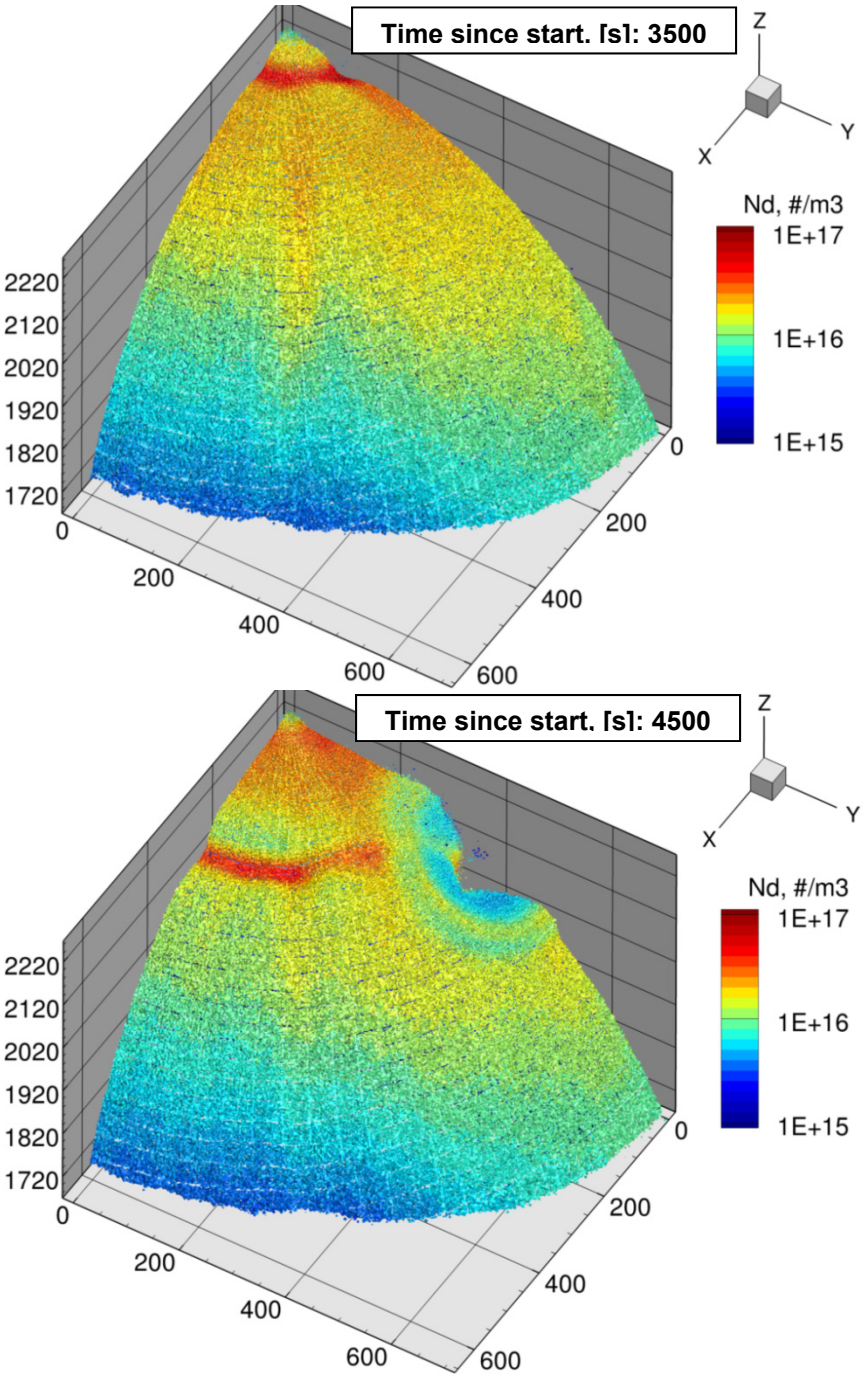

Fig. 5.26a: As the initial wave of gas falls back to the surface, it collides with the steady rising flow and a density perturbation emanates radially outward from the pole through the settling canopy. In the AS-03 case, this perturbation is observed to be unstable along the canopy major axis. These isosurfaces show the limiting upper sublimation boundary, as in Fig. 5.11(a,b).

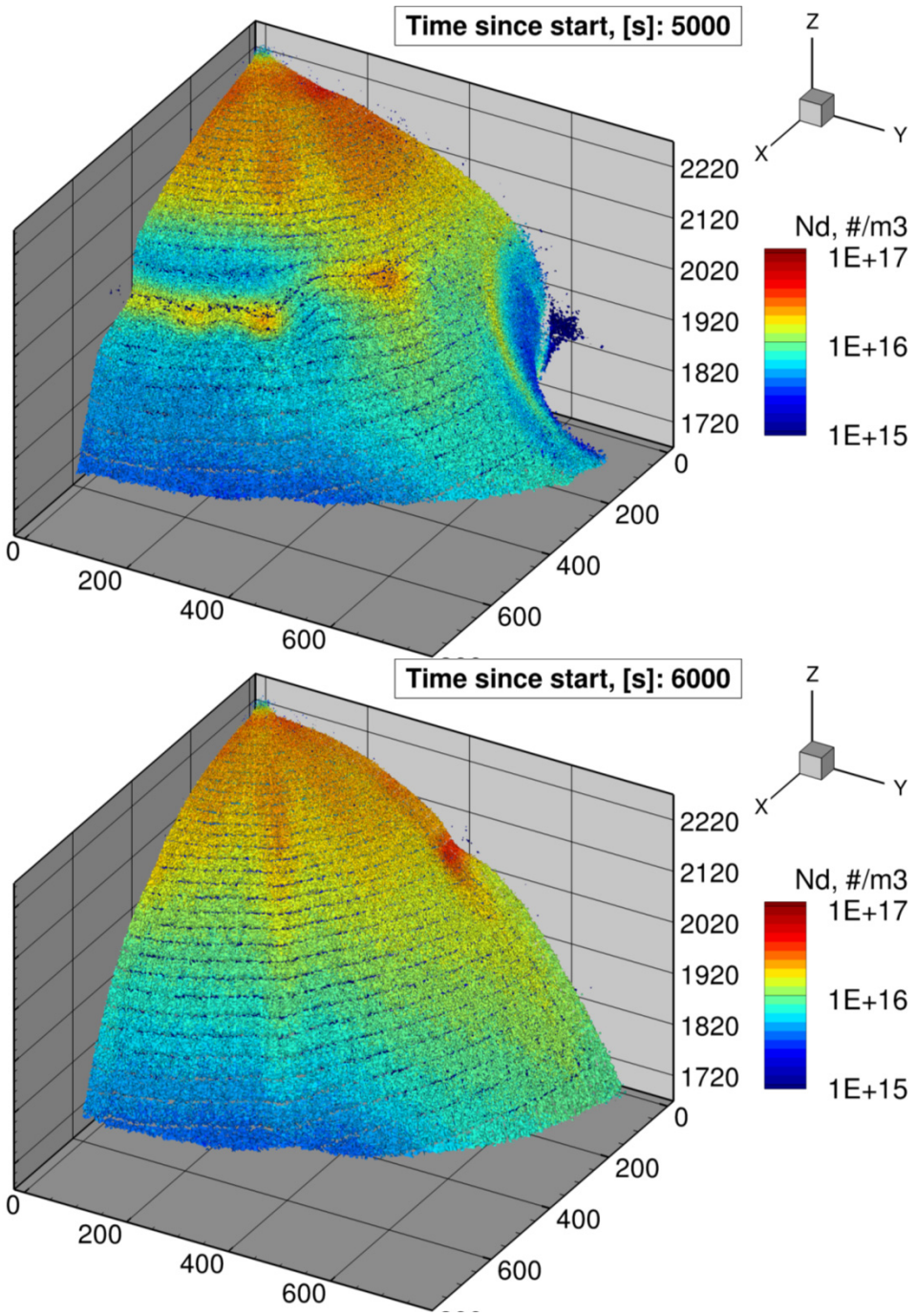

Fig. 5.26b: When the rising material can no longer support the high-density bubble, the canopy abruptly collapses to the surface completely within a localized pocket. However, it reforms almost as quickly – within 1,000 s, a canopy shock has already begun to stabilize, although it will oscillate somewhat in radius and experience smaller density perturbations for about another hour.

5.7 CONCLUSIONS[40]

Novel potential constraints on vent configuration derived from the flowfield include the extent and rate of canopy descent / slope along the vent broad axis direction; the contours of integrated column density along the vent broad direction; relative magnitude of canopy column density given knowledge of mass flow rate from the vent. Canopy height has a strong relation to initial stagnation temperature, as suggested by McDoniel (2015), which is complicated by modeling the opacity of the gas field. The extent of the depositional ring along the canopy major axis will not change substantially regardless of aspect ratio, but the minor axis direction will retreat quickly as aspect ratio increases (holding vent area constant). The AS-03 parametric condition best meets the NH observation (both in vent thermodynamic properties with direct constraints, and in indirect constraints like canopy height, mass aloft, column density, canopy shape and structure, and depositional ring shape and width). The other cases considered in this work could prove useful analogs to observations of future Pele-class plumes.

[40] Further methodological notes relevant to the simulations of this chapter are addressed in Appendix I.

Chapter 6: Conclusions

Each chapter of this dissertation is essentially self-contained, with its own review, conclusions, and outline for future work. I have collected the essential conclusions here.

6.1 A Novel Model for Earth's Rarefied Upper Atmosphere

- I present a novel, fully 3-D and transient DSMC model of Earth's rarefied neutral-density upper atmosphere: to my knowledge, this is the first such comprehensive rarefied-gas-dynamic terrestrial atmospheric model.
- Presently, upper-atmospheric simulations in the space weather or satellite operations communities are performed with either semi-empiric (i.e. non-predictive) or continuum (i.e. invalid near and above the exobase) models.
- The Earth DSMC is a *physical* model that offers predictive capability and insight into the processes driving Earth's atmosphere. It is also a *rarefied*-gas-dynamic model with applicability in non-equilibrium regimes.
- Trial simulations within 1-D and 3-D domains demonstrate the capability of this new model in a variety of configurations; notes and future work are outlined in Appendices B and C.

6.2 RGD Simulation of Transfer and Escape in the Pluto-Charon System

- I present a novel 3-D DSMC model of the plutonian upper atmosphere, including the processes of its escape and transfer to Charon.
- Pre- and post-New Horizons (NH) encounter cases are simulated and well-resolved flowfields shown for a range of solar heating cases (Appendix F).

- Density fields are shown to exhibit a gas transfer structure that arcs through the L1 Lagrange point toward Charon's trailing hemisphere.
- A simulated escape rate of 7×10^{25} CH_4 s^{-1} at encounter conditions agrees with the NH observations (Gladstone *et al.,* 2016).
- Total flux to Charon is 2×10^{24} CH_4 s^{-1} at ~98 % CH_4, with peak values (by about a factor of two) onto Charon's leading hemisphere.
- Charon may retain a thin atmosphere sourced from Pluto's escape, but below levels that would have been observable by NH.
- The atmospheric growth process and Charon's influence in gravitationally focusing or capturing the escaping plutonian atmosphere are examined in Appendices G and H.

6.3 Developing Hybrid Simulations of Io's Tvashtar Plume

- I present a novel hybrid model combining DSMC gas field simulations with a comparatively cheap particle-tracking scheme, by which the spatial and temporal scales of structure in Tvashtar's transient canopy may be simulated and traced back to their origins at the vent.
- We reproduce complex filamentary structures and tendrils that echo those observed at Tvashtar with simple variance in the parameters of dust emission at the vent.
- DSMC simulations of a Pele-like Tvashtar plume are performed that form the starting point for the parametric results of Chapter 5.

6.4 PARAMETRIC DSMC SIMULATION OF THE 2007 TVASHTAR PLUME

- Novel potential constraints on vent configuration derived from the flowfield include the extent and rate of canopy descent / slope along the vent broad axis direction; the contours of integrated column density along the vent broad direction; relative magnitude of canopy column density given knowledge of mass flux.
- Canopy height has a strong relation to initial stagnation temperature, as suggested by McDoniel (2015), which is complicated by modeling the opacity of the gas field.
- The extent of the depositional ring in the major axis direction will not change substantially regardless of aspect ratio, but the minor axis direction will retreat quickly as aspect ratio increases (holding vent area constant).
- The AS-03 parametric condition best meets the NH observation (both in vent thermodynamic properties with direct constraints, and in indirect constraints like canopy height, mass aloft, column density, canopy shape and structure, and depositional ring shape and width). The other cases considered in this work could prove useful analogs to observations of future Pele-class plumes.

Appendix A: Ionian Atmospheric Simulation

A.1 Overview and Introduction

Three primary mechanisms populate Io's atmosphere: sublimation of insolated frost, material sputtering due to the impact of energetic ions from the Jovian plasma torus, and plume emission related to volcanic activity. This complexity distinguishes Io among the satellites of our solar system (Bagenal *et al.,* 2004). Atmospheric flows are collisional at low altitudes on portions of the day-side, but rapidly trend toward the free-molecular limit with altitude and on the moon's night-side – necessitating a rarefied gas dynamic approach to modeling and analysis. To that end, the work described in this Appendix – and throughout this dissertation – employs Direct Simulation Monte Carlo methods through a planetary science code developed over the past decades within this research group. The essential physics and boundary conditions of the Ionian atmospheric simulations are complex, and have been discussed in depth in the dissertations of Walker (2012) and Moore (2011) and also in Walker *et al.* (2012a,b). They are modeled by unique functions developed primarily by those authors – including, for example, Io-specific considerations of the surface SO_2 frost map, of hot spots and their gas-field interactions, and of S and O plasma dynamics. My own refinements to the physics specific to our Ionian atmospheric model are modest and have included the consideration of photochemistry in periods of quiet and active solar activity; adjustments to our treatment of the highly-energetic Jovian torus plasma that induces surface sputter; corrections to our calculations of cell volume, of Jupiter's shadow, and our surface frost integration; the inclusion of updated rates for multi-species collisional chemistry; and the addition of a latent heat model allowing investigation of the significance of molecular

adsorption and desorption in altering surface temperature. Methodological improvements during this project included my revision of the Io atmospheric functions for their compatibility with new load-balancing schemes (McDoniel, 2015); the restructuring and commenting of much of the codebase for ease-of-use; and the introduction of a version control system with remote repository access for the planetary-atmospheric project, a step intended to streamline merges amongst group members working on disparate branches.

A.2 SIMULATING GLOBAL ATMOSPHERIC FLOWS

While learning to use and program the planetary codebase, I produced a novel set of comprehensive Ionian atmospheric calculations at sub-1°×1° resolution that capture the formation and evolution of the rarefied atmosphere to a steady-state over six orbits.

A.2.1 Details and Methodology

Given the complex, tripartite sourcing of the Ionian atmosphere, a wide variety of physics prove significant in this problem. Multiple neutral and charged gas species are featured in this work, each with the appropriate rotational and vibrational degrees of freedom. To account for the restrictive time scales of motion in the case of Jovian torus ions – which are incident onto Io at 57 km/s – multi-step overlay techniques are employed to model plasma impact, fast/charged particle transport, the diffusion of excited species, and radiation from excited rotational and vibrational states. Ions spiral along magnetic field lines, may re-accelerate or exchange charge after collision with neutral gas, and cause ion energy- and surface temperature-dependent sputtering when they strike the surface. High-energy collision outcomes from MD-QCT calculations inform the chemical reactions induced by neutral gas collisions with the rapid influx of

Jovian torus plasma at high velocities (Parsons *et al.,* 2013). Neutral gas may photodissociate or photoionize. Variable surface temperatures for the frost and dirt surfaces are determined as the moon rotates, passes through eclipse, and experiences Jupiter-shine[41]. The effects of planetary rotation, including a non-inertial reference frame, are included here for the first time.

Following the methods outlined in Walker *et al.,* (2012a,b), these comprehensive simulations are *staged* to reduce computational expense without loss of accuracy. At each stage an additional physical model is enabled, and a periodic result is achieved over multiple day-night cycles before the complexity of simulated physics is increased. Simulations extend through portions of the Ionian day with all physics packages enabled, expending O[10^4] computational hours, and are computed in parallel on the Stampede supercomputer[42]. Improvements to the efficiency of the codebase by myself and McDoniel – notably, for this work, his adoption of vectorized random number generation – and advancing supercomputer architectures allow for quicker and better-resolved calculations than were previously possible. These calculations are performed in 3-D domains that span Io's surface and extend hundreds of kilometers vertically into the exobase. Within processors, collision cells are adapted on-the-fly in the *r* coordinate and statically balanced in their latitude coordinate to tighten the resolution of the equatorial band. Results are presented for three stages as Io transits Jupiter. Thus the subsolar point is the anti-Jovian point; as the calculation starts with subsolar and sub-Jovian longitude equivalent in eclipse, these occur 2.5, 4.5, and 5.5 orbits after start-up. Flowfield results are then shown for the comprehensive simulation.

---

[41] Latent heat exchange with the atmosphere is safely neglected here, as I demonstrated it to alter surface temperatures by no more than hundredths of Kelvin.

[42] Stampede was a flagship 6,400+ node supercomputer operated by the Texas Advanced Computing Center (TACC) between 2012 and 2017. It debuted at #7 on the Top 500 list, which ranks the world's most powerful supercomputers. It was replaced by Stampede-2 in mid-2017.

A.2.2 Forming a Sublimation Atmosphere

The process of sublimation from condensed surface frost is a primary mechanism for the population of the Ionian atmosphere; it certainly drives the atmosphere's diurnal SO_2 component (Bagenal *et al.,* 2004; Jessup *et al.,* 2004; Walker *et al.,* 2012a,b). In the single-species sublimation model, insolation is shown to populate a thin, nascent atmosphere at vapor pressure equilibrium that achieves periodicity within three orbital cycles and is confined to an equatorial band. As demonstrated in Figure A.1, the non-uniform frost distribution and inhomogeneous, temporally-variant surface temperature give rise to asymmetry about the equator. Collisions are insufficient to drive SO_2 flow to the poles; as SO_2 is here modeled as condensable onto the dirt surface with a temperature-dependent residence time, it will stick near-permanently outside the sunlit band. The influence of the surface's thermal inertia is evident: peak column density lags the subsolar point by 30° longitude. A dawn atmospheric enhancement (DAE) occurs when SO_2 desorbs from the non-frost surface that heats rapidly just after sunrise.

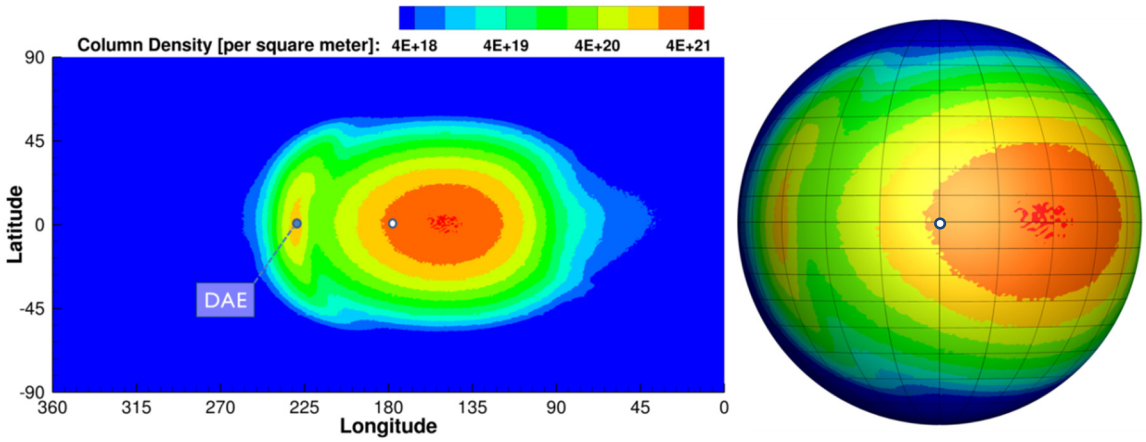

Figure A.1: A single-species sublimation atmosphere is confined to the insolated region. The column density of SO_2 (molecule count per unit area, integrated along radial lines) is shown on both an equirectangular mapping and a globe. The colorbar is uniform, and the subsolar point at 180° is marked in white. The dawn atmospheric enhancement is marked DAE.

A.2.3 Photodissociation and Multi-Species Chemistry

Multi-species chemistry is critical in shaping the Ionian atmosphere. In the subsequent stage, photo-dissociative processes are activated to populate the neutrally-charged SO_2 daughter species: S, O, SO, and O_2. Collisional dissociative reactions are likewise available, but prohibitively unlikely to occur at these temperatures (< 200 K) without the influence of charged particles. All species excepting O_2 are well-modeled as condensable onto the surface, and form a frost surface trailing the subsolar point and sublimation atmosphere, as in the right panel of Figure A.2. O_2 photodissociation rates are exceptionally slow – an order of magnitude less than any other species. Periodic solutions in the column densities of S, O, and SO are attained; without a charged-particle model, O_2 lacks a substantial loss process, yielding its resultant expansion of atmosphere to the polar zones and Io's nightside.

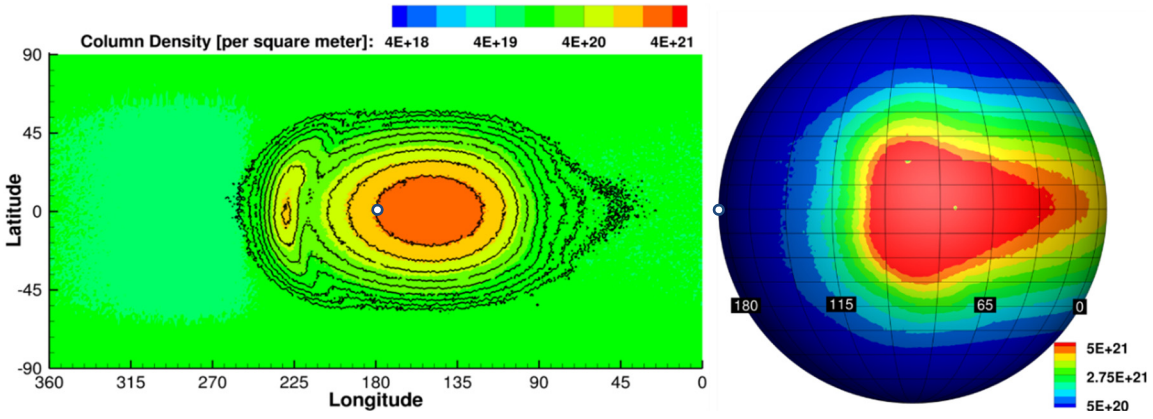

Figure A.2: Photo-dissociated daughter species populate the nightside and polar regions. (Left) The total atmospheric column density is shown in color contours, while the black lines mark just the SO_2 column. (Right) Frost deposition trailing the sublimation atmosphere, as condensable species fall onto the cold surface and stick. Those stuck to dirt may eventually be re-emitted.

A.2.4 Photoionization and Plasma Dynamics

Hyper-velocity ions from the Jovian plasma torus significantly impact Io's atmospheric dynamics. A particle-based plasma model is next activated: sulfur and oxygen ions stream into the domain through its upper boundary, and interact with neutral gas at low altitude. In addition to gravitational forces and reference frame effects, ions are subject to Lorentz forces, and tend to spiral along field lines. Photo-ionization is activated and hyper-velocity collisions prompted by the introduction of the plasma particles induce chemical reactions. Plasma – a trace species, with velocity orders of magnitude in excess of the bulk gas thermal speed – increases calculation stiffness. The magnetic field angle with respect to the equatorial plane at the moment of transit results in an inclination of the trailing (dusk) edge of the atmosphere, as observed in Figure A.3.

A.2.5 The Complete Atmosphere

In the multi-species atmosphere with plasma and magnetic field effects, simulation molecules are cloned up by a full order of magnitude (to O[10^6] per processor) and allowed to collide without limitation. Evolution of global wind patterns as observed by Moullet *et al.* (2008) requires resolution of the collisional nature of the Ionian atmosphere. Consistent with Walker *et al.* (2012a,b), I observe circum-satellite flow that is asymmetric about the subsolar point and drives atmosphere from the warmer, dayside hemisphere toward the colder nightside and poles. The structure of this velocity field is demonstrated for O_2 in Figure A.4, while Figure A.5 shows the extent of the Ionian atmosphere in altitude and latitude on its dawn and dusk edges and its number density at the surface. The dawn hemisphere shows a less developed atmospheric column than the dusk hemisphere: the sublimation atmosphere is asymmetric about the subsolar point, reflecting the thermal inertia of the moon's surface.

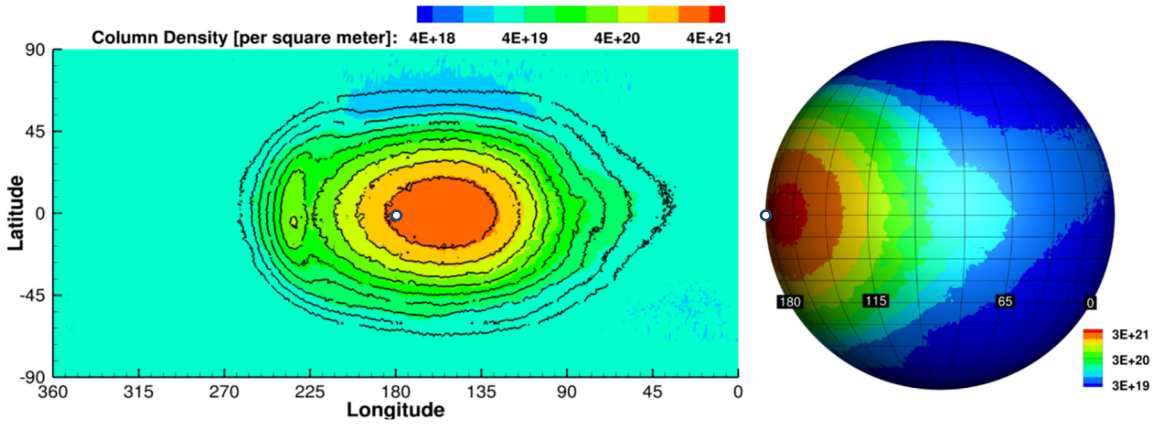

Figure A.3: Incident plasma works to thin the nightside atmosphere to a steady-state, physical configuration, and it increases overall flow asymmetry. (Left) Total column density in colored contours, with black lines marking just the SO_2 column. (Right) Total column density of the dusk atmosphere in m^{-2}; note the different colorbar for this figure. Plasma introduces N-S asymmetry.

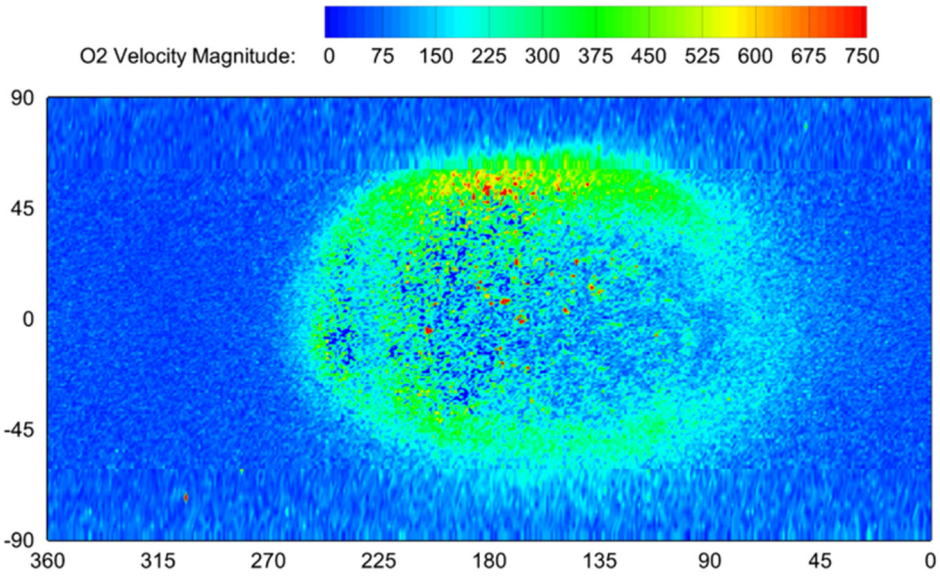

Figure A.4: The speed of O_2 [m/s], shown on an instantaneous planar slice at 20 km altitude. High speeds occur around the sublimation atmosphere's perimeter, as neutral species are driven away from the high-pressure insolated zone and toward the low-pressure nightside and poles. The highest-speeds, flecks of red, are either the result of an O_2 forming in a plasma- or photo-induced SO_2 dissociation, or colliding with a particle that was energized in such an event.

A.3 ADDITIONAL AND FUTURE WORK

Following the presentation of this work at the 2013 Division for Planetary Sciences conference and the Io Workshop, a number of improvements were made to the planetary DSMC codebase; both to the Io application specifically as outlined in this Appendix's introduction, and to the broader codebase as addressed throughout the remainder of this dissertation. A treatment of active and quiet sun cycle photo-chemistry rates was incorporated, as was a scaling of solar flux with Io's distance from the sun. These modifications substantially alter the production of nightside O_2 and condensable daughter species in the sublimation atmosphere, although the overall effect is simply that of a uniform scaling of the total column density, with perhaps a factor of two higher density in the quiet case. A number of revisions were made by McDoniel and myself to the plasma generation routines, including corrections to the generation of inward flux that may substantially change the overall atmospheric result. McDoniel (2015) demonstrated the updated version of `PLASMA` in its interaction with the Pele canopy, and I tested it in a number of frost sputtering cases (e.g. Figure A.6) but its effect on the complete atmospheric model remains unexamined[43]. Fig. A.6 demonstrates the sputtering process on its own, without a background sublimation atmosphere, and onto a uniform frost surface. Incident high-velocity S and O ions from the plasma torus create a striking pattern on the Ionian surface, which is comparable to observed patterns of plasma-induced heating on two of Saturn's moons. Figure A.7 shows a test of the sublimation model with adaptive load-balancing[44] and radial weighting around hot spots, during the atmospheric start-up on 1152 cores – these features are essential to the next generation of

[43] It may be worth testing the high-order integration scheme of Appendix E in integrating the Lorenz equations for charged particle motion to reduce the necessity of substepping to resolve gyro-radii.
[44] And surface thermal inertia and residence time functions rewritten to be consistent with a dynamic grid.

simulations because of the computational limits otherwise imposed by the severe dayside/nightside imbalance in Ionian atmospheric density. I have checked that individual components of the revised Ionian model function properly post-merge, but have not run all of them simultaneously in a comprehensive calculation. I expect the many changes made to the planetary codebase since 2013 will significantly alter the results of these comprehensive atmospheric calculations. In future work, this project could readily be continued with a series of full-scale simulations to evaluate the influence of the new physical and methodological refinements, and to compare new results against prior computations and observations in the literature – specifically observations of atmospheric collapse during eclipse.

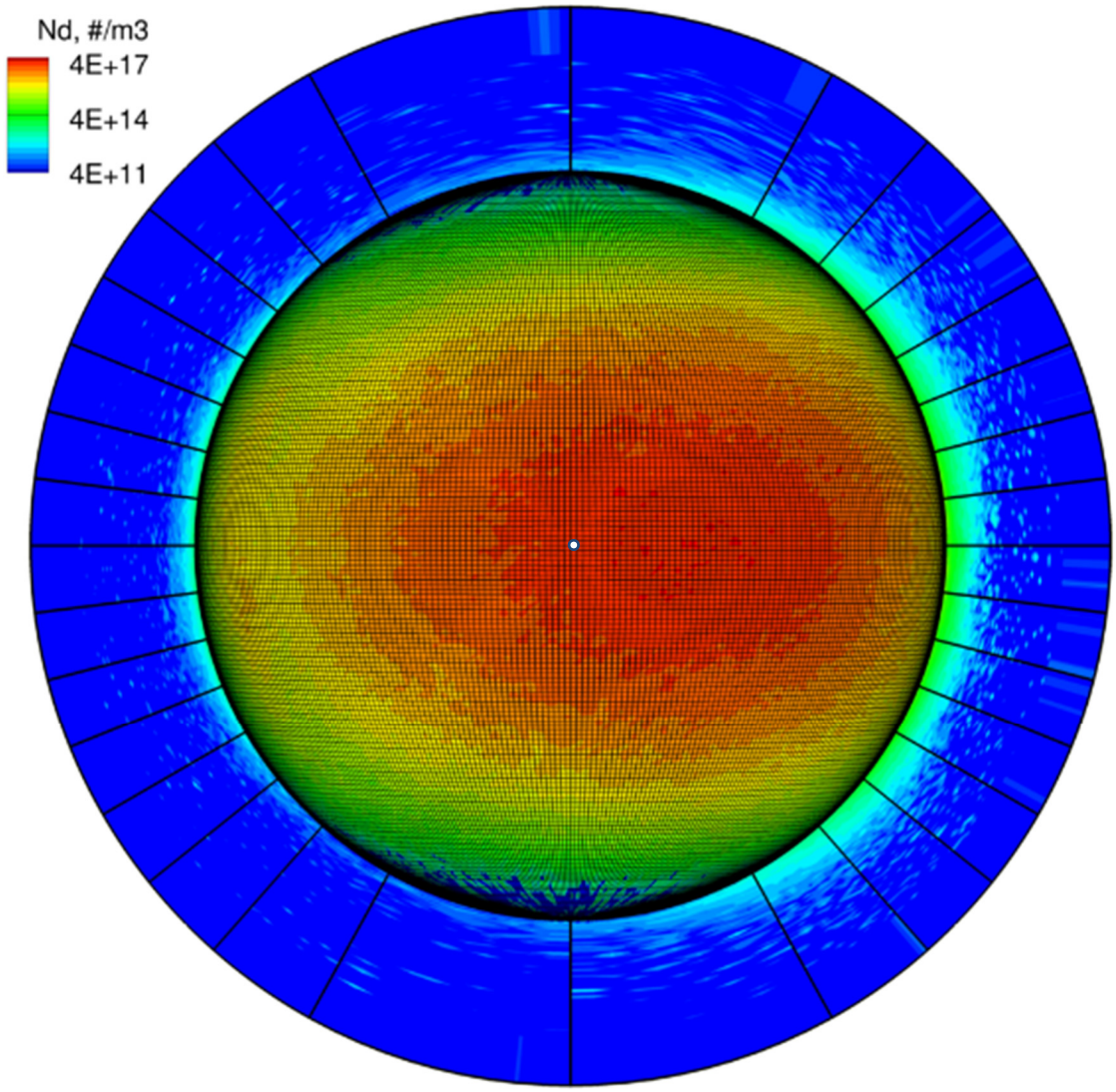

Figure A.5: The total number density [m^{-3}] is shown in color contours both on Io's surface and in a plane cutting through the polar axis and origin and normal to the viewer that extends to 800 km altitude. The view is directly down onto the subsolar point, positioned at the anti-Jovian longitude of 180° as in the previous figures. Collision cells in latitude and longitude are drawn on the surface; resolution is O[1°×1°] and, at the equator, 0.7°×0.9°.

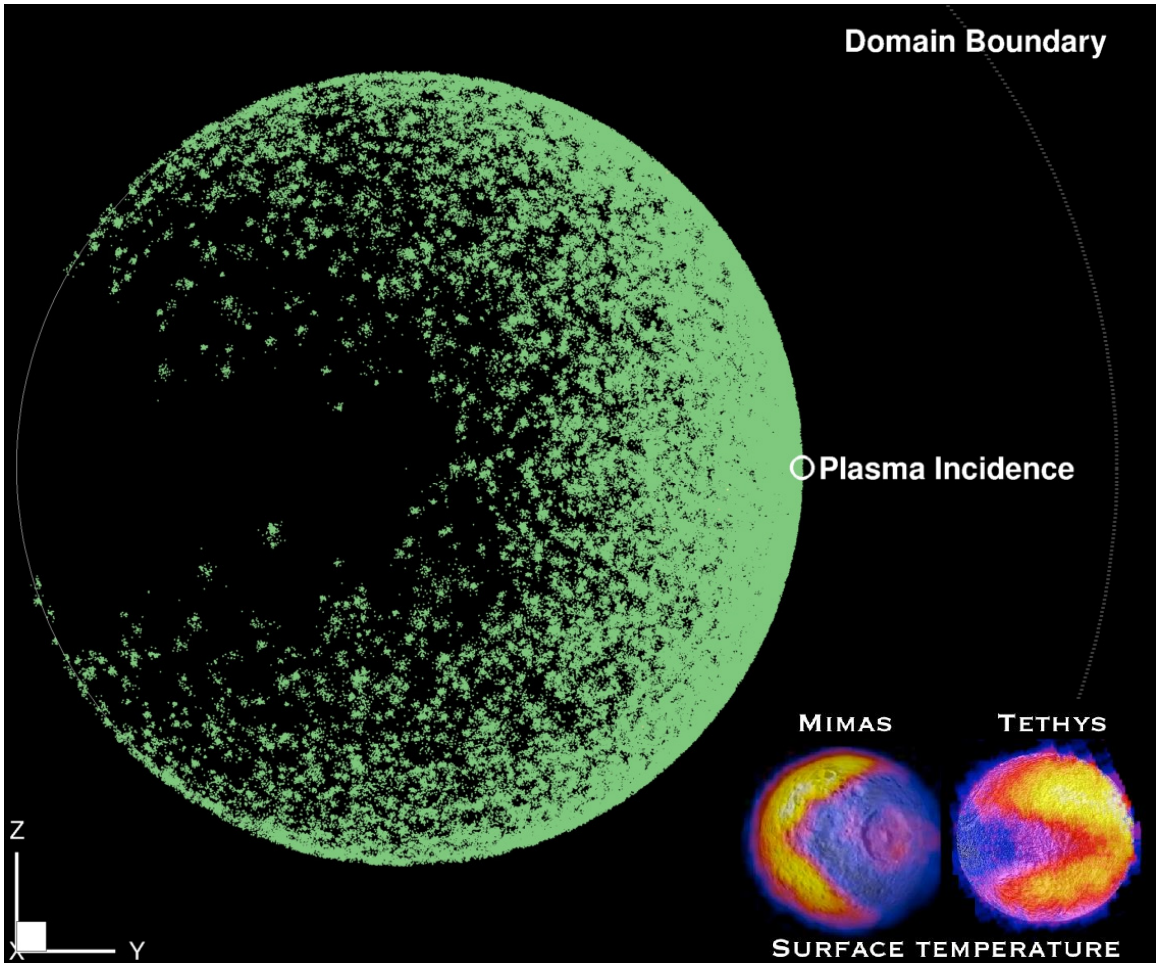

Figure A.6: The sites of sputtering events along Io's surface. Bulk plasma flux (charged S / O), incident at 57 km/s relative to Io's surface, spirals along field lines and sputters SO_2 from surface frosts, while collisional and photo-chemistry yield daughter species. Plasma incidence onto Io from the Jovian plasma torus evokes the 'Pac-Man' patterns of surface temperature observed on Mimas and Tethys thought to be caused by comparable charged particle incidence as they orbit Saturn. (Inset: NASA/JPL-Caltech/GSFC/SWRI).

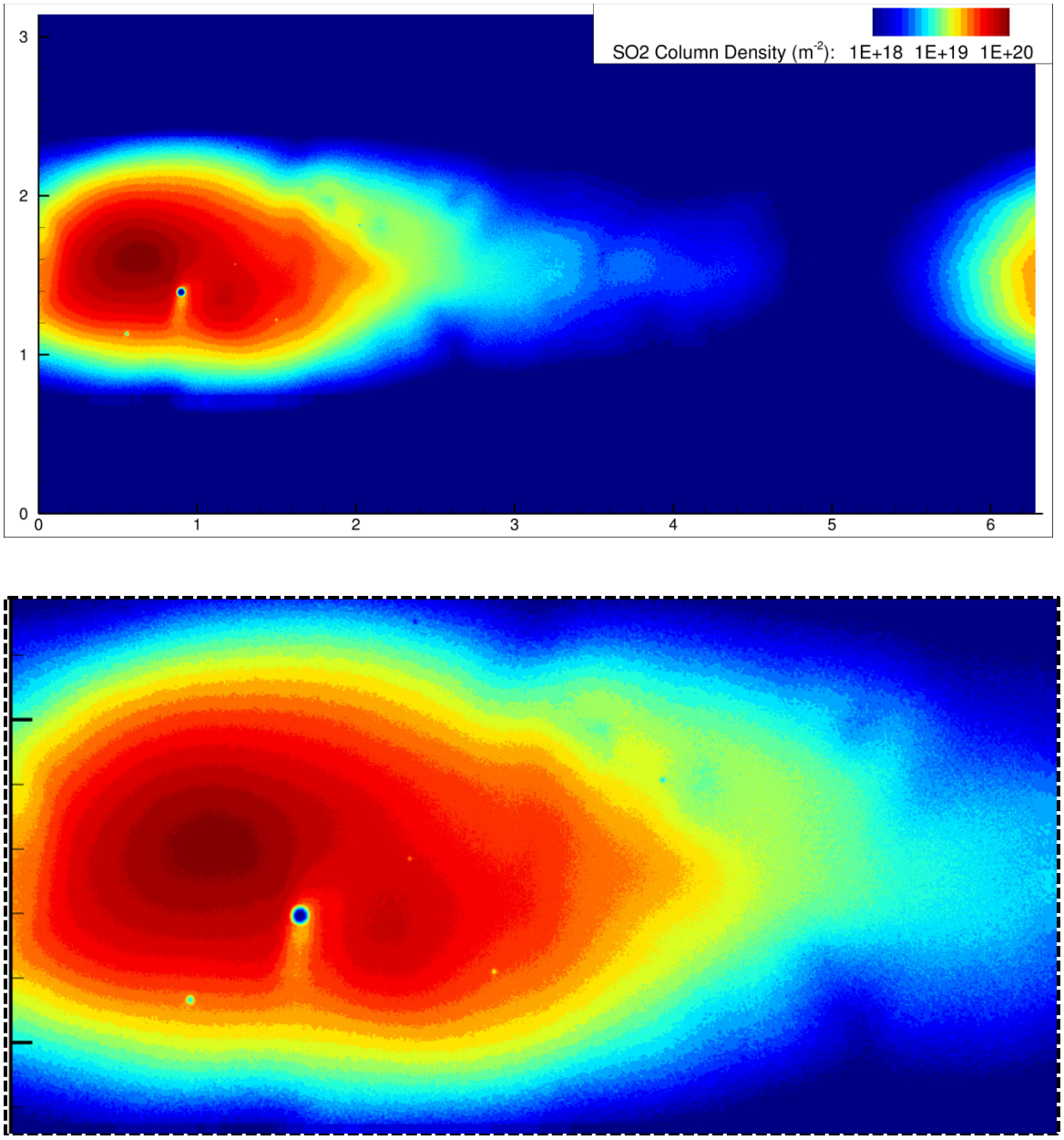

Figure A.7: Column density of SO_2 shown during the start-up of a 1152 processor calculation incorporating all code refinements and modifications, including adaptive load-balancing coupled with local weighting schemes around hot spots. The cell resolution of such calculations is far higher than previously possible, and the code, and supercomputers, are now developed enough that staging may no longer be necessary.

Appendix B: Toward Future Earth Atmospheric Work

B.1 Overview

I developed the Earth code during the summer of 2014, as outlined in Chapter 2. In order to keep that code compact for future distribution – and to help me, a relatively new user, navigate its complexity – I built as streamlined a version of the planetary DSMC as possible. In doing so, I opted to eliminate many complex features developed by prior users that could serve no purpose in terrestrial upper-atmospheric simulations, including trimming features related to surface processes (i.e. sputtering), cutting ground flags from the molecule structure, eliminating the patching and impact / interface routines used in the lunar comet simulations and the plume creation routines used in simulations of volcanism, and so forth. I also revised and commented much of the code for clarity, most notably `main.c` and the precompiler definitions file `defs.h`.

B.2 Review of Alterations and Additions Unique to the Earth Code

The first major alteration I made to the extant codebase was to link it with a C distribution of the NRLMSISE-00 semi-empirical terrestrial atmospheric model, and to develop the generation subroutine for upward flux through an arbitrary mid-atmospheric lower-boundary surface. The second was to link with the shielding and attenuation and Monte-Carlo photon transport subroutines developed by Prem (2017), and to adapt them to heat trace species in the terrestrial thermosphere via rotational absorption.

Other, secondary alterations include a number of modifications to our linear segments and exponential grid generation routines, including their generalization for cases in which the simulation lower boundary surface is not necessarily the planetary

surface; the introduction of a standard, uniform date and time into the code linked to our sun position (in the longitude coordinate); the incorporation of a number of new species, including the seven sourced by MSIS and a number of supplementary trace absorptive species; and the ability to toggle between photo-rates for quiet and active solar cases to better match specific dates.

While I later adapted the Earth code for my plutonian atmospheric simulations, including such major functional changes as rewriting our integration routines to use high-order, adaptively-stepped schemes from the GSL library, I did not port those changes backward into the Earth code, and it remained an unmaintained branch until only recently. At the point of its branching, the Earth codebase, an extension of the branch developed by Walker (2012) for the Ionian atmospheric simulations, hadn't been merged with our other codes for several years.

A first step in the continuation of our Earth upper-atmospheric simulations was to introduce the improvements and bug-fixes developed in the interim. Of primary importance are the replacement and revision of the shielding and photon transport routines from Prem's work (2017), which were incomplete in 2014.

B.3 Preparing the Earth Code for New Simulations

In Oct. 2017, I merged the Earth code with Prem's final branch and performed a limited selection of tests on its basic functions to ensure they hadn't been compromised. Significant testing still needs to be performed to ensure the code's physics operate accurately; however, testing of the essential radiative functions will have to wait until those functions are adapted for Earth's complex, multi-species environment. Without modeling radiation from molecular rotational or vibrational states (now toggled by

ROT_COOLING and VIB_COOLING, respectively), and likewise without accounting for photo-dissociation (PHOTO), a 240-processor transient calculation of the full terrestrial atmosphere above 300 km evolves to a state commensurate with the MSIS expectation, as demonstrated in Figure B.1. This calculation interfaces correctly with MSIS on its lower boundary, initializes and progresses smoothly across three hours of the diurnal cycle, applies a linear segments scheme with an initially exponential profile in adapting its cells with altitude, and can be stopped and restarted without issue.

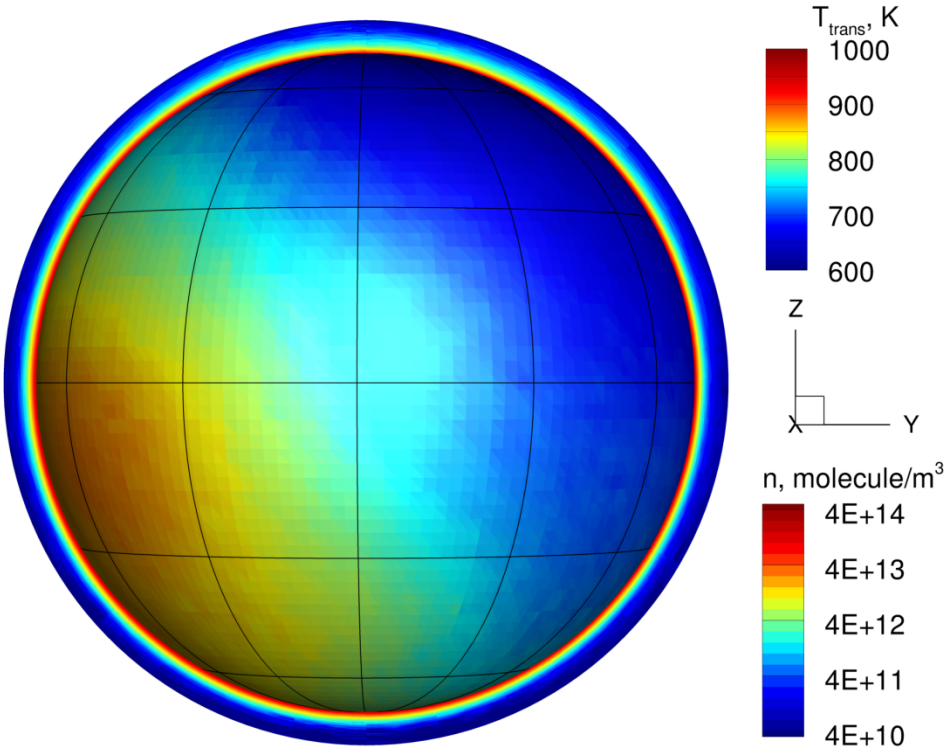

Figure B.1: A time-averaged flowfield between 22:47 and 22:57 UTC after three hours of simulation is viewed looking directly downward onto (0°, 0°). The lower boundary surface at 300 km altitude is colored by the DSMC translational temperature, and drawn with latitude and longitude lines spaced 30° apart. A slice through the atmosphere is colored exponentially by number density and extends up to 1000 km. At 120 CPU-hrs, this is an inexpensive result.

As-is, all radiative functions – e.g. `shielding()`, `mc_photons()`, etc. – compile when toggled on but their use has not been tested for the terrestrial case, and they will require significant edits to reflect atmospheric conditions markedly different than the lunar environs for which they were developed, which I outline below.

The lunar impact work specifically addressed rotational absorption / emission from water, so it will be necessary to extend Prem's functions to consider the wider variety of species present in the terrestrial upper atmosphere – specifically the trace, absorptive species. On Earth, almost all neutral gas above 500 km is monatomic: above 500 km He and H dominate, while O is generally the predominant species between 300 and 500 km. O_2 and N_2 are the only diatomic species generated by MSIS; neither absorbs appreciably into its rotational states[45], and both are trace above 300 km. Heating instead occurs through species with permanent dipoles, most notably NO at high altitudes but potentially including OH, H_2O, and CO if calculations are pushed substantially below 300 km. It will thus be necessary to edit `shielding()` and `mc_photons()` to loop over such species; the necessary line-by-line absorption rates for each may be sourced from HITRAN, and transformed as outlined in Chapter 3 of Prem's dissertation (2017). Figure B.2 demonstrates the NO rotational absorption line strengths S for lines with values exceeding a minimum cutoff of 10^{-23} $cm^{-1}/(molecule/cm^2)$ for a HITRAN query of wavenumbers between 1 and 500 cm^{-1} at a reference temperature of 300 K (with results above the cutoff falling between 11.7 and 147.8 cm^{-1}).

NO, and any other trace absorptive species not represented in MSIS, will need to be sourced through an additional code or results in the literature. For instance, Marsh *et*

[45] O_2 has a weak absorption near 760 nm that is electric dipole forbidden but magnetic dipole allowed. Though the absorption is weak it can have an effect over kilometer path lengths. This creates a population in a low lying electronic energy level. Rotation and vibration states may be simultaneously excited. (Personal communication, P. Varghese, Oct. 2017).

al. (2004) developed a relevant model for NO in the lower thermosphere (between 100 and 150 km) by performing an empirical orthogonal function analysis on the observations of the Student Nitric Oxide Explorer; the model, NOEM, takes inputs similar to MSIS.

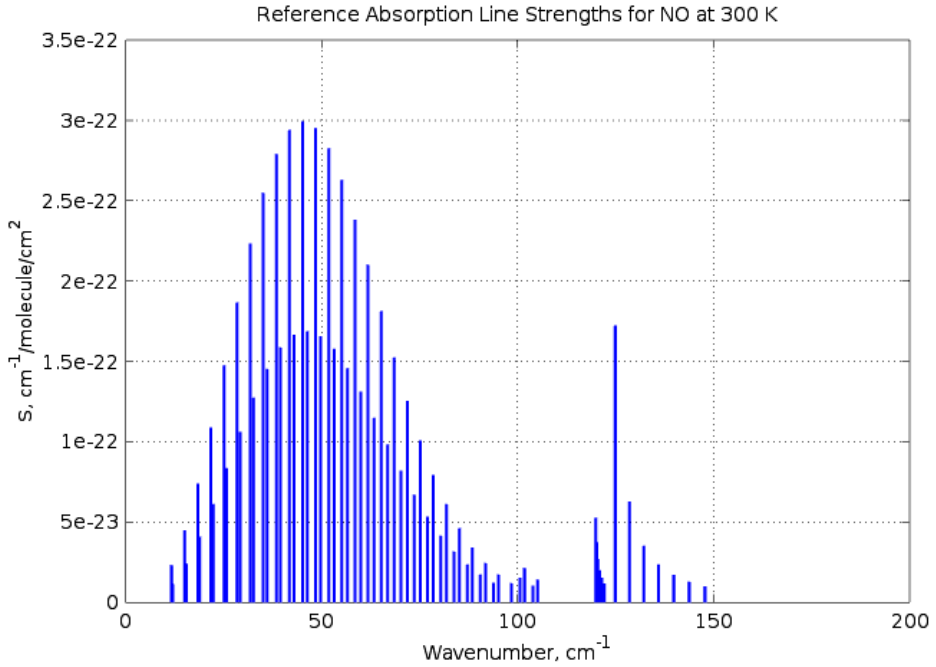

Figure B.2: A selection of the strongest line strengths for NO as a function of wavenumber, in units of $cm^{-1}/(molecule/cm^2)$, as reported by HITRAN.

In the lunar environs, Prem argued that temperatures are low enough that vibrational absorption can be neglected as vibrational states won't remain populated – this may not be the case for Earth, where upper-atmospheric temperatures range from 600 to 1200 K. Extending the radiative code to cover vibrational absorption would be non-trivial, not least because the planetary DSMC models rotation as continuous but accounts for quantized vibrational states. Bird reports a vibrational characteristic temperature for

NO of 2719 K, so we can conclude that vibration may be appreciably excited: for instance, evaluating the internal energy relation

$$\frac{e_{vib}}{RT} = \frac{\theta_v/T}{e^{\frac{\theta_v}{T}}-1} \tag{B.1}$$

at the high end of our expectation for Earth's atmosphere (i.e. 1200 K) returns ~0.26, demonstrating an appreciable vibrational contribution to total internal energy. CO and OH have higher characteristic temperatures of 3103 K and 5360 K, respectively.

Dynamic load-balancing as developed by McDoniel (2015) and Prem (2017) was not included in the updated Earth code. Column density integration along radial lines through the upper terrestrial atmosphere demonstrates a factor of merely 2–3 difference between the minimum and maximum values across the planet at any given point in the diurnal cycle, as demonstrated in Figure B.3. As we divide the domain between processors in latitude and longitude, this column density is a good proxy for molecule count, which is itself a useful proxy for computational expense. During a diurnal cycle we can expect the densest pockets of atmosphere to progress across the globe in the longitude coordinate with sunlight, and to remain adjacent to the equatorial band. Therefore, a static distribution that allocates processors to maintain roughly equal *surface areas* and *volumes* by non-uniformly spacing boundaries in the latitude coordinate – i.e. by stretching the span of polar processors, and commensurately shrinking equatorial processors – ought to adequately load-balance any standard 3-D terrestrial neutral-density calculation in which expense can be expected to scale with molecule count. I found such processor distributions effective in my early Ionian atmospheric simulations. Alternately, one might apply a processor-by-processor weighting scheme to *force* each to have an

equivalent particle count; Walker (2012) and Moore (2011) prototyped such a scheme for Io, which remains in the code as `ADAPT_WEIGHTS`. I have not tested it thoroughly in the new Earth code though preliminary checks did perform as expected. I used the adaptive scheme in producing several of the smooth column density integrations shown in Ch. 2 (which may be compared against the visible noise in the uniformly weighted Fig. B.3).

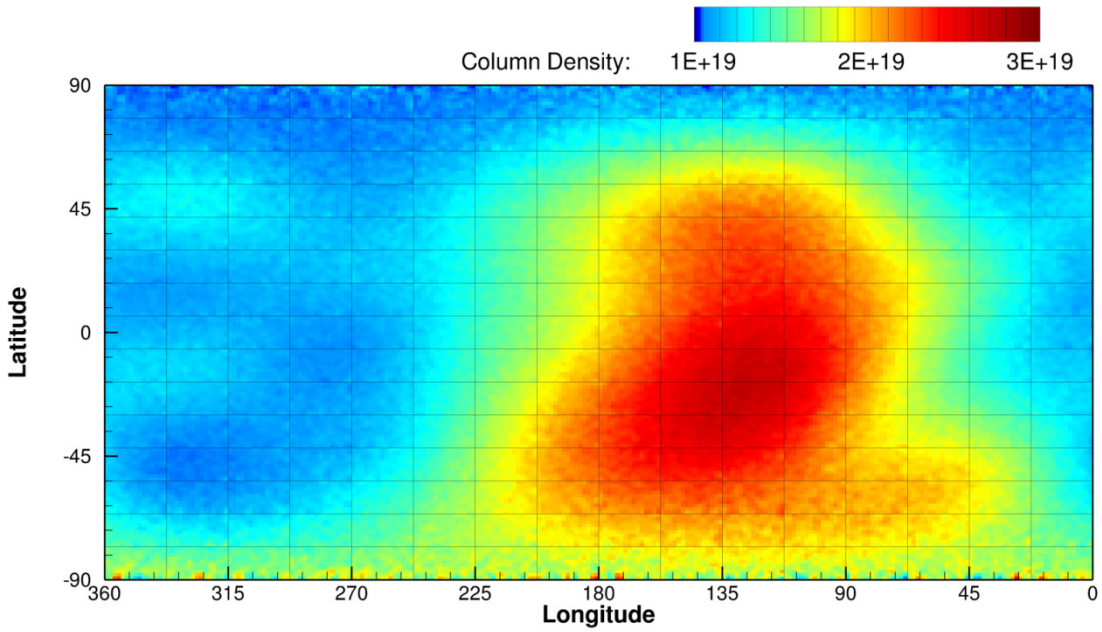

Figure B.3: Total column density above 300 km, integrated along radial lines through the representative calculation. The subsolar point is at 162° longitude, but peak atmospheric temperature and density lag behind it by several hours. Lines reflect static processor boundaries; this equirectangular distribution is naïve, as it forces polar processors to cover far less volume than their equatorial counterparts with the same number of cells.

At present, the Earth code generates flow on its lower boundary without any surface-tangential bulk velocity components; in reality, this condition ought at least to

reflect pressure-driven zonal and meridional winds.[46] A useful empirical model for this purpose – particularly in the lower thermosphere – might be the Horizontal Wind Model, most recently released as HWM-07 (Drob *et al.*, 2008). Bulk horizontal velocities generated by HWM-07, or by coupling with a full GCM, could simply be superposed with the upward flux through the DSMC lower boundary surface to provide a more realistic initial condition.

Even without radiative heating or photo-dissociation routines active, the planetary DSMC evolves to a transient solution quite similar to that suggested by MSIS, as shown in Figure B.4. Note that the top-left panel has all cells blanked with fewer than two representative molecules; this representative calculation is underresolved at altitude. In fact, its 240 processors held anywhere from 18,000 to 500,000 molecules each during the flowfield sampling, with a uniform F_{NUM} of 2×10^{26}. Decreasing F_{NUM} to improve resolution would increase the molecule count by the same proportion in each processor, so some form of load-balancing (i.e. `NON_UNIFORM_THETA` or `ADAPT_WEIGHTS`) should first be applied in improving on these results.

[46] I have observed that appreciable pressure-driven winds *do* evolve in the DSMC-simulated atmosphere to O[10 m/s] magnitudes, albeit from the physically-unrealistic boundary condition of a windless mid-atmospheric generation surface.

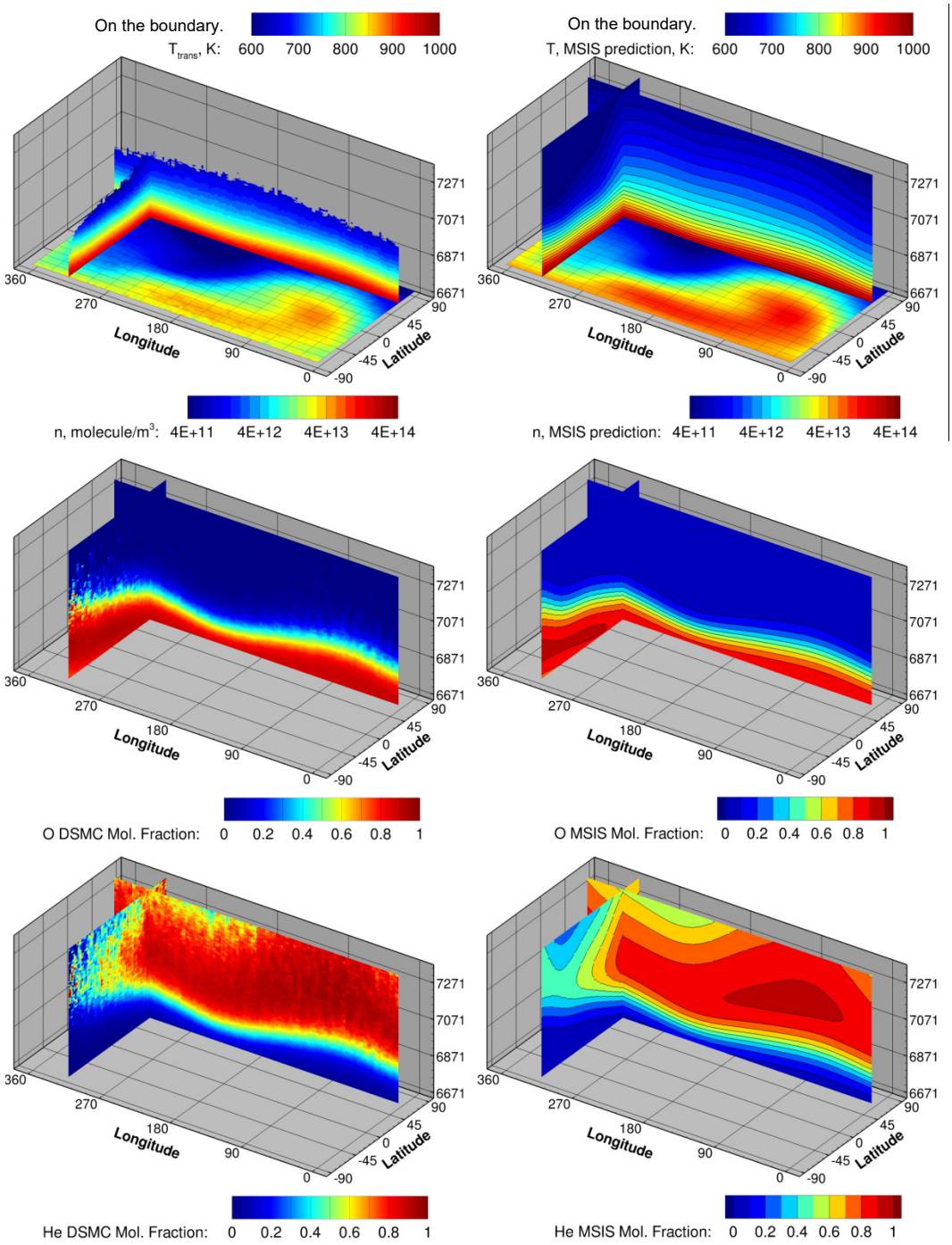

Figure B.4: At left, DSMC-calculated properties throughout the representative flowfield; at right, their MSIS-predicted counterparts. The lower surface is at 300 km altitude, and two additional orthogonal cut-planes are shown up to 1000 km: one at 60° latitude, the other 315° longitude.

Note that the lower surface of the top row, drawn at 300 km altitude (6671 km in radius from the origin), shows the DSMC translational temperature to be substantially lower than the MSIS temperature on the generation surface. This result is probably linked to the lack of any radiative or photo-dissociative models that could induce heating, as I observed in the 1-D and 3-D results of Chapter 2 that calculations with the earlier (i.e. 2014) versions of the code do closely match MSIS temperatures on the boundary surface.

For this case, each cell column uses 40 `LINEAR_SEGMENTS` to distribute 400 collision cells in altitude along an adaptive, near-exponential profile. This version of `LINEAR_SEGMENTS` is based on that developed by Moore (2011) for the Io work, with modifications made to permit multi-species calculations with arbitrary lower boundaries. It has the desirable trait of sizing collision cells to resolve density gradients in altitude, but permits adjacent cells and processors to have quite different profiles as a result of natural DSMC noise, which can lead to jagged and often incoherent flowfield sampling output when visualized in Tecplot. To avoid this problem, `OUTPUT_GRID` can be useful to impose a uniform cell distribution with altitude. Note also that McDoniel (2015) wrote an alternate version of `LINEAR_SEGMENTS` for application to Pele: the atmospheric version implicitly assumes that density falls off monotonically with altitude, which is not the case for canopy-shock problems. That version features an additional precompiler switch for smoothing cell distribution profiles between adjacent columns, which could be adapted for the atmospheric case as a standalone function.

Finally, note that solar incidence ought to be adjusted to reflect Earth's 23.5° axial tilt, and, if gravitational waves or tidal effects are of interest, the moon's position ought to be added and tracked as a function of date and time and its influence on the equations of motion accounted for in the integration function (i.e. `trans()`).

Appendix C: Notes on the Significance of Collisional Effects on Upper-Atmospheric Simulations

C.1 Overview

Whether and to what extent collisions influence the upper-atmospheric flow in a DSMC calculation depends largely on the selection of the lower boundary condition as a function of Kn_H, defined as the ratio of the characteristic mean free path to the atmospheric scale height. Ideally, that boundary is selected at or just below the transition to rarefied flow at Kn_H O[0.1], such that it is still reasonable to represent the upward flux as Maxwellian; pushing too far below this limit increases computational expense and, for many problems, there are inexpensive continuum or hybrid methods that can be trusted in such regimes. When selecting such a boundary, consider that density and thus molecule count scale roughly exponentially with altitude, but also that evaluations of `collide()` are, on the whole, more costly than `move()` – as the generation boundary pushes into the continuum regime, expense grows nonlinearly with the number of computed collisions. However, simulating these collisions appropriately as the flow transitions to the rarefied regime is essential to accurately represent atmospheric physics and escape processes.

C.2 The Influence of Collisions in Promoting Flux to Charon

I considered this problem in some depth in the course of the Pluto-Charon work, including examining the flux to Charon to steady-state at Case A conditions both with and without accounting for intermolecular collisions, i.e. collisional and ballistic flow respectively. The easiest way to achieve a ballistic result in the planetary DSMC code is to comment out the call to `collide()` in `main.c`). As seen in Figures C.1 and C.2 and

noted in Chapter 3, I found collisions enhance the flux to Charon by O[10 %] and reduce the bias in favor of the origin of this flux from Pluto's Charon-facing hemisphere. I also examined the selection of the lower boundary surface itself, varying it in altitude while drawing density and temperature conditions from the results of Tucker *et al.* (2012). The boundary surface selected for the Case A simulations, at 3000 km from Pluto's center, reflects a Kn_H of ~0.4: this value was chosen to balance expense against the accuracy of generating increasingly non-equilibrium flow from a Maxwellian distribution. I did not observe marked different solutions between this case and one with its boundary Kn_H ~0.2.

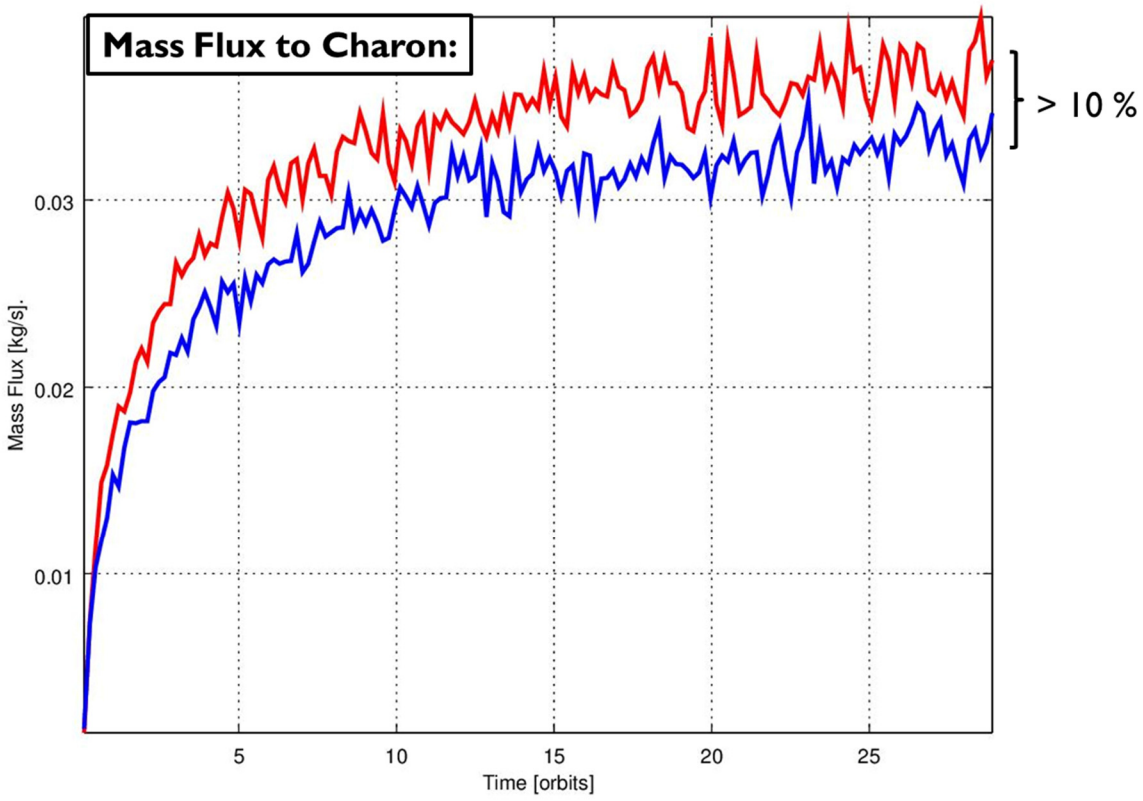

Figure C.1: Collisional (red) and ballistic (blue) calculations of the net mass flow rate to Charon: neglecting the influence of collisions underpredicts flux to Charon by about 10 %. The steady-state rates shown, ~0.035 kg/s, are for a single hemisphere of the equatorially-symmetric calculation.

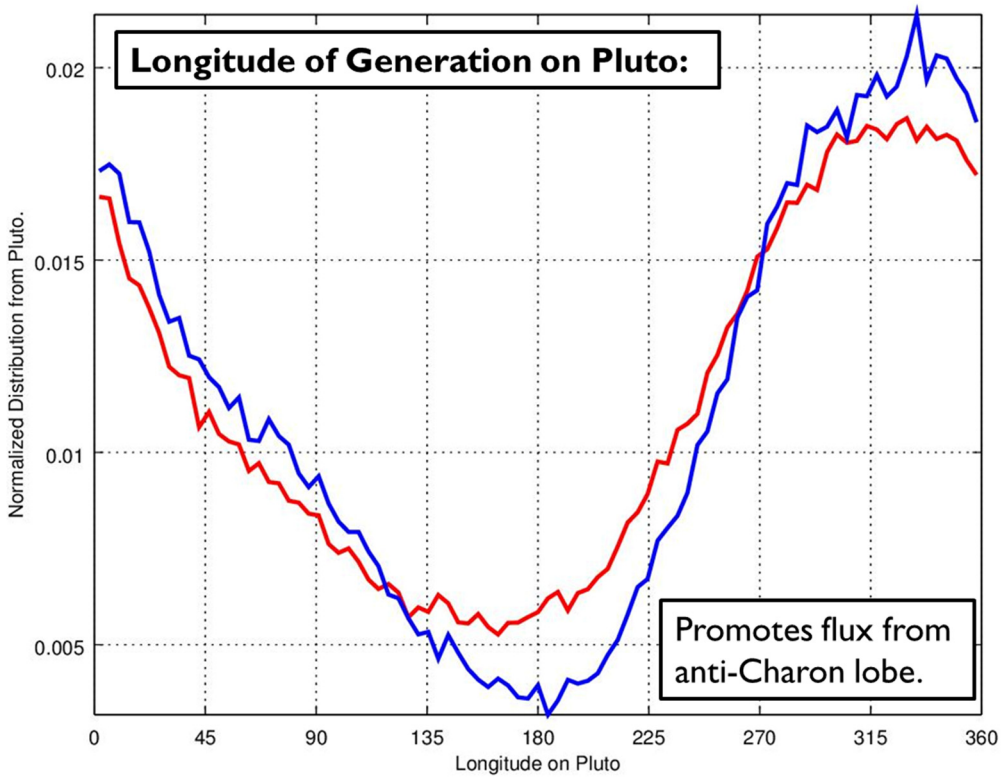

Figure C.2: Collisional (red) and ballistic (blue) results for the fraction of the net flux to Charon generated from within each 4° bin in longitude on the generation surface; Pluto's Charon-facing and anti-Charon points are at 0° and 180°. Ballistic calculations overpredict flux from Pluto's Charon-facing side, while underpredicting flux from the anti-Charon side.

Figures C.1 and C.2 demonstrate that while, volumetrically, the vast majority of the Pluto-Charon DSMC domain contains non-collisional flow, collisions – most of which occur near the exobase – exert significant qualitative and quantitative influence on that flow. Once satisfied that collisions appreciably altered the amount and morphology of flux to Charon, I didn't continue to explore our own free-molecular simulations. However, the DSMC results of Chapter 3 – particularly Case B, sourced from the New Horizons observation – proved quantitatively different than free-molecular simulations in

the literature (i.e. in terms of system escape rates, depositional fluxes to Charon, and the proportional significance of methane in both escape and transfer), and a portion of that difference is due to our simulation of collisional processes.

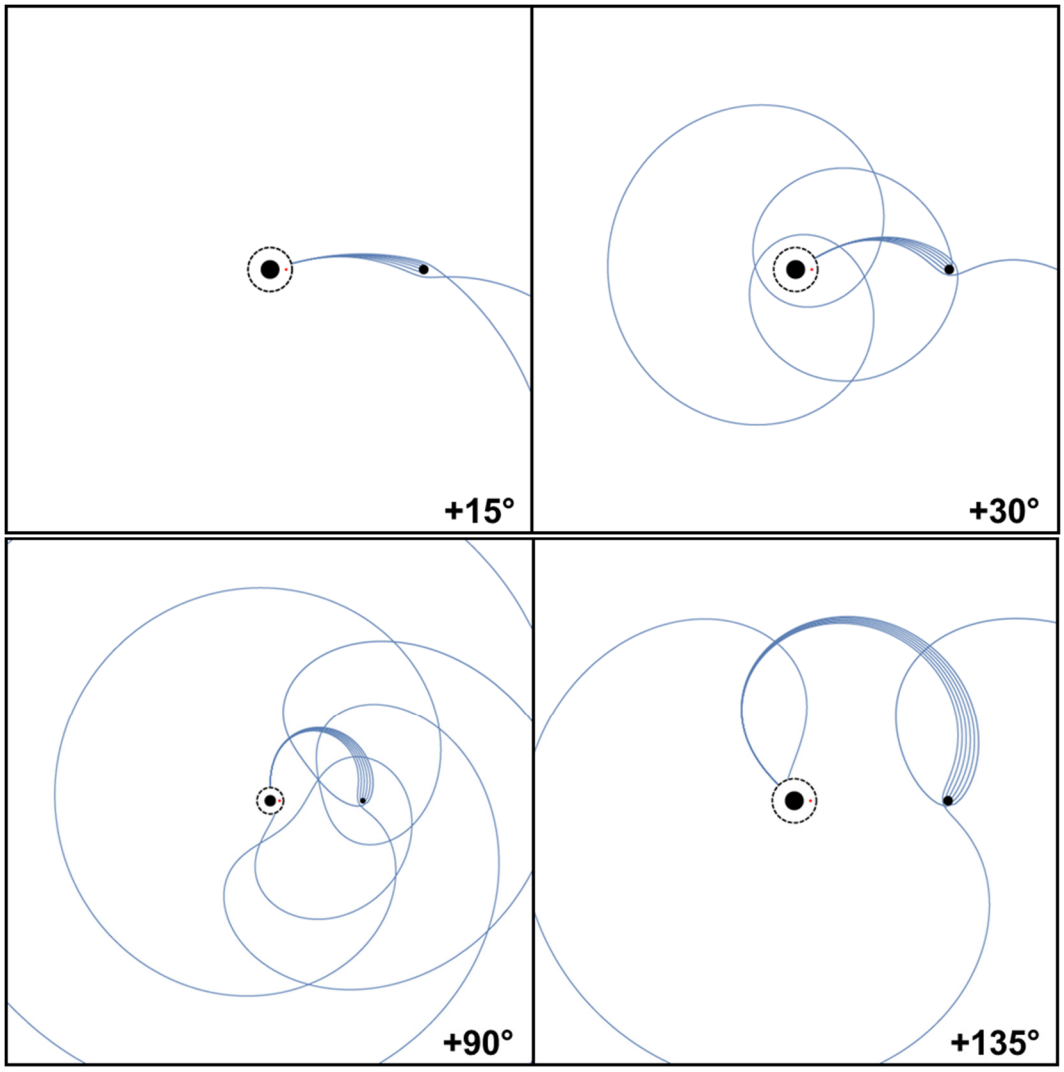

Figure C.3: In a free-molecular code, packets of particles are released in the equatorial plane with velocities normal to the generation surface (R=3000 km) and speeds distributed such that the particles just pass Charon. Each figure's point of generation is marked in E longitude. Flow through this largely free-molecular system is represented by billions of such trajectories that rarely interact; any notion of a 'bulk velocity' in such a system is misleading.

In such a predominantly free-molecular flowfield, most of the computational expense of the DSMC calculation occurs in movement: in the integration of each molecule's equations of motion, and in the MPI 'movement' of molecules between processors as they cross internal simulation boundaries. At any point, the flowfield itself is a superposition of the largely-independent trajectories of hundreds of millions of representative molecules; an interesting selection of such trajectories is demonstrated in Figure C.3. Figure C.1 showed the difference between collisional and ballistic fluxes to Charon to be about 10 %: therefore the majority of molecules in the DSMC result can reach Charon without having experienced a single collision above the generation surface, simply by being generated from the Maxwellian tail – and at an initial position and angle that will carry each within Charon's gravitational influence (i.e. approximately within its critical impact parameter, ζ_{CR}, in the BHL problem). Figure C.3 shows such ballistic pathways to Charon for molecules generated on the equatorial plane, and with trajectories initially normal to the generation surface, at several initial longitudes. This aids in the interpretation of Figure C.2, which demonstrated that, in both ballistic and collisional cases, molecules that reach Charon are more likely to have been generated on Pluto's Charon-facing hemisphere than on its converse. Of course, such results are somewhat dependent on the arbitrary selection of a DSMC simulation's lower boundary surface: any real molecule that has reached the exobase, or any adjacent mid-atmospheric plane, will have experienced countless collisions in its journey upwards from Pluto's surface.

C.3 Ballistic and Collisional Results in 1-D Terrestrial Simulations

The terrestrial atmospheric simulations described in Chapter 2 are generated from a mid-thermospheric boundary surface at 300 km altitude with its interface linked to the

NRLMSISE-00 model; one advantage of MSIS is that, as a semi-empirical model built on observational datasets, its validity does not hinge on the continuum assumption. It can therefore provide valid lower boundary conditions at *any* arbitrary mid-atmospheric plane, up to its maximum altitude of 1000 km.

Following the investigation of the importance of collisional effects in shaping flow through the Pluto-Charon system, and in response to questions as to the minimum possible operational altitude of the terrestrial DSMC, I ran a range of test simulations with generation surfaces at 50 km intervals between 150 and 300 km altitude in both ballistic and collisional configurations. Each distributes 16 processors in a uniform 4×4 grid across a 3° by 3° column in latitude and longitude about (0°, 0°), and begins at 20:00 UTC on 8 January 2005. The 1-D calculations proceed through 9 January, a date selected to match the 3-D, transient, full-planet simulation described in Chapter 2 and one for which the AP geomagnetic activity index is well modeled as zero (without a linked charged particle model, we cannot reproduce geomagnetic effects). Key objectives of these simulations include the determination of a lower operational bound for the terrestrial DSMC in its 1-D configuration, and whether and to what extent the simulation of upper-atmospheric collisions affects our result (i.e. is it sufficient to model the neutral atmosphere as ballistic above the exobase at ~300 km?).

A baseline test is performed with a 300 km lower boundary and with collisions, photo-dissociation events (with rates un-attenuated and for the quiet portion of the solar cycle), and radiation from rotational and vibrational states to space modeled, but without the adapted versions of Prem's functions for rotational / infrared absorption, photon

transport, and shielding processes described in Chapter 2.[47] This result can still be compared to the 1-D result from that chapter, which models many of the same processes in the same domain, albeit at a different date and with the 2014 solar heating model active. Results are shown in Figs. C.4 and C.5 for the system length scales and molar fractions respectively, and may be compared to Figs. 1.1 and 2.3.

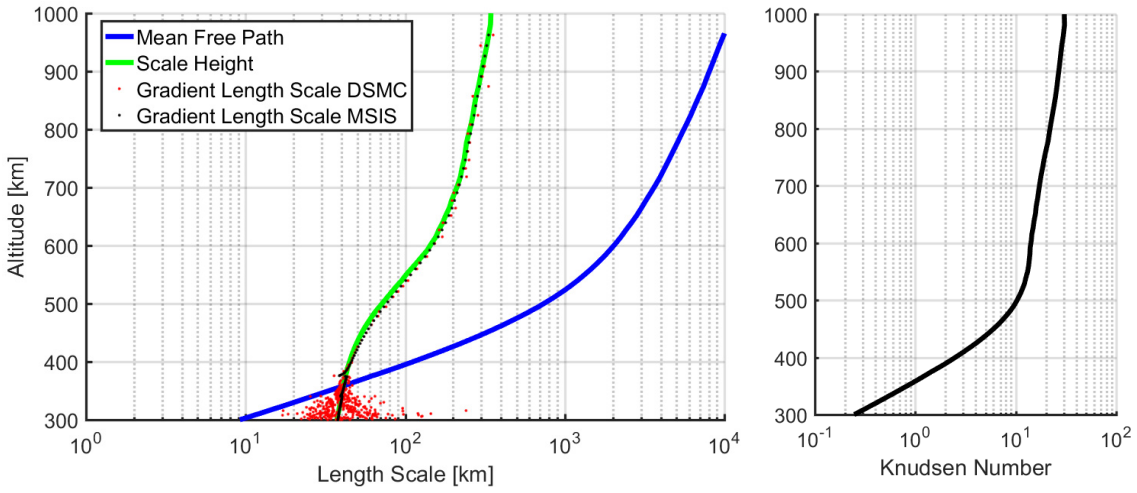

Figure C.4: (Left) A selection of atmospheric length scales are shown during a time average from 6:15 to 6:35 UTC. The mean free path ranges between 10 and 10,000 km, while density gradient length scales closely match the scale height. (Right) This Knudsen number Kn_H is the ratio of mean free path to scale height. The value of ~0.25 at the lower boundary is quite high.

Between 6:15 and 6:35 UTC sunlight has just begun to heat the 1-D column, and local densities are near their nighttime trough; as solar heating to this time is negligible, we are not yet disadvantaged by having disabled the heating functions. The mean free path at the 300 km lower boundary is about 10 km and the interface Knudsen number

[47] Note that the code applied in Appendix C is the 2014 version of Chapter 2, i.e. that prior to incorporating the updated versions of Prem's `mc_photons()` and `shielding()` routines described in Appendix B. For this reason, I don't use either in producing these results, eliminating a primary means of solar heating.

with respect to scale height is ~0.25, slightly above the intended generation surface adjacent to the transition from continuum to rarefied flow, i.e. $Kn_H \leq 0.1$. Despite being of trivial expense (< 10 SU) the simulation is highly over-resolved, with O[10^5] molecules per processor distributed among 400 cells in altitude. These factors suggest that such 1-D calculations can be performed at reasonable expense with far lower generation surfaces. However, as we extend our calculations deeper into Earth's atmosphere, additional and increasingly complex models are needed to properly represent the terrestrial environs. The collisional results of Fig. C.5 (in black) are consistent with the 1-D results of Chapter 2 in that species fractions match their MSIS expectations closely throughout the atmosphere[48]: in fact, this case performs even closer to the MSIS expectation for H, and MSIS and the DSMC code only show appreciable deviation for O and N when they comprise less than 1 part-per-thousand of the atmospheric column. Without testing the influence of collisions and boundary surface selection on our results, however, we cannot be sure whether the quality of this match is because our DSMC model correctly represents an essential and complex set of physical processes that shape Earth's neutral upper-atmosphere, or whether the problem is instead a simple one of near-ballistic evolution of each species to its separate scale height.

The same test is then performed with collisions deactivated (i.e. ballistic DSMC motion) and with an equivalent 300 km lower boundary. All other processes, timescales, and geometries remain unchanged. Fig. C.5 shows species concentrations for the ballistic case in blue, and the interesting result that the concentration of N deviates sharply from the MSIS expectation above 700 km, even as the remaining species behave in largely the same fashion as in the collisional calculation. Fig. C.6 compares translational temperature

[48] There are also significant qualitative *differences* between this case and that of Chapter 2 (see Fig. 2.3 for comparison). Both cases feature the same physical models and occur in early January in identical columns about (0°, 0°); the key difference is in time-of-day.

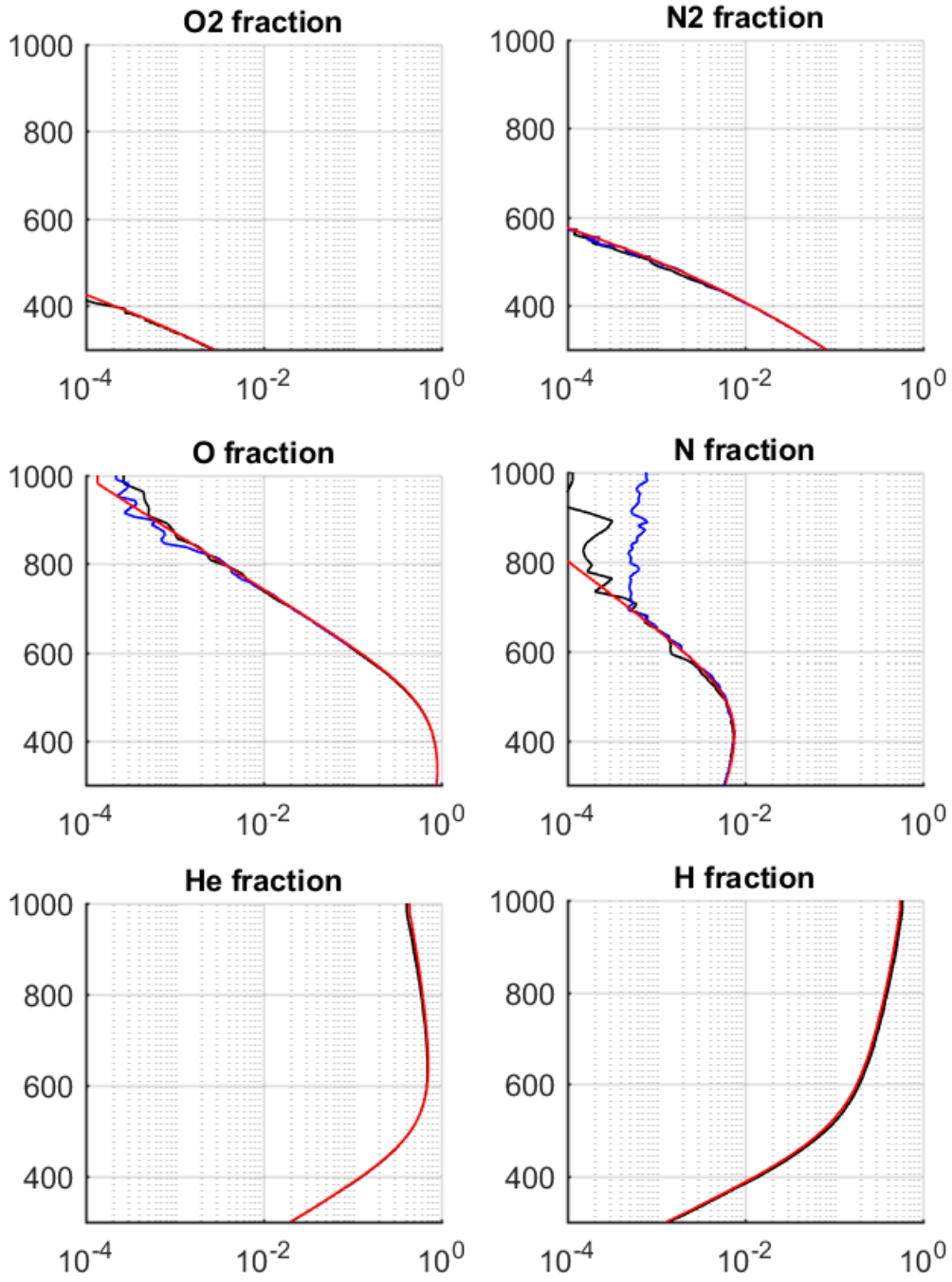

Figure C.5: Concentrations of each MSIS species in the 1-D ballistic and collisional simulations with a lower boundary at 300 km from 6:15 to 6:35 UTC. Collisional DSMC results are shown in black, ballistic results in blue, and the local MSIS expectation in red. Note the substantial deviation in the concentration of N in the ballistic calculation.

profiles of the collisional and ballistic flows with the MSIS total temperature; T_{TR} rises sharply and aphysically with altitude in the ballistic case, while the collisional case remains nearly constant. Taken together, these effects show that collisions *are* necessary to reproduce the behaviors of certain species and properties with altitude. However, with a 300 km lower boundary at Kn_H ~0.25, neglecting collisions does not otherwise grossly change the flow.

Again, since these calculations equilibrate 'overnight' and the time-averaged results are shown before solar heating substantially influences the real atmospheric column, we are not disadvantaged here by having deactivated the outdated versions of `shielding()` and `mc_photons()`.

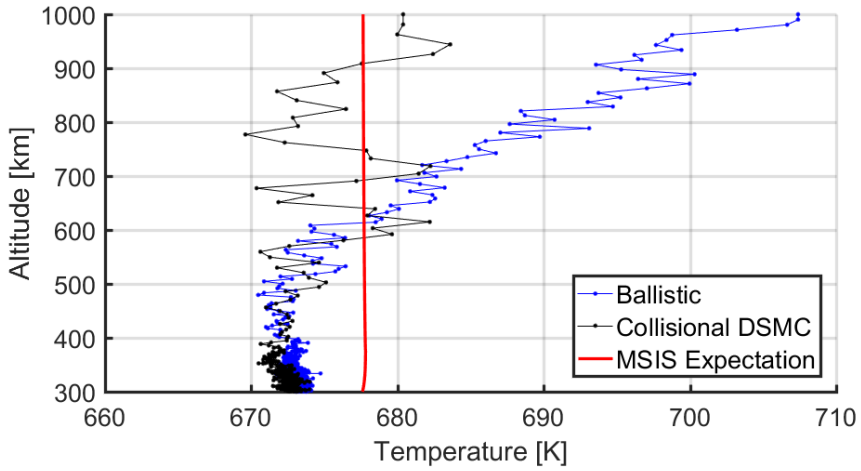

Figure C.6: The translational temperatures for ballistic (blue) and collisional (black) cases with lower boundaries at 300 km from 6:15 to 6:35 UTC, compared with bulk MSIS temperature in red. A ballistic model cannot capture the constant temperature profile of Earth's upper atmosphere.

The deviations in both N concentration and translational temperature with altitude for the ballistic case are linked to the photo-dissociation of diatomic nitrogen. As N_2 is a relatively heavy species that only remains in substantial concentration near the exobase,

the excess energy of its photo-products should generally be redistributed via collision. In a ballistic calculation, however, daughter N molecules remain energetic and are free to achieve high effective scale heights – even as photo-products scatter isotopically after the dissociation, those directed upward will increase in influence as atmospheric density falls off near-exponentially. In doing so, such molecules will skew the average T_{TR} and N concentration profiles at high altitudes. O_2 will likewise photo-dissociate, which may cause a similar effect for O under different initial atmospheric conditions. However, in this case, relative to N_2, O_2 makes up far less flow into the domain (0.25% vs 8%). While O_2 photo-dissociates rapidly (4.23×10^{-6} s^{-1} vs 6.61×10^{-7} s^{-1}), it also imbues photo-products with less excess energy than N_2 (1.431 eV vs 3.380 eV). Furthermore, O comprises most of this atmospheric column, which serves to 'wash out' the effect of O photo-products.

Pushing the 1-D calculations deeper into the atmosphere, I examine additional ballistic and collisional test cases with lower boundaries at 250, 200, and finally 150 km. Results for species concentrations in ballistic and collisional calculations with 200 km lower boundaries are shown in Figure C.7 during the 6:15 to 6:35 UTC window. Deviations in O and N concentration occur at the part-per-thousand level in collisional results, although these otherwise continue to mirror MSIS predictions; the ballistic case performs markedly worse for N than it did in the 300 km lower boundary case.

As sunlight heats the atmosphere, different species will become predominant; Figure C.8 shows species concentrations in the column at mid-day, between 11:35 and 11:55 UTC. Without an activated model for solar heating via absorption into the rotational states of trace species (i.e. NO), we cannot hope to reproduce the temperature increase that occurs in Earth's atmosphere during day and between 200 and 300 km. This effect is evident in the departure of even the collisional concentrations from MSIS values.

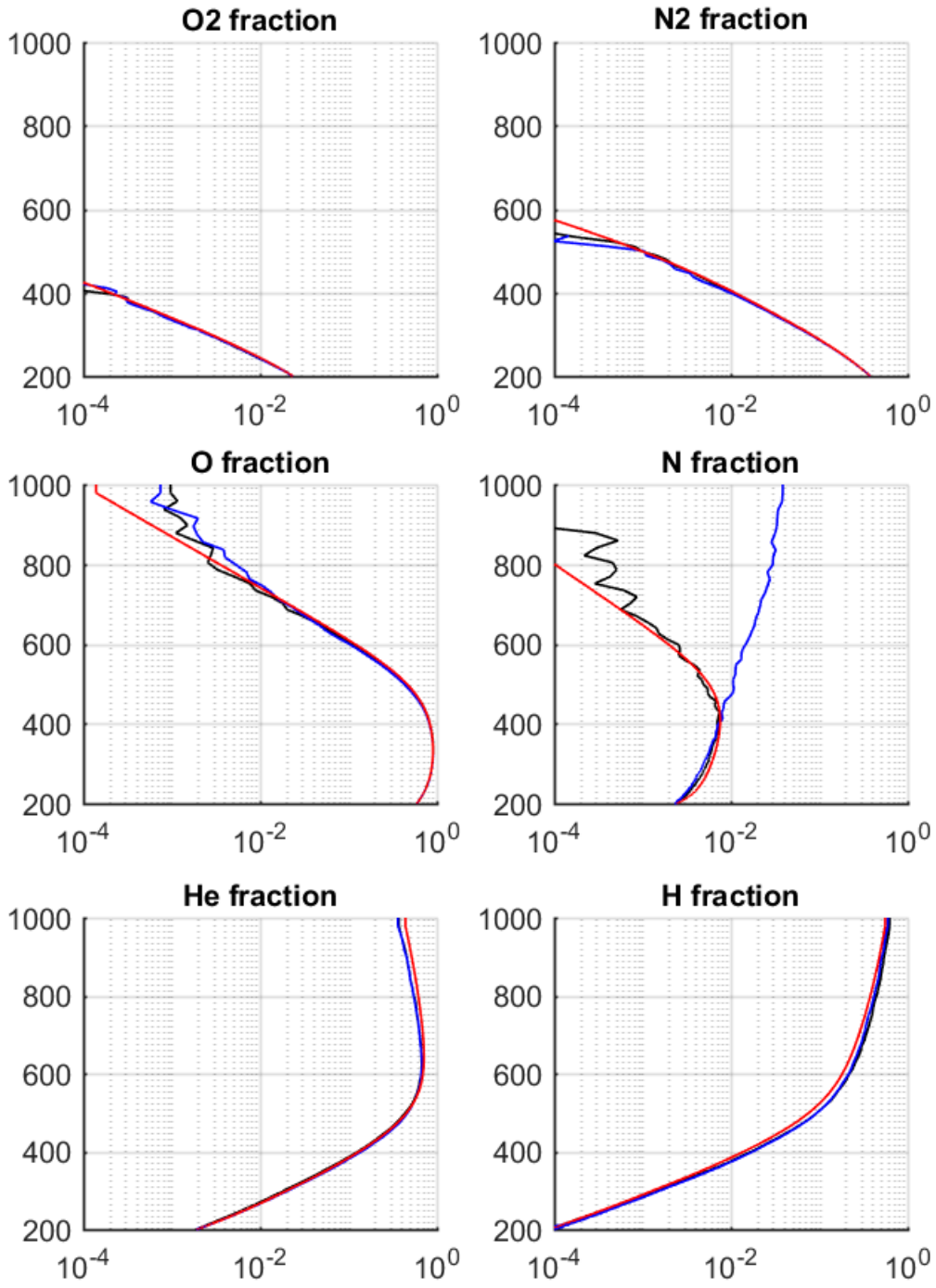

Figure C.7: Concentrations of each MSIS species in the 1-D ballistic and collisional simulations with a lower boundary at 200 km from 6:15 to 6:35 UTC. Collisional DSMC results are shown in black, ballistic results in blue, and the local MSIS expectation in red.

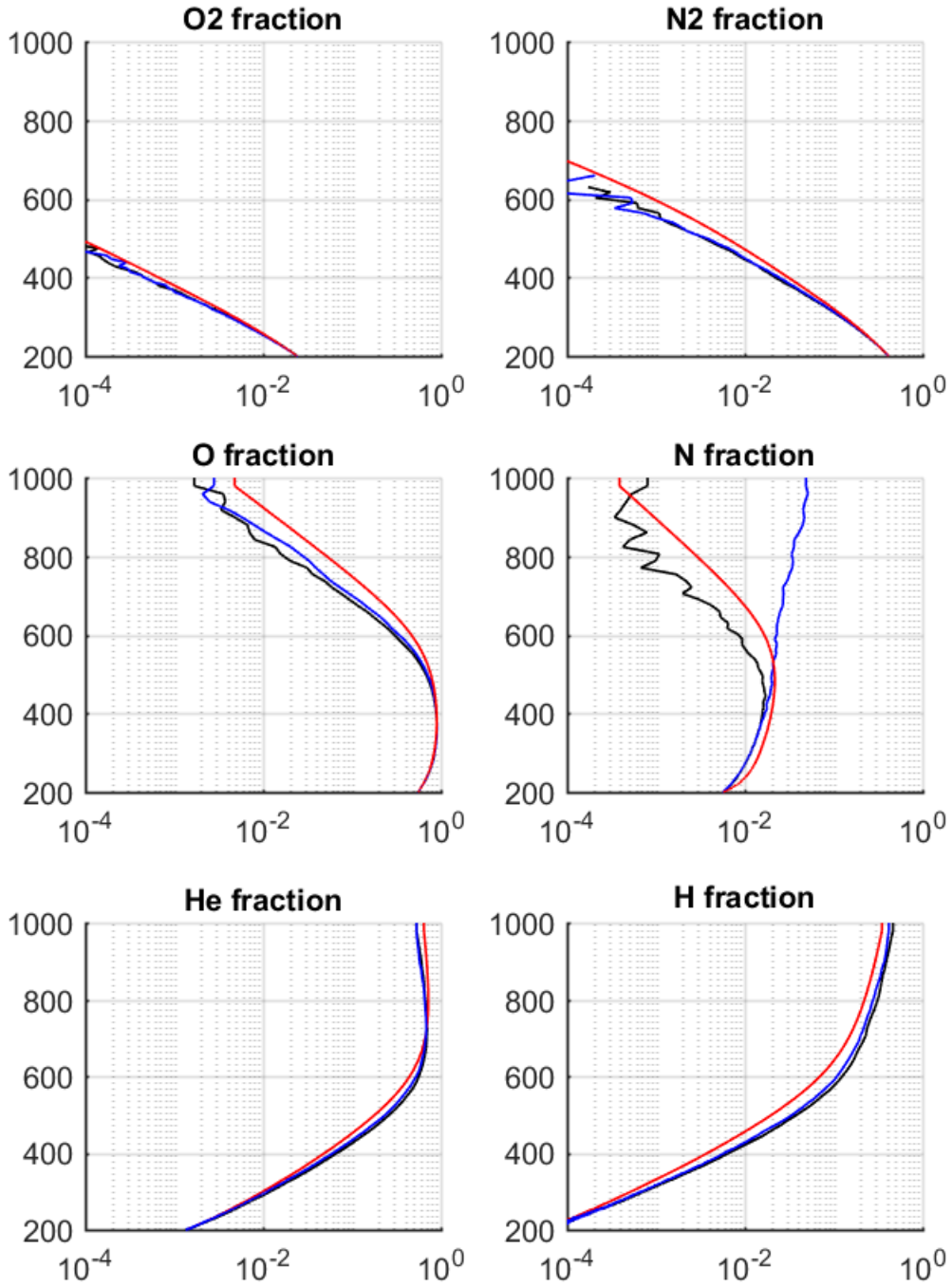

Figure C.8: Concentrations of each MSIS species in the 1-D ballistic and collisional simulations with a lower boundary at 200 km from 11:35 to 11:55 UTC. Collisional DSMC results are shown in black, ballistic results in blue, and the local MSIS expectation in red.

With 800 cells distributed through the vertical column and balanced in a nearly-exponential `LINEAR_SEGMENTS` scheme, even the 200 km lower boundary calculation is over-resolved in both cell size and molecule count. Between 16:55 and 17:15 UTC, for instance, cells stretch from 50 m to 20 km in vertical spacing between 200 km and 1000 km; the mean free path expands from 500 m to 10,000 km in the same range. Meanwhile cells at the generation surface have ~200 molecules, and even the large, nearly-free-molecular cells at the domain's top hold at least 10 molecules. Fig. C.9 compares cell sizes and mean free paths, and shows cell molecule counts. Thus, 1-D calculations can easily be pushed below 200 km, at least on the bases of resolution and computational expense[49]. Table C.1 summarizes such results for several collisional test cases.

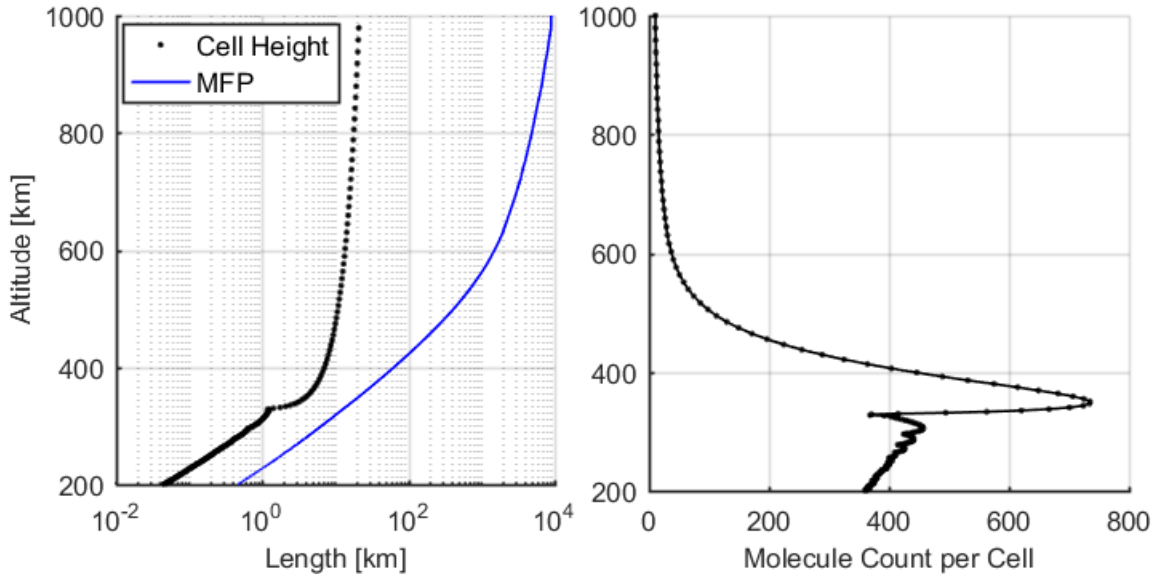

Figure C.9: Cell height vs. local mean free path (left) and molecule count per cell (right) for the 1-D collisional calculation between 16:55 and 17:15 UTC.

[49] A trial ballistic calculation with its lower bound at 150 km suggested that might prove a feasible limit in resolution: the standard 800 vertical cells were stretched to match the mean free path all throughout the flow. An F_{NUM} of 2×10^{25} produced 400,000 particles per processor during that calculation's 6:15 to 6:35 UTC time-average, which is far more than necessary.

Lower Bound	F_{NUM}	Mol. / proc.	Col'n / proc. / s	Cells / proc.	**CPU hrs.**
300 km	10^{24}	90,000	2,250	400	< 4
250 km	2×10^{24}	155,000	16,500	800	8
200 km	5×10^{24}	260,000	140,000	800	20

Table C.1: Metrics of the increasing expense of the 16-processor, 1-D, collisional simulations described in this Appendix as the generation boundary is reduced in altitude from 300 to 200 km. Even as low as 200 km, the computational expense of a resolved calculation is minimal. All results shown are for the 6:15 to 6:35 UTC window of 09 January 2005.

During the diurnal cycle, Kn_H will naturally vary through the atmospheric column; this effect is captured in Fig. C.10. At these conditions the variation in Kn_H is slight, and to capture the continuum breakdown at ~0.1 over the full day would only require a boundary surface at perhaps 250 km. It is interesting that the Knudsen number grows very slowly with altitude above 600 km, as lighter species (H and He) begin to dominate the upper atmosphere while temperature remains nearly constant.

In reviewing these results for terrestrial atmospheric simulation, I emphasize that collisional effects are demonstrated to be significant in shaping the DSMC-simulated atmosphere for cases in which our generation surface is below the exobase (at $Kn_H = 1$). This is at least in part because ballistic calculations do not permit energy exchange between photo-products (or molecules generated from the high-energy tail of the Maxwellian distribution) and the bulk atmosphere. Although we can see in these results that shielding, rotational absorption, and photon transport models are unnecessary in matching to nightside upper-atmospheric conditions, their effects on the dayside flow remain unclear. The 1-D results of Chapter 2, which featured now-outdated versions of those models, performed fairly well in matching to the MSIS atmospheric composition

and temperature profiles during daylight (i.e. between 17:15 and 17:25 UTC). However, if the lower boundary surface is pushed substantially below 300 km, rotational heating becomes a primary influence on the dayside atmosphere and must be modeled for a range of trace absorbing species to reproduce the steep temperature increases of Earth's daytime atmosphere between 200 and 300 km. Likewise, properly modeling attenuation becomes more important as the lower boundary is pushed downward into denser regimes. Notes on extending the Earth model for such future work are included in Appendix B.

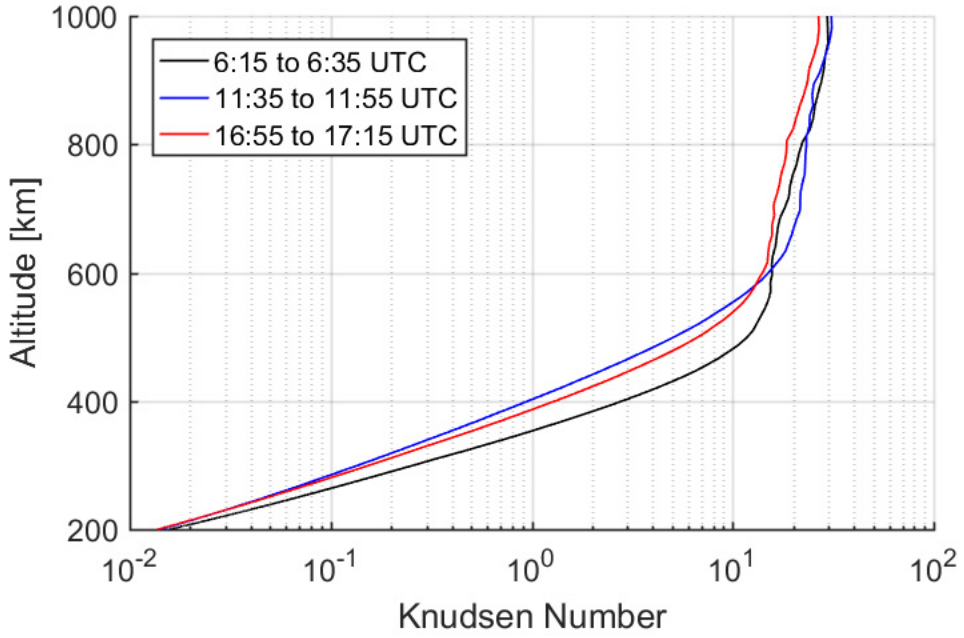

Figure C.10: Knudsen numbers Kn_H for 1-D collisional simulations with lower boundary at 200 km throughout the day of 09 January 2005, calculated with DSMC density and translational temperature values.

Appendix D: Geometries and Scales of the Pluto-Charon System

System Parameters	*New Horizons*	*This Work*	*Tucker et al. (2015)*
Rotational Period (d)	6.3872	6.3872	6.3657
Rotational Period (s)	551854	551857	550000
Radius, Pluto (km)	1187 ± 4	1185	1150
Radius, Charon (km)	606 ± 3	603.5	606
Mass, Pluto (10^{22} kg)	1.303 ± 0.003	1.304	1.3
Mass, Charon (10^{21} kg)	1.586 ± 0.015	1.519	1.5
Charon axis (km)	19596	19571	19550

Table D.1. Parameters of Pluto-Charon system used in DSMC simulations.

Species Parameters	N_2	CH_4
Mass (kg)	4.652×10^{-26}	2.663×10^{-26}
Diameter (m)	3.580×10^{-10}	4.830×10^{-10}
Rotational DOF	2	3
Vibrational DOF	1	4
VHS Viscosity Exponent	0.68	0.84

Table D.2. Species parameters used in Pluto-Charon DSMC simulations.

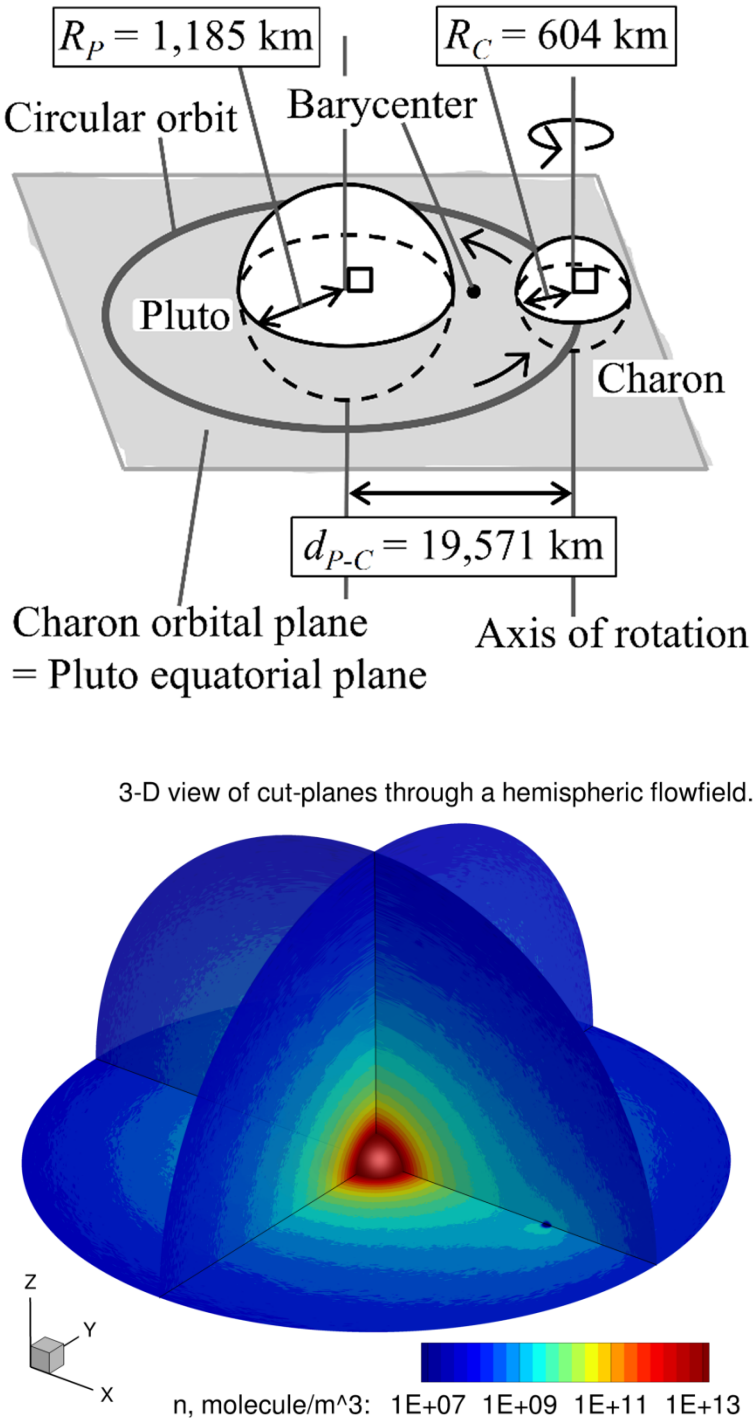

Figure D.1: (Top) Schematic of the Pluto-Charon system (not to scale, by S. Yeoh). (Bottom) A 3-D representation of the computed flowfield, demonstrating system geometry and highlighting number densities about Charon.

Appendix E: A High-Order Scheme for Particle Trajectory Integration

A consideration of integrator accuracy is motivated by steep gradients in effective potential around each of the Lagrange points as illustrated in Fig. E.1, and the long time scales of settling (O[10^6] s) in system fluxes compared to the most limiting collision timescales (O[10^2] s). A simple but restrictive study may be performed by placing test particles at the five Lagrange points of the system, all of which are unstable for the Pluto–Charon case, and determining the time it takes the particles to start moving away from these positions. For such a case we find that, for the second-order scheme, it takes O[10^5] s for all five test particles to depart their equilibrium positions. By comparison, for the higher-order RKPD scheme we employ in the DSMC simulations, only after 10^6 s are the L1 and L2 particles perturbed from their equilibrium Lagrange positions, while after 5×10^6 s the L4 and L5 test particles remain unmoved. A representative trajectory of an L1 test particle is indicated in Fig. E.2. Since transfer from Pluto to Charon occurs roughly along their axis and through L1, we were therefore motivated to use the RKPD higher-order scheme to ensure accuracy in this critical region. This higher-order and adaptively time-stepped integrator also allowed us to use time-steps limited by the mean time between collisions at the exobase (~200 s) instead of the O[1 s] time-steps used in applying the RK2 scheme in our prior work. An additional motivating factor was our observation of the existence of a class of particles that remain in flight over many millions of seconds: even if such particles are unlikely to occupy satellite orbits given Charon's perturbative effect, integrating their trajectories accurately was a priority.

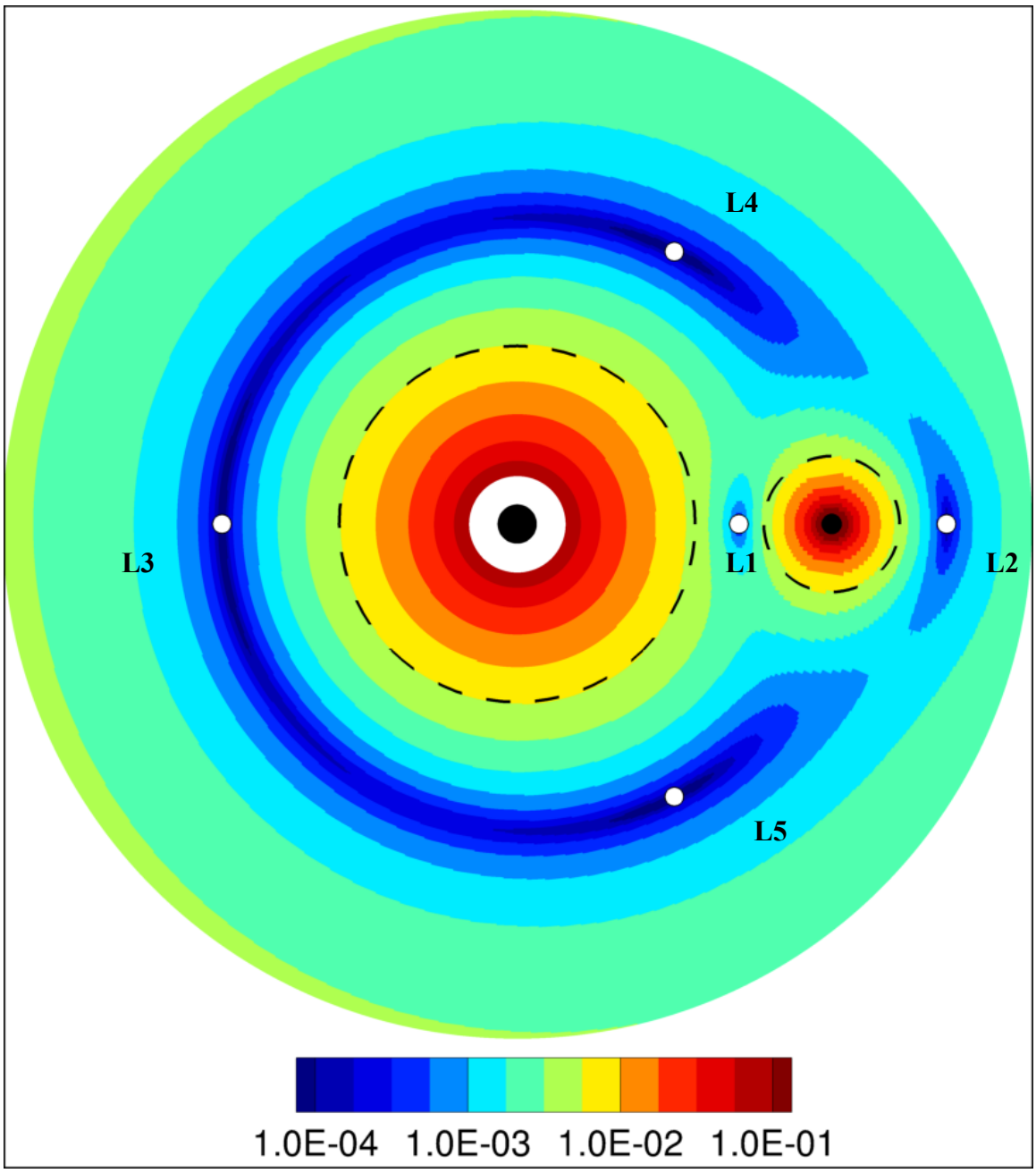

Figure E.1: Schematic of the gradient of effective potential (i.e. forcing) in the Pluto–Charon system, with Lagrange point coordinates indicated in white and labeled, and Pluto and Charon in black.

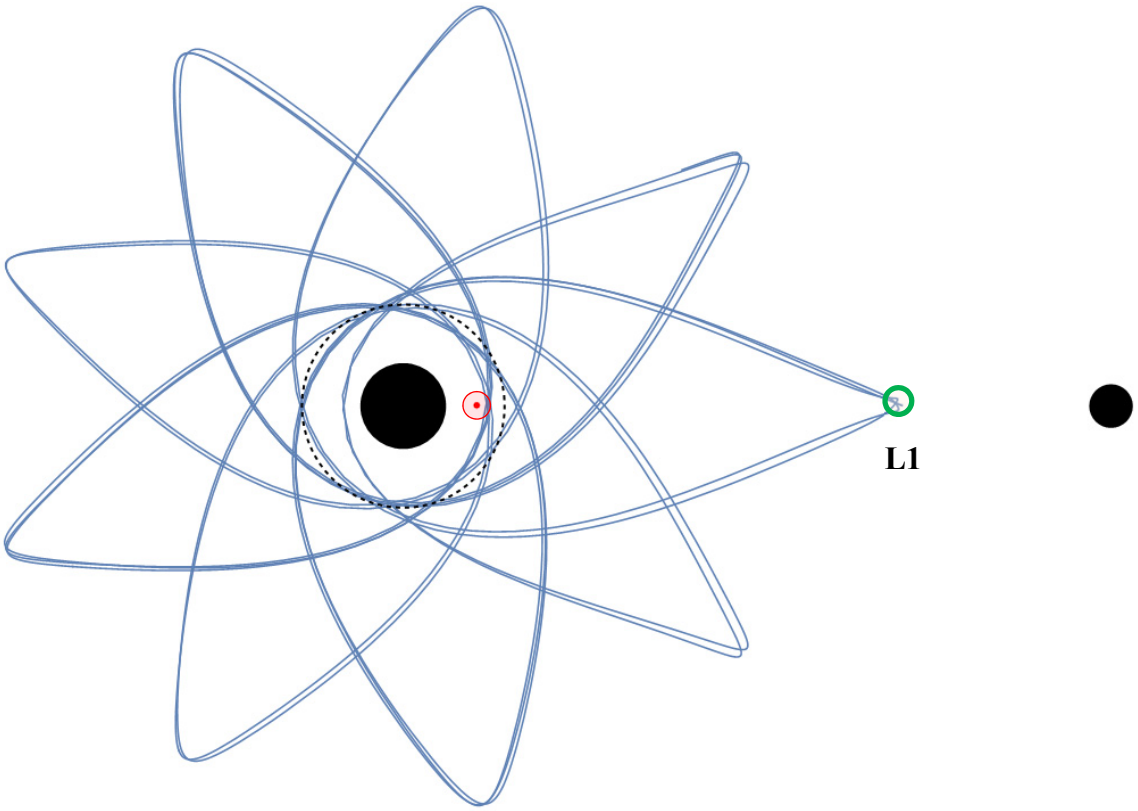

Figure E.2: The trajectory of a test particle perturbed from L1 equilibrium, from initialization to 5×10^6 s. The system barycenter is marked in red, the L1 point in green, and the plutonian exobase in a black, dashed line.

Appendix F: Simulations of the Tucker *et al.* (2015) Heating Cases

The exobase boundary conditions reported in Tucker *et al.* (2015) for a series of solar heating conditions are employed in that work in free-molecular simulations of an escaping flow of nitrogen at the medium solar heating condition. In this Appendix, 3-D DSMC simulations of each heating case are presented for an F_{NUM} of 10^{26} and for a molecular sticking condition at Charon's surface. While the exobase values from Tucker *et al*. overestimate the extent, escape rates, and nitrogen fraction of the observed plutonian atmosphere at the time of the New Horizons encounter, Gladstone *et al.* (2016) hypothesize that past nitrogen escape rates must have occasionally been much greater in order to explain the primarily erosional features on Pluto's surface. These DSMC simulations of transfer and escape for a variety of solar heating values and corresponding levels of exobase expanse are thus potentially illustrative of Pluto and Charon's past atmospheres. Table F.1 indicates the lower boundary conditions employed in these DSMC simulations, while Table F.2 reports the results for the fluxes into and out of the system for each case. The Tucker *et al.* (2015) case for medium solar heating is included for comparison. Our DSMC simulations are fully kinetic, representing collisions and physics absent from Tucker's free-molecular calculation, and are about two orders of magnitude better-resolved in particle count (related to F_{NUM}). The high resolution of the present calculations allows for the three-dimensional visualization of their flowfields (Figs. F.1, F.2, and F.3), which demonstrate the archetypal features of a bridging structure arcing wakeward through the L1 point, preferential deposition onto Charon's leading hemisphere, and an asymmetric distortion of the number density field behind Charon also visible in Cases A and B. It is notable that in the maximum-heat case, with

the exobase extended fully 9.8 R_P and nearly to the L1 point (Fig. F.1), Charon retains an atmosphere of order exobase density, even as all particles incident on its surface stick.

Exobase Conditions	*Minimum*	*Medium*	*Maximum*
Exobase radius (R_P)	5.3	6.84	9.8
Temperature T (K)	87	79	66
Jeans parameter λ_x	5.7	4.8	4.5
Number density (10^{11} m^{-3})	7.0	5.0	3.0

Table F.1: Exobase conditions reported in Tucker *et al.* (2015) employed as lower boundary conditions in the minimum, medium, and maximum solar heating cases addressed in Appendix F.

Solar Heating Case	*Maximum*	*Minimum*	*Medium (DSMC)*	*Medium (Tucker)*
F_{NUM}	10^{26}	10^{26}	10^{26}	$< 10^{28}$
Flux into domain (10^{28}/s)	2.8	2.2	2.5	2.5
Return flux into exobase (10^{28}/s)	2.2	2.1	2.3	> 2.0
System escape (10^{27}/s)	5.8	1.1	2.2	2.2
Flux to Charon (10^{26}/s)	2.1	0.36	0.80	0.57
Ratio of Charon flux to system escape (%)	3.6	3.3	3.6	2.6

Table F.2: Results for DSMC simulations at the various solar heating cases and exobase parameters.

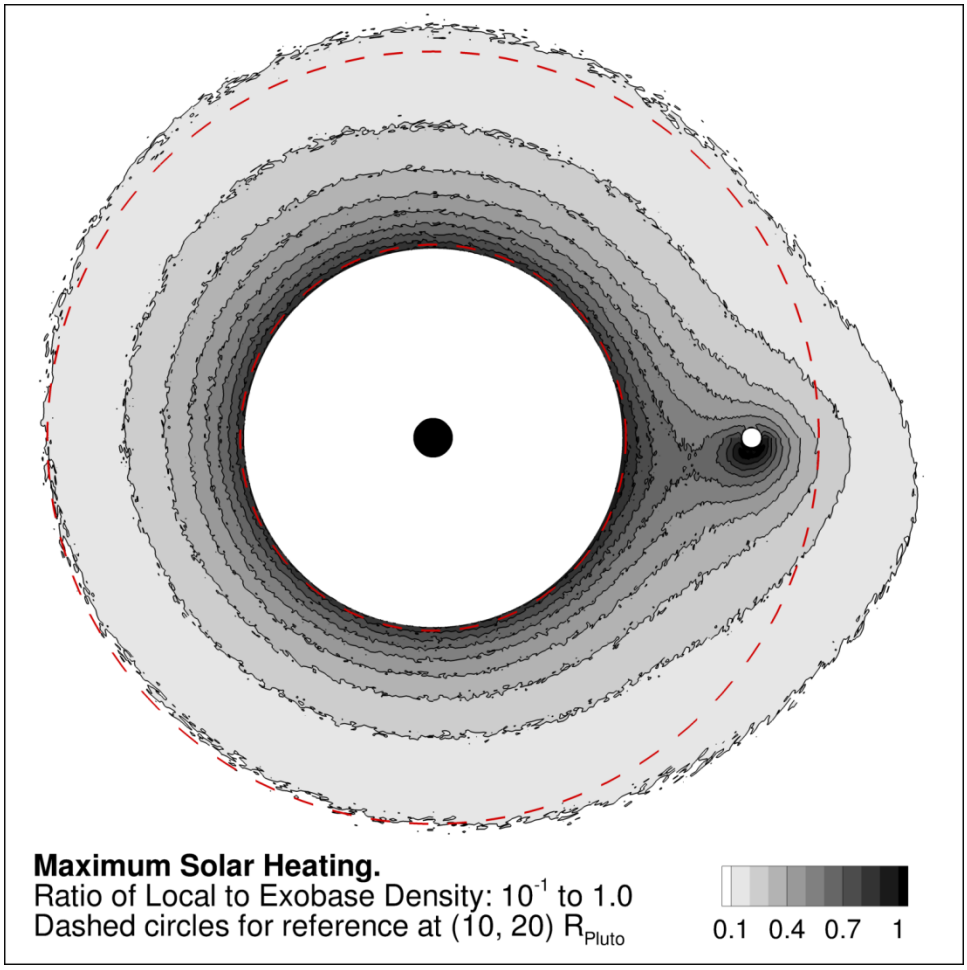

Figure F.1: The ratio of local to exobase number density through the flowfield for a steady-state solution of the maximum heat case from Tucker *et al.* (2015). The outer dashed circle at 20 R_P corresponds to a factor of O[10^1] depletion for this expansive case, which could represent a highly-active plutonian atmosphere in a past configuration. Even with a sticking condition at Charon's surface, a substantial transient atmosphere has developed.

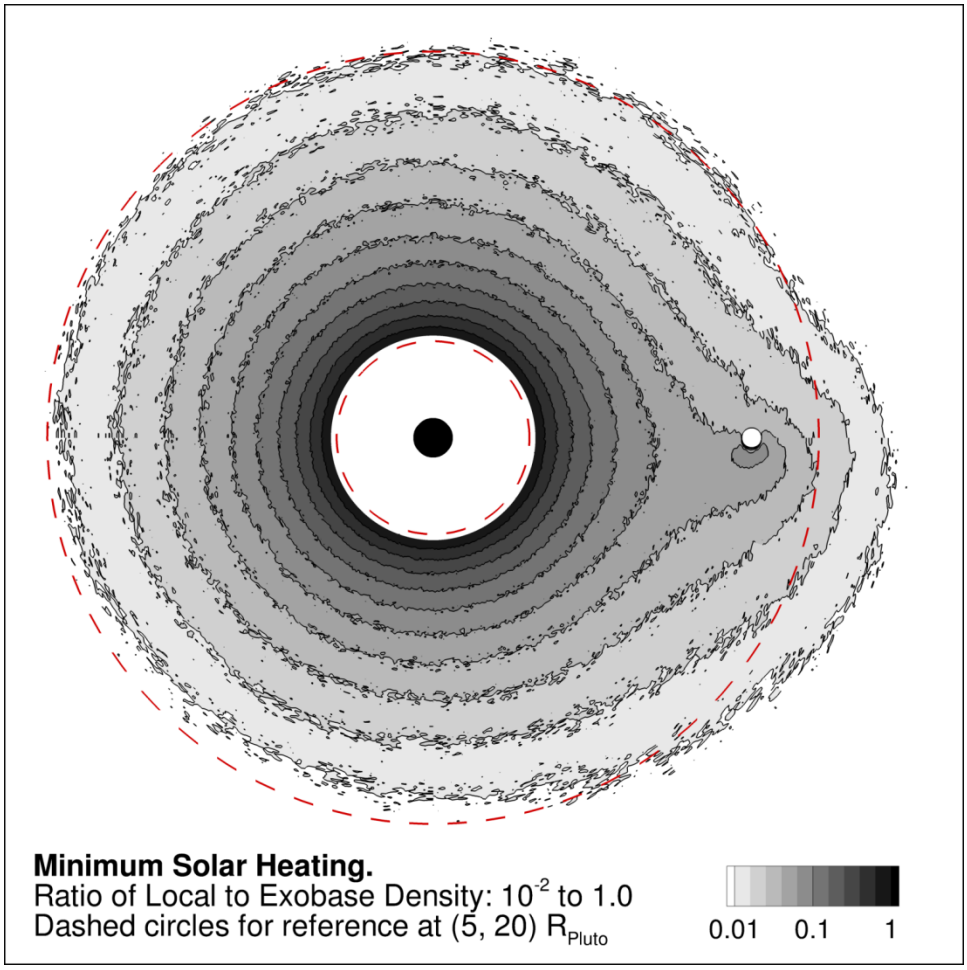

Figure F.2: The ratio of local to exobase number density through the flowfield for a steady-state solution of the minimum heat case from Tucker *et al.* (2015). The outer dashed circle at 20 R_P corresponds to a factor of O[10^2] decrease in number density from the exobase for this compact atmosphere.

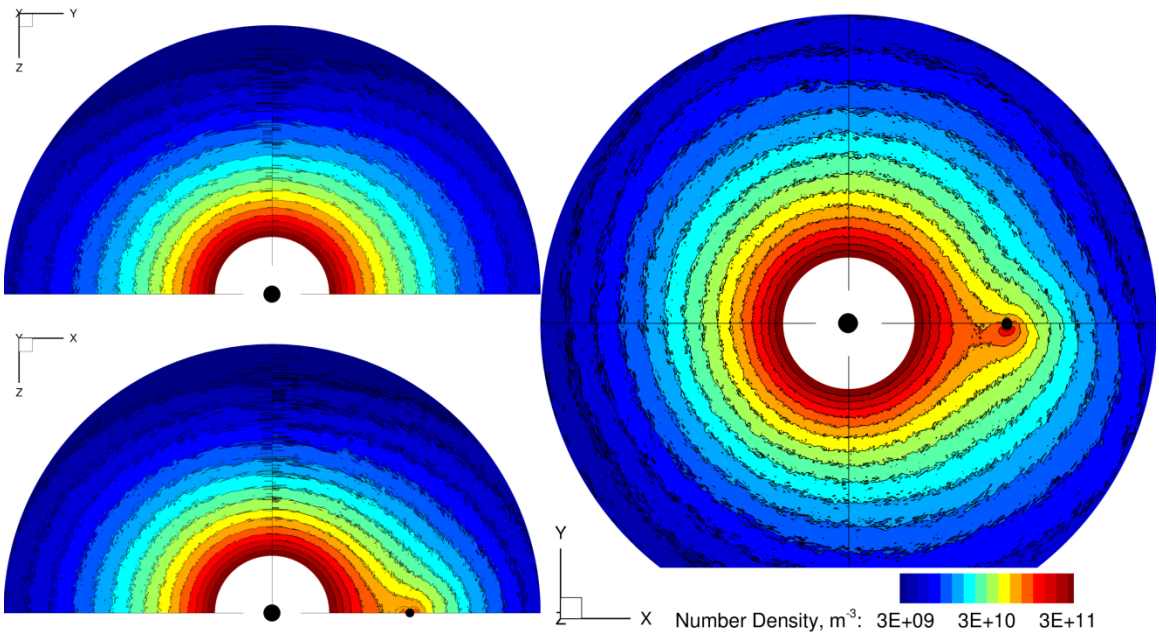

Figure F.3: A steady-state 3-D flowfield computed for the medium heating case (Tucker *et al.* 2015), which shows comparable structure to the Case A and B results (which may be compared to Figs. 3.2 and 3.7).

Appendix G: The Bondi-Hoyle-Lyttleton Accretion Problem

An interesting result that emerges from simulations of rarefied gas dynamic transfer in the plutonian system is the apparent contradiction between the peak depositional flux from Pluto oriented onto Charon's leading hemisphere, opposite the occurrence of the peak flowfield density in Charon's wake. In explaining this phenomenon, an analogy can be made between Charon travelling through Pluto's escaping atmosphere and a point mass traveling on a linear path through an infinite, uniform-density gas cloud. The Bondi-Hoyle-Lyttleton accretion problem considers the gravitational focusing of such a cloud in the wake of a rapidly-travelling star and can be stated as an axisymmetric problem in cylindrical coordinates, with ζ an impact parameter representing distance normal to the symmetry axis infinitely far from the star, and v_∞ a freestream velocity oriented along that axis. Edgar (2004) presents a useful derivation of BHL theory in a polar coordinate system with its center at the point mass, followed here. The equations of motion and conservation of angular momentum for this system are

$$\ddot{r} - r\dot{\theta}^2 = -\frac{GM}{r^2}, \tag{G.1}$$

$$r^2\dot{\theta} = \zeta v_\infty. \tag{G.2}$$

With a substitution of variables and application of the axisymmetric, steady-state continuity equation, analytic solutions for the radial coordinate r and flowfield density ρ are derived as functions of θ and ζ, as

$$r = \frac{\zeta^2 {v_\infty}^2}{GM(1+\cos\theta) - \zeta {v_\infty}^2 \sin\theta}, \tag{G.3}$$

$$\rho = \frac{\rho_0 \zeta^2}{r \sin\theta (2\zeta - r\sin\theta)}. \tag{G.4}$$

For gas in the infinite cloud, the velocity (v_∞) of the mass effectively acts as a hyperbolic excess velocity, as expressed in Equation G.5. Solving for velocity components and setting the radial component to zero at Charon's radius, R, allows for an expression of the impact parameters of the critical family of hyperbolae which will pass just tangent to the surface of Charon, as

$$v^2 = {v_\infty}^2 + \frac{2\,GM}{r} = {v_r}^2 + {v_\theta}^2, \tag{G.5}$$

$$\frac{\zeta_{CR}}{R} = \sqrt{1 + \frac{2\,GM}{R\,{v_\infty}^2}}. \tag{G.6}$$

Given a point of Charon's mass traveling through an infinite and uniform cloud of density ρ_0 in a straight line at Charon's angular velocity of ~199.4 m/s, Figure G.1. represents the analytic solution to the cloud's normalized density. The critical, surface-tangent hyperbolae in this case have impact parameters of $\zeta_{CR} = 3.102\,R$, and are drawn in black (the dashed trajectory is the continuation of the solid trajectory across the symmetry axis). All material ahead of the point mass and within ζ_{CR} will be drawn into Charon's leading hemisphere, and all remaining material will be focused into Charon's wake. The distance behind Charon's center at which the convergence of these tangent trajectories occurs can be expressed

$$\frac{D_{CR}}{R} = 1 + \frac{R\, v_\infty{}^2}{2\, GM}. \qquad \text{(G.7)}$$

For Charon's parameters, this convergence occurs $0.1160\, R$ behind Charon's trailing hemisphere. If Charon were to be considered as a body with radius R capable of impeding the flow, instead of a point, no trajectories would pass through the region between this convergence and Charon for the BHL problem.

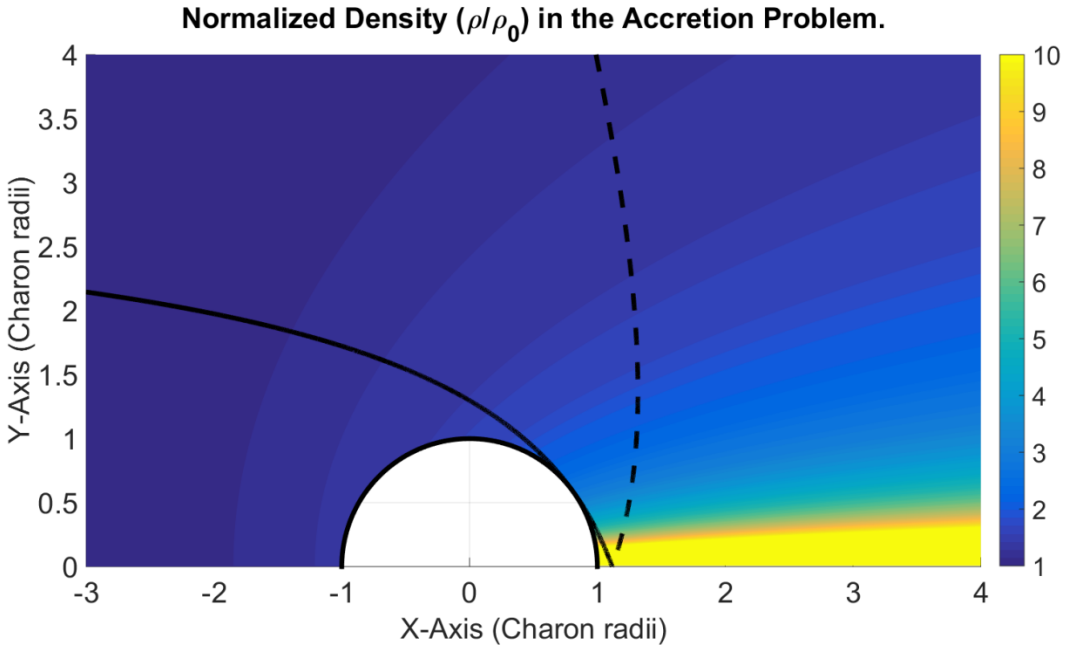

Figure G.1: Contours of normalized density calculated for the analytic solution to the BHL accretion problem applied to Charon. All material between the (solid) critical trajectory and the axis will be incident onto Charon's face, while all other material will, in the BHL formulation, be drawn through the symmetry axis in Charon's wake. If we consider that Charon impedes trajectories with initial impact parameters less than ζ_{CR}, the analytic density solution to the BHL problem is invalid between solid and dashed trajectories.

The BHL analysis demonstrates how gravitational focusing draws material into Charon's leading hemisphere while increasing density in its wake as Charon travels through Pluto's escaping atmosphere. There are a number of simplifications that cause departure from this result in the DSMC simulations. Charon travels on a nearly circular orbit about the system barycenter, not in a straight line, and Pluto exerts a perturbing gravitational influence on the flow about its moon. Furthermore, Charon travels through a non-uniform gas cloud with a complex and non-equilibrium velocity distribution. These effects deflect the focused density in Charon's wake from the BHL problem's symmetry axis and shift the location of peak deposition onto Charon from the moon's leading face towards its sub-Pluto face, as evident in Figs. 3.1 and 3.2, respectively. The wide distribution of particle velocities and trajectories in the escaping plutonian flow also produces trajectories that are incident onto Charon's trailing hemisphere, where the BHL problem suggests no deposition will occur.

In addition to its utility as a simple model for the gravitational focusing process, the BHL analysis can be useful in explaining the 'hollow' regions in the density field that form behind Charon and ahead of the density convergence (particularly evident in the top-right panel of Fig.3.6) and in estimating the total flux onto Charon's surface given the average flowfield density at Charon's distance.

Consider the critical convergence distance for the Charon system derived in Equation G.7. The BHL analysis for a spherical mass predicts that the region bounded by the moon and these hyperbolae form a wakeward region of zero density that extends to, given Charon's parameters, $0.1160\,R$. While the nonequilibrium and rarefied nature of the flow at Charon's distance from Pluto ensures that some class of particles will have trajectories that do carry them through this 'shadow region,' the BHL prediction aligns

with presence and extent of the small pockets of low density visible between Charon and the high-density wake region evident in Fig. 3.3(b) and the top-right panel of Fig. 3.6.

Likewise, an accurate analytic estimate of the total flux to Charon can be made given only a density result at Charon's distance from Pluto in a 1-D simulation. As all particles within the BHL problem's critical hyperbolae will be incident onto the sphere's face, this net number flux can be expressed

$$\zeta_{CR}^2(\pi R^2 v_\infty)n_\infty, \tag{G.8}$$

which, for Charon's parameters, reduces to $2.195 \times 10^{15}\, n_\infty$ s^{-1} for a number density in #/m^3. Estimates from this simple model are compared to the results of the Tucker *et al.* (2015) and our DSMC simulations of fully three-dimensional flowfields in Table G.1., given only n_∞ as the number density at Charon's distance, roughly estimated by the flowfield-averaged (or 1-D if available) density at Charon's distance.

Parameters	*Case A DSMC*	*Case B DSMC*	*Med. Heat DSMC*	*Med. Heat (Tucker)*
n_∞ at Charon (10^9 m^{-3})	~ 5	~ 0.8	~ 30	~ 23
Flux to Charon, BHL (10^{24}/s)	~ 11	~ 1.8	~ 66	~ 51
Flux to Charon, 3-D model (10^{24}/s)	14 – 15	2.0	80	57

Table G.1. Comparison of BHL model for flux to Charon vs. full 3-D calculations.

Appendix H: Novel Study of Rarefied Flow about Gravitating Spheres

H.1 Overview and Motivation

The Bondi-Hoyle-Lyttleton accretion problem described in Appendix G provides a useful framework for understanding Charon's gravitational effect in focusing and capturing the escaping plutonian atmosphere. However, it cannot describe or represent the complex, rarefied-gas-dynamic effects that shape the Charon environs, nor those that result from the focusing of free-molecular flow into a dense wake, or even into a captured atmosphere. In fact this may be considered as a general class of problems, an extension of the more familiar study of rarefied flow about non-gravitating spheres. For instance, we might consider the initial (pre-continuum) stages of atmospheric formation about a planet, phenomena like the lunar antipodal shock formation following cometary impact (Prem 2017), or, in the spirit of the BHL problem's original formulation, collisional interactions within wakes focused behind gravitating bodies passing through gaseous clouds. Therefore, I developed a novel model within the planetary DSMC code for the simulation of BHL problems about gravitating spheres of arbitrary radii.

H.2 Toward a DSMC BHL Code: Methodology

New functions are wrapped in the precompiler definition `BHLCOLN` and include `create_bhl()` and `create_bhl_flux()`, which supersede the mid-atmospheric creation functions; likewise the model applies a version of the GSL high-order integration schemes I configured for the Pluto-Charon system in my re-write of our integration function, `trans()`. Inputs are the freestream parameters $(n_\infty, v_\infty, T_\infty)$ and, for the Charon case, molar fractions of nitrogen and methane. For the cases discussed in this

Appendix the mass and radius of the gravitating sphere are Charon's, but in general these parameters may be varied freely. Finally, the boundary condition at the sphere's surface may be any of the standard surface conditions, although the limiting cases selected for this study are those in which either 1) all molecules that strike the surface stick (i.e. sticking coefficient 1.0) as they might onto a frost surface, or within a cold trap; or 2) all molecules that strike are diffusely reflected, equilibrating instantly to a uniform surface temperature of 53 K (i.e. sticking coefficient 0.0). These conditions match those applied for Charon in Chapter 3.

The usual spherical coordinate system is rotated such that the BHL symmetry axis, pointed into the incident flow, aligns with our north pole; therefore any slice in the φ coordinate is axisymmetric. Generally, I apply a slice of 2-3° to prevent the domain from becoming too narrow toward the axis and 'trapping' particles that focus into the wedge. Of course, this has the general problem of reducing the molecule count and thus the quality of DSMC statistics as the axis is approached; this could be countered by applying a radial weighting scheme, although that is not explored in this work. The calculations herein apply 64 processors that divide the domain into equal sections in θ with no subdivision in φ; the calculation is axisymmetric and additional tiers of cells in φ would only serve to add noise. In the version of the code that produced the results discussed in this Appendix, all incident flow is generated on the outer edge of the calculation's vacuum buffer cell with its initial velocity aligned with (i.e. parallel to) the system symmetry axis. This only reflects the BHL mathematics if the generation surface is *infinitely* distant from the gravitating sphere; as we generate molecules at finite distances, their trajectories at generation ought to have already been bent toward the sphere.

In any future simulations, the system-edge velocities and generation densities ought to be modified to reflect these hyperbolic trajectories; the necessary mathematics

follow. This correction will make the simulations more accurate – at least, to the extent that we want their ideal case to reflect the BHL formulation. It will also make them much cheaper: in this Appendix the flow had to be generated far enough from Charon such that it was reasonable to assume initially straight trajectories (e.g. at over 20,000 km distant, or 33+ R_{CH}) and integrated over the long flight inward.

Flow into the domain is generated as a Maxwellian flux through the system outer boundary surface, with each molecule's bulk velocity superposed onto the thermal velocity set by the freestream temperature T_∞. The count of representative molecules created per species, per time-step, per surface cell is a Poisson-distributed integer about

$$N_{create} = n_E \, f_{SP} \, A_{cell} \, (\vec{v} \cdot \vec{n}_{cell}) \, \Delta t \, F_{NUM}^{-1}, \tag{H.1}$$

for n_E the total density at the generation surface; f_{SP} the mole fraction of that total density represented by each species; Δt the time-step duration; and F_{NUM} the weighting factor of real molecules per representative molecule. A_{cell}, the area of any element of the system boundary surface, can be expressed

$$A_{cell} = {R_E}^2 \, \Delta\phi \, [\cos(\theta_{cell\,L}) - \cos(\theta_{cell\,R})], \tag{H.2}$$

in which R_E is the radius at the cell's outer edge, $\Delta\phi$ is the cell width in the azimuthal coordinate, and $\theta_{cell\,L,R}$ are the left and right edges of the cell in its polar coordinate. For the case in which the flow is generated uniformly parallel to the symmetry axis, $(\vec{v} \cdot \vec{n}_{cell})$ reduces to $v_\infty \cos(\theta_{cell\,C})$ for $\theta_{cell\,C}$ the cell-center theta coordinate. Accounting for the sphere's gravitational influence on the incident flow, however, we must progress

the BHL analysis of Appendix G; the impact parameter can be normalized by the radius coordinate, and that expression simplified and solved as

$$\frac{\zeta}{r} = f(\theta, r) = \left(\frac{\sin(\theta)}{2}\right)\left(1 \pm \sqrt{1 + \frac{2GM}{r\, v_\infty^2} \csc^2\left(\frac{\theta}{2}\right)}\right). \tag{H.3}$$

Divided into velocity components, following Edgar (2004) this yields functions of the dimensionless group, likewise in θ and r:

$$v_r = -v_\infty \sqrt{1 + \frac{2GM}{r\, v_\infty^2} - \left(\frac{\zeta}{r}\right)^2}, \tag{H.4}$$

$$v_\theta = v_\infty \left(\frac{\zeta}{r}\right). \tag{H.5}$$

These can be rotated into the Cartesian frame of the BHL problem as

$$\begin{Bmatrix} v_x \\ v_y \end{Bmatrix} = \begin{Bmatrix} \cos\theta & \sin\theta \\ \sin\theta & -\cos\theta \end{Bmatrix} \begin{Bmatrix} v_r \\ v_\theta \end{Bmatrix}. \tag{H.6}$$

At the generation surface on the finite domain's outer edge, R_E, the gravitational focusing effect likewise modifies density as

$$n_E = n_\infty \left(\frac{\zeta}{R_E}\right)^2 \left(2 \sin\theta \left(\frac{\zeta}{R_E}\right) - \sin^2\theta\right)^{-1}. \tag{H.7}$$

The mass flow rate can be adjusted from the case in which molecules are generated with velocities aligned with the symmetry axis to their proper BHL hyperbolic trajectories by modifying the system-edge density, n_E, as above and by replacing $(\vec{v} \cdot \vec{n}_{cell})$ with v_r.

The three freestream parameters $(n_\infty, v_\infty, T_\infty)$ can be uniquely specified in dimensionless groups: two of these, the Mach and Reynolds[50] numbers, are familiar fluid dynamics terms. For the third, I suggest the normalized critical impact parameter,

$$\frac{\zeta_{CR}}{R} = f(v_\infty) = \sqrt{1 + \frac{2\,GM}{Rv_\infty^2}}, \tag{H.8}$$

which incorporates the freestream velocity, v_∞, and relates the radius of the body, R, to its influence in gravitationally focusing incident flow. The critical impact parameter defines the radius from the symmetry axis on the infinitely distant plane of the BHL problem *on* which all flow will sweep tangentially past the body, and *within* which all flow will be swept into its leading surface. Figure H.1 shows the family of hyperbolic trajectories in the Charon case, for which v_∞ is 199.4 m/s and ζ_{CR} is 3.102 R_{CH}.

Holding the sphere's mass and radius constant, increasing v_∞ *decreases* the curvature of the incident hyperbolic trajectories, and so decreases the range of the impact parameters ζ for which trajectories will impact the surface. However, increasing v_∞ will increase flux to the surface, as per Equation G.8. The problem's non-gravitating limit can be approached either by decreasing the mass of the sphere or by increasing v_∞, although changes to v_∞ are also reflected in the Mach and Reynolds numbers.

[50] With respect to the sphere's radius; taken throughout this Appendix to be R_{CH}.

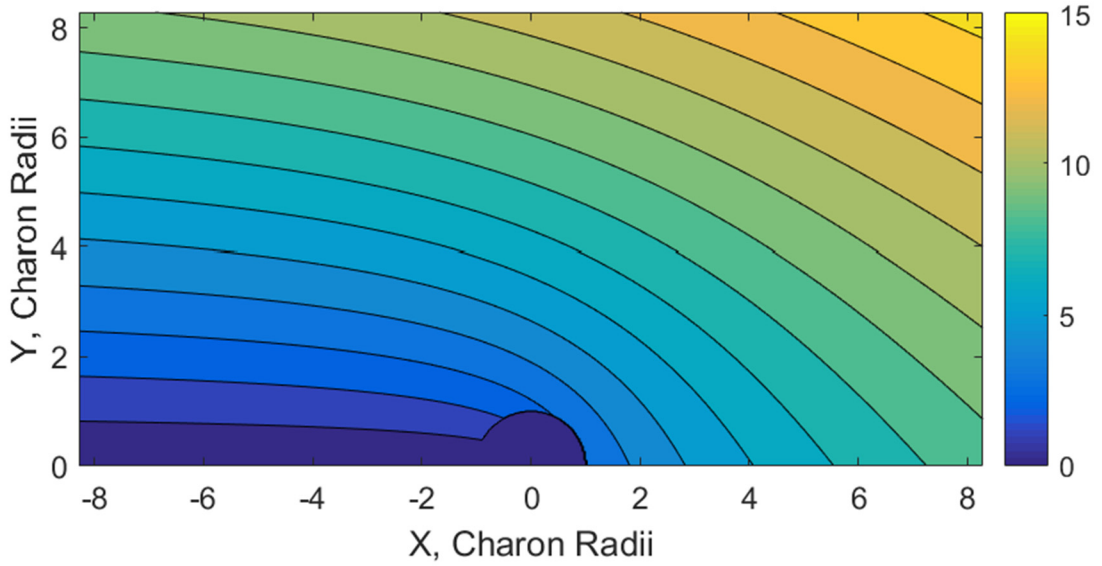

Figure H.1: The analytic solutions for hyperbolic trajectories through the Charon system in the BHL problem drawn at unit spacing for ζ values up to 15. These trajectories are lines of constant ζ, and contours are colored in ζ.

H.3 Parametric Simulations and Results

I performed preliminary simulations at a range of conditions similar to those I calculated for the Charon environs during Chapter 3, and demonstrate here an analog for the medium-heating case from Tucker *et al.* (2015). I select this case in particular because its relatively high density at Charon – 30 times that during the NH encounter – suggests collisional physics at reasonable conditions for the Pluto-Charon system during past epochs. Undergraduate researcher Natalie Atkinson performed a range of additional simulations using the same code; Table H.1 lists the dimensionless groups and freestream parameters for several further interesting cases. For each, a calculation is performed with sticking coefficient 1.0 to steady-state, and then transitioned to a sticking coefficient 0.0

boundary condition at Charon's[51] surface. Each molecule that strikes Charon is then diffusely reflected, and 'hops' along its surface until achieving sufficient energy to escape, either through a reflection event or by collision.

If all material that strikes the surface sticks, the steady-state of a free-molecular flow can be achieved quickly – nearly as soon the first wave of flow has transited the domain. This is complicated by the formation of transient, collisional effects if the freestream density is increased and by the gradual accumulation of atmosphere as the sticking coefficient is transitioned to 0.0. The steady-state timescale for the formation of a collisionless atmosphere ought to be limited by the product of the average number of reflection hops it takes a molecule to escape and the ballistic time for each hop. However, as a nascent atmosphere increases the density near Charon's surface, new portions of the flowfield may grow collisional, promoting the formation of a bow shock structure. Likewise, even a weakly collisional atmosphere will tend to increase Charon's effective radius by enabling the capture of more of the incident flow in a 'snowballing' effect. Thus the steady-state of sticking coefficient 1.0 cases can be reached in $O[10^5]$ s, while sticking coefficient 0.0 cases take at least $O[10^7]$ s to settle, increasing all the while in expense with increasing collision counts. The results in this Appendix, then, generally show coefficient 1.0 cases to steady-state, while 0.0 cases may not yet be mature.

[51] I use 'Charon' throughout this discussion to refer to the gravitating sphere as it has Charon's mass, radius, and surface temperature in each case shown but, in general, the body could be any arbitrary sphere.

Case	Re_∞	M_∞	ζ_{CR}/R_{CH}	n_∞, m^{-3}	T_∞, K	v_∞, m/s	[N_2]	[CH_4]
Med. Heat	0.06	1.2	3.1	3×10^{10}	40.0	199.4	0.02	0.98
1 (Natalie)	0.42	7.6	3.1	6×10^{10}	1.0	199.4	0	1
2 (Natalie)	10.00	10.0	2.0	1.1×10^{12}	1.7	342.0	0	1

Table H.1: The dimensionless groups and freestream parameters for the range of cases analyzed in this Appendix. Each case employs Charon's radius and mass, although their results should hold for systems with the same dimensionless values about spheres of arbitrary size.

Figures H.2 and 3 show the time-averaged number density and translational temperature for the 'medium heating' case after 400,000 s. The effect of T_∞ on the flow is to superpose a thermal velocity onto the bulk velocity of the BHL problem, which results in a more diffuse flow than suggested by that analysis – particularly in the wake. As the sticking coefficient at Charon's surface switches from 1.0 to 0.0, a weakly-collisional atmosphere begins to form; however, Figure H.4 demonstrates that it is not at steady-state when the time-average was captured. The low density of this case is insufficient to produce either a bow shock ahead of Charon or a focused collisional wake. These results can be directly compared to the results for the near-Charon environs predicted with the full Pluto-Charon model of Chapter 3, i.e. Figs. 3.6 and F.2.

The remaining two cases explore higher initial Mach numbers and thus lower freestream temperatures than the 'medium heat' case and so their results are comparable to the BHL analysis, which neglects any thermal velocity component. This tends to tightly focus flow into Charon's wake, as in Natalie's Case 1 (Figs. H.5 and H.6) even as ζ_{CR} is held constant between this and the 'medium heat' case.

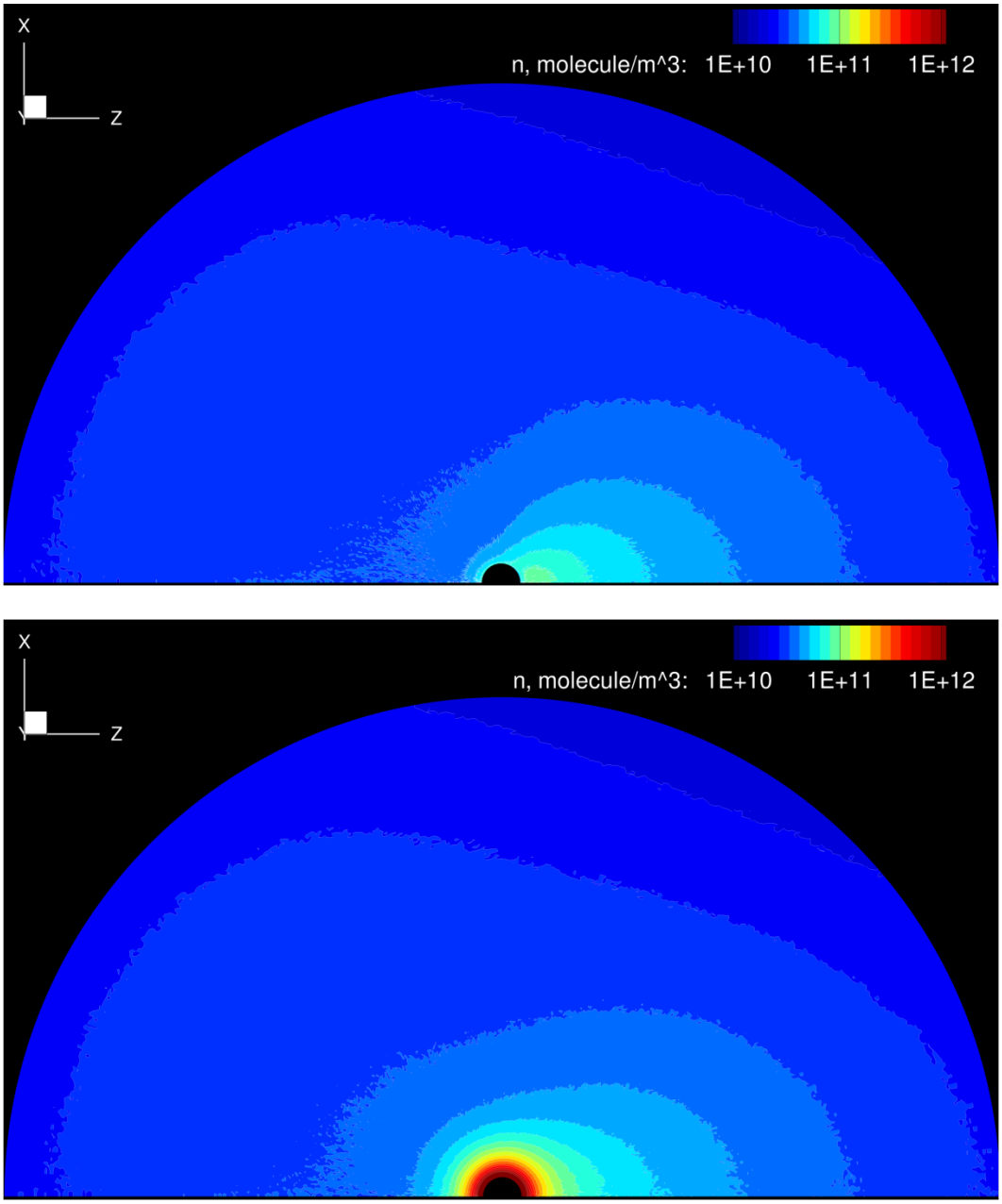

Figure H.2: Number density through an axisymmetric slice of the flowfield at the 'medium heating' conditions; Charon is shown at center. Flow is initially uniformly incident in the +Z direction. (Top) Molecules that strike Charon stick, preventing the formation of an atmosphere. (Bottom) Molecules that strike Charon 'hop' along its surface until they escape, equilibrating to a surface temperature of 53 K at each hop. The resultant atmospheric growth is complex; 'hopping' material collides with the incident flow, increasing Charon's effective radius.

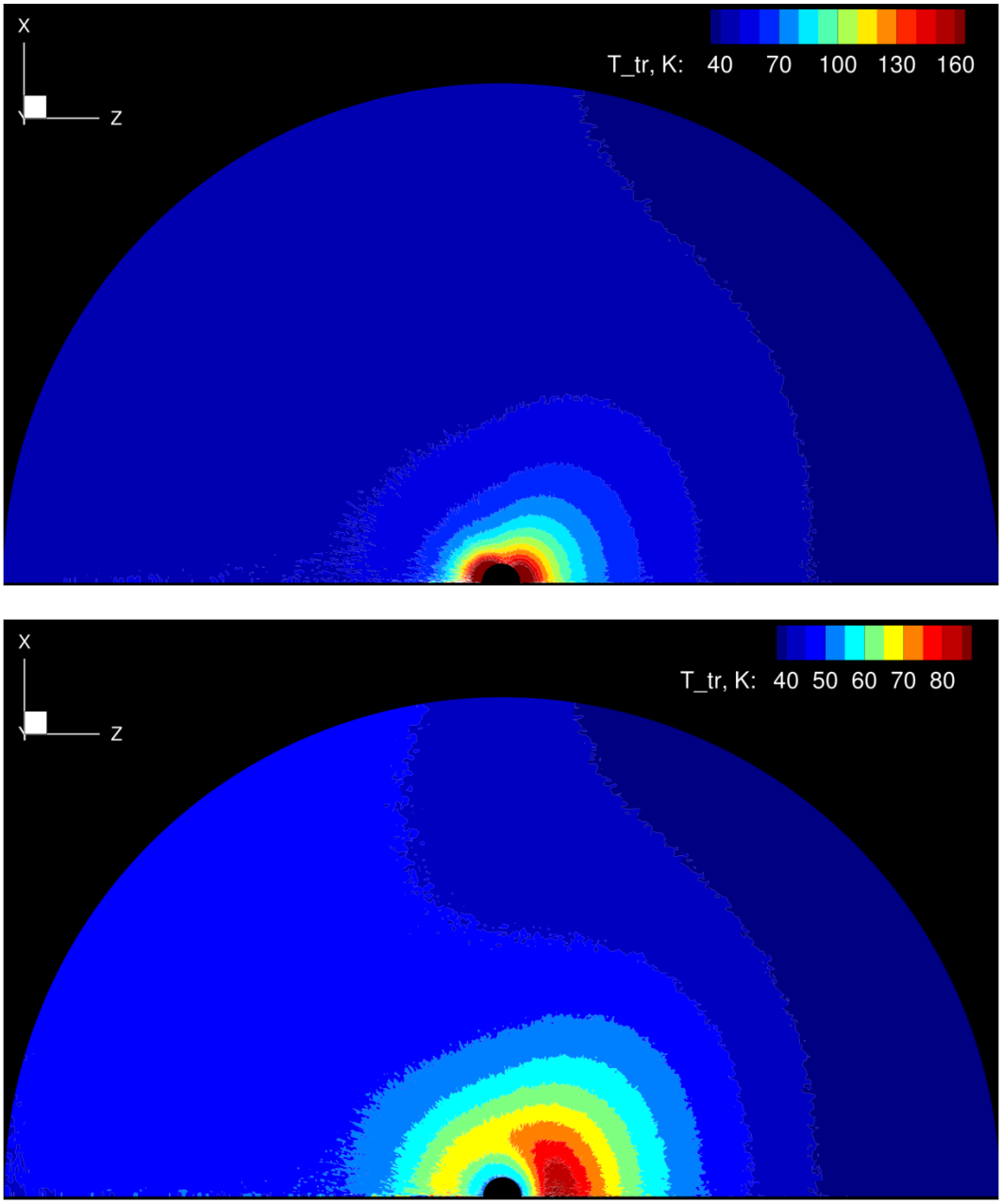

Figure H.3: Translational temperature through an axisymmetric slice for the medium heating case. Note the difference in colorbar scaling. (Top) Flow accelerates as it approaches Charon, creating high T_{TR} regions adjacent to the moon's leading and trailing faces. (Bottom) As the sticking coefficient is switched to 0.0, a nascent atmosphere forms that has equilibrated to the surface condition of 53 K. The flow accelerated past Charon and through its wake remains a high-energy structure that can be compared to Fig. 7 in Chapter 3.

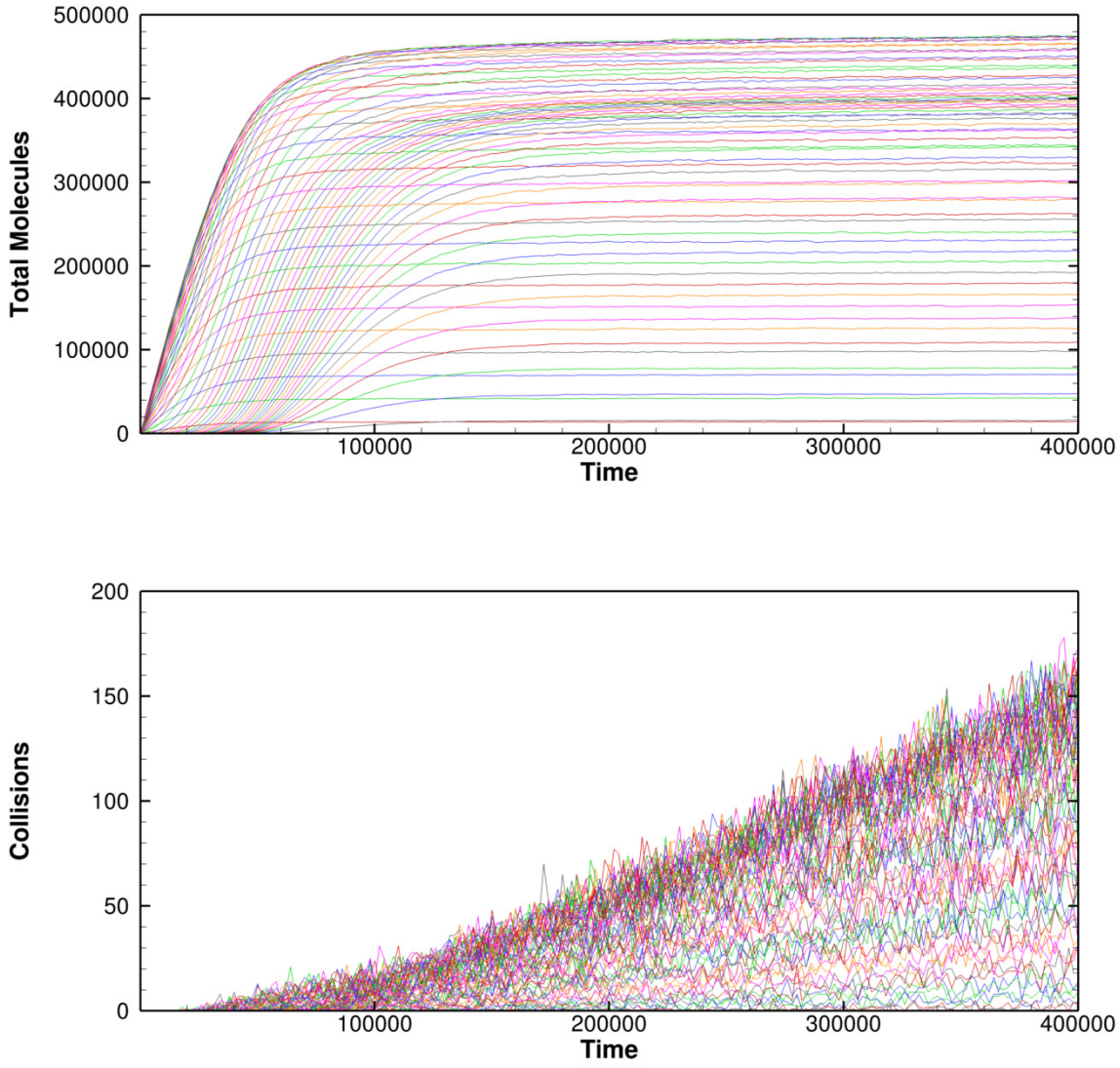

Figure H.4: (Top) In the atmospheric-formation case, the count of molecules per processor throughout the simulation appears to show minimal growth after 200,000 s. However, even this slight accumulation is significant, as it occurs in the nascent, collisional atmosphere. (Bottom) The count of collisions per processor per time-step demonstrates that the problem's steady-state will take far longer to arrive: as the atmosphere grows in density, it begins to collide with and capture additional incident flow.

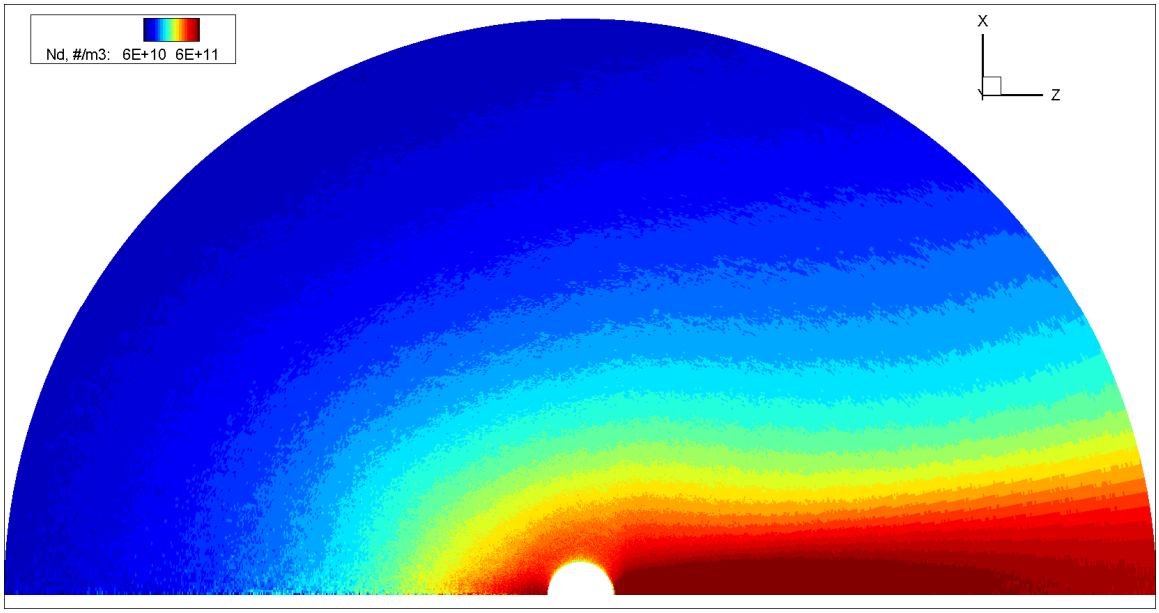

Figure H.5: In a low T_∞ / high M_∞ flow a dense tail forms in the wake of the gravitating sphere, as predicted by the BHL analysis (Case 1 result, for sticking coefficient 1.0).

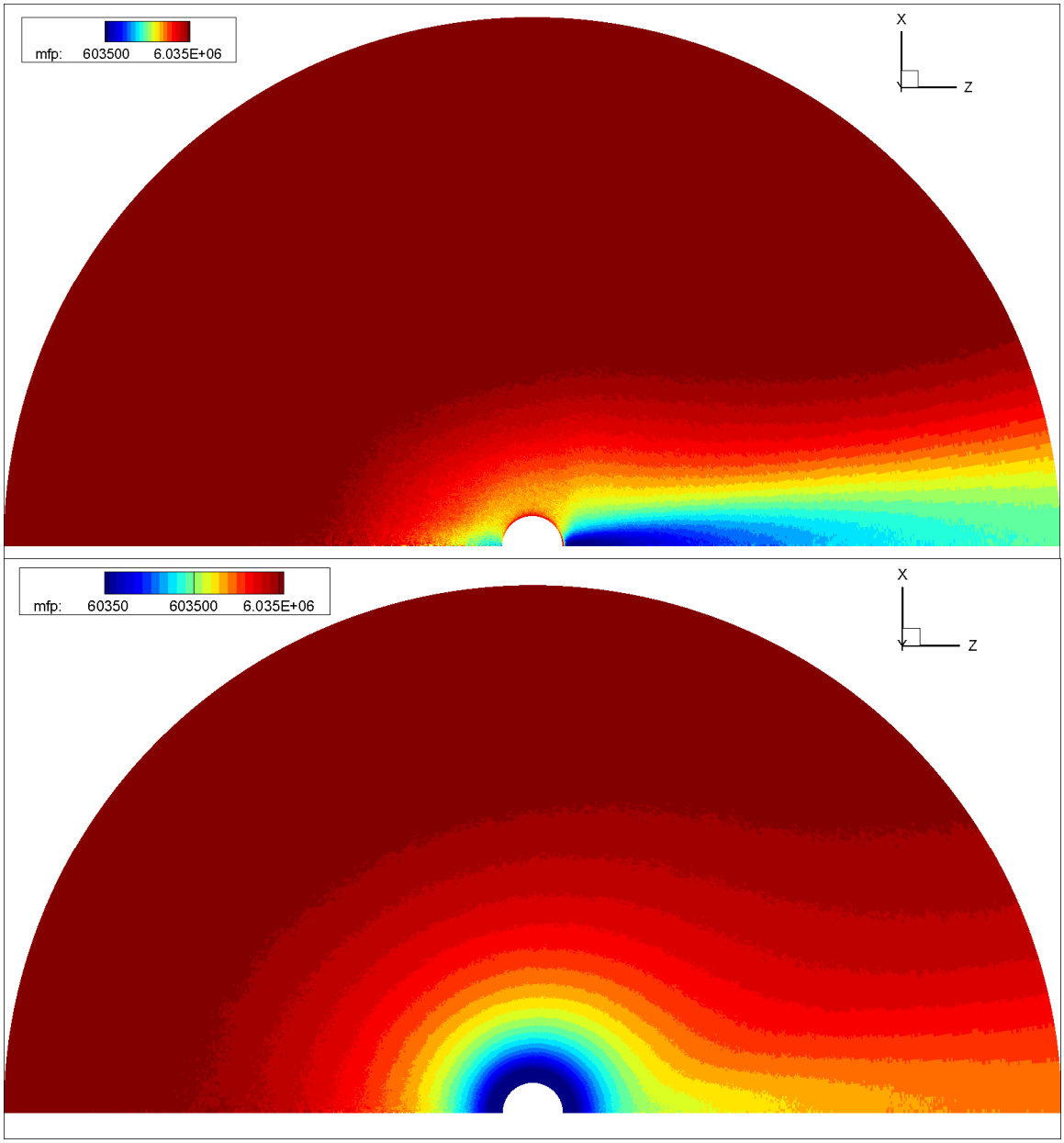

Figure H.6: Mean free path, in m; the scales are set in multiples of R_{CH}, so these also provide a useful estimate of local Knudsen number. (Top) At sticking coefficient 1.0, the most collisional region of the Case 1 flow forms in Charon's wake which approaches $Kn_R \sim 1$. (Bottom) As an atmosphere forms the surface Kn_R drops to 0.1, suggesting a substantially collisional flow could extend to 2-3 R_{CH}. The freestream density in Case 1 is double that for the 'medium heating' case of Tucker *et al.* (2015), and so could reflect a very active plutonian atmosphere.

Case 2 features an n_∞ much higher than any projection for that about Charon, and applies an arbitrary value for v_∞ unrelated to Charon's angular velocity. It features a collisional wake and, for sticking coefficient 0.0, both the formation of a bow shock and atmosphere-wake interaction. Figs. H.7 and H.8 demonstrate these phenomena in contours of number density, mean free path, and translational temperature.

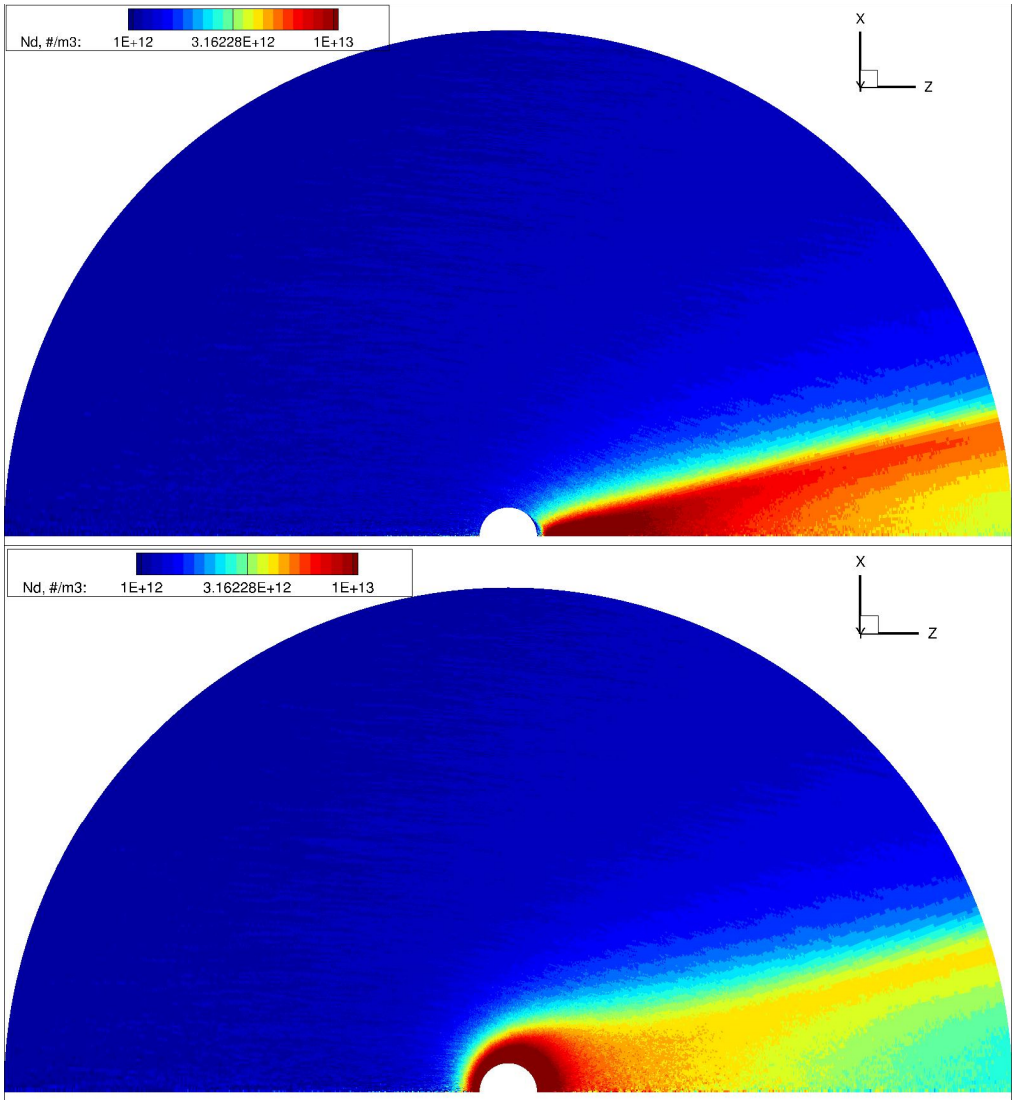

Figure H.7: Number density through the Case 2 flowfield for sticking coefficients of (top) 1.0 and (bottom) 0.0 at Charon's surface; uniform colorbar.

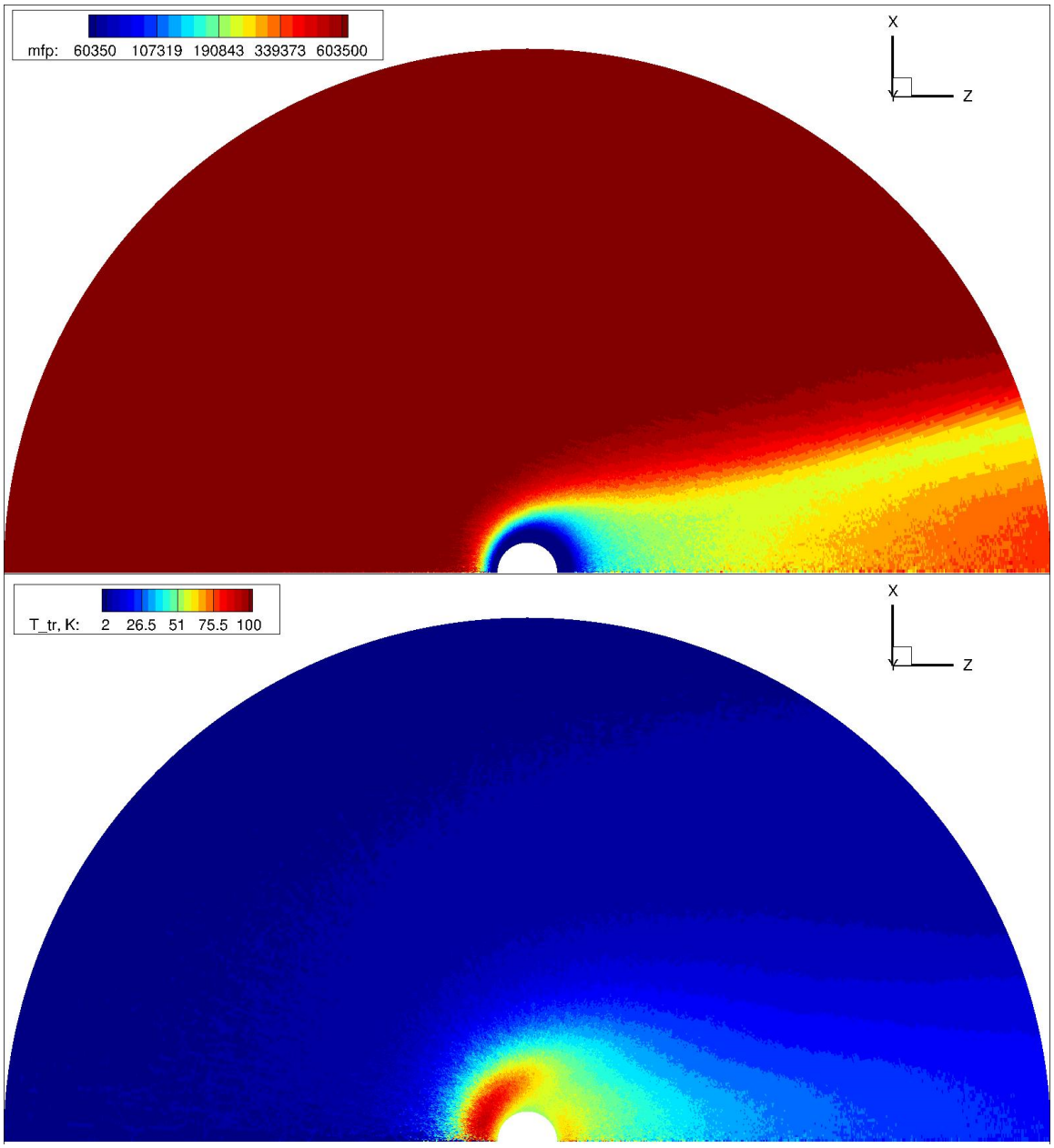

Figure H.8: (Top) Mean free path through the Case 2 flowfield at sticking coefficient 0.0. Kn_R at Charon's surface drops below 0.1, while much of the wake is now collisional. The evident departure of the wake from the symmetry axis may be a transient effect, as this result is not yet at steady-state. (Bottom) Contours of translational temperature show the formation of a bow shock structure on Charon's leading edge.

Appendix I: Further Methodological Notes on Plume Simulations

I.1 Canopy Insensitivity to Non-Inertial Effects

The DSMC reference frame is fixed to Io; prior work (McDoniel, 2015) accounted for non-inertial reference frame effects in simulations of canopy formation at Pele and deduced their influence to be minor. However, Pele is a near-equatorial plume, and Tvashtar near-polar, which could exacerbate such effects. The dimensionless parameter that relates a system's inertial to Coriolis forcing is the Rossby number, calculated from

$$Ro = \frac{U}{Lf} = \frac{U}{L}\frac{T}{4\pi \sin(\theta)}, \tag{I.1}$$

for U a characteristic system velocity, L a characteristic length scale, T the rotational period of Io, and θ the latitude. Rossby numbers of unity or below reflect systems that experience appreciable Coriolis forcing. Using a range of canopy tangential velocities O[100-1000 m/s] for U, and the mean canopy height of 380 km for L, Ro for Tvashtar will reach a minimum of about 3.6 directly above the source, and will never drop below O[10] as the canopy approaches the pole. I check this with an AS-03 stage 4 canopy simulated at Tvashtar's actual location and orientation on Io and computed to steady state, by rotating and resampling the molecules from that calculation within the polar quadrant. The results demonstrate that, as at Pele, non-inertial reference frame effects are only of minor significance in shaping Tvashtar's canopy structure. Figures I.1 through I.3 show these results for the defining canopy isosurfaces and for the depositional pattern of gas onto the surface. They support a key assumption of the parametric simulations, i.e.

that calculations may be performed within the polar quadrant (thus exploiting symmetry axes to reduce computational expense by a factor of four) without any substantial loss of accuracy in representing canopy structure.

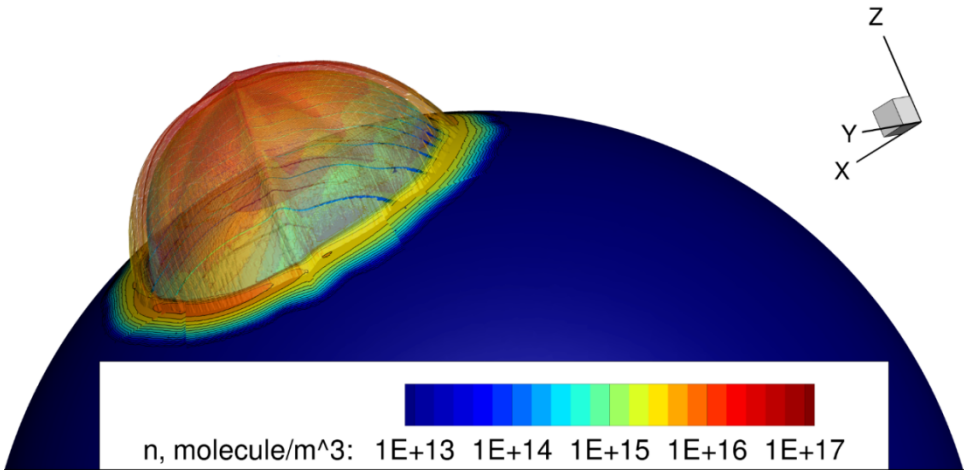

Figure I.1: An AS-03 canopy, computed at Tvashtar's location on Io with non-inertial reference frame effects. The translucent isosurfaces show the canopy shock and the upper and lower boundaries of the suspended gas layer, and are colored by number density, as is Io's surface.

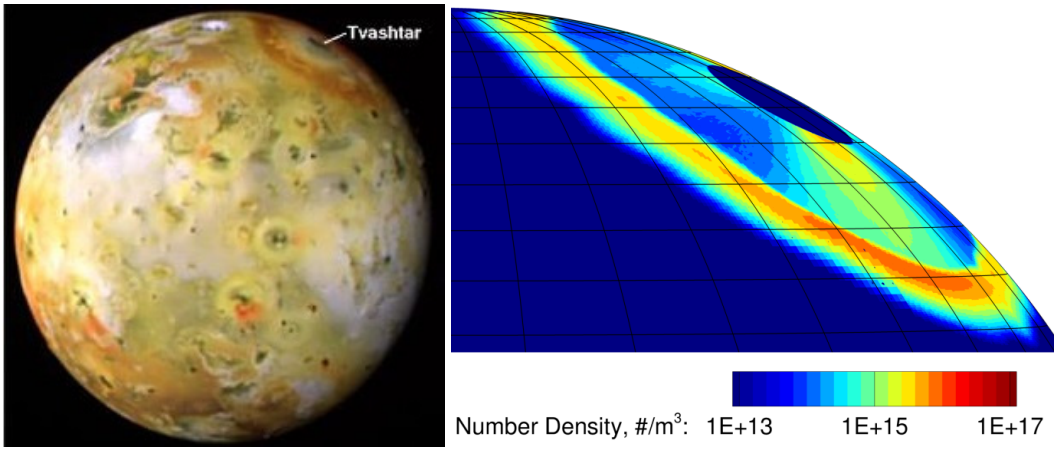

Figure I.2: (Left) In 2001, Galileo captured this image of a mature depositional ring at Tvashtar during I29. (Right): In this view, the Tvashtar vent is placed on the limb and the observation angle is approximately that in the Galileo image. The vent conditions here reflect the 2007 eruption, but the ring location, orientation, and thickness are also comparable to the 2001 observation.

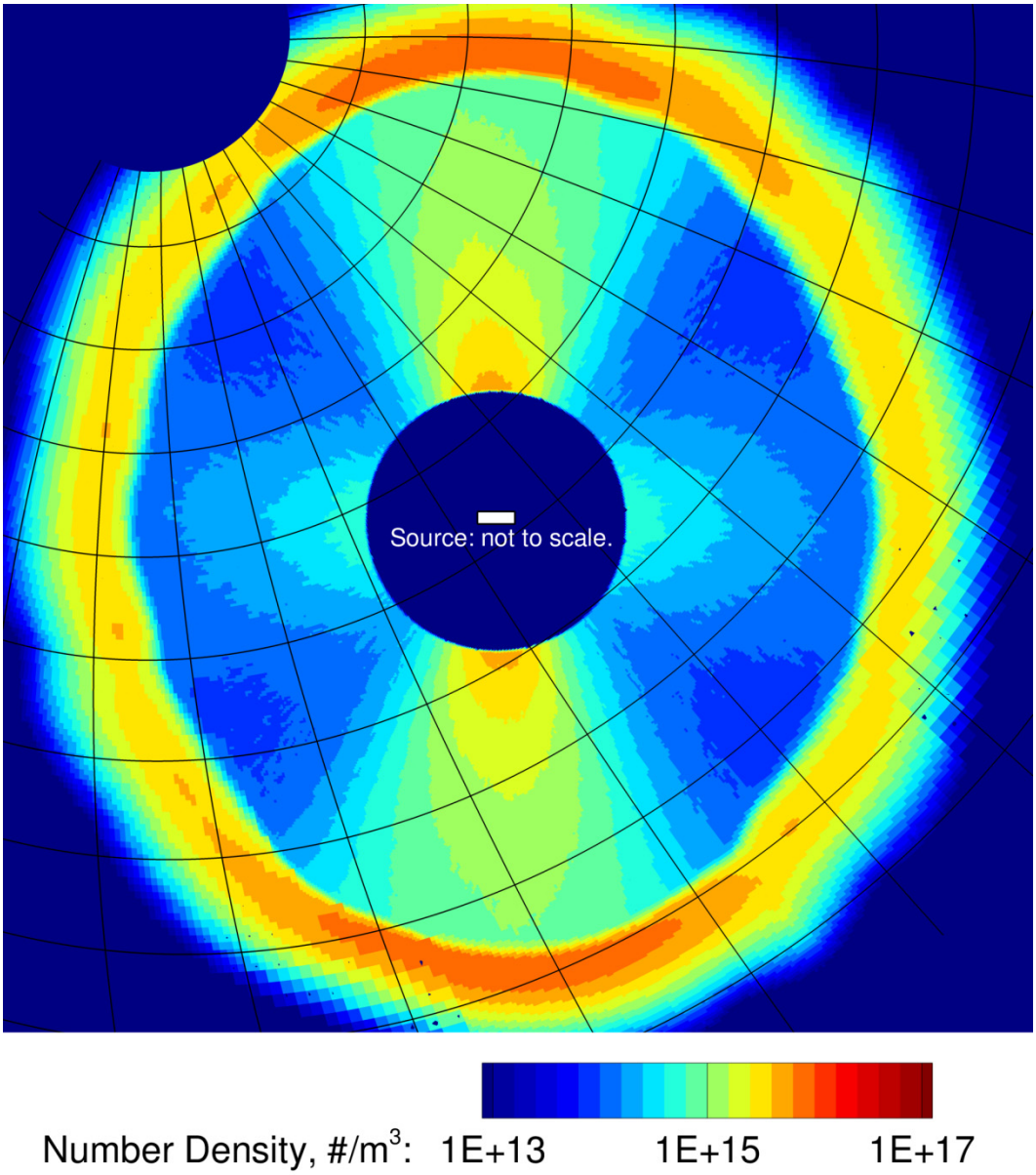

Figure I.3: Number density on the curved surface of Io, positioned directly above the AS-03 source (marked in white). Latitude and longitude are marked in black, and the blank region at Io's north pole reflects the end of the computational domain. Rotation about the pole is CCW. Realistic non-inertial reference frame effects (centrifugal and Coriolis forcing) applied in simulating an eruption at Tvashtar's location provoke only slight deformations of the depositional ring and canopy structure.

I.2 THE 'AXIS BUG' AND DISCUSSION OF A RADIAL WEIGHTING SCHEME.

`WEIGHT_TVASHTAR` adapts a version of the radial weighting scheme tested in the simulations of atmospheric-plume interaction in McDoniel (2015) in an effort to combat the 'axis bug' by which cells along the symmetry axis reduce to infinitesimal size, and therefore house insufficient molecules to sample for collisions. This process introduces instability into the canopy as axis cells fail to support material above them, and inject a narrow column of unphysically ballistic flow into the canopy center. Both Zhang (2004) and McDoniel (2015) explored the possibility of radial weighting schemes emanating outward from the axis that effectively 'clone up' material in polar cells, with mixed results. Cloning can amplify noise, if it occurs on timescales more rapid than the local collision time scale, as the process generates multiple copies of simulation particles that primarily differentiate via collision. This amplification can be counteracted by load balancing – as more simulation particles accumulate in the axis region, processors cluster closer together along the axis, and the grid size is further reduced, perhaps more rapidly than cloned particles can fill it. In general, for his plume-only simulations, McDoniel did not apply spatially variant weighting schemes for these reasons. Instead, for axis-centered simulations, he incorporated a polar cap (preprocessor flag `POLAR_CAP`) that covers the pole with a single processor, forcing larger cells and reducing their tendency to under-represent collisions. The polar cap approach has its own complications, however: within the cap, cells will still shrink rapidly in volume as they approach the pole. Likewise, the tier of processors just outside the cap will still tend to have very small cell sizes approaching the cap, and sharp discrepancies in cell volume at this interface can yield minor unphysical perturbations in the flow. In axis-centered simulations, the polar cap is useful in *mitigating* the axis bug and preventing the sorts of major unphysical instabilities that provoke complete canopy collapse – but it does not correct the root cause of this

'bug:' the inevitable convergence at the axis of the spherical coordinate system. McDoniel (2015) notes that these effects can of course be corrected by performing calculations away from the pole, perhaps at the equator where the surface grid approaches Cartesian or even at the plume's actual location on the surface. Of course, this complicates any exploitation of symmetry axes. In the Tvashtar simulations, all four stages are generally computed in a single quadrant with two symmetry planes and centered at the polar axis. Initial results were promising for test cases that scaled the cap weight modestly[52], reducing its F_{NUM} (increasing its particle count) by a factor of 10. The unphysical increase in density with altitude inside the polar cap column, visible in both McDoniel (2015) for Pele and my own work for Tvashtar, is eliminated, and cells within the cap region tend to be better resolved in particle count. For future work on axis-centered plumes, it may be useful to find a balance between polar cap and a weighting scheme like `WEIGHT_TVASHTAR`.

[52] In an application of constant weight within some distance of the axis, encompassing the polar cap (e.g. 20 km), and a different constant weight outside some critical distance from the pole at which grid sizes have stabilized (e.g. 100-200 km), with a logarithmic scaling between the two.

Appendix J: Relevant Publications and Presentations

J.1 Reviewed Publications

Hoey, W., Yeoh, S., Trafton, L., Goldstein, D., Varghese, P., 2017. "Rarefied Gas Dynamic Simulation of Transfer and Escape in the Pluto-Charon System." *Icarus*, **287**, 87-102. *Chapter 3*

Hoey, W., Ackley, P., Trafton, L., Goldstein, D., Varghese, P., 2016. "DSMC Simulation of Io's Unsteady Tvashtar Plume." *30th Int'l Symp. Rarefied Gas Dynamics, AIP Conf. Proc.* **1786**, 160006:1-8. *Chapter 4*

J.2 Conference Presentations

Goldstein, D., **Hoey, W.**, Prem, P., Atkinson, N., Trafton, L., Varghese, P. "Simple DSMC Simulation of Flow about Spheres – It Ain't Necessarily So Simple." Invited talk; Direct Simulation Monte Carlo 2017 Conference, Santa Fe, NM; Aug. 2017. *Chapter 3* *App. G, H*

Goldstein, D., **Hoey, W.**, Prem, P. "DSMC Simulation of Complex Rarefied Flow Problems: Techniques, Tricks and Applications." Talk; Recent Advances on Particle Systems in Kinetic Theory, Institute for Computational Engineering and Sciences, Austin, TX; May 2017. *Chapter 3* *App. G, H*

Trafton, L., **Hoey, W.**, Ackley, P., Goldstein, D., Varghese, P. "Tvashtar's Plume during the New Horizons Flyby of the Jovian System." Abstract, talk; 48th mtg. Div. Planetary Sciences, Amer. Astronomical Society, Pasadena, CA; Oct. 2016. *Chapter 4* *Chapter 5*

Hoey, W., Ackley, P., Trafton, L. Goldstein, D., Varghese, P. "DSMC Simulation of Io's Unsteady Tvashtar Plume." Abstract, talk; 30th International Symposium on Rarefied Gas Dynamics, Victoria, British Columbia, Canada; Jul. 2016. *Chapter 4*

Hoey, W., Yeoh, S. Trafton, L. Goldstein, D., Varghese, P. "Rarefied Gas Dynamic Simulation of Transfer and Escape in the Pluto-Charon System." Abstract, poster; Lunar and Planetary Science Conference, The Woodlands, TX; Mar. 2016. *Chapter 3*

Hoey, W., Walker, A., Goldstein, D., Varghese, P., Trafton, L. "On the Simulation of Rarefied Planetary Atmospheres with the DSMC Method." Abstract, talk; Direct Simulation Monte Carlo 2015 Conference, Kapaa, HI; Sep. 2015. *Chapter 2* *Chapter 3* *App. A*

Hoey, W., Walker, A., Goldstein, D., Varghese, P., Trafton, L. "Application of the DSMC Method in Modeling Earth's Rarefied Upper Atmosphere." Abstract, poster; American Geophysical Union fall meeting, San Francisco, CA; Dec. 2014. *Chapter 2*

Hoey, W., Walker, A., Goldstein, D., Varghese, P., Trafton, L. "Simulation of Global Flow in Io's Rarefied Atmosphere." Talk; Io Workshop, Southwest Research Institute Planetary Science Directorate, Boulder, CO; Oct. 2013. *App. A*

Hoey, W., Walker, A., Goldstein, D., Varghese, P., Trafton, L. "Simulation of Global Flow in Io's Rarefied Atmosphere." Abstract, poster; 45th mtg. Div. Planetary Sciences, Amer. Astronomical Society, Denver, CO; Oct. 2013. *App. A*

J.3 REPORTS

Hoey, W., Walker, A., 2014. "Application of the DSMC Method in Modeling Earth's Rarefied Upper Atmosphere." *Los Alamos Space Weather Summer School Report*, **LA-UR 15-20136**: 37-44. *Chapter 2*

References

[1] Bagenal, F. *et al.*, 2004. Jupiter: The Planet, Satellites, Magnetosphere. Cambridge University Press.

[2] Bagenal, F., *et al.*, 2016. Pluto's interaction with its space environment: Solar wind, energetic particles, and dust. *Science* **351**, aad9045 (8 pp).

[3] Belehaki, A., Stanislawska, I, Lilensten, J., 2009. An overview of ionosphere – thermosphere models available for space weather purposes, *Space Science Review*, Vol. **147**, 271-313.

[4] Beth, A., Garnier, P., Toublanc, D., Dandouras, I., Mazelle, C., Kotova, A., 2014. Modeling the satellite particle population in planetary exospheres: Application to Earth, Titan, and Mars. *Icarus* **227**, 21–36.

[5] Berg, J., Goldstein, D.B., Varghese, P.L., Trafton, L.M., 2016. DSMC simulation of Europa water vapor plumes, *Icarus* **277** 370-380.

[6] Bird, G. A. Molecular Gas Dynamics and the Direct Simulation of Gas Flows. Oxford University Press: New York, NY, 1994.

[7] Blondin, J. M., Richards, M. T., Malinowski, M. L., 1995. Hydrodynamic simulations of the mass transfer in Algol. *Astrophysical Journal* **445**, 939–946.

[8] Borgnakke, C., Larsen, P. S., 1975. Statistical collision model for Monte Carlo simulation of polyatomic gas mixture. *J. Comp. Phys.* **18**, 405-420.

[9] de Kleer, K., Skrutskie, M., Leisenring, J., Davies, A. G., *et al*., 2017. Multi-phase volcanic resurfacing at Loki Patera on Io, *Nature* **545**, 199-202.

[10] Drob, D. P., Emmert, J. T., Crowley, G., Picone, J. M., *et al.*, 2008. An empirical model of the Earth's horizontal wind fields: HWM07, *Journal of Geophysical Research*, **113**, A12304.

[11] Edgar, R., 2004. A review of Bondi–Hoyle–Lyttleton accretion. *New Astronomy Reviews*, **48**, 843-859.

[12] Elliot, J.L., Dunham, E.W., Bosh, A.S., Slivan, S.M., Young, L.A., Wasserman, L.H., Millis, R.L., 1989. Pluto's atmosphere. *Icarus* **77**, 148–170.

[13] Elliot, J.L., *et al.*, 2007. Changes in Pluto's atmosphere: 1988–2006. *Astrn. J.* **134**, 1–13.

[14] Garcia, A. L., Wagner, W., 2006. Generation of the Maxwellian inflow distribution, *Journal of Chemical Physics*, Vol. **217**, 693–708.

[15] Geissler, P., McEwan, A., Philips, C., Keszthelyi, L., Spencer, J., 2004. Surface changes on Io during the Galileo mission, *Icarus* **169**, 29-64.

[16] Gladstone, G. R., Stern, S. A., *et al.*, 2016. The atmosphere of Pluto as observed by New Horizons. *Science* **351**, aad8866 (6 pp).

[17] Grundy, W.M., *et al.*, 2016. The formation of Charon's red poles from seasonally cold-trapped volatiles. *Nature*, **19340** (4 pp.).

[18] Grundy, W.M., Olkin, C.B., Young, L.A., Holler, B. J., 2014. Near-infrared spectral monitoring of Pluto's ices II: Recent decline of CO and N_2 ice absorptions. *Icarus* **235** 220-224.

[19] Halir, R., and Flusser, J., 1998. Numerically stable direct least squares fitting of ellipses.

[20] Huang, T., Hickey, M., 2007. On the latitudinal variations of the non-periodic response of minor species induced by a dissipative gravity-wave packet in the MLT region, *J. Atmospheric and Solar-Terrestrial Physics*, Vol. **69**, 741-757.

[21] Hubbard, W.B., Hunten, D.M., Dieters, S.W., Hill, K.M., Watson, R.D., 1988. Occultation evidence for an atmosphere on Pluto. *Nature* **336**, 452–454.

[22] Hubbard, W.B., Yelle, R.V., Lunine, J.I., 1990. Nonisothermal Pluto atmosphere models. *Icarus* **84**, 1-11.

[23] Huebner, W. F., Keady, J. J., Lyon, S. P., 1992. Solar photo rates for planetary atmospheres and atmospheric pollutants, *Astrophysics and Space Science*, Vol. **195**, 1-294.

[24] Huebner, W. F., Mukherjee, J., 2015. Photoionization and photodissociation rates in solar and blackbody radiation fields. *Planetary and Space Sci.*, **106**, 11-45.

[25] Hunten, D.M., Watson, A.J., 1982. Stability of Pluto's atmosphere. *Icarus* **51**, 665–667.

[26] Ingersoll, A.P., 1990. Dynamics of Triton's atmosphere. *Nature* **344**, 315–317.

[27] Jessup, K.L., Spencer, J., Ballester, G.E., Howell, R.R., Roesler, F., Vigil, M., Yelle, R. 2004. The atmospheric signature of Io's Prometheus plume and anti-Jovian hemisphere: Evidence for a sublimation atmosphere, *Icarus* **169**, 197-215.

[28] Jessup, K.L., Spencer, J.R., 2012. Characterizing Io's Pele, Tvashtar and Pillan plumes: Lessons learned from Hubble, *Icarus* **218** 378-405.

[29] Krasnopolsky, V.A., 1999. Hydrodynamic flow of N_2 from Pluto. *J. Geophys. Res.* **104**, 5955–5962.

[30] Lellouch, E., de Bergh, C., Sicardy, A., Forget, F., Vangvichith, M., Käufl, H.-U, 2015. Exploring the spatial, temporal, and vertical distribution of methane in Pluto's atmosphere. *Icarus* **246** 268-278.

[31] Lopes, R.M.C., Kamp, L.W., Smythe, W.D., et al., 2003. Lava lakes on Io: observations of Io's volcanic activity from Galileo NIMS during the 2001 fly-bys, Icarus 169 140-174.

[32] Marsh, D. R., Solomon, S. C., Reynolds, A. E., 2004. Empirical model of nitric oxide in the lower thermosphere, *Journal of Geophysical Research*, **109**, 2156-2202.

[33] McDoniel, W.J., Goldstein, D.B., Varghese, P.L., Trafton, L.M., Buchta, D.A., Freund, J., Kieffer, S.W., 2011. Simulating Irregular Source Geometries for Ionian Plumes, *Rarefied Gas Dynamics, AIP Conference Proceedings* **1333**, 1157-1162

[34] McDoniel, W.J., Goldstein, D.B., Varghese, P.L., Trafton, L.M., 2015. Three-dimensional simulation of gas and dust in Io's Pele plume, *Icarus* **257**, 251-274.

[35] McDoniel, W.J., 2015. Realistic Simulation of Io's Pele Plume and its Effects on Io's Atmosphere. PhD dissertation, University of Texas at Austin.

[36] McNutt Jr., R.L., 1989. Models of Pluto's upper atmosphere. *Geophys. Res. Lett.* **16**, 1225–1228.

[37] Milazzo, M. P., Keszthelyi, L. P., Radebaugh, J., *et al.*, 2005. Volcanic activity at Tvashtar Catena, Io. *Icarus* **179**, 235-251.

[38] Millis, R.L., Wasserman, L.H., Franz, O.G., Nye, R.A., Elliot, J.L., Dunham, E.W., Bosh, A.S., Young, L.A., Slivan, S.M., Gilmore, A.C., 1993. Pluto's radius and atmosphere: Results from the entire 9 June 1988 occultation data set. *Icarus* **105**, 282–297.

[39] Moore, C.H., Goldstein, D.B., Varghese, P.L., Trafton, L.M., Stewart, B., 2009. 1-D DSMC simulation of Io's atmospheric collapse and reformation during and after eclipse. *Icarus* **201**, 585–597.

[40] Moore. C. H., 2011. Monte Carlo simulation of the Jovian plasma torus interaction with Io's atmosphere and the resultant aurora during eclipse. PhD dissertation, University of Texas at Austin.

[41] Morris, A.B., Goldstein, D.B., Varghese, P.L., Trafton, L.M., 2015. Approach for modeling rocket plume impingement and dust dispersal on the moon. *J Spacecraft Rockets* **52**, 362–374.

[42] Moullet, A., Lellouch, E., Moreno, R., Gurwell, M.A., Moore, C., 2008. First disk-resolved millimeter observations of Io's surface and atmosphere. *Astronomy and Astrophysics* **482**, 279-292.

[43] Nanbu, K., 1986. Theoretical basis of the direct simulation Monte Carlo method. In: Rarefied Gas Dynamics: 15th International Symposium Proceedings 1, Teubner, Stuttgart, 369–383.

[44] Olkin, C., *et al.* 2014. Pluto's atmospheric structure from the July 2007 stellar occultation. *Icarus* **239** 15-22.

[45] Olkin, C., *et al.* 2015. Evidence that Pluto's atmosphere does not collapse from occultations including the 2013 May 04 event. *Icarus* **246** 220-225.

[46] Olkin, C., Young, E., Young, L., Grundy, W., Schmitt, B., Tokunaga, A., Owen, T., Roush, T., Terada, H., 2007. Pluto's spectrum from 1.0 to 4.2 μm: Implications for surface properties. *Astr. J.* **133**, 420–431.

[47] Owen, T.C., Roush, T.L., Cruikshank, D.P., Elliot, J.L., Young, L.A., de Bergh, C., Schmitt, B., Geballe, T.R., Brown, R.H., Bartholomew, M.J, 1993. Surface ices and the atmospheric composition of Pluto. *Science* **261**, 745–748.

[48] Ozawa, T., 2007. Improved Chemistry Models for DSMC Simulations of Ionized Rarefied Hypersonic Flows. PhD dissertation, Pennsylvania State University.

[49] Parsons, N., Levin, D.A., van Duin, A.C.T., 2013. Molecular dynamics based chemistry models of hypervelocity collisions of O(3P) + SO2(X, 1A1) in DSMC. *J. of Chem. Phys.* **138**, 044316.

[50] Pasachoff, J.M., Souza, S.P., Babcock, B.A., Ticehurst, D.R., Elliot, J.L., Person, M.J., Clancy, K.B., Roberts Jr., L.C., Hall, D.T., Tholen, D.J., 2005. The structure of Pluto's atmosphere from the 2002 August 21 stellar occultation. *Astron. J.* **129**, 1718–1723.

[51] Person, M.J., *et al.*, 2008. Waves in Pluto's upper atmosphere. *Astron. J.* **136**, 1510–1518.

[52] "PIA02584: Eruption at Tvashtar Catena on Io." NASA JPL Photojournal, NASA / JPL-Caltech / University of Arizona, 2001. <https://photojournal.jpl.nasa.gov/catalog/PIA02584>

[53] Picone, M., Hedin, A. E., Drob, D., 2002. NRLMSISE-00 empirical model of the atmosphere: Statistical comparisons and scientific issues, *Journal of Geophysical Research*, Vol. **107**, No. A12, 1468-1483.

[54] Prem, P., Artemieva, N.A., Goldstein, D.B., Varghese, P.L., Trafton, L.M., 2015. Transport of water in a transient impact-generated lunar atmosphere. *Icarus* **255**, 148–158.

[55] Prem, P., 2017. DSMC Simulations of Volatile Transport in a Transient Lunar Atmosphere and Ice Deposition in Cold Traps after a Comet Impact. PhD dissertation, University of Texas at Austin.

[56] Protopapa, S., Boehnhard, H., Herbst, T. M., Cruikshank, D. P., Grundy, W. M., Merlin, F., Olkin, C.B., 2008. Surface characterization of Pluto and Charon by L and M band spectra. *Astronomy and Astrophysics* **490** 365-375.

[57] Rathbun, J.A., Spencer, J.R., Lopes, R.M., Howell, R.R., 2014. Io's active volcanoes during the New Horizons era: Insights from New Horizons imaging, *Icarus* **231** 261-272.

[58] Rusch, D. W., Gerard, J., Fesen, C. G., 1991. The diurnal variation of NO, N(^{2}D), and ions in the thermosphere: A comparison of satellite measurements to a model, *Journal of Geophysical Research*, Vol. **96**, No. A7, 11331-11339.

[59] Saito, M., Matsumoto, M., 2006. SIMD-Oriented Fast Mersenne Twister: a 128-bit Pseudorandom Number Generator, *Monte Carlo and Quasi-Monte Carlo Methods 2006,* 607-622.

[60] Schlatter T. W., 2009. Atmospheric Composition and Vertical Structure, National Oceanic and Atmospheric Administration (NOAA), Boulder, CO.

[61] Sicardy, B., Widemann, T., Lellouch, E., *et al.*, 2003. Large changes in Pluto's atmosphere as revealed by recent stellar occultations. *Nature* **424**, 168–170.

[62] "Surface temperature and appearance of Saturn's moons Mimas and Tethys." PIA16198: A Pair of 'Pac-Men,' NASA Cassini-Huygens Multimedia, NASA / JPL-Caltech / GSFC / SwRI, 2011. <https://www.nasa.gov/mission_pages/cassini/multimedia/pia16198.html>

[63] Spencer, J.R., Stansberry, J.A., Trafton, L.M., Young, E.F., Binzel, R.P., Croft, S.K., 1997. Volatile transport, seasonal cycles, and atmospheric dynamics on Pluto. In: Stern, S.A., Tholen, D.J. (Eds.), Pluto and Charon. University of Arizona Press, Tucson, pp. 435–473.

[64] Spencer, J.R., Stern, S.A., *et al*., 2007. Io volcanism seen by new horizons: a major eruption of the Tvashtar volcano, *Science* **318**, 240-243.

[65] Stern, S.A., 1981. Theoretical investigations of the atmospheric environment of Pluto. Thesis, University of Texas, Austin. 232 pp.

[66] Stern, S.A., *et al.*, 2015. The Pluto system: Initial results from its exploration by New Horizons. *Science* **350**, aad1815 (8 pp).

[67] Stern, S.A., *et al.*, 2016. New Horizons constraints on Charon's present day atmosphere. *Icarus* (submitted).

[68] Stewart, B.D., Pierazzo, E., Goldstein, D.B., Varghese, P.L., Trafton, L.M., 2011. Simulations of a comet impact on the Moon and associated ice deposition in polar cold traps. *Icarus* **215**, 1–16.

[69] Stewart, B.D., 2010. Numerical Simulations of the Flow Produced by a Comet Impact on the Moon and its Effects on Ice Deposition in Cold Traps. PhD dissertation, University of Texas at Austin.

[70] Strobel, D.F., 2008. N_2 escape rates from Pluto's atmosphere. *Icarus* **193**, 612–619.

[71] Tian, F., Toon, O., 2005. Hydrodynamic escape of nitrogen from Pluto. *Geophys. Res. Lett.* **32**, L18201.

[72] Trafton, L.M., 1990. A two-component volatile atmosphere for Pluto. 1. The bulk hydrodynamic escape regime. *Astrophys. J.* **359**:521–523.

[73] Trafton, L.M., Hunten, D.M., Zahnle, K.J., McNutt Jr., R.L., 1997. Escape processes at Pluto and Charon. In: Stern, S.A., Tholen, D.J. (Eds.), Pluto and Charon. University of Arizona Press, Tucson, pp. 475–522.

[74] Trafton, L.M., Stern, S.A., 1983. On the global distribution of Pluto's atmosphere. *Astrophys. J.* **267**, 872–881.

[75] Tucker, O.J., Erwin, J.T., Deighan, J.I., Volkov, A.N., Johnson, R.E., 2012. Thermally driven escape from Pluto's atmosphere: A combined fluid/kinetic model. *Icarus* **217**, 408–415.

[76] Tucker, O.J., Johnson, R. E., Young, L.A., 2015. Gas transfer in the Pluto–Charon system: A Charon atmosphere. *Icarus* **246**, 291–297.

[77] Vincenti, W. G., Kruger, C. H., 1965. Introduction to Physical Gas Dynamics. John Wiley & Sons, Inc.

[78] Volkov, A.N., Johnson, R.E., Tucker, O.J., Erwin, J.T., 2011. Thermally driven atmospheric escape: Transition from hydrodynamic to Jeans escape. *Astrophys. J. Lett.* **729**:L24 (5 pp).

[79] Wagner, W., 1992. A convergence proof for Bird's direct simulation Monte Carlo method for the Boltzmann equation. *J. Stat. Phys.* **66**, 1011–1044.

[80] Walker, A.C., 2012. A comprehensive numerical model of Io's chemically-reacting sublimation driven atmosphere and its interaction with the Jovian plasma torus. PhD dissertation, University of Texas at Austin.

[81] Walker, A.C., Gratiy, S.L., Goldstein, D.B., Moore, C.H., Varghese, P.L., Trafton, L.M., Levin, D.A., Steward, B., 2010. A comprehensive numerical simulation of Io's sublimation-driven atmosphere. *Icarus* **207**, 409–432.

[82] Walker, A.C., Moore, C.H., Goldstein, D.B., Varghese, P.L., Trafton, L.M., 2012. A parametric study of Io's thermophysical surface properties and subsequent numerical atmospheric simulations based on the best fit parameters. *Icarus* **220**, 225–253.

[83] Yelle, R.V., Elliot, J.L., 1997. Atmospheric structure and composition: Pluto and Charon. In: Stern, S.A., Tholen, D.J. (Eds.), Pluto and Charon. University of Arizona Press, Tucson, pp. 347–390.

[84] Yeoh, S.K., Chapman, T.A., Goldstein, D.B., Varghese, P.L., Trafton, L.M., 2015. On understanding the physics of the Enceladus south polar plume via numerical simulation. *Icarus* **253**, 205–222.

[85] Yeoh, S.K., 2015. On Understanding the Physics and Source Conditions of the Enceladus South Polar Plume via Numerical Simulation. PhD dissertation, University of Texas at Austin.

[86] Young, E.F., *et al.*, 2008. Vertical structure in Pluto's atmosphere from the 2006 June 12 stellar occultation. *Astron. J.* **136**, 1757–1769.

[87] Young, L.A., Elliot, J.L., Tokunaga, A., de Bergh, C., Owen, T., 1997. Detection of gaseous methane on Pluto. *Icarus* **127**, 258–270.

[88] Zalucha, A. M., Gulbis, A. A. S., Zhu, X., Strobel, D. F., Elliot, J. L., 2011. An analysis of Pluto occultation light curves using an atmospheric radiative-conductive model. *Icarus* **211** 804–818.

[89] Zhang, J., 2004. Simulation of Gas Dynamics, Radiation, and Particulates in Volcanic Plumes on Io. PhD dissertation, University of Texas at Austin.

[90] Zhang, J., Goldstein, D.B., Varghese, P.L., Gimelshein, N.E., Gimelshein, S.F., Levin, D.A., 2003. Simulation of gas dynamics and radiation in volcanic plumes on Io. *Icarus* **163**, 182–197.

[91] Zhang, J., Goldstein, D.B., Varghese, P.L., Trafton, L.M., Moore, C., Miki, K., 2004. Numerical modeling of Ionian volcanic plumes with entrained particulates. *Icarus* **172**, 479–502.

[92] Zhu, X., Strobel, D. F., Erwin, J. T., 2014. The density and thermal structure of Pluto's atmosphere and associated escape processes and rates. *Icarus* **228**, 301–314.

Vita

William Andrew Hoey was born in Norfolk, Virginia. He received his B.S. from the University of Notre Dame in 2012 and his M.S. from the University of Texas in 2014, both in Aerospace Engineering. He began his graduate studies at the University of Texas in 2012. While with the Computational Fluid Physics Laboratory, he researched a range of topics in the simulation of rarefied planetary atmospheric and volcanic processes on Io, Earth, and in the Pluto-Charon system with Direct Simulation Monte Carlo (DSMC) methods under the guidance and supervision of Profs. Goldstein and Varghese in the Dept. of Aerospace Engineering and Dr. Trafton in the Dept. of Astronomy. He has broad research interests in the planetary sciences, specifically in the simulation of atmospheres and plumes; other interests include rarefied gas dynamics, computational fluid dynamics, high-performance computing, and topics in numerical analysis and model development. His personal interests skew toward mountains, dogs, and the arts and humanities.

"When I heard the learn'd astronomer,

When the proofs, the figures, were ranged in columns before me,

When I was shown the charts and diagrams, to add, divide, and measure them,

When I sitting heard the astronomer where he

lectured with much applause in the lecture-room,

How soon unaccountable I became tired and sick,

Till rising and gliding out I wander'd off by myself,

In the mystical moist night-air, and from time to time,

Look'd up in perfect silence at the stars."

Walt Whitman, Drum Taps, 1865.

Email: whoey@utexas.edu; wahoey2@gmail.com. This dissertation typed by the author.